REPORT DOCUMENTATION PAGE

Public Reporting burden for this collection of information is estimated to average 1 hour per response, including the time for reviewing instructions, searching existing data sources, gathering and maintaining the data needed, and completing and reviewing the collection of information. Send comment regarding this burden estimates or any other aspect of this collection of information, including suggestions for reducing this burden, to Washington Headquarters Services, Directorate for information Operations and Reports, 1215 Jefferson Davis Highway, Suite 1204, Arlington, VA 22202-4302, and to the Office of Management and Budget, Paperwork Reduction Project (0704-0188,) Washington, DC 20503.

1. AGENCY USE ONLY (Leave Blank)	2. REPORT DATE 05-06-00	3. REPORT TYPE AND DATES COVERED Final

4. TITLE AND SUBTITLE Particulate Sol-Gel (PSG) Synthesis and Characterization of $LiMO_2$ (M=Ni, $Ni_{0.75}Co_{0.25}$) Using the Thermal and Mass Spectrometry Analyses Work Station

5. FUNDING NUMBERS

DAAG55-97-1-0077

6. AUTHOR(S)
Chun-Chieh Chang and P.N. Kumta

7. PERFORMING ORGANIZATION NAME(S) AND ADDRESS(ES)
Carnegie Mellon University, Dept. of Materials Sci. and Eng., 5000 Forbes Ave., Pittsburgh, Pa. 15213

8. PERFORMING ORGANIZATION REPORT NUMBER

9. SPONSORING / MONITORING AGENCY NAME(S) AND ADDRESS(ES)

U. S. Army Research Office
P.O. Box 12211
Research Triangle Park, NC 27709-2211

10. SPONSORING / MONITORING AGENCY REPORT NUMBER

ARO 36539.1-CH-RIP

11. SUPPLEMENTARY NOTES
The views, opinions and/or findings contained in this report are those of the author(s) and should not be construed as an official Department of the Army position, policy or decision, unless so designated by other documentation.

12 a. DISTRIBUTION / AVAILABILITY STATEMENT

Approved for public release; distribution unlimited.

12 b. DISTRIBUTION CODE

13. ABSTRACT (Maximum 200 words)

See Attached Report

14. SUBJECT TERMS
Particulate Sol-Gel, Fine Powders, Lithiated Transition Metal Oxide, Mass Spectroscopy, Thermal Analysis, Potentiostat

15. NUMBER OF PAGES 273

16. PRICE CODE

17. SECURITY CLASSIFICATION OR REPORT UNCLASSIFIED	18. SECURITY CLASSIFICATION ON THIS PAGE UNCLASSIFIED	19. SECURITY CLASSIFICATION OF ABSTRACT UNCLASSIFIED	20. LIMITATION OF ABSTRACT UL

NSN 7540-01-280-5500

Enclosure 1

20000707 039

DTIC QUALITY INSPECTED 4

FINAL PROJECT REPORT

Particulate Sol-Gel Synthesis and Characterization of LiMO$_2$ (M=Ni, Ni$_{0.75}$Co$_{0.25}$) Using the Thermal and Mass Spectrometry Analyses Work-Station

Report Submitted by:

Chun-Chieh Chang and Prashant N. Kumta

Abstract

Lithiated transition metal oxides, $LiMO_2$ (M= Ni, Co, Mn) are useful cathode materials for high voltage 4V Li-ion batteries. Among these, $LiCoO_2$ and $LiNiO_2$ have received considerable attention. Solid state processes are conventionally used for synthesizing these oxides. These methods do not in general provide good control of the stoichiometry, particle size, point defects and morphology. In the present study, the particulate sol-gel (PSG) process has been developed for synthesizing electrochemically active $LiNiO_2$ and $LiNi_xCo_{1-x}O_2$ (x=0.75) powders. Four different processes: (a)rotary evaporation (b)gelation (c)spray drying and (d)spray decomposition have been developed and studied using inorganic and organometallic precursors other than metal alkoxides. Three aspects were studied on each newly developed process, namely the structure of the synthesized xerogels, the phase evolution pathways, and the electrochemical response of the desired $LiMO_2$ (M=Ni, $Ni_{0.75}Co_{0.25}$) oxide. The final oxide in each of the processes is formed by a reaction between the in-situ synthesized intimate mixture of Li_2CO_3 and the transition metal oxide. The reaction kinetics and mechanisms involved in the formation of the lithiated oxide have also been elucidated in this study using the $LiNiO_2$ xerogel derived from the rotary evaporation process as the model system.

The results of these studies show that the structure of the xerogel is influenced by the processing method, which in turn influence the kinetics of formation of the desired oxide. For example, the xerogels obtained by rotary evaporation of an aqueous solution of LiOH and nickel acetate $Ni(OAc)_2$ show the formation of Ni(OH)(OAc) species in the synthesized xerogel. In contrast, the xerogel generated by the spray drying of LiOH and $Ni(OAc)_2$ in a polar non-aqueous solvent leads to hydrolysis and condensation reaction resulting in a xerogel containing a polymeric network of metal-oxygen-metal chains.

These structural differences actually affect the molecular distribution of the reacting species and consequently, the homogeneity of Li_2CO_3 and NiO that are formed as the intermediate products during heat treatment. Thermal analysis and electron

microscopy studies on the rotary evaporated xerogel have shown that the carbonate directly reacts with the NiO resulting in the formation of $LiNiO_2$ with an activation energy of Ea = 98.65 kJ/mole. Electron microscopy results show that the carbonate and NiO are nano crystallines (~20nm for Li_2CO_3 and 30 ~50nm for NiO) and are homogeneously distributed in the decomposed xerogel. The presence of Li_2CO_3 however, not only affects the formation of $LiNiO_2$ during subsequent heat treatment but also the defect chemistry of the resultant oxide. Moreover, the carbonate tends to cover the surface of the oxide and thus degrades the electrochemical response of the synthesized oxide. The intimately mixed state of nano crystalline Li_2CO_3 and NiO lead to rapid kinetics of formation of $LiNiO_2$ at $750^{\circ}C$ in comparison to the corresponding solid state reaction.

Modification of the heat treatment conditions help to enhance the reaction kinetics and prevent the decomposition of the final oxide. The $LiNiO_2$ thus synthesized from the rotary evaporation process using the modified heat treatment conditions exhibit a discharge capacity as high as 205mAh/g under a charge/discharge rate of C/2 (charge/discharge in 2 hours). This result indicates the superior performance of the PSG derived $LiNiO_2$ in comparison to the oxide generated by other processes reported in the literature.

Table of Contents

V. RESULTS AND DISCUSSION

v

List of Tables

List of Figures

5-21 The morphology of $LiNi_{0.75}Co_{0.25}O_2$ powders generated by the rotary evaporation process observed at a magnification of (a) 30X, (b) 1000X and (c) 10000X respectively.

5-22 The morphology of $LiNi_{0.75}Co_{0.25}O_2$ powders generated by the spray drying process observed at a magnification of (a) 30X, (b) 1000X and (c) 10000X respectively.

5-23 The morphology of $LiNiO_2$ powders generated by the gelation process observed at a magnification of (a) 30X, (b) 1000X and (c) 10000X respectively.

5-24 Plot of the heat treatment time versus first discharge capacity using different starting Li to Ni ratios in the precursor. Li : Ni = 1 : 1 is represented by (-o-). 1.05 : 1 and 1.08 : 1 are represented by (- -) and (-×-) respectively.

5-25 A demonstration of the effect of Li_2CO_3 on the electrochemical property of the oxide. (-o-) represents the variation capacity with heat treatment time using a starting ratio of Li: Ni = 1.05 : 1 in the precursor. The lithium content of the material versus heat treatment time using the experimental formula concluded by Dahn. et al. is represented by (- -), which is used as an indicator for Ni disorder.

5-26 Plot of the voltage versus Li content for the first 2 cycles of the two samples synthesized using a Li to Ni ratio of 1.05 to 1. (a) The sample heat treated at 800°C for 5 hours and (b) the sample which is heat treated at 800°C for 8 hours.

5-27. The TEM bright field images showing the morphology of the materials (a) at a magnification of 13500X and (b) 36000X respectively. The EDX data which corresponds to the spots "α" and "β" indicated in (b) are shown in (c) and (d) respectively, for the purpose of distinguishing the $LiNiO_2$ and Li_2CO_3 phases.

5-28 The morphology of Li_2CO_3 is also investigated using STEM. (a) morphology at a magnification of 200kX and (b) 500kX. The EDX data which corresponds to the spots "α" and "β" indicated in (b) are shown in (c) and (d) respectively. A light colored phase corresponding to Li_2CO_3 actually surrounds the $LiNiO_2$ particles.

5-29 Proposed reaction mechanism illustrating the formation of $LiNiO_2$ from the xerogels derived by rotary evaporation.

5-30 The capacity versus cycle number of $LiNiO_2$ synthesized using xerogels generated by the rotary evaporation, gelation and spray drying processes. The plots represent the highest capacities of the materials synthesized using the three processes.

5-31 Voltage versus composition of $LiNiO_2$ synthesized using xerogels generated by (a)rotary evaporation, (b)gelation and (c)spray drying processes. These plots are representative of the materials which show the highest capacities.

5-42 The first cycle voltage versus Li content plot for the low defect concentration $LiNiO_2$. A very small current density of $10\mu A/cm^2$ which corresponds to a C-rate of ~C/100 was utilized for this test electrode.

5-43 The differential capacity dQ/dV versus V plot for the same battery tested above in Fig. 5-42. Sharp peaks observed in the figure can be attributed to the characteristic first order phase transition of the material during cycling.

5-44 The results of Rietveld refinement conducted on the X-ray diffraction patterns of the powders that were heat treated in oxygen for 5, 15 and 30 hours under oxygen atmosphere.

5-45 The morphology of the samples heat treated for 5h ((a)~(c)), 15h ((d)~(f)) and 30h ((g)~(I)). Each set of micrographs represent a magnification of 5k, 10k and 25k respectively. All micrographs were taken at the same magnification for comparison.

5-46 Plot of crystallite size with heat treatment time showing a growth in the crystallite with heat treatment time. The crystallites grow from ~0.4µm size for the sample heat treated for 5 hours to ~1µm for the sample heat treated for 30 hours.

5-47 Plot showing the variation of the capacity versus current density for the three sets of materials that were heat treated at 750°C for 5 (o), 15 (□) and 30 (◊) hours respectively.

5-48 Plot of the capacity versus heat treatment time. Four different current densities ($10\mu A/cm^2$, $500\mu A/cm^2$, $2mA/cm^2$, $5mA/cm^2$) were used for the battery tests. The drop in capacity can be attributed to the increase in crystallite size that is proportional to the heat treatment time.

5-49 The first cycle differential capacity dQ/dV versus V curves for the three sets of samples that were heat treated for the three different time periods. A current density of $0.5mA/cm^2$ corresponding to a C-rate of C/2 was utilized for the battery tests.

5-50 The evolution of carbon dioxide during heat treatment detected by the mass spectrum.

5-51 The weight loss of lithium carbonate measured by TGA with the evolution of carbon dioxide detected by the mass spectrum.

5-52 The TGA analysis conducted on the Li_2O-NiO mixture. A weight gain started at ~450°C suggests that direct reaction between lithium oxide and nickel oxide is possible.

5-53 (a) The TGA analysis of lithium carbonate decomposition. At the same time, the TGA analysis of lithium carbonate-nickel oxide mixture is also shown in (b). The

5-66 (a) The diffraction pattern of the decomposed xerogel sample decomposed in the TGA instrument. (b) The corresponding bright field image. (c) The dark field image of lithium carbonate taken at the same region as shown in the bright field image. (d) The dark field image corresponding to nickel oxide.

Chapter 1

Introduction

Lithiated transition metal oxides, $LiCoO_2$, $LiNiO_2$ and $LiNi_xCo_{1-x}O_2$ ($0<x<1$) are important cathode materials that have been identified for 4V Li-ion battery application [1-10]. Traditionally, these materials are synthesized using solid-state processes. The synthesis of $LiMO_2$ (M=Co, Ni, Ni_xCo_{1-x}) using the solid state process with different precursors and atmospheres have been investigated and reported in the literature[11-18]. The electrochemical properties of these solid state derived materials synthesized using different precursors reveal the importance of the nature of the precursors. The conventional solid state process used for synthesizing $LiMO_2$ (M= Co, Ni, $Ni_{0.75}Co_{0.25}$) is based on mixing powders and heat treating them at high temperatures for a prolonged period of time (usually more than 12 hours). Thus the attainment of single phase stoichiometric material is largely dependent on the particle size and homogeneity of the precursors. Although phase pure materials can be obtained by heat treating the precursors for a long time at high temperatures, the resultant materials synthesized using solid state processes under these conditions do not necessary yield materials with good electrochemical properties. Agglomeration of particles, and exaggerated grain growth during prolonged heat treatment together with the loss of lithium at high temperatures contribute to reducing the specific capacity of the materials which is reflected by an increase in the polarization during cycling. This is particularly

true in the case of $LiNiO_2$ where numerous attempts have been made to synthesize stoichiometric form of this material. All the methods have met with partial success. The deficiency of Li caused by prolonged heat treatment at high temperatures induces the misposition of Ni on the Li sites creating anti-site defects thereby retarding the diffusivity of Li [19-20]. Thus there is a need for synthesizing the material at low temperature and in short period of time which is not easily realized in conventional solid state processes. Alternative methods and processes could offer the promise of synthesizing high purity $LiMO_2$ (M = Ni, $Ni_{0.75}Co_{0.25}$) materials which exhibit superior electrochemical activity.

Chemical processes have been studied for the past four decades and are well known for synthesizing refractory materials at low temperatures. The methods are also powerful for generating a variety of morphological forms. There are a number of chemical processes that have evolved over the years. These include the oldest and the most common popular precipitation processes to the more elegant sol-gel complexation and hydrothermal processes. The sol-gel process has been successfully utilized for generating a variety of ceramic materials at a much lower temperature in comparison to the conventional solid state processes [21-30]. The main component of the sol-gel process is the utilization of metal-organic compounds such as alkoxides as starting materials which can react with water in the presence of a solvent to undergo hydrolysis and condensation reactions. The desired oxide can therefore be synthesized at a significantly lower temperature due to a better mixing at the molecular level of the chemical species leading to the formation of M-O-M (M = Metal) linkages in the solid precursors. Furthermore, the method allows the flexibility to control the kinetics of the reactions to yield unique morphologies. The ability to process high purity materials at low temperatures with controlled morphologies and microstructure makes the sol-gel process ideal for synthesizing $LiMO_2$ (M = Ni, $Ni_{0.75}Co_{0.25}$) for lithium ion battery applications. Unfortunately, in the case of nickel and cobalt, the alkoxides are not only expensive but are also not easily soluble in common polar solvents. Therefore it is extremely difficult to use the conventional solution sol-gel process for generating these materials in the bulk. Due to these factors described above, there is a need for developing alternative simpler processes to generate precursors that yield materials with good electrochemical activity. At the same time, the approach should possess all the attributes

2

of the sol-gel process. Keeping in mind the useful features of the sol-gel process, a new modified approach called the particulate sol-gel (PSG) process has been developed for synthesizing $LiMO_2$ (M=Ni, $Ni_{0.75}Co_{0.25}$).

The PSG process is a variation of the sol-gel technique and is used for synthesizing $LiMO_2$ (M=Ni, $Ni_{0.75}Co_{0.25}$) compounds. The most important feature of the PSG process is the utilization of organo-metallic compounds other than alkoxides traditionally used in the sol-gel process which are easily soluble in common solvents. By either inducing hydrolysis and condensation of these organo-metallic compounds or promoting the formation of molecular oligomers using chelating agents [31, 32], it is possible to obtain a polymeric oxide network in a solvent phase comprising of molecularly mixed species without the utilization of expensive alkoxides. Extraction of the solvent from the gel leads to the as-prepared precursor, which will be termed "xerogel" in the subsequent discussions to follows. This xerogel can then be processed subsequently. The entire approach thus maintains the advantages of the traditional sol-gel process and also provides the flexibility of the use of a variety of non-alkoxide starting materials. The particulate sol-gel (PSG) process is thus unique and it provides all the benefits of the traditional sol-gel process without the use of expensive metal-alkoxides. The details about the terminology, the mechanisms involved, the preparation of the precursors as well as the techniques used for obtaining the xerogels will be described. The structure of the precursors and their transformation to single phase materials will also be discussed. In addition, the microstructure of the oxide, the defect structure and their combined influence on electrochemical properties will also be outlined. Finally, the mechanism involved in the transformation and the kinetics of the overall reaction will also be discussed.

The present study will mainly focus on achieving four goals. The first objective is the synthesis of the xerogel and its structural characterization. Powder X-ray diffraction (XRD), Fourier transform infrared spectroscopy (FTIR), and thermo gravimetric analysis/differential thermal analyses (DTA/TGA) techniques are used for characterizing the structure of the xerogel powders. The second goal is the study of the formation of the precursors and the desired oxides during heat treatments. XRD and Rietveld refinement have been used for investigating the phase evolution and the reaction mechanisms

responsible for the formation of the desired oxides during heat treatments. The morphology and the specific surface area of the resultant oxide powders have been studied using scanning electron microscopy (SEM) and the Brunauer, Emmett and Teller (BET) method. The third goal of this study is the evaluation of the electrochemical property and conducting a systematic analysis of the processing factors influencing the electrochemical behavior of the resultant oxides. Further investigation of the influence of processing parameters on the phase evolution and consequently the electrochemical properties of the synthesized oxides have been conducted using transmission electron microscopy TEM (Philips EM 420T) with energy dispersive X-ray analysis EDXA (Princeton PGT EDX) and scanning transmission electron microscopy STEM (VG HB501) with EDX (Oxford EDX). Finally, the reaction kinetics as well as the reaction mechanisms responsible for the formation of $LiNiO_2$ utilizing the xerogel precursors are investigated using simultaneous TGA/DTA combined with the mass spectroscopy (MS). The faster kinetics of formation of $LiNiO_2$ achieved utilizing the PSG derived precursors in comparison to the conventional solid state method is also demonstrated. Results of these studies are systematically described and discussed in detail in the subsequent chapters.

References

1. M. Broussely, F. Perton, P. Biensan, J.M. Bodet, J. Labat, A. Lecerf, C. Delmas, A. Rougier, J.P. Peres, Journal of Power Sources, 54 (1995) 109-114
2. Tsutomu Ohzuku, Atsushi Ueda, Masatoshi Nagayama, Yasunobu Iwakoshi and Hideki Komori, Electrochimica Acta, Vol. 38, No. 9, pp. 1159-1167, 1993
3. D. Caurant, N. Baffier, B. Garcia, J.P. Pereira-Ramos, Solid State Ionics, 91 (1996) 45-54
4. T. Nohma, H. Kurokawa, M. Uehara, M. Takahashi, K. Nishio, T. Saito, Journal of Power Sources, 54 (1995) 522-524.
5. B. Banov, J. Bourikov, M. Mladenov, Journal of Power Sources, 54 (1995) 268-270.
6. T. Ohzuku, A. Ueda, M. Nagayama, Y. Iwakoshi, K. Sawai, Chemistry Express, 7 (1992) 689-692.
7. R. Yazami, N. Lebrun, M. Bonneau, M. Molteni, J. Power Sources, 54 (1995) 389-392.
8. A. Hirano, R. Kanno, Y. Kawamoto, Y. Takeda, K. Yamaura, M. Takano, K. Ohyama, M. Ohashi, Y. Yamaguchi, Solid State Ionics, 78 (1995)123-131.
9. J. R. Dahn, U. von Sacken, C.A. Michal, Solid State Ionics, 44 (1990) 87-97.
10. R. V. Moshtev, P. Zlatilova, V. Manev, A. Sato, J. Power Sources, 54 (1995) 329-333.
11. Tsutomu Ohzuku, Atsushi Ueda, Masatoshi Nagayama, J. Electrochem. Soc., 140 (1993) 1862-1870.
12. W. Ebner and F.L. Xie, Solid State Ionics, 69 (1994) 238-256.
13. J.R. Dahn, Solid State Ionics, 44 (1990) 87-97.
14. W. Li, J. N. Reimers and J. R. Dahn, Solid State Ionics, 67 (1993) 123-130.
15. M. Broussely, F. Perton and J. Labat, R. J. Staniewicz and A. Romero, J. of Power Sources, 43-44 (1993) 209-216.
16. C. Delmas and I. Saadoune, Solid State Ionics, 54-56 (1992) 370-375.
17. C. Delmas, I. Saadoune and A. Rougier, J. of Power Sources, 43-44 (1993) 595-602.
18. R. J. Gommow and M. M. Thackeray, Solid State Ionics, 53-56 (1992) 681-687.
19. Shuji Yamada, Masashi Fujiwara, Motoya Kanda, Journal of Power Sources, 54 (1995) 209-213.
20. W. Li, J.N. Reimer and J.R. Dahn, Phys. Rev. B, 46 (1992) 3236-3246.
21. B. E. Yoldas, J. Ploymer Science: Part A, Vol. 24, (1986) 3475-3490.
22. R. M. Stolen and G. E. Walrafen, J. Chem. Phys., 64 (1976) 2623.
23. M. F. Bechtold, R. D. Vest and L. P. Plambeck, Jr., J. Am. Chem. Soc., 90 (1968) 4590-4598.
24. K. S. Mazdiyasni, C. T. Lynch and J. S. Smith, J. Amer. Ceram. Soc. 48 (7) (1965) 372.
25. K. S. Mazdiyasni, C. T. Lynch and J. S. Smith, J. Amer. Ceram. Soc. 50 (10) (1967) 532.
26. D. C. Bradley, R. C. Mehrota and D. P. Gaur, " Metal Alkoxides" (Academic Press, New York, 1978).
27. Idem, Nature 182 (1958) 1211.
28. R. L. Martin and G. Winter, J. Chem. Soc., (1961) 2947.

29. D. W. Hoffman, R. Roy and S. Komarneni, J. Amer. Ceram. Soc., 67 (1984) 468.
30. S. Komarneni, Y. Suwa and R. Roy, J. Amer. Ceram. Soc., 69 (1986) C155.
31. K. S. Weil and P. N. Kumta, J. Solid State Chem., 128 (1997) 185-190.
32. K. S. Weil and P. N. Kumta, Materials Sci. and Eng. B, 38 (1996) 109-117.

Chapter 2

Background

2.1 Intercalation compounds and rocking chair cells:

Intercalation compounds are in general materials which allow reversible insertion of guest species into a lamellar host structure without altering the structural features of the host material. According to the type of intercalation paths (channels) adapted by the guest species, the host can be easily classified into three categories, namely, one, two and three dimensional intercalation compounds. Examples of each category are shown in Table 2-1. The insertion guest species could be small single ions such as Li^+, Na^+ K^+ …etc. or big molecular species such as metallocene[1]. The processes which describe the insertion or de-insertion of the guest species into or from the host are called intercalation or de-intercalation reactions. The intercalation and de-intercalation reactions offer a unique pathway to cycle lithium ions through ceramic hosts thereby leading to the concept of rechargeable lithium-ion battery. The earliest rechargeable (secondary) batteries using intercalation compounds as cathode materials were developed in the 1970s in which Li metal was usually used as the anode. Ideally, lithium metal is the preferred choice for the anode in a lithium battery since elemental lithium is the most electro positive metal and offers the maximum in terms of electrochemical energy.

Two main disadvantages however, limit the development of secondary batteries using lithium metal as the anode. First, the formation of dendrites due to the evolution of

a passivation layer on the lithium anode in contact with the available liquid or polymer electrolyte reduces the cycle life of the battery [2]. Second, based on the safety considerations, lithium metal is not a good choice since even a slight leakage of moisture into the battery will cause vigorous oxidation of the lithium metal itself thereby rendering the battery flammable [3]. The use of an intercalation compound allows the safe transfer of lithium ions without the need for a metal. This concept makes it possible to use intercalation compounds for both anodes as well as cathodes. It was not until the late 1980s, that coke and graphite were found to be the potential anode materials suitable for replacing lithium metal. Identification and utilization of intercalation compounds for both electrodes made the virtual concept of secondary batteries turn into reality. These batteries developed were called "Rocking chair cells" or "Shuttlecock batteries" or "Li-ion batteries". The term "Rocking chair cell" arises from the fact that both electrodes undergo intercalation type reactions during the charge and discharge steps of the cycle. The reactions which occur at both electrodes during the charge cycle could be expressed by the following equations:

$$LiMO_2 \text{--------}> Li_{1-x} MO_2 + x\ Li^+ + x\ e^- \ (M = Ni, Co\ etc.) \cdots\cdots\cdots \text{ Cathode}$$

$$x\ Li^+ + x\ e^- + C_6 \text{---------}> Li_xC_6 \cdots\cdots\cdots\cdots\cdots\cdots\cdots\cdots\cdots \text{ Anode}$$
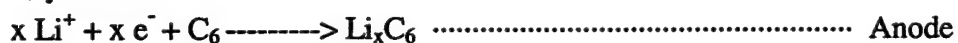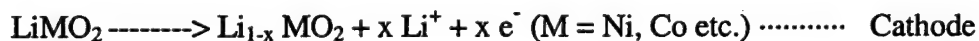
The reverse reaction will occur at both electrodes during the discharge cycle.

Table 2-1. Types of intercalation compounds.

Type of intercalation Compound	Examples	Comments
One Dimensional	$LiKFeS_2$, Na_xWO_3	Little Practical Use*
Two Dimensional	TiS_2, $LiCoO_2$, $LiNiO_2$	High Theoretical Capacity
Three Dimensional	$LiMn_2O_4$	Low Theoretical Capacity

*Presence of defects such as dislocations and stacking faults rendering the intercalation process difficult [4].

8

2.2 Why are layered compounds such as $LiNiO_2$ and $LiCoO_2$ technically important?

Transition metal oxides, $LiNiO_2$ and $LiCoO_2$ are technically important materials for secondary lithium ion batteries. This is because of the following considerations:

1. *High theoretical capacity:*

The capacity of an electrochemical cell reflects the energy stored in the electrodes, which is determined by the number of ions transported per unit weight of the material. The theoretical capacity of a material can be calculated using the formula:

$$Theoretical \quad Capacity = \frac{N \times F}{M} \quad (\frac{Columb}{g})$$

$$= (\frac{N \times F}{3.6\,M}) \quad (\frac{mAh}{g})$$

N = moles of transportable and usable ions in one mole of the material

F = Faraday's constant

M= Formula weight of the material

A high theoretical capacity of the electrode material is beneficial for several technologically important applications. Compounds such as $LiNiO_2$ and $LiCoO_2$ have a high molar percentage of transportable ions (Li^+) and a low formula weight. This yields a high theoretical capacity (~275mAh/g) rendering the material advantageous and technologically attractive as a safe, light-weight and compact energy source. Table 2-2 lists the theoretical capacities of some materials possessing the layered $LiMO_2$ (M= transition metal) structure.

Table 2-2. The theoretical capacities of materials possessing the layered $LiMO_2$ structure.

Materials	Capacity (mAh/g)	Materials	Capacity (mAh/g)
$LiTiO_2$	308.6	$LiCoO_2$	273.9
$LiVO_2$	298.2	$LiNiO_2$	274.5
$LiCrO_2$	294.7	$LiMoO_2$	198.7
$LiMnO_2$	285.5	$LiRuO_2$	191.4
$LiFeO_2$	282.8	$LiWO_2$	120.3

2. *High energy density:*

Energy density can be represented either in terms of mass (Wh/kg) or volume (Wh/l). The theoretical energy density of the cathode materials can be calculated using the following equation:

$$Theoretical\ energy\ density = (Theoretical\ capacity \times \overline{V})$$

$$\overline{V} = (\int_{Q_l}^{Q_2} VdQ)/Q$$

$\overline{V}$ = *average voltage, Q = charge in Coulombs*

High energy density of the battery is potentially attractive and necessary because a battery with a higher energy density ensures a better performance (energy output) of the electronic device. Since energy density of the battery is directly reflected by the voltage difference between the cathode and the anode, a high potential difference between the cathode with respect to the anode is favorable with regards to energy supply. In comparison to conventional secondary battery systems such as Ni-Cd or lead acid or nickel metal hydride batteries, utilization of $LiNiO_2$ and $LiCoO_2$ as cathode materials are important because these materials not only exhibit a high capacity but also display a high potential difference with respect to lithium (about 4V) or other insertion anode materials such as coke or graphite (about 3.5V). Table 2-3 shows the specific capacities (nominal capacity) of some common intercalation compounds used in secondary batteries. Meanwhile, Fig. 2-1 shows the progress in the energy densities of various electrochemical systems that have evolved over the past two decades.

2.3 Considerations for synthesizing good cathode materials:

Three important factors need to be taken into account when synthesizing cathode materials. These are enumerated and discussed below:

1. *Phase purity:*

In order to obtain electrochemically active material that exhibits capacity closer to its theoretical value, it is of paramount importance that the material be synthesized

in a phase pure form. Furthermore, it is essential to eliminate phase impurities that could lead to adverse and deleterious problems of the electrodes during cycling [5].

Table 2-3. The specific capacities (nominal capacity) of some common intercalation compounds used in rechargeable secondary batteries [2].

	Cathode material	Molecular weight	Density (g/cm3)	Reversible range (Δx)	Specific Capacity (Ah/Kg)	Capacity density (Ah/l)
Discharged	Li_xTiS_2	112	3.27	1	239	782
	Li_xMoS_2	160.06	5.06	0.8	134	678
	$Li_xV_2O_5$	181.9	3.357	1	147	495
	$Li_xV_6O_{13}$	513.64	3.91	3.6	188	734
	Li_xMnO_2	86.94	5.03	0.5	154	775
	Li_xNbSe_3	329.81	8.7	3	244	2121
Charged	$Li_{1-x}CoO_2$	97.9	5.16	0.5	137	706
	$Li_{1-x}NiO_2$	97.6	4.78	0.7	192	919
	$Li_{1-x}Mn_2O_4$	180.82	4.28	1	148	634
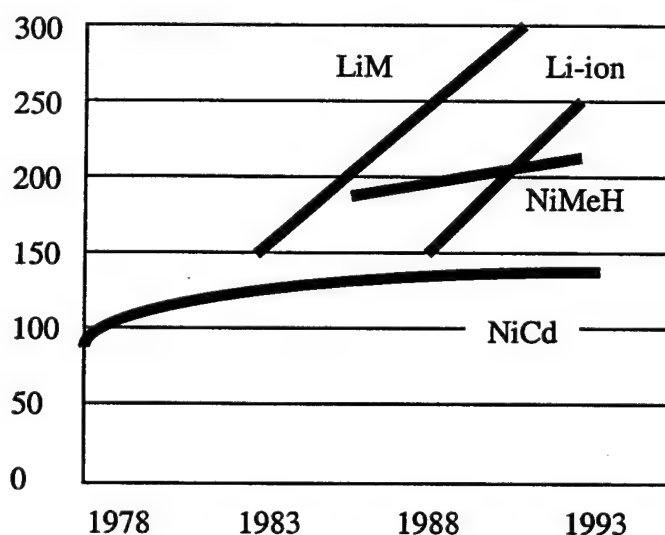
Fig. 2-1. The development of the energy densities of various electrochemical systems [2].

2. *Small crystallite, particle size, and high surface area:*

A smaller crystallite and particle size (higher surface area), implies a reduced diffusion distance for the guest species to diffuse into or from the electrolyte during the charge/discharge cycles. This therefore increases the current or rate capability of the material. It should be mentioned that powders of materials which

11

have small crystallite size may not necessarily have a small particle size and a high surface area. However, high surface area materials always possess small crystallite and particle sizes. Another reason for requiring fine particles arises from the fact that a reduction in the particle size causes a smaller change in the volume of the particles during the charge/discharge cycle. As a result, good contact between particles and the current collector is maintained. Since R_e (the internal resistance to collection of the electronic current within the electrodes) increases as the contact area decreases resulting in a decrease in the capacity, it is beneficial to have a smaller particle size in order to decrease or maintain the value of R_e [4]. An optimum particle size is preferred depending on the system since an extremely high surface area can lead to a reactive solid-electrolyte interface contributing to polarization.

3. *Minimized defect concentration:*

Another important consideration to be factored in when synthesizing materials for Li-ion battery application is to minimize the defect concentration. This is the major type of defect particularly in the case of $LiNiO_2$ for example, and invloves the disorder of Ni atoms on Li sites[6,7]. This disorder impedes the diffusion of Li and therefore increases the internal resistance of the material[8]. In order to obtain a material that exhibits high capacity and current capability, it is absolutely necessary to minimize the defect concentration.

2.4 Crystal structure and simulation of diffraction pattern of $LiMO_2$ (M=Ni, Co or $Ni_{0.75}Co_{0.25}$):

The crystal structure of $LiNiO_2$ is shown in Fig. 2-2. Stoichiometric $LiNiO_2$, exhibits an $R\bar{3}m$ symmetry with Li^+ occupying the (3a) site, and Ni^{3+} and O^{2-} occupying the (3b) site and (6C) site respectively as reported in the literature [8,9]. The ABCABC...... stacking sequence consists of alternating oxygen nickel oxygen lithium layers constituting a 12 layer unit cell. Fig. 2-3 shows the layered structure of the material containing Li^+ and Ni^{3+} ions occupying the octahedral sites of the fcc packed oxygen ions. This enables the Li ions to intercalate and de-intercalate during the charge/discharge cycles. Fig. 2-4 is the polyhedral representation of $LiNiO_2$ structure with Li atoms occupying the octahedral holes between the edge shared NiO_6^- polyhedra.
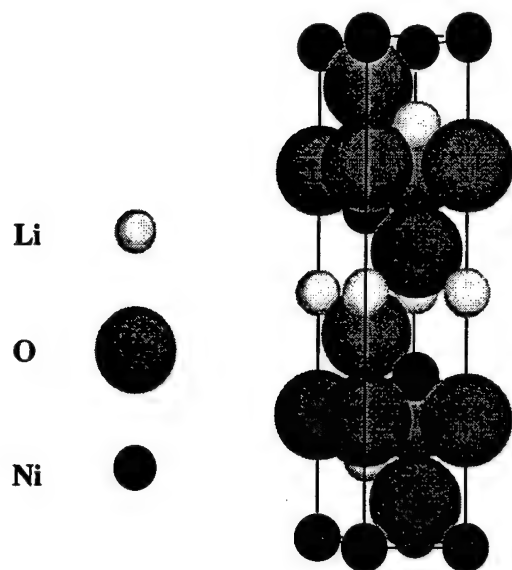
Fig. 2-2. The crystal structure of $LiNiO_2$. The ABCABC...... stacking sequence with alternating oxygen nickel oxygen lithium constituting a 12 layer unit cell.
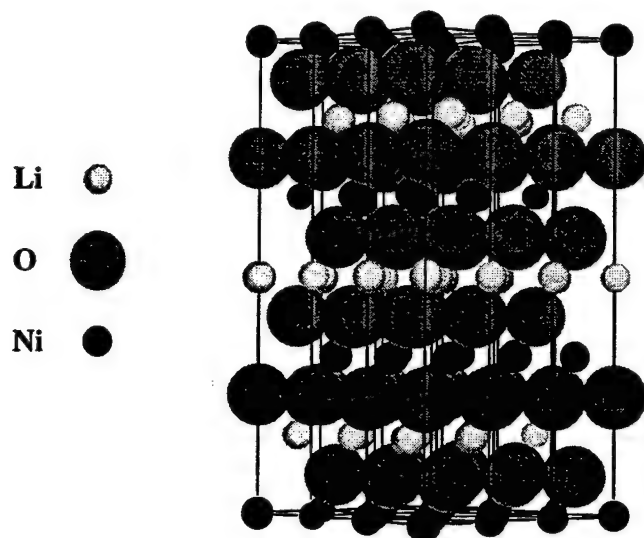
Fig. 2-3. The layered structure of the material contains Li^+ and Ni^{3+} ions occupying the octahedral sites of fcc packed oxygen ions. This enables the Li ions to undergo the intercalation and de-intercalation reactions during the charge/discharge cycle.
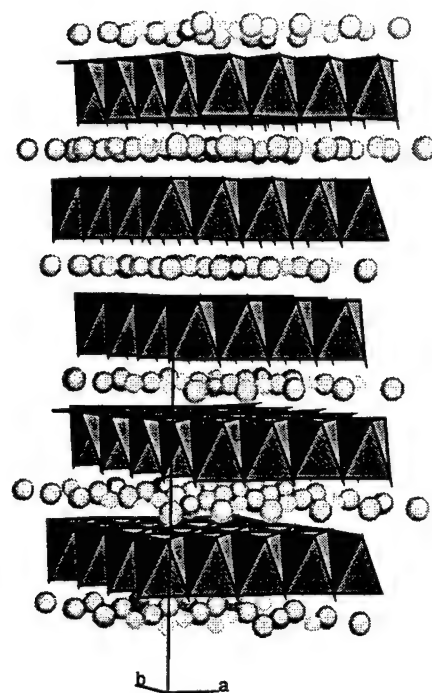
Fig. 2-4. The polyhedral representation of $LiNiO_2$ with Li atoms occupying in the octahedral holes within the edge shared NiO_6^- polyhedra.

The corresponding simulated X-ray powder diffraction pattern for the $R\bar{3}m$ lattice assuming a lattice parameter of a= 2.9 Å and c=14.2 Å. is shown in Fig. 2-5.

Goodenough et al.[10] and Bronger et al. [11] showed that partial cation ordering occurs for $x > 0.6$ in the $Li_xNi_{2-x}O_2$ lattice, which implies that there are some Li ions in Ni rich layers and some Ni ions in Li rich layers. Dahn et al. [7] further indicated that even for stoichiometric $LiNiO_2$ (x=1), full order is still not obtained. Due to the fact that Ni ions in the lithium layers not only directly decrease the utilization of Li_xNiO_2 but also impede the lithium ion diffusion, it is very important to control the Li/Ni ratio during the preparation of Li_xNiO_2. The ratio of lithium to nickel and the disorder of Ni atoms on Li sites have a profound effect on the X-ray peak intensities. Simulated XRD patterns shown in Fig. 2-6 assuming a 5% and a 10% occupancy of Ni atoms on Li sites clearly reflects the changes in the peak intensity caused by this misposition of Ni on Li sites. The reason for this drastic change in intensity, especially for the (003) and the (104) peaks, can be clarified by the structure factor calculation shown in Table 2-4. As shown in Table 2-4,

14

the intensity of the (003) peak should decrease with an increase in the misposition of nickel ions on the Li sites.

Theoretical X-ray Powder Diffraction Pattern for LiNiO₂

- By using the lattice parameters obtained experimentally and the formula $I_{hkl}=|S_{hkl}|^2 M_{hkl} Lp(\theta) \exp[-B(Sinq/\lambda)]^2$ for intensity calculation, the theoretical X-ray powder diffraction pattern for LiNiO₂ is obtained.
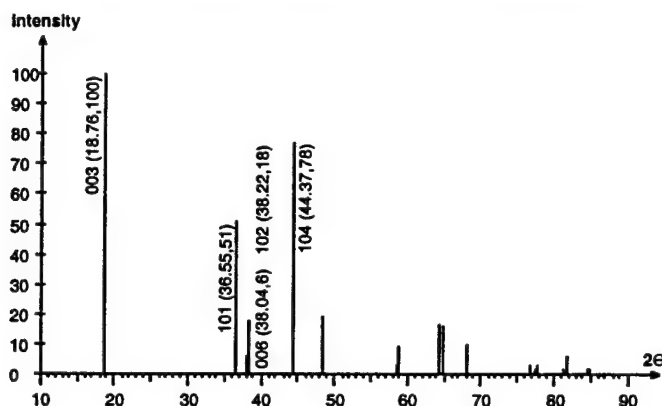
Fig. 2-5. The simulated X-ray powder diffraction pattern of LiNiO₂. The simulation is conducted by assuming the $R\bar{3}m$ crystal structure with a lattice parameter of a= 2.9 Å and c=14.2 Å.

X-ray pattern generated for Ni on Li site
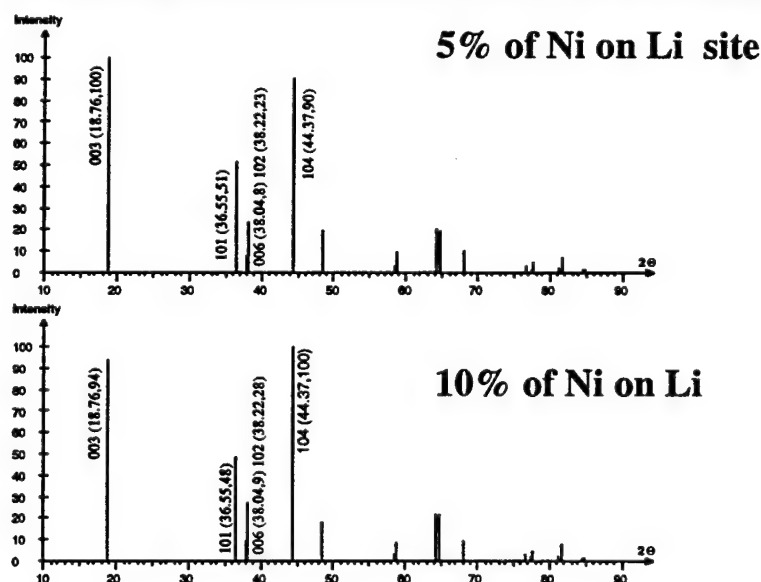
Fig. 2-6. The simulated X-ray powder diffraction pattern showing the influence of disorder of Ni atoms on Li sites on the peak intensity ratio. A 5% and a 10% occupancy of Ni atoms on Li sites were assumed in this simulation.

15

Table 2-4. Structure factor calculations showing the change in the peak intensities of the X-ray diffraction pattern caused by the disorder of Ni atoms on Li sites.

hkl	S_{hkl}	$Sin\theta/\lambda$	S_{hkl}	$|S_{hkl}|^2$
(003)	$3f_{Li}-3f_{Ni}$	0.208	$3\times1.8-3\times20.7$	3215
(101)	$3f_{Li}-3f_{Ni}$	0.385	$3\times1.33-3\times14.99$	1679
(102)	$3f_{Li}+3fNi-6f_{O}$	0.400	$3\times1.3+3\times14.6-6\times2.9$	918
(104)	$3f_{Li}+3fNi+6f_{O}$	0.453	$3\times1.41+3\times13.59+6\times2.53$	3526

Simultaneously there will be a corresponding increase in the (104) peak intensity due to the increase in the contribution from the atomic scattering factor of the Li site.

Besides qualitatively assessing the misposition of Ni on the Li sites by visualizing the evolution of peak intensity in the X-ray analysis, Dahn et. al. proposed an equation to qualitatively monitor the variation of the lithium content in the as-prepared lithium nickel oxide. According to Dahn et. al.[6], the lithium content of $LiNiO_2$ can be monitored by examining the peak intensity ratio of (101),(006) and (102) peaks. The peak intensity ratio R, represented as:

$$R = [I(006)+I(102)]/I(101) \qquad (2\text{-}1)$$

can be obtained experimentally. This value of "R" is then substituted into the equation:

$$R = 0.461+0.997(1\text{-}x) + 27.37 (1\text{-}x)^2 \qquad (2\text{-}2)$$

in order to obtain the value of x in $Li_xNi_{2-x}O_2$. Equation (2-2), is experimentally determined by plotting the variation of the parameter "R" with Li content (x in $Li_xNi_{2-x}O_2$). The lithium content, "x" was obtained from the cell volume of the rhombohedral lattice using a least squares fit to a second order polynomial. The x value (Li content) obtained from this calculation can serve as an indicator of the Ni disorder on the Li sites. This is based on the structure model that "sum of the ions on the nickel site and lithium site is equal to the oxygen site", corresponding to the general formula of the non-stoichiometric lithium nickel oxide $Li_xNi_{2-x}O_2$.

The above information can serve as a guideline for not only determining the purity of the oxide, but also the defect chemistry in the synthesized $LiNiO_2$. Both these aspects

also help to predict the electrochemical response. These aspects have been used in the present work to assess the disorder of the particulate sol-gel (PSG) derived $LiNiO_2$ and $LiNi_{0.75}Co_{0.25}O_2$. A more exact analysis of the disorder using Rietveld refinement of the XRD pattern has also been conducted. In the case of $LiNi_{0.75}Co_{0.25}O_2$, although equation (2-2) is not applicable, the qualitative conclusion obtained from the X-ray simulation is still valid since the atomic scattering factor of Co and Ni are very similar.

2.5   Methods to synthesize lithiated transition metal oxides:

1. *The solid state process:*

Solid state processes form the conventional methods used to synthesize $LiCoO_2$ and $LiNiO_2$ cathode materials [6, 8, 9, 12-23]. In these methods, generally, the starting materials are mixed and ground using either ball milling or simple grinding procedures involving the use of mortar and pestles. Some examples of synthesizing $LiNiO_2$ using solid state reactions involving different precursors, the reaction atmosphere and temperature are shown in Table 2-5. Similar methods have also been used for synthesizing $LiNi_xCo_{1-x}O_2$[18-23].

Table 2-5. Examples of solid state processes utilized for synthesizing $LiNiO_2$ and $LiNi_xCo_{1-x}O_2$.

Starting materials	Atmosphere	Temperature (°C)	Time (hr)	References
LiOH, Ni metal	O_2	900	< 1000	1
LiOH, $Ni(NO_3)_2$	Air	800	?	1
LiOH, NiOOH	Air	850	?	1
LiOH,$NiCO_3$	O_2	750	24	1
$LiNO_3$,$NiCO_3$	O_2	750	24	1
$LiNO_3$,$Ni(OH)_2$	Air	750	24	9
Li_2CO_3, $NiCO_3$	O_2	750	24	9
LiOH, $Ni(OH)_2$	Air	700	2	6
LiOH, $Ni(OH)_2$	O_2	625	7	8
Li_2CO_3, NiO, Co_3O_4	O_2	800-1000	48	18
Li_2CO_3, NiO, Co_3O_4	O_2	600-900	? (with intermittent grinding)	19
Li_2CO_3, $NiCO_3$ $CoCO_3$	Air	900	24	20
LiOH, $(Co_xNi_{1-x})_3O_4$	Air or O_2	450-850	7 days	21
Li_2CO_3, $NiCO_3$ $CoCO_3$	Air	850	24	22
Li_2CO_3, $NiCO_3$ $CoCO_3$	Air	900	24	23

Although solid state processes are easy and simple to execute (simple grinding and heating), there are several limitations of these methods. These limitations pertain to the prolonged heat treatments at high temperatures necessary to promote adequate diffusion of the reacting species. As a result, grain growth occurs making it difficult to control the particle size and morphology. Moreover, the thermodynamic instability of the oxide at high temperatures $\geq 800^{\circ}C$ could lead to decomposition and subsequent loss of lithium. There is therefore a need to investigate alternative low temperature approaches. Solution-based chemical approaches offer an ideal platform for synthesizing these materials. This is because these methods, of which there are many that have evolved over the past several decades, offer the unique ability to directly react at the solution stage and yield a precursor with characteristic structures. The structures of the molecular units created could have short range structural similarity to the desired final material. Thus, moderate heat treatment would yield the final compound that is intended. Furthermore, chemical processes offer an excellent pathway for the starting materials to undergo mixing at a molecular level. This molecular mixing also favors faster diffusional kinetics thereby promoting the formation of final oxide. A number of different forms of chemical processes have evolved over the past hundred years. Ever since the most common precipitation techniques were first known and used for ceramic powder synthesis.

2. *Chemical approaches:*

As mentioned above, chemical processes are very attractive for synthesizing fine ceramics for a number of applications. Prior to 1950, the only solution based methods know to ceramic processing were the common precipitation based techniques conducted mostly in aqueous medium. However, since the application of the sol-gel methods by Rustum Roy in 1955 [24] known until then only to mineralogists in clay processing [25] for processing of ceramics, there has been a tremendous surge of activity in exploring this process for synthesizing a variety of oxide ceramics, glosses and thin films. However, its applicability for synthesizing lithiated transition metal oxides of rechargeable lithium ion batteries was only explored in the early 1990's. The approach involves the used for metal alkoxides which are made to undergo hydrolysis and condensation reactions to yield serpentine polymeric networks of metal-oxygen-metal. Metal alkoxides are very powerful starting materials and render the flexibility to the sol-gel process [26]. The only

18

disadvantage is the tremendous moisture sensitivity and the expense involved. There has been no metal alkoxide based solution sol-gel based process developed for synthesizing lithiated transition metal oxides. This is however mainly because of the solubility problems associated with the alkoxides which can be overcome by modified sol-gel approaches. One such modification is the particulate sol-gel (PSG) process which is the focus of this thesis. There have also been some solution based chemical processes other than the solid state process that have been used for synthesizing $LiMO_2$ (M = Ni, Co or Ni_xCo_{1-x}) [27-34]. These approaches are based on either colloidal precipitation or formation of mixed metal alcoholates to yield precursors that are then pyrolyzed to form the oxides. There are other solution-based processes as well such as the Pechini process which has attracted considerable attention for synthesizing mixed cation oxides [35-46] during the past three decades. The main concept involved in the Pechini process is to mix cations homogeneously in the solution state utilizing condensation reactions between organic reagents such as citric acid, poly(acrylic acid), ethylene glycol …etc. to either chelate or bridge cations together in order to achieve homogeneity of the cations at the molecular level. A schematic of the typical reactions involved in the formation of the precursor in the Pechini process is shown in Fig. 2-7. The chelated metal cations attached to the carboxylic acids undergo polymerization reaction with the glycol to yield a polymeric resin. The important aspect to note is that the polymerization reaction is induced by reaction of the solvents in which the metal cations remain chelated. Thus in this sense alone, the Pechini process is similar to the particulate sol-gel process. After drying and calcination, the desired inorganic mixed oxides can be obtained with the removal of the organics by oxidation. Characteristics of the Pechini process are outlined as follows:

1. Molecular level mixing of the cations is achieved by inducing other organic polymers or organic chemicals with at least two reactive functional groups.

2. The organic polymer forms a "resin" phase with the metal cations bonded to the organic polymer chains by either chelation or coordination.

3. During calcination, owing to the immobility of the cationic species bonded to the organic polymers, phase separation can be minimized.
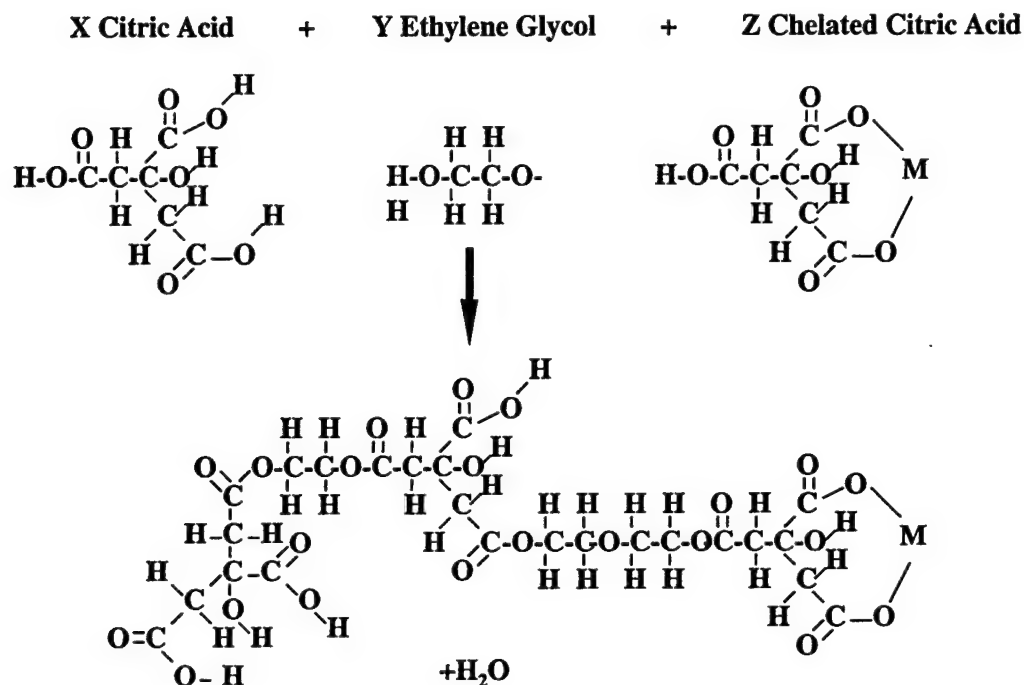
Fig. 2-7. Schematic of a typical structure of the synthesized Pechini precursor. The cations could be either bridged or chelated by the polymeric resin phase [35].

4. Owing to the good molecular level mixing, there is significant reduction in the diffusion distances and hence, reduction in both reaction temperature and time can be achieved.

5. By controlling the composition ratio of the resin phase (e.g. the ratio of citric acid to ethylene glycol), the morphology of the resultant oxide can be controlled due to the diffusion of the cations which is controlled by the viscosity of the resin phase.

6. Due to the use of organic reagents that contribute to the formation of a resin, the yield of the oxide could be low. Furthermore, the presence of a large amount of organics may cause some deleterious effects on the property of the resultant oxides. This is particularly true in the case of systems containing lithium. Lithium has a large tendency to form carbonates when heated in air in the presence of carbon. Thus

pyrolysis of the resin would most likely lead to Li_2CO_3 formation which has a very adverse affect on the electrochemical response of the oxide which is discussed in the later chapters. A schematic of the resin structure obtained in the Pechini process is schematically represented in Fig. 2-8.

In comparison to the Pechini process, the particulate sol-gel (PSG) approach also yields precursors with very good mixing at the molecular level. However, these precursors are obtained without the utilization of a reaction between any organic reagents to form a resin phase. Furthermore, the PSG process does not involve the use of any expensive metal alkoxides. Instead, the PSG process yields precursors in the form of agglomerates or polymerized particles suspended in the solution phase. The agglomerates or polymerized particles can be obtained by using chelating agents to complex the metal species or inducing hydrolysis and condensation of the metal organic salts in solution. The continuous gel phase is obtained by polymerization of the organo-metallic species directly to form the M-O-M network with the solvent trapped in the polymeric oxide. Subsequent drying of the solvent phase leads to the formation of the xerogel, which is then heat treated to obtain the desired final oxide. The most prominent advantage of the PSG process in comparison to the Pechini process is that no separate organic additives or gelling agents are incorporated in the solution state. This considerably reduces the possible deleterious effect caused by the presence of excess carbon. The concept of the PSG process can be indicated by a schematic representation of the morphology of as-prepared precursor in Fig. 2-9.

The utilization of the PSG process for synthesizing lithiated transition metal oxides $LiMO_2$ (M=Ni, $Ni_{0.75}Co_{0.25}$) and identification of the structure of the as-prepared precursors form a major part of this study. The results of this study are fully described and discussed in the subsequent chapters.
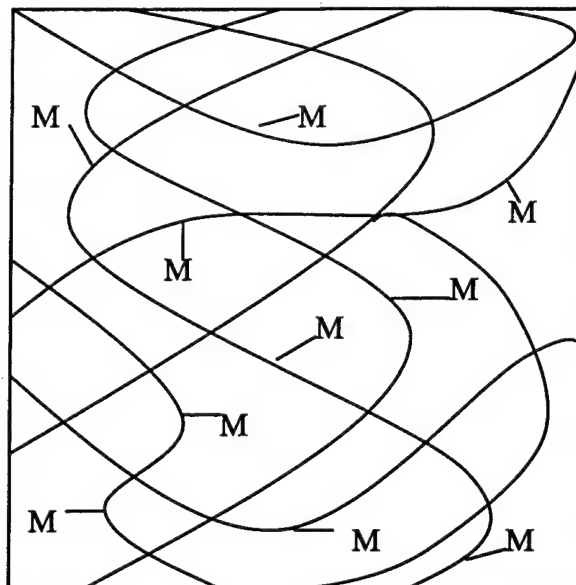
Fig. 2-8. Schematic representation of the structure of the precursor synthesized using the Pechini process.
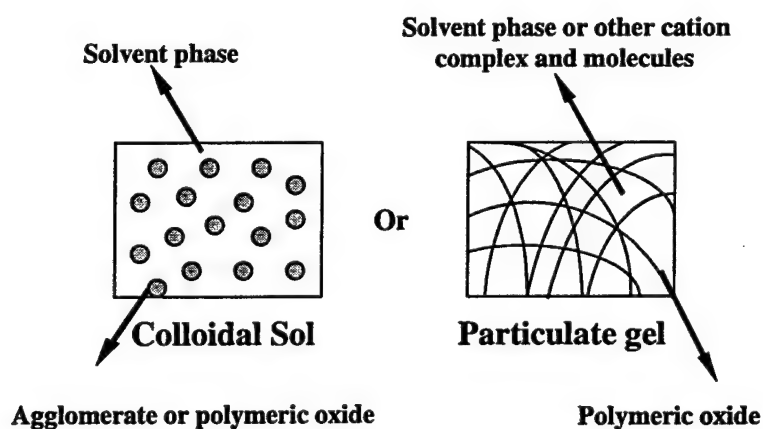
Fig. 2-9. Schematic representation of the structure of the as-prepared precursors generated by the PSG process.

2.6   Reaction kinetics in solids:

Chemical processes as described earlier result in a molecularly mixed precursor containing molecular units that very closely mimic the structure of the desired final compound. The extent of this structural similarity is dictated by the method and the reaction mechanisms. In any event, the formation of the final desired phase of the target compound is dictated by rapid diffusion in the solid state of the reacting species. The kinetics of these reactions in the solid state are thus an important factor governing the overall efficiency of these processes contributing to the numerous advantages characteristic to these processes described earlier. The present section describes in brief the methods that are employed to assess the kinetic parameters in solid state reactions.

The chemical kinetics have been reviewed and summarized by Bamford et. at. [47]. Two alternative methods have been used in kinetic investigations. The first method is to measure the yield-time relationships by maintaining constant reaction temperature. This method is known as the conventional isothermal method. The other alternative is to measure the yield-time relationships by controlling the rise in temperature. This method on the other hand is called the non-isothermal method. The typical yield-time plot for an isothermal heat treatment is shown in Fig. 2-10. The entire curve shown in Fig. 2-10 can be separated into several segments according to the reaction mechanism. The point A represents an initial reaction, sometimes associated with the decomposition of impurities or unstable superficial materials. B is the induction period, usually regarded as being terminated by the development of stable nuclei (often completed at a low value of α which is related to the completion of a reaction). C is the acceleratory period of growth of such nuclei, perhaps accompanied by further nucleation, and which extends to the maximum rate of reaction at D. Thereafter, the continued expansion of nuclei is no longer possible, due to impingement and consumption of reactant and this leads to the deceleratory or decay period, E, which continues until completion of reaction, F. From this short description on the typical yield-time curve, it can be realized that the shape of the curve on the yield-time curve is dictated by the mechanisms involved in the reaction. The biggest disadvantage of the isothermal method originates from a finite time that is required to heat the material to the reaction temperature.
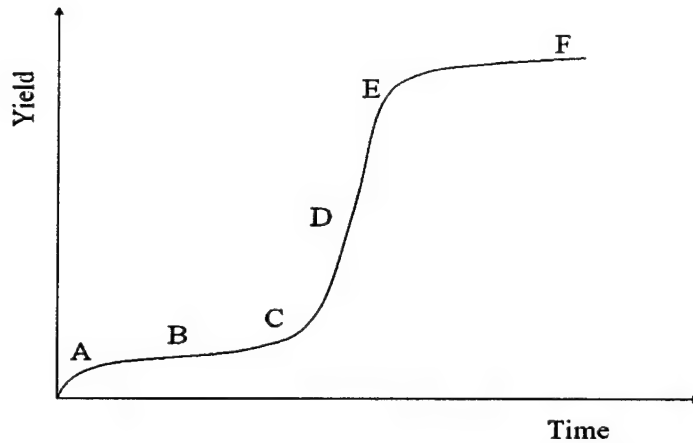
Fig. 2-10. The typical yield-time plot for an isothermal heat treatment [47].

As a result, the initial segment of the yield-time plot cannot refer to the isothermal conditions. This problem is even more severe when the reaction rate of the investigated reaction is high. Owing to this reason, a non-isothermal method can be is preferred as the alternative method for measuring the kinetics of the reaction. For an isothermal condition, a mathematical description of the yield-time curve can be given by :

$$\alpha = f(t) \tag{2-3}$$

The reaction rate can therefore be written as:

$$d\alpha/dt = df(t)/dt = f(\alpha) \tag{2-4}$$

The new function $f(\alpha)$ is therefore directly related to the reaction mechanism involved in the reaction. An example is given here to clarify the characteristics of the function $f(\alpha)$. The Avrami-Erofeev equation derived by assuming continuous nucleation throughout the entire reaction at a constant rate N and a continuous growth of the spherical nuclei at a constant rate v is given as:

$$\alpha = 1 - \exp\left[-(kt)^n\right] \tag{2-5}$$

24

$$d\alpha/dt = n(kt)^{n-1} \cdot \exp[-(kt)^n]$$

$$= n(kt)^{n-1} \cdot (1-\alpha)$$

$$= n[-\ln(1-\alpha)]^{(n-1)/n} \cdot (1-\alpha) = f(\alpha)$$

Thus different form of $f(\alpha)$ can be realized for different values of n as shown in Table 2-6. The most commonly used reaction mechanisms $f(\alpha)$ are listed in Table 2-6. The meaning of α shown in Table 2-6 represents the extent of completion of the reaction which can be quantitatively measured by either weight loss, heat released, evolved gas concentration...etc. according to the characteristics of the interested reactions.

In the case of a non-isothermal condition, α is no longer a function of time only. Instead, α is a function of both time and temperature given by:

$$\alpha = f(t, T) \tag{2-6}$$

$$d\alpha/dt = df(t, T)/dt = f(\alpha)k(T)$$

where $k(T)$ is the rate constant which follows the Arrhenius form. This equation can thus be used for determing the kinetic parameters The utilizaiotn of this equation is discussed in further detail in section 5-14.

Table 2-6. The most commonly used reaction mechanisms $f(\alpha)$ [48, 49].

Mechanism		$f(\alpha)$
Acceleratory α-t curve		
P1	Power law	$4\alpha^{3/4}$
		$3\alpha^{2/3}$
		$2\alpha^{1/2}$
		1
		$(2/3)\,\alpha^{-1/2}$
E1	Exponential law	α
S-shaped α-t curve		
A1.5	Avrami-Erofeev	$1.5(1-\alpha)[-\ln(1-\alpha)]^{1/3}$
A2	Avrami-Erofeev	$2(1-\alpha)[-\ln(1-\alpha)]^{1/2}$
A3	Avrami-Erofeev	$3(1-\alpha)[-\ln(1-\alpha)]^{2/3}$

A4	Avrami-Erofeev	$4(1-\alpha)[-\ln(1-\alpha)]^{3/4}$
B1	Prout-Tompkins	$\alpha(1-\alpha)$
		$0.5(1-\alpha)[-\ln(1-\alpha)]^{-1}$
		$(1.3)(1-\alpha)[-\ln(1-\alpha)]^{-2}$
		$(1.4)(1-\alpha)[-\ln(1-\alpha)]^{-3}$
Deceleratory α-t curve		
R2	Contracting surface	$2(1-\alpha)^{1/2}$
R3	Contracting volume	$3(1-\alpha)^{2/3}$
D1	1-D Diffusion	$1/2\alpha$
D2	2-D Diffusion	$-[\ln(1-\alpha)]^{-1}$
D3	3-D Diffusion	$1.5[1-(1-\alpha)^{1/3}]^{-1}(1-\alpha)^{2/3}$
D4	Ginstling-Brouns	$1.5[1-(1-\alpha)^{1/3}]^{-1}$
F1	First order	$1-\alpha$
F1	Second order	$(1-\alpha)^2$
F1	Third order	$0.5(1-\alpha)^3$

2.7 Design considerations for Li-ion batteries:

This section will focus mainly on two aspects: The first aspect is based on the thermodynamic treatment of an electrochemical device. The second aspect is the general review of the electrode and electrolyte materials. Fig. 2-13(a) shows the schematic of an electrochemical device consisting of solid (crystalline) electrodes with liquid (molecular) electrolyte. This is a typical electrochemical device consisting of a liquid electrolyte with both intercalation compounds as cathode and anode. For convenience, assume that the cathode material is $LiNiO_2$ and the anode material is graphite.

1. *Theories for battery design:*

For the typical electrochemical device shown in Fig. 2-11, the maximum work that can be exerted by the device can be represented as:

$$\Delta G = -\Delta W_{Max} \tag{2-7}$$

The ΔG is originated from the free energy difference arising between the cathode and the anode which is essentially the driving force for the functioning of the electrochemical device. The free energy difference can be represented as:
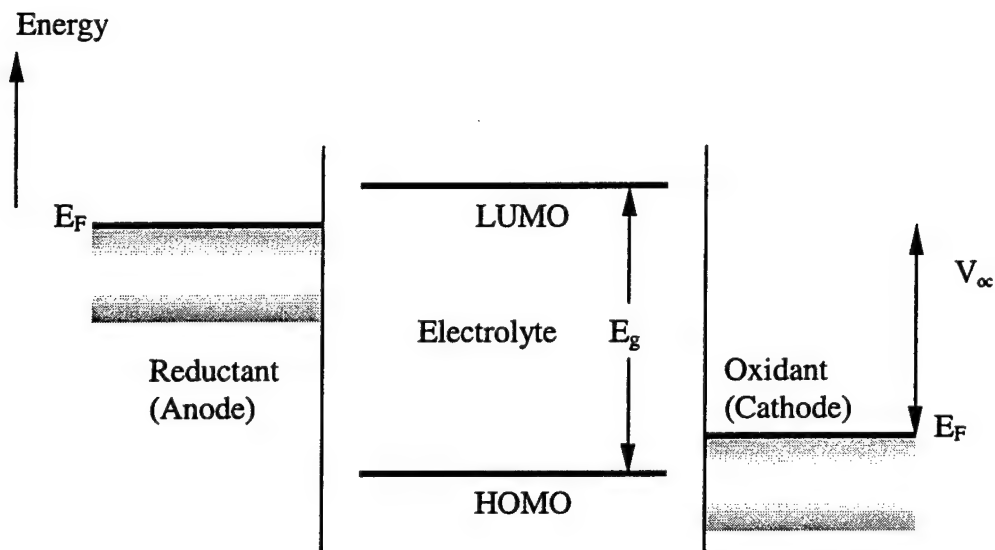
Fig. 2-11. A schematic of a typical electrochemical device consisting of a liquid electrolyte and two intercalation compounds as cathode and anode [4].

$$\Delta G = (\bar{\mu}_A - \bar{\mu}_C) \tag{2-8}$$

Where μ_A and μ_B represent the electrochemical potential of the anode and cathode respectively. The open circuit voltage of the device can therefore be represented by the characteristic Nernst equation:

$$V_{OC} = (\bar{\mu}_A - \bar{\mu}_C) / -nF \tag{2-9}$$

In this equation, 'n' represents the mole of electrons and 'F' is the Faraday constant. During the discharge process of the electrochemical device (a spontaneous process), the cathode undergoes a reduction reaction which can be represented as:

27

$$MO_2 + x\,Li^+ + x\,e- \longrightarrow Li_xNiO_2 \quad (\Delta G_C < 0) \qquad (2\text{-}10)$$

The electrochemical potential of the cathode increases with an increase in the accumulation of electrons and so does the Fermi energy of the electrons. At the same time, the anode undergoes an oxidation reaction which can be represented as:

$$LiC_6 \longrightarrow Li_{1\text{-}x}C_6 + x\,Li^+ + x\,e- \qquad (\Delta G_A > 0) \qquad (2\text{-}11)$$
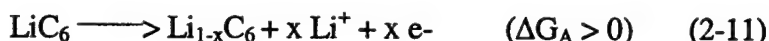
The electrochemical potential of the anode decreases with the loss of electrons resulting in lowering the Fermi energy of the electrons as well. By summing equation (2-10) and (2-11), the overall reaction of the electrochemical device can be represented as:

$$MO_2 + LiC_6 \longrightarrow Li_xNiO_2 + Li_{1\text{-}x}C_6 \qquad (\Delta G_T = \Delta G_C + \Delta G_A < 0) \quad (2\text{-}12)$$

At any instance during the discharge process (under equilibrium conditions), the electromotive force (open circuit voltage) of the electrochemical device can always be calculated by equation (2-9) as shown above. This discharge process (a spontaneous process) should progress until the electrochemical potential of the cathode and the anode are equal and so does the Fermi energy level of the cathode and the anode.

Similar approaches can be used to describe the 'charge' process of the electrochemical device. But it should be mentioned that during the 'charge' process of the electrochemical device, the Fermi energy of the cathode may decrease to the extent that it is lower than the HOMO (highest occupied molecular orbital) of the molecular species in the electrolyte (e.g. Li_4ClO_4, $LiPF_6$, EC, DEC, DMC, PC etc.). This could cause an electron (or hole) transfer between the cathode and the electrolyte which is the characteristic of a 'reaction'. Similarly, the Fermi energy of the anode can also possibly increase to the level that it is higher than the LUMO (lowest unoccupied molecular orbital) of the electrolyte species, therefore allowing the electron to be transferred into the unoccupied molecular orbitals. This electonic transfer from the anode to the LUMO of the electrolyte causes the decomposition of the electrolyte species. As a result, a large

energy gap (large E_g) of the electrolyte is very crucial for the stability of the electrochemical device. For an ideal energy storage device, the electrochemical potential difference between the cathode and the anode should be as large as possible along with the energy window of the electrolyte in order to prevent any electrochemical reaction between the electrolyte and the electrodes.

During the discharge process of the electrochemical device, assuming that equilibrium condition (e.g. using an infinitesimal current density) is obtained, the free energy change, or the maximum work delivered by the electrochemical device during the entire discharge process can be calculated as:

$$\Delta G = \Delta W_{Max} = \int_{Q_0}^{Q_f} V_{OC} dQ \qquad (2\text{-}13)$$

Where 'Q' represents the electrons transferred from the anode to the cathode. In a non-equilibrium condition (e.g. as current increases between the cathode and the anode), the voltage exerted by the electrochemical device is no longer equal to the open circuit voltage of the electrochemical device. A voltage drop owing to the resistance of the entire electrochemical device will be encountered. This leads to a reduction of the available work to:

$$\Delta W = \int_{Q_0}^{Q_f} (V_{OC} - V_{IR}) dQ \qquad (2\text{-}14)$$

The term V_{IR} can originate from the cathode, the anode as well as the electrolyte. Recalling the Ohm's law:

$$J = \sigma\, \mathcal{E} \qquad (2\text{-}15)$$

'J' represents the current density, σ represents electrical conductivity and $\mathcal{E}$ represents the electric field. The term V_{IR} can therefore be represented as:

$$V_{IR} = V_{IR,C} + V_{IR,A} + V_{IR,E}$$

$$= J(\int_{0}^{x_1} \frac{dx}{\sigma_T^C} + \int_{x_1}^{x_2} \frac{dx}{\sigma_T^A} + \int_{x_2}^{x_3} \frac{dx}{\sigma_T^E}) \qquad (2\text{-}16)$$

Where $V_{IR,C}$, $V_{IR,A}$ and $V_{IR,E}$ represent the voltage drop caused by the cathode, anode and the electrolyte respectively. σ_T^C, σ_T^A and σ_T^E represent the total electrical conductivity possessed by the cathode, anode and electrolyte. The limits used for each integration are the dimensions (thickness) of cathode, anode and electrolyte respectively which is shown schematically in Fig. 2-12. The total electrical conductivity of the cathode material arises from contribution of both electronic and ionic conductivity which can be represented as:

$$\sigma_T^C = \sigma_e^C + \sigma_i^C \qquad (2\text{-}17)$$

Furthermore, $\sigma_e^C = \mu_e(N_e e)$, $\sigma_i^C = \mu_i(N_i e)$, where μ_e and μ_i represent the mobility of the electrons and the ions, $N_e e$ and $N_i e$ represent the charge density of electrons and ions respectively. As a result, the resistance of the cathode (or cathode material) is actually dependent on the mobility of the electrons as well as the Li ions.
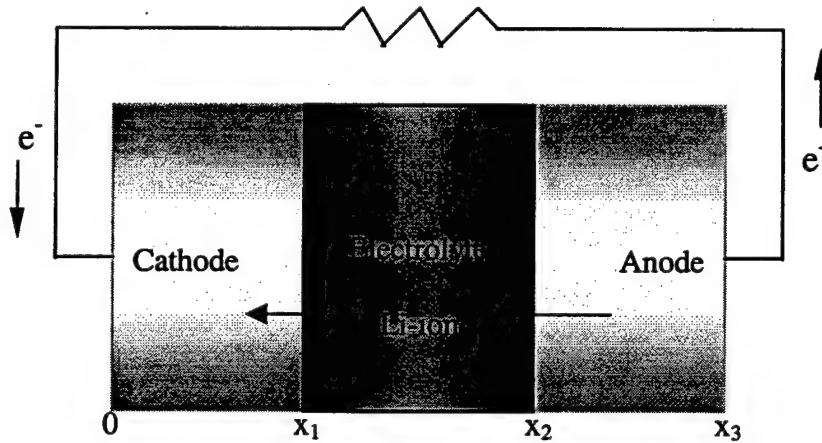
Fig. 2-12. The schematic of a battery representing the dimensions of the cathode, anode and electrolyte respectively.

In other words, if the mobility of the electrons and ions are increased, the voltage drop (also known as polarization) will be decreased. Similar conclusions can be made for the case of the anode (or anode material). It should be mentioned that in the case of the

30

electrolyte, the conductivity contributed by the electrons will be neglected since the electrolyte should not possess any electronic conductivity.

Based on the above considerations, a number of criteria can be set up for analyzing good cathode, anode and electrolyte materials. First, the cathode and the anode materials should be good electronic conductors. Thus, metallic or small band gap semiconductors are favored. Second, the cathode and the anode materials should have excellent ionic conductivity for lithium ions. Owing to the polarization effect discussed earlier, the ionic conductivity of both the cathode and anode materials determine the nominal capacity of the material. In the case of the electrolyte, a large band gap is definitely necessary for the stability of the electrochemical device. The requirements of a large band gap implies that the electrolyte posses no electronic conductivity and does not undergo reduction or oxidation by reactions with electrodes in order to be used in electrochemical device. By utilizing the working principles and the set of criteria for the selection of proper materials for cathodes, anodes and electrolytes, a number of developments in the battery designs as well as the synthesis of materials were initiated.

Recently, there has been considerable interest in solid state batteries because they potentially possess higher energy and power densities utilizing the bipolar design, no leakage of the electrolyte, and variable geometric flexibility. Thin film batteries and Li-polymer batteries have thus been developed for different solid state battery applications. The thin film batteries were developed with the idea of creating the micro batteries for microelectronics applications (e.g. memory backup). In the case of Li-polymer batteries, the impetus is not only to provide batteries for general consumer usage (e.g. cellular phone, lap top computer applications) but also for use in electrical vehicle applications. From the materials science view point, this thesis will focus on the development of the electrode and electrolyte materials rather than design consideration for fabricating new battery designs.

2. *The electrode materials:*

In terms of the electrode materials, we can simply classify the materials into two categories, namely, crystalline and amorphous glass materials.

With regards to the crystalline cathode materials, transition metal oxides are most attractive due to the high theoretical capacity and high energy density as discussed in section 2.2. In addition to high energy density (including weight energy density and volume energy density), high operating voltage, light weight as well as small unit cell volume are essential attributes that the material must exhibit. Some general trends with regards to the suitability of $LiMX_2$ (M = transition metal, X = O, S, Se, Te) type of materials are reported by Ozuku et. al. [50]. For example, in terms of the operating voltage, the oxides possess the highest operating voltages in comparison to the sulfides, selenides and tellurides. Furthermore, the unit cell volume decreases in the following order; tellurides > selenides > sulfides > oxides. Based on these two simple trends, it can be realized that why transition metal oxides such as $LiCoO_2$ and $LiNiO_2$ are the most attractive materials for practical applications. However, there are still problems related to the decomposition of the electrolyte [51-53], irreversible capacity loss during cycling, current capability and safety [54-55] which need to be addressed and improved. Recently, we have reported the substitution of divalent cations on the transition metal sites in the $LiMO_2$ (M = Ni or $Ni_{0.75}Co_{0.25}$) systems. The substitution of divalent cations on the transition metal cations helps to not only improve the cyclability of the material but also minimize and delay the exothermic decomposition reaction of the materials especially when charged to high voltages > 4.4V. These results are included in Appendix C and D respectively.

The spinel $LiMn_2O_4$ is another class of intercalation compound that attracts a lot of attention owing to the abundance and environmentally benign nature of manganese [56-61]. The spinel manganese oxide has similar l operating voltage to $LiMO_2$ (M =Ni, Co) compounds but relatively smaller theoretical capacity (148mAh/g). The improved capacity retention in $LiMn_2O_4$ with the addition of Li^+, Mg^{2+}, Zn^{2+} to increase the oxidation state of manganese as been reported by Gummow et al [56]. Recently, the layered form of the manganese oxide has been reported to be synthesized utilizing the ion exchange reaction between $NaMnO_2$ and n-butyl lithium in hexanol to form layered $LiMnO_2$ [62, 63]. The successful synthesis of the layered form of $LiMnO_2$ is evidence for the need to develop high capacity transition metal dioxide using manganese as the starting

material. Other than the early transition metal oxides, some late transition metal non-oxides are also interesting. For example, amorphous MoS_2 [64,65] and amorphous WO_3 [66] reported in the literature. These amorphous dichalcogenides and oxides usually possess high capacities but relatively low operating voltages (~2.2V reported for amorphous MoS_2, 2.5V for WO_3) with several plateaus.

The development of high operating voltage materials have been reported by Fey et. al in the $LiNiVO_4$ spinel structures system with an operating voltage at ~4.8V [67]. Similar voltage plateau has also been observed in the $LiNi_xMn_{2-x}O_4$ [68] and $LiCr_xMn_{2-x}O_4$ [69] systems respectively. More recently, high voltage materials have also been reported by West et. al [70,71] by substituting the Mn cations in the spinel with Co. Similar voltage plateau is also reported to be observed in the $LiCu_xMn_{2-x}O_4$ [72]. These materials possess a high voltage plateau at ~5V. In addition to the development of oxide materials, the amorphous oxyiodides have been reported [73] which possess moderate operating voltages (~4V). The synthesis procedures for preparing these materials are very tedious and hence optimization and improvements are required.

With respect to the anode materials, other than conventional systems such as graphite and coke [74-82], Sn-based oxides such as SnO, SnO_2, $SnBPO_6$ have received a considerable attention because of the high theoretical capacity of the material [83]. Furthermore, this materials show a good cyclability unlike Sn metal which reveals large volume expansions (>300%) resulting in cracking and debonding of the material during cycling, rendering the cyclability of the material poor. However, the large first cycle irreversible loss of these Sn-based oxides due to the reduction of oxide to form a mixture of Sn and Li_2O in the first cycle causes severe problems for practical applications. Recent approaches have been focused on developing methods to lower the irreversible loss and maintain good capacity retention [84].

3. *The electrolyte materials:*

The solid electrolytes can be classified into these categories namely, crystalline, glass and polymer materials. The crystalline Li-ion conductors can be simply classified into two types. The first type exhibit Li-ion conductivity via diffusion of lattice defects

such as in LiI and Li$_2$S. LiI has a rock salt structure and possess an ionic conductivity of ~2 × 10^{-7} Scm^{-1} at room temperature [85]. The ionic conductivity mainly originates from the Schottky type of defects that allow the conduction of Li ions. It is also reported that with the addition of aliovalent cations such as Ca and Al, ionic conductivity of the material can be enhanced by creating more Li vacancies [86]. In comparison to the rock salt structure of LiI, Li$_2$S has an antiflurite structure [87] and exhibits good Li-ion conductivity, however only at high temperatures (>400°C). It is believed that with the formation of Frenkel type of defects in Li$_2$S, Li ions can diffuse through the vacant lattice sites. The second type of crystalline Li-ion conductors possess a three-dimensional framework of channels that allow the conduction of Li-ions. The most prominent of these is the lthium superionic conductor abbreviated as LISICON after Hong et. al [88]. This family of material has a prototypical chemical formula of Li$_{16-2x}$M$_x$(NO$_4$)$_4$ with M = Mg, Zn; N= Si, Ge. Following the development of LISICON, lithium orthosilicate (Li$_4$SiO$_4$) based binary or ternary solid solutions, such as Li$_4$SiO$_4$-Li$_3$PO$_4$, Li$_4$SiO$_4$-Li$_3$AsO$_4$, Li$_4$SiO$_4$-Li$_4$GeO$_4$, Li$_4$SiO$_4$-Li$_3$AsO$_4$-Li$_3$PO$_4$, Li$_4$SiO$_4$-Zn$_2$SiO$_4$, and Li$_4$GeO$_4$-Li$_2$ZnGeO$_4$-Li$_3$PO$_4$ systems have also been extensively studied [89-99]. Recently, we proposed the fabrication of a composite electrode material consisting of the electrode (LiNi$_{0.75}$Co$_{0.25}$O$_2$) and electrolyte (Li$_4$SiO$_4$) to overcome possible Li-ion conduction problems particularly in thick electrodes. The results of the chemically synthesized lithium orthosilicate and the feasibility of synthesizing an electrode-electrolyte composite in one step are included in Appendix E.

With regards to the inorganic glass electrolytes, the lithium oxide based systems such as Li$_2$O-B$_2$O$_3$ (+SiO$_2$, Li$_2$SO$_4$, LiI...) [100], the sulfide based compositions Li$_2$S-SiS$_2$ [101], or multi-component oxynitrides such as Li-Si-P-O-(N) [102, 103] have been reported. Generally, the effective charge carrier concentrations, the composition and the correlation of the structure to the Li-ion conductivity are of concern. The exact mechanism of Li-ion conduction in these glasses is usually not clear owing to the difficulties in analyzing the exact structure of the glasses. Some common Li-ion conducting glasses are tabulated in Table 2-7.

Table 2-7. Ionic conductivity and activation energy of lithium oxide-based glasses with various compositions[a] [104].

Material	Composition	Conductivity (S/cm)	Temperature (°C)	Activation energy (eV)
$Li_2B_4O_7$		1.0×10^{-4}	300	0.74
$LiBO_2$		4.0×10^{-3}	300	0.58
$Li_2O-B_2O_3$	(42.5-57.5)	6.1×10^{-3}	350	0.60
$Li_2O-B_2O_3$	(63-37)	6.3×10^{-11}	25	0.73
$Li_4B_7O_{12}Cl$		2.5×10^{-4}	200	0.50
$Li_4B_7O_{12}Cl$		8.0×10^{-3}	300	0.50
$Li_2O-Li_2Cl_2-Li_2SO_4-SiO_2-B_2O_3$	(35-10-30-12.5-12.5)	9.7×10^{-2}	350	0.53
$Li_2O-(LiCl)_2-B_2O_3$	(31.8-12.3-55.9)	1.7×10^{-2}	300	0.50
$Li_2O-(LiCl)_2-Al_2O_3-B_2O_3$	(29-24-3-44)	1.5×10^{-2}	350	0.49
$Li_2O-LiF-Li_2SO_4-Li_2SO_3-B_2O_3$	(22.1-12-6-15.8-20.5-28.5)	2.3×10^{-3}	200	0.57
$Li_2O-LiF-B_2O_3$	(20-36-44)	3.1×10^{-4}	200	0.58
$Li_2O-Li_3PO_4-B_2O_3$	(25-10-65)	1.0×10^{-3}	330	0.62
$Li_2O-Li_2SO_4-B_2O_3$	$(0.5-0.15-1)^f$	2.4×10^{-3}	350	0.80
$Li_2O-Li_2SO_4-B_2O_3$	$(0.71-1.1-1)^f$	2.1×10^{-2}	300	0.58
$Li_2Si_2O_5$		1.9×10^{-3}	350	0.70
$Li_2O-Si_2O_2$	(40-60)	1.0×10^{-6}	100	0.63
$Li_2Al_2Si_4$		4.0×10^{-4}	300	0.68
$Li_2O-Nb_2O_3$		6.1×10^{-4}	200	0.40
$Li_2O-B_2O_3-LiNbO_3$	(40-55-5)	2.3×10^{-4}	350	0.82
$Li_2O-B_2O_3-LiNbO_3$	(40-35-25)	8.0×10^{-4}	350	0.65
$Li_2O-Al_2O_3-SiO_2$	(25-25-50)	6.1×10^{-4}	250	0.72
$Li_2O-B_2O_3-SiO_2$	(39-13-48)	1.5×10^{-3}	350	0.67
$Li_2Si_2O_5-Li_2SO_4$	(71.5-28.5)	8.7×10^{-3}	350	0.66
$LiNbO_2-SiO_2$	(65-35)	1.0×10^{-4}	200	-
$Li_2O-Y_2O_3-SiO_2$	(40-6-54)	1.4×10^{-3}	300	0.62
$LiPO_3-LiF$	(60-40)	6.7×10^{-9}	25	0.63
$LiPO_3-LiCl$	(70-30)	1.0×10^{-3}	220	0.63
$LiPO_3-LiI$	(67-33)	1.0×10^{-3}	194	0.56
$LiPO_3-LiBr$	(67-33)	1.3×10^{-3}	220	0.57
$LiPO_3-Li_2SO_4$	(67-33)	3.5×10^{-3}	250	0.66
$B_2O_3-0.56Li_2O-0.08LiF$		6.3×10^{-4}	300	0.7
$B_2O_3-0.56Li_2O-0.08LiCl$		1.0×10^{-3}	300	0.60
$B_2O_3-0.56Li_2O-0.08LiBr$		1.3×10^{-3}	300	0.58
$B_2O_3-0.56Li_2O-0.08LiI$		3.2×10^{-3}	300	0.52
$Li_2O-LiF-Al(PO_3)_3$	(30-50-20)	1.0×10^{-2}	300	0.56
$Li_2O-LiF-Al(PO_3)_3$	(15-70-15)	1.3×10^{-3}	220	0.53
$Nb_2O_5-Li_2O$	(50-50)	5.3×10^{-3}	350	0.44
$Ta_2O_5-Li_2O$	(50-50)	6.4×10^{-3}	350	0.39

[a]Concentrations in mol%

Polymer electrolytes have attracted a considerable attention recently. Conventional polymer electrolytes such as PEO-(LiX)n, where PEO is poly (ethylene oxide) and LiX is a low lattice energy Li Salt with large anions such as AsF_6^-, PF_6^-, BF_4^-, ClO_4^-, $CF_3SO_3^-$, and $(CF_3SO_2)_2N^-$ are mechanically strong, free-standing films but their conductivities ($10^{-9} \sim 10^{-5}$ S/cm at 25°C) are usually too low for use in room temperature batteries [105]. The reason could be attributed to the loss of Li-ion mobility caused by the coupling of the Li ions to the polymer chains. The mobility of the lithium ion have been reported to be improved following two methods; First, by substituting the polymer host with some amorphous polymers. For example, utilizing polymers such as poly[bis-((methoxyethoxy)ethoxy)phosphazene] (MEEP) as the amorphous phase. The composite electrolyte containing MEEP-(LiX)n is then formed using PEO, poly(propylene oxide) (PPO), poly (ethylene glycol diacrylate) (PEGDA) or poly(vinyl pyrrolidinone) (PVP) as a skeleton phase to form a free-standing film with good mechanical strength. The second approach involves utilizing some small molecular species such as propylene carbonate (PC), sulfolane (SL), ethylene carbonate (EC), etc. as the plasticizers. The skeleton host polymers could be polyacrylonitrile (PAN), poly(vinyl chloride) (PVC), PVP or ploy(vinyl sulfone) (PVS). The function of plasticizers is to lower the bonding of the Li ions to the surrounding oxygen anions thereby promoting their mobility. This is schematically shown in Fig. 2-13. The results of the Li-ion conductivity of the composite electrolytes utilizing PC, EC or SL as the plasticizers are shown in Table 2-8.

Before adding plasticizer ——————→ After adding plasticizer
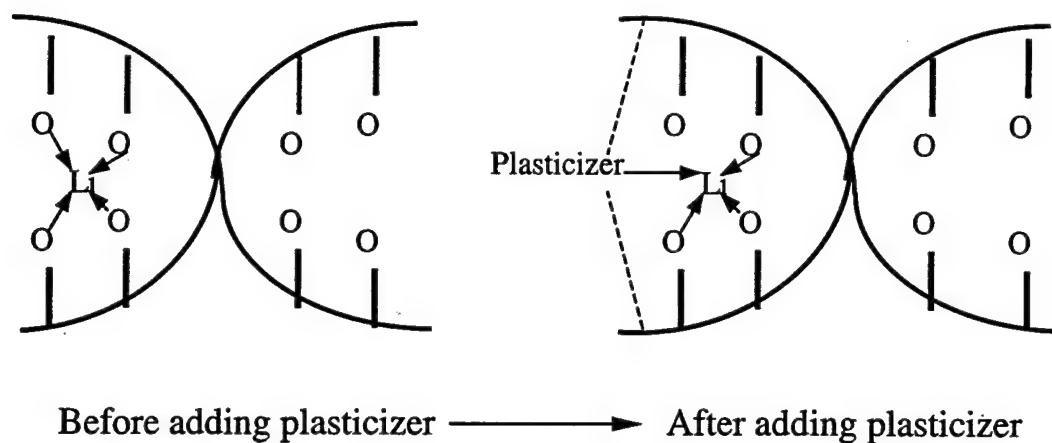
Fig. 2-13. A schematic showing the proposed function of the plasticizers [105].

Table 2-8. The Li-ion conductivity of the composite electrolytes utilizing PC, EC or SL as the plasticizers [105].

Electrolyte	Conductivity (S/cm) at 20°C
21 m/o PAN-38 m/o EC / 33 m/o PC-8 m/o LiAsF$_6$	2×10^{-3}
21 m/o PAN-40 m/o EC / 35 m/o PC-4 m/o LiN(SO$_2$CF$_3$)$_2$	2×10^{-3}
15 w/o PVC-40 w/o EC / 40 w/o PC-5 w/o LiClO$_4$	1.2×10^{-3}
15 w/o PVC-80 w/o PC -5 w/o o LiN(SO$_2$CF$_3$)$_2$	1.1×10^{-3}
35 m/o PVS-30 m/o PC / 30 m/o SL-5 m/o LiN(SO$_2$CF$_3$)$_2$	2.4×10^{-3}
37.5 m/o PVS-30 m/o PC / 30 m/o SL-3.5 m/o LiAsF$_6$	1.5×10^{-3}
25 m/o PVP-35 m/o EC / 30 m/o PC-10 m/o LiN(SO$_2$CF$_3$)$_2$	4×10^{-3}
27 m/o PVP-24 m/o EC / 21 m/o PC-10 m/o Tetra-glyme-18 m/o LiClO$_4$	8×10^{-3}

References

1. M. Stanley Whittingham and Allan J. Jacobson, Intercalation Chemistry, Academic press.
2. K. Brandt, Solid State Ionics, 69 (1994) 172.
3. U. von Sacken, E. Nodwell, A. Sundher, J.R. Dahn, Solid State Ionics, 69 (1994) 284.
4. John B. Goodenough, Solid State Ionics, 69 (1994) 184.
5. T. Nohma, H. Kurokawa, M. Uehara, M. Takahashi, K. Nishio, T. Saito, Journal of Power Sources, 54 (1995) 522.
6. J.R. Dahn, Solid State Ionics, 44 (1990) 87.
7. W. Li, J.N. Reimers and J.R. Dahn, Physical Review B, vol.46 no.6.
8. W. Ebner and F.L. Xie, Solid State Ionics, 69 (1994) 238.
9. Tsutomu Ohzuku, Atsushi Ueda and Masatoshi Nagayama, J. Electrochem. Soc.,140 (1993) 1862.
10. J.B. Goodenough, D.G. Wickham and W.J. Groft, J. Appl. Phys., 29 (1958) 382.
11. V.W. Bronger, H. Bade and W. Klemm, Z . Anorg. Allg. Chem., 333 (1964) 188.
12. W. Li, J. N. Reimers and J. R. Dahn, Solid State Ionics, 67 (1993) 123.
13. M. Broussely, F. Perton and J. Labat, R. J. Staniewicz and A. Romero, J. of Power Sources, 43-44 (1993) 209.
14. R. J. Gommow and M. M. Thackeray, Solid State Ionics, 53-56 (1992) 681.
15. Qiming Zhong, Ulrich von Sacken, J. of Power Sources, 54 (1995) 221.
16. R.V. Moshtev, P. Zlatilova, V. Manev, Atsushi Sato, J. of Power Sources, 54 (1995) 329.
17. K. Sawai, A. Ueda, M. Nagayama, Y. Iwakoshi, T. Ohzuku, Denki Kagaku, 61 (1993) 715.
18. C. Delmas and I. Saadoune, Solid State Ionics, 54-56 (1992) 370.
19. C. Delmas, I. Saadoune and A. Rougier, J. of Power Sources, 43-44 (1993) 595.
20. A. Ueda, T. Ohzuku, J. Electrochem. Soc., 141 (1994) 2010.
21. J. Morales, R. Stoyanova, J. L. Tirado and E. Zhecheva, J. Solid State Chem., 113 (1994) 182.
22. T. Ohzuku, A. Ueda, M. Nagayama, Y. Iwakoshi, H. Komori, Electrochim. Acta, 38 (1993) 1159.
23. T. Ohzuku, H. Komori, K. Sawai, T. Hirat, Chem. Express, 5 (1990) 733.
24. R. Roy.
25. J. C. Brinker and G.W.Scherer, 'Sol-gel Science: The Physics and Chemistry of Sol-Gel Processing', Academic Press, Boston, MA, 1990.
26. D. C. Bradley, R. C. Mehrota and D. P. Gaur, ' Metal Alkoxides' (Academic Press, New York, 1978).
27. T. Ohzuku, H. Komori, M. Nagayama, K. Sawai, T. Hirat, Chem. Express, 6 (1991) 161.
28. H. Noguchi, T. Miyashita, K. Yamato, M. Yoshio, Denki Kagaku, 61 (1993) 720.
29. D. Gallet, A. Waghray, P.N. Kumta, G.E. Blomgren and M. Setter, Proc. Symp. Role of Ceramics in Advanced Electrochemical Synthesis, Am. Ceram. Soc. Proc. 65 (1996) 177.

30. D. Gallet, A. Waghray, P.N. Kumta, M.P. Setter, G.E. Blomgren, J. Power sources, (1998) in press.

31. X. Xiao, Y. Xu, J. Mat. Sci., 31 (1996) 6449.

32. T. Ohzuku, A. Ueda, M. Nagayama, Y. Iwakoshi and K. Sawai, Chem. Exp., 7 (1992) 689.

33. B. Garcia, P. Barboux, F. Ribot, A. Kahn-Harari, L. Mazerolles, N. Baffier, Solid State Ionics, 80 (1995) 111.

34. B. Garcia, J. Farcy, J.P. Percira-Ramos, J. Perichon, N. Baffier, J. Power Sources, 54 (1995) 373.

35. P. A. Lessing, Ceramic Bulletin, 68 (1989) 1002.

36. M. Pechini, U.S. pat. No. 3330697, July 11, 1967.

37. P. A. Lessing, G. R. Miller, H. Yamada, J. Electrochem. Soc., 133 (1986) 1537.

38. E. Zhecheva, R. Stoyanova, M. Gorova, R. Alcantara, J. Morales, J.L. Tirado, Chem. Mater., 8 (1996) 1429.

39. D. M. Schleich, Solid State Ionics, 70-72 (1994) 407.

40. R. Yazami, N. Lebrun, M. Bonneau, M. Molteni, J. Power Sources, 54 (1995) 389.

41. D. Hennings, W. J. Mayr, Solid State Chem., 26 (1978) 329.

42. D. J. Anderton, F. R. Sale, Powder Metall., 22 (1979) 14.

43. M.S.G. Baythoun, F. R. Sale, Mater. Sci., 17 (1982) 2757.

44. A. Douy, M. Odier, Mater. Res. Bull., 24 (1989) 1119.

45. J.H. Choy, Y. S. Han, J. T. Kim, Y. H. Kim, J. Mater. Chem., 5 (1995) 57.

46. V. K. Sankaranarayanan, Q. A. Pankhurst, D. P. E. Disckon, C. E. Johnson, J. Magn. Magn. Mater., 120 (1993) 73.

47. M.E. Brown, D. Dollimore and A.K. Galwey, in C.H. Bamford and C.F.H. tipper (Eds.), Comprehensive Chemical Kinetics, Elsevier, Amsterdam, Vol. 22, (1985).

48. D. Chen, X. Gao, D. Dollimore, Thermochim. Acta, 215 (1993) 65.

49. D. Chen, X. Gao, D. Dollimore, Thermochim. Acta, 215 (1993) 109.

50. Tsutomu Ohzuku, Atsushi Ueda, Solid State Ionics, 69 (1994) 201.

51. J. R. Dahn, E. W. Fuller, M. Obrovac, U. von Sacken, Solid State Ionics, 69 (1994) 265.

52. W. Juzkow, S.T. Mayer, The 12th Annual Battery Conference on Applications and Advances, California State University, Long Beach, CA. January 14-17, 1997.

53. Z. Zhang, D. Fouchard, J.R. Rea, J. Power Sources, 70 (1998) 16.

54. K. Ozawa, M. Yokokawa, Proc. 10th Internat. seminar on primary and secondary battery technology and application, March 1993, Deerfield Beach, FL.

55. T. Nagaura, K. Tozawa, Prog. Batteries Solar Cells, 9 (1990) 209.

56. R.J. Gummow, A. de Kock, M.M. Thackeray, Solid State Ionics, 69 (1994) 59.

57. M. N. Richard, E.W. Fuller, J.R. Dahn, Solid State Ionics, 73 (1994) 81.

58. A. Yamada, K. Miura, K. Hinokuma, M. Tanaka, J. Electrochem. Soc., 142 (1995) 2149.

59. M. Hosoya, H. Ikuta, T. Uchida, M. Wakihara, J. Electrochem. Soc., 144 (1997) L52.

60. J.M. Tarascon, W.R. McKinnon, F. Coowar, T.N. Bowmer, G. Amatucci, D. Guyomard, J. Electrochem. Soc., 141 (1994) 1421.

61. J.M. Tarascon, D. Guyomard, J. Electrochem. Soc., 138 (1991) 2864.

62. A.R. Armstrong, P.G. Bruce, Nature, 381 (1996) 499.

63. C. Masquelier, A. Kondo, R. Kanno, J. Electrochem. Soc., 145 (1998) L49.
64. A.J. Jacobson, R.R. Chianelli, M.S. Whittingham, J. Electrochem. Soc., 131 (1984) 2006.
65. C. Julien, S.I. Saikh, G.A. Nazri, Mater. Sci. Eng. B, 15 (1992) 73.
66. K.H. Cheng, M.S. Whittingham, Solid State Ionics, 1 (1980) 151.
67. G. T.-K. Fey, Wu Li, J.R. Dahn; J. Electrochem. Soc., 141 (1994) 2279.
68. Q. Zhong, A. Bonakdarpour, M. Zhang, Y. Gao, J.R. Dahn, J. Electrochem. Soc., 144 (1997) 205.
69. C. Sigala, D. Guyomard, A. Verbaere, Y. Piffard, M. Tournoux, Solid State Ionics, 81 (1995) 167.
70. H. Kawai, M. Nagata, H. Tukamoto, A.R. West, Electrochem. and Solid-State Lett. 1 (1998) 212.
71. H. Kawai, M. Nagata, H. Tukamoto, A.R. West, J. Mater. Chem., 8 (1998) 837.
72. Yair E.-E., W.F. Howard, Jr., S. H. Lu, S. Mukerjee, J. McBreen, J.T. Vaughey, M. M. Thackery, J. Electrochem. Soc., 145 (1998) 1238.
73. J. Kim, A. Manthiram, Nature, 390 (1997) 265.
74. K. Sawai, Y. Iwakoshi, T. Ohzuku, Solid State Ionics, 69 (1994) 273.
75. R. Yazami, P. Touzain, J. Power Sources, 9 (1983) 365.
76. A. Watanabe, K. Mori, H. Ishikawa, Y. Nakamura, J. Electrochem. Soc.,134 (1987) 1318.
77. M. Mohri, N. Yanagisawa, Y. Tajima, H. Tanaka, T. Mitate, S. Nakajima, M.Yoshida, Y. Yoshimoto, T. Suzuki, H. Wada, J. Power Sources, 26 (1989) 545.
78. I. Tanahashi, A. Yoshida, A. Nishino, J. Electrochem. Soc., 137 (1990) 3052.
79. R. Kanno, Y. Kawamoto, Y. Takeda, S. Ohashi, N. Imanishi, O. Yamamoto, J. Electrochem. Soc., 139 (1992) 3397.
80. M. Morita, T. Hanada, H. Tsutsumi, Y. Matsuda, M. Kawaguchi, J. Electrochem. Soc., 139 (1992) 1227.
81. T. Ohzuku, Y. Iwakoshi, K. Sawai, J. Electrochem. Soc., 140 (1993) 2490.
82. J. R. Dahn, A. K. Sleigh, H. Shi, B.M. Way, W.J. Weydanz, J.N. Reimers, Q. Zhong, U. von Sacken, in: Lithium Batteries, ed. G. Pistoia (Elsevier, Amsterdam, 1993).
83. Ian, A. Courtney, J.R. Dahn, J. Electrochem. Soc., 144 (1997) 2943.
84. Unpublished work at Carnegie Mellon University.
85. J.H. Jackson, D.A. Young, J. Phys. Chem. Solids, 30 (1969) 1973.
86. C.C. Liang, A.V. Joshi, N.T. Hamilton, J. Appl. Electrochem., 8 (1978) 445.
87. U. von Alpen, M.F. Bell, in: P. Vashishta, J.N. Mundy and G.K. Shenoy (Eds.), Fast Ion Transport in Solids, North-Holland, Amsterdam, (1979), p. 463.
88. Y-P. Hong, Mat. Res. Bull., 13 (1978) 117.
89. D. Tranqui, R.D. Shannon, H.Y. Chen, Acta Cryst., B35 (1979) 2479-2487.
90. A. Khorassani, A.R. West, Solid State Ionics, 7 (1982) 1-8.
91. Ian M. Hodge, Malcolm D. Ingram, A. R. West, J. Am. Ceram. Soc., 7-8 (1976) 361.
92. A. Khorassani, G. Izquierdo, A.R. West, Mat. Res. Bull., 16 (1981) 1561.
93. Y.W. Hu, I.D. Raistrick, R.A. Huggins, Mat. Res. Bull., 11 (1976) 1227.
94. J.G. Kamphorst, E.E. Hellstrom, Solid State Ionics, 1 (1980) 187.
95. J. Kuwano, A.R. West, Mat. Res. Bull., 15 (1980) 1661.
96. U.v. Alpen, M.F. Bell, W. Wichelhaus, Electrochim. Acta, 23 (1978) 1395.

97. P.G. Bruce, A.R. West, Mat. Res. Bull., 15 (1980) 379.

98. A.K. Ivanov-Shits, S.E. Sigaryov, Solid State Ionics, 27 (1988) 89.

99. A.R. West, J. Appl. Electrochem., 3 (1973) 327.

100. S. Smedley, C. Angell, Mater. Res. Bull., 15 (1980) 421.

101. A. Pradel, M. Ribes, Solid State Ionics, 18/19 (1986) 351.

102. K. Miyauchi, K. Kanehori, K. Matsumoto, T. Kudo, Solid State Ionics, 9/10 (1983) 1445.

103. J. B. Bates, N.J. Dudney, G.R. Gruzalski, R.A. Zuhr, A. Choudhary, C.F. Luck, J.D. Robertson, Solid State Ionics, 53-56 (1992) 647.

104. C. Julien, G.-A. Nazri, in: H.L. Tuller (Eds.), Solid State Batteries: Materials Design and Optimization, Kluwer Academic Publisher, Boston, (1994), p. 228.

105. K.M. Abraham, M. Alamgir, Solid State Ionics, 70/71 (1994) 20.

Chapter 3

Objectives

$\mathbf{T}$he objectives of the present research are outlined in three parts:

Part I. *Synthesis and design of precursors*

1. Development of the particulate sol-gel (PSG) approach for synthesizing $LiMO_2$ (M=Ni, $Ni_{0.75}Co_{0.25}$). Two main solution systems have been investigated:

   a. Pure aqueous system

   b. Mixture of aqueous and non-aqueous solvent system

2. Four different variants of the PSG process are studied:

   a. Rotary evaporation process

   b. Spray drying process

   c. Gelation process

   d. Spray decomposition process

Investigation of the solution and sol-gel chemistry as well as the structure of the synthesized precursors derived from these processes will form the main focus of the study.

Part II. Investigation of the reaction pathways leading to the formation of the resultant oxides during heat treatments

The studies on the formation of the resultant oxides consist of:

1. Phase evolution of the oxides from the as-prepared xerogels.

2. Reaction paths and reaction mechanisms responsible for the formation of the desired oxides.

3. Kinetics of formation of the desired oxide.

4. Microstructural characterization of the precursors and the resultant oxide powders.

5. Study of the variation in the specific surface area of the precursors and resultant powders.

Part III. Electrochemical characterization

The electrochemical response of the synthesized oxides, were evaluated in order to elucidate the effects of xerogel preparation as well as the heat treatment conditions on the electrochemical properties. Processing parameters related to the synthesis of the oxides that influences the electrochemical properties of the oxides will also be investigated. The results of electrochemical characterization will be used as a guideline for both understanding the electrochemical behavior of the synthesized oxides as well as improving the synthesis conditions in order to prepare a superior material. Three main issues will be studied with regards to the evaluation of the electrochemical response:

1. Evaluation of the capacity of the synthesized materials.

2. Study of the cyclability of the materials.

3. Evaluation of the rate capability and phase transformation behavior of the materials during cycling.

Chapter 4

Experimental Procedures

Part I.   *Chemical processes*

The particulate sol-gel (PSG) approach has been used to synthesize the lithiated transition metal oxides $LiMO_2$ (M= Ni, $Ni_{0.75}Co_{0.25}$). Four different variants of the PSG process have been selected for the present study. These are: 1. Rotary evaporation, 2. Gelation, 3. Spray drying and 4. Spray decomposition. The following sections give a complete description of the procedures involved in the four different processes employed to yield the precursors.

4.1   Rotary evaporation process:

The general procedure involved in obtaining xerogels using this process consists of dissolving starting chemicals in a suitable solvent. Thus appropriate starting chemicals containing the required stoichiometric quantities of lithium, nickel, cobalt etc. are dissolved in a suitable solvent (containing the appropriate amounts of water and ethanol) to obtain either a homogeneous solution or a homogeneous suspension. This solution or suspension is then dried in a rotary evaporator under conditions necessary to obtain a homogeneous solid. This homogeneous solid, also called the precursor or xerogel, is heat

treated in a suitable atmosphere under various temperature conditions necessary to obtain the electrochemically active materials.

A schematic flow chart of the rotary evaporation process is shown in Figure 4-1. Detailed description of the procedures used for the preparation of xerogels and the heat treatment conditions employed are described in the subsequent sections.

Rotary Evaporation Process for Synthesizing LiNiO$_2$
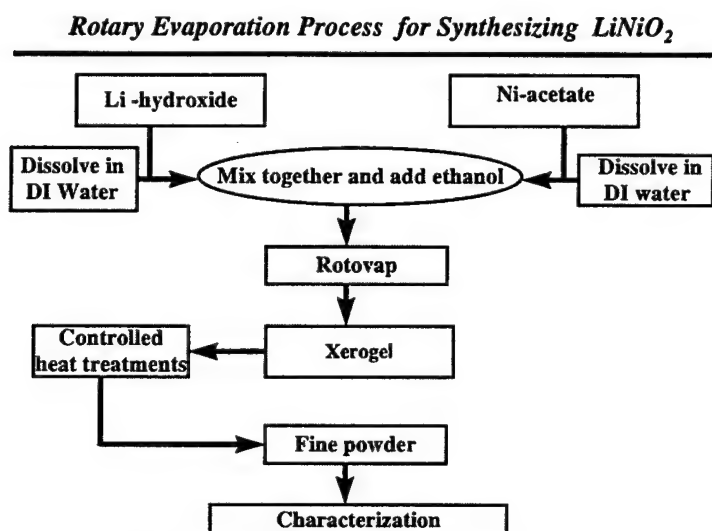
Figure 4-1. Schematic of the procedure used in the rotary evaporation process for synthesizing LiNiO$_2$.

4.1.1 Preparation of Xerogel:

In this section the rotary evaporation process used for synthesizing LiNiO$_2$ is introduced as an example. Generally, 0.1 moles of the starting reagents are used to create the batch of xerogels. The procedure used to prepare the xerogel powders is described below:

1. 0.1 mole (4.196g) of lithium hydroxide (Aldrich, FW=41.96, 99 %) is dissolved in 30 ml deionized (DI) water to form a clear solution.

2. 0.1 mole (24.886g) of nickel (II) acetate (Aldrich, FW=248.86, 98 %) is dissolved in 150 ml DI water to form a dark green but clear solution.

3. The solution prepared in 1 is transferred to the solution prepared in 2. At this stage, some pale green precipitate (probably nickel hydroxide) is formed.

4. 90ml of dehydrated ethyl alcohol (200 proof) is added to the solution prepared in step 3 and the solution is stirred for 15 minutes.

5. The well mixed turbid solution obtained in 4 is then placed in a rotary evaporator (Buchi, Switzerland). The conditions used to obtain the xerogels in the rotary evaporator are: 500mbar at 120°C for 3 hours, after which the pressure is reduced to 100mbar at 140°C for another 1 hour to induce complete drying.

6. The precipitate obtained from step 5 is collected and ground. The weight of the collected as-prepared powder is approximately 19 ~ 20 g.

4.1.2 Heat treatments:

Alumina crucible was used to load the xerogel powders obtained from the rotary evaporation process described in the earlier section. A box furnace (Lindberg, Watertown, WI) was used for conducting the heat treatments in this study. Heat treatment temperatures in the range of 300 to 800°C were used in the present study, with a typical heating and cooling rate of 2°C/min. The dwell time ranged from 2 to 8 hours for the present study. All the different heat treatments were conducted in air.

4.2 Spray drying process:

The steps used for spray drying are schematically shown in Figure 4-2. A mini-spray drier (Yamato, model ADL31, Japan) was used in this process for generating the xerogel powders. Since the nozzle of the spray drier is small (~500μm), it is necessary to obtain a clear solution for the spray drying process. The clear solution is then sprayed using air as the atomizing gas through the atomizing nozzle into a chamber wherein the temperature is maintained above the drying temperature of the solvent (either by external heating or by flowing heated air into this chamber). The dried powder is then collected and subjected to appropriate heat treatments. The powders generated by spray drying are very fine (much less than a micron). Good mixing at a molecular level is expected for the powders generated by this process. Detailed description of the procedure employed for
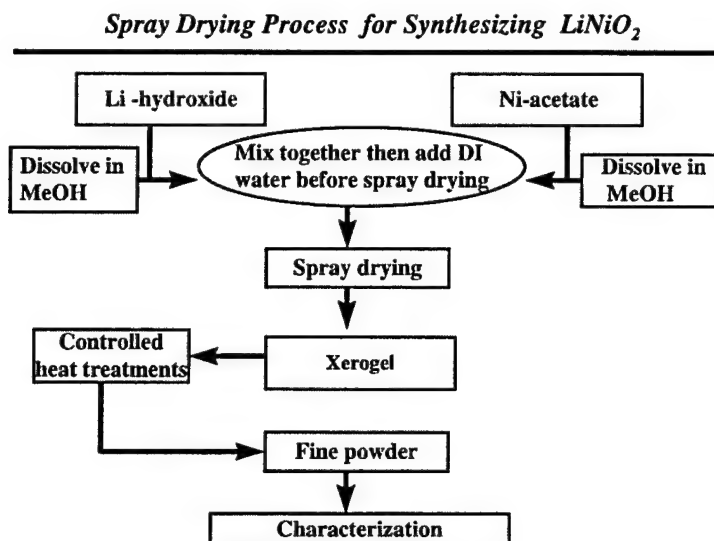
Figure 4-2. Schematic of the spray drying process used for synthesizing LiNiO$_2$.

preparing the solution and synthesizing the xerogel powder is described in the next section.

4.2.1 Xerogel powder preparation:

The procedure for synthesizing xerogels using this process is described below for the case of LiNiO$_2$ selected as an example:

1. 0.3 mole of lithium hydroxide monohydrate is dissolved in 150 ml methanol.
2. 0.3 mole of nickel (II) acetate tetrahydrate is dissolved in 360 ml of methanol.
3. The solution prepared in 1 is transferred to the solution prepared in 2. At this stage, again some pale green colored precipitates are generated. After 10 to 15 minutes of stirring, these precipitates dissolve back yielding a clear green colored solution.
4. The clear solution prepared in step 3 is then transferred to the spray drier. The experimental conditions used in the spray drier are:
   a. Pressure: 1.5Kfg/cm^2 for the inlet gas.
   b. The inlet gas temperature is set at 225°C. The outlet gas temperature is maintained at a constant temperature of 80°C.

c. The pump rate (control of the volume of inlet solution) is approximately 12~13ml/min.

d. The aspirator rate is set at 1, which corresponds to 70~100L/min.

5. The collected powders weigh approximately 48 g. The spray dried powders are pale green in color.

4.2.2 Heat treatments:

The heat treatment conditions used are similar to those described in section 4.1.2

4.3 Gelation process:

In this process, lithium hydroxide and the appropriate chemicals containing one or more of the transition metals, e.g. nickel or cobalt acetates, are dissolved in methanol and water respectively. These two solutions are then mixed together and stored until gelation occurs. The main difference between the gelation and the rotary evaporation process is that in the former, a gel is obtained at the solution stage. After one day (24h) of aging, the gel is then dried using a rotary evaporator following the procedure described in section 4.1.1. A schematic of the steps involved in the gelation process is shown in Fig. 4-3.

Gelation Process for Synthesizing LiNiO$_2$

```
    Li -hydroxide                          Ni-acetate

  Dissolve in    →  Mix together followed  ←  Dissolve in
    MeOH             by stirring until the      DI water
                     solution becomes clear

                  Keep stationary for 24 hrs

      Xerogel    ←    Rotovap

   Controlled   →   Fine powder
  heat treatments

                  Characterization
```
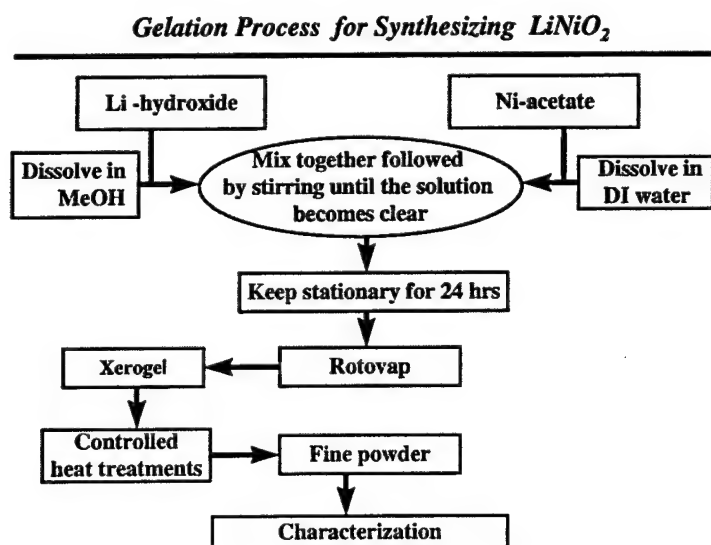
Figure 4-3. Schematic of the gelation process used for synthesizing LiNiO$_2$.

4.3.1 Preparation of xerogel powders:

A detailed description of the procedure used for preparing the xerogel powder of $LiNiO_2$ using the gelation process is as follows:

1. 0.1 mole of lithium hydroxide monohydrate is dissolved in 40ml methanol.

2. 0.1 mole of nickel (II) acetate is dissolved in 150ml DI water.

3. The solution prepared in 1 is transferred to 2. At the same time, 10ml of methanol is used to rinse the beaker which contained solution 1. At this stage, some pale green colored precipitate is formed. After 15 to 20 minutes stirring, the precipitates redissolve back into the solution yielding a transparent green colored solution ready to be aged for gelation.

4. The solution prepared in 3 is allowed to gel for one day. After one day of aging, a stiff gel is formed which is green in color.

5. The gel formed in step 4 is then transferred to the rotary evaporator for drying. The drying conditions are: 100 mbar at 80°C for 2 hours, at 120°C for another 2 hours and at 140°C for an additional hour.

6. The precipate (xerogel) is then collected and ground to a fine powder for further heat treatment. The powders collected typically weigh about 20 g.

4.3.2 Heat treatments:

The heat treatment conditions used are similar to those described in section 4.1.2

4.4 Spray decomposition process:

The spray decomposition process is similar to the spray drying process, except that the powder obtained from the drying chamber is passed through a tube furnace held at 800°C which is higher than the decomposition temperature of the different starting precursors. Therefore, when the powder exits the decomposition tube and is collected in the cyclone separator, it is already partially or fully decomposed to yield the

electrochemically active material. Alternatively, the temperature of the drying gas is higher than the decomposition temperature of the solid that is normally obtained after "spray drying", so that the solid collected in the separator is already partially or completely decomposed. This powder may then be subjected to further heat treatment (which is usually at a low temperature for a short time) in order to reproducibly ensure complete decomposition of the powder. The spray decomposition set up is schematically shown in Figure 4-4. The experimental procedure and conditions used in this process are described in detail in the next section.

Schematic of the Spray Decomposition Set Up
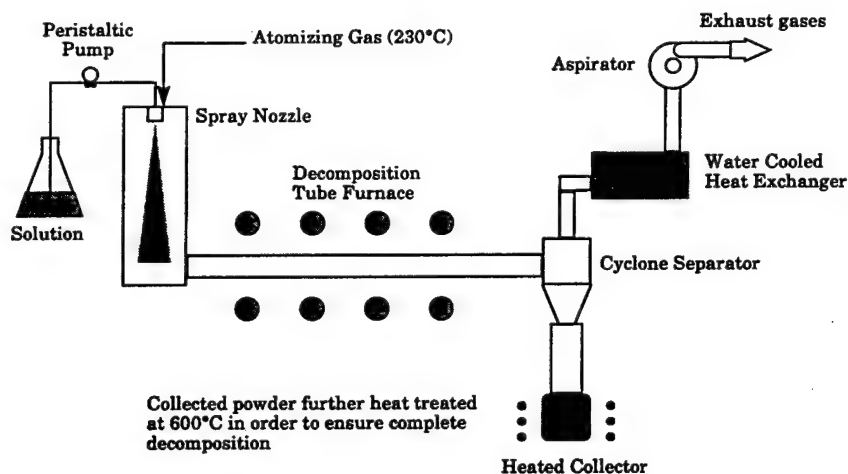
Figure 4-4. Schematic of the spray decomposition set up developed for synthesizing LiNiO$_2$.

4.4.1 Experimental procedure and conditions:

The procedure adapted in preparing the clear solution and the experimental parameters used for spray decomposition is identical to those described earlier in section 4.3.1 for the spray drying process. A box furnace was used for subsequent heat

treatments. The exact heat treatment conditions of each individual sample will be described in the later sections whenever necessary.

Part II. *Characterization of the xerogels*

4.5 Infrared spectroscopy:

Fourier transform infrared spectroscopy (FTIR, Mattson, Galaxy series FTIR 5000) was conducted using the KBr pressed pellet technique to determine the structure of the as- prepared precursors. The procedure used prepare the samples is described below:

1. 200 mg of KBr (spectroscopy grade) is first ground using a mortar and pestle.
2. 2 mg of the xerogel powder is then transferred to the ground KBr powders followed by further grinding.
3. 80 mg of the resultant powders is then transferred to a die for the preparation of a pellet.
4. A pressure of 1000 lb/cm^2 ($\approx$4,450 N/m^2) is applied for 60 seconds to prepare the disk.
5. The pressed pellet is then transferred to the FTIR sample chamber in the presence of an ultra high purity (UHP) N$_2$ gas flow. The sample is scanned after purging for 5 minutes in order to remove any moisture that could have accumulated during sample transfer.
6. 400 cm^{-1} to 4000 cm^{-1} is the frequency range used for the spectroscopic analysis.

4.6 TGA/DTA analysis:

Thermogravimetric (TG) and differential thermal (DT) analyses were conducted using a TA Instrument (TA 2960, New Castle, DE). Usually 10~20 mg of the xerogel powders was used for the analysis. A general heating rate of 5°C/min was employed to heat treat all the samples from room temperature to 800°C in the presence of air.

4.7   TGA/DTA/Mass analysis:

Evolved gas analysis during heat treatment is conducted using a simultaneous TGA/DTA/Mass spectroscopy instrument (Cahn TG-171, Madison, WI) that allows in-situ analysis of the gases evolved during heat treatment. The weight of the sample loaded can range from 1mg to 100g according to the need of the experiments. Electron impact (70eV) is used for the creation of charged ions for mass analysis. Helium is used as a purge gas to prevent any damage to the microbalance. Owing to the insulation of helium, the reaction gas can be ambient air or inert gas such as argon as well as corrosive gases such as hydrogen sulfide or ammonia. In the present study, usually 0.1g of the xerogel powders was used for the analysis. A general heating rate of 5°C/min was employed to heat treat all the samples from room temperature to 800°C or 900°C using either argon or air as the reaction gas.

Part III.   *Characterization of the heat treated powders*

4.8   X-ray diffraction (XRD):

X-ray powder diffractometer (Rigaku, θ/θ diffractometer, Tokyo, Japan) was used for the phase analysis and structural characterization of the resultant powders. The parameter used were as follows: $2\theta = 10$ to $90°$, voltage: 35kV, current: 20mA, step size 0.05° and a collection time of 2 seconds for each step. Usually, the sample powders were packed on a brass sample holder. In the case of the samples used for Rietveld analysis, usually a step size of 0.05° and a collection time of 14 seconds were set for each scan.

4.9   Scanning electron microscopy (SEM) analysis:

The morphology and microstructure of the resultant powders was investigated using a scanning electron microscope (Series 4, CamScan, Cambridge, UK). A 25kV working voltage is used to observe the morphology. Samples for the SEM analysis are usually prepared by sprinkling the oxide powders on aluminum stubs covered with carbon tapes. It was found that there was no need to heat the powders with a conducting Au film

prior to observing the powders in the SEM. This is because the oxides are semiconductors and do not charge when exposed to an electron beam.

4.10 Brunaner, Emmett and Teller (BET) specific surface area:

The specific surface area measurements were conducted using the Brunaner, Emmett and Teller (BET) method (N_2 adsorption, Quantachrome Instruments, Syosset, NY). Samples were dried at 150°C in a vacuum for 3 hours before measuring the specific surface area.

4.11 Transmission electron microscopy (TEM) and scanning and transmission electron microscopy (STEM) analyses:

The morphology of the resultant powders and the interfaces between the resultant oxide and the impurity phases were investigated using a transmission electron microscope (TEM, Phillips EM420T) equipped with an energy dispersive X-ray analysis unit (EDX, Princeton PGT), and a scanning transmission electron microscope (STEM, VG HB501) also having an attachment for EDX (Oxford EDX) analysis. The powders used for the electron microscopy analysis were first dispersed in ethanol in an ultrasonic bath, followed by placing a few droplets on the copper grid sample holder. The sample holder was then dried in a vacuum drying oven for 8 hours at room temperature prior to loading in the sample chamber.

Part IV. *Electrochemical characterization*

4.12 Cathode preparation:

Cathodes of the active oxide materials were prepared in the following manner. A slurry comprising of 1.000g of the heat treated oxide material, 0.087g acetylene black, 0.061g copolymer binder (ethylene/propylene copolymer containing 60% ethylene content) was well mixed in the solvent TCE (trichloro ethylene). The as-prepared slurry was then coated and dried on an aluminum foil. After evaporating the residual solvent

overnight, the coated aluminum foil was punched and then dried in a vacuum oven at 140°C for 12 hours. Finally, the cathode disks were transferred to a glove box (VAC, Hawthorne, CA. Argon atmosphere with both oxygen and moisture content less than 0.2ppm) for electrochemical testing. The thickness and weight of the coated aluminum foil are usually in the range of 0.0025 to 0.0045 inch (0.0064 ~0.0114 cm) and 0.0080 to 0.0120g, respectively.

4.13   Test cell assembly:

The "hockey-puck" cell, shown in Figure 4.5, was assembled in a glove box for electrochemical characterization. The cell is composed of a top piece, a bottom piece and two middle sections made of teflon which are held together by four long steel bolts. A channel inside the two middle pieces is filled with an aluminum block, a punched cathode, separator (glass fiber, Whatman) and lithium anode arranged in a bottom to top sequence. Another lithium foil, acting as a reference electrode is placed near the edge of the cathode for voltage measurements. 1M $LiPF_6$ in EC/DMC (Ethylene carbonate/ Dimethyl carbonate) with a EC to DMC ratio 2:1(67:33 wt%) was used as the electrolyte. A glass microfiber filter (Whatman) was used as the separator.

4.14   Evaluation of electrochemical behavior:

Electrochemical characterization was conducted using a potentiostat (Arbin Instrument, college station, TX). A voltage range of 3.1 to 4.4V and a constant current density of 0.25 mA/cm^2 was normally used for the charge and discharge cycles to evaluate the constant current electrochemical performance of the test batteries. Each discharge and charge step was separated by a rest period of 60 seconds. Varying current densities of 0.01 mA/cm^2 to 5 mA/cm^2 were also used in certain cases where the rate capability of the oxide was assessed.
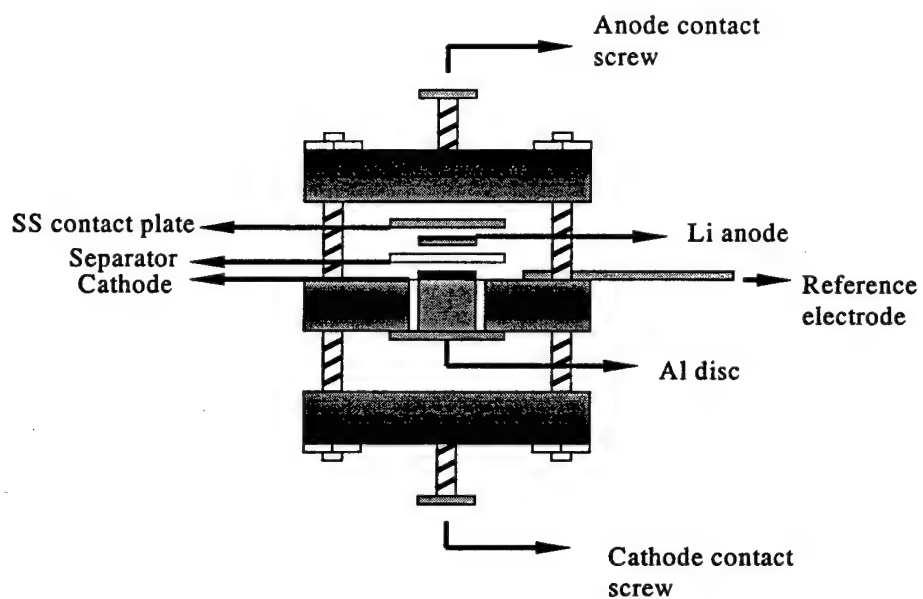
Figure 4.5. The "hockey-puck" cell utilized for evaluation of the electrochemical response.

Chapter 5

Results and Discussion

Four processes developed for synthesizing $LiMO_2$ (M= Ni, $Ni_{0.75}Co_{0.25}$) based on the concept of the particulate sol-gel (PSG) approach form the basis of the present study. As mentioned earlier, two main solvent systems have been utilized for synthesizing $LiMO_2$ (M=Ni, $Ni_{0.75}Co_{0.25}$) powders. The first system employs deionized (DI) water. The second solvent system is based on the use of non-aqueous protic polar solvents such as methanol. According to the characteristics of the xerogel preparation, these processes are named as: a) the rotary evaporation process, b) the spray drying process, c) the gelation process and d) the spray decomposition process. The rotary evaporation process developed in the present study utilizes only deionized (DI) water as the solvent. In contrast, the spray drying, gelation, as well as the spray decomposition processes use non-aqueous polar protic solvents such as methanol in addition to water for the preparation of the xerogels. The results and discussion on each newly developed process will include the characterization of the xerogels, the study of phase evolution as well as the morphology of the powders during and after heat treatment, and finally, the evaluation of the electrochemical response of the resultant oxide. In addition, the reaction mechanism and the kinetics of the formation of the resultant oxides are also investigated and discussed.

Part I.   Structural characterization of xerogels

5.1 Xerogels generated using the rotary evaporation process:

The as-prepared powders used for generating $LiNiO_2$ and $LiNi_{0.75}Co_{0.25}O_2$, derived by rotary evaporation were characterized using TGA, XRD and FTIR. Since the results of the analyses of the xerogel powder are very similar for both $LiNiO_2$ and $LiNi_{0.75}Co_{0.25}O_2$, only the results of the as-prepared powders for $LiNiO_2$ are discussed in this section. The TGA analysis plot obtained for the as-prepared powders corresponding to $LiNiO_2$ is shown in Fig. 5-1. The heating rate utilized in this case is 5°C/min to 800°C. A 1.72% weight loss prior to the decomposition temperature ~ 230°C could be attributed to the evaporation of either residual water contained in the xerogel or the absorption of moisture by the as-prepared powder prior to its analysis. At 230°C, decomposition occurs resulting in a significant weight loss of ~ 43.04% until a temperature of 300°C. X-ray diffraction of the sample heat treated at 300°C reveals nickel(II) oxide (NiO) and lithium carbonate (Li_2CO_3) to be the only major crystalline products, as shown in Fig. 5-2. Based on the close similarity of the calculated weight losses of 31% between the starting precursors and the xerogel, combined with the observed 43.04% and calculated (44.2%) weight loss of the xerogel to form the intermediate products of nickel oxide and lithium carbonate, the following reactions can be proposed for the formation of the xerogel and the decomposition products at 300°C:
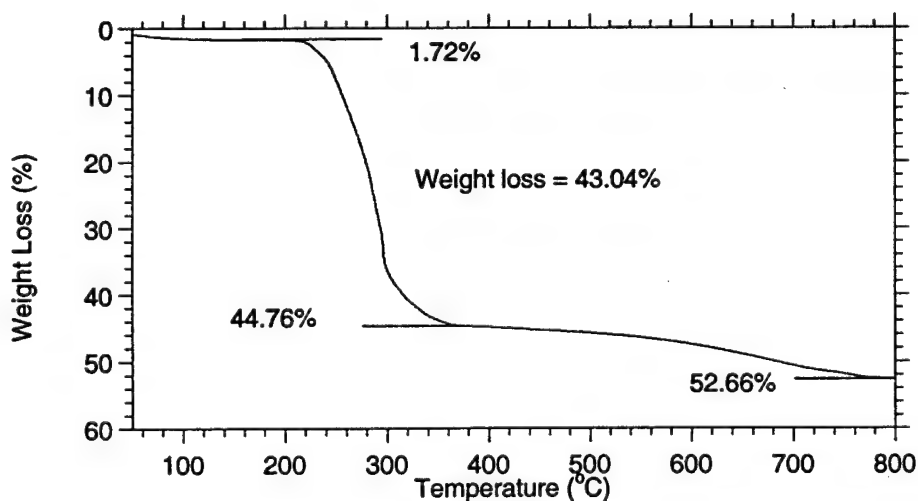
Figure 5-1. The TGA analysis of the xerogels generated for the synthesis of $LiNiO_2$.
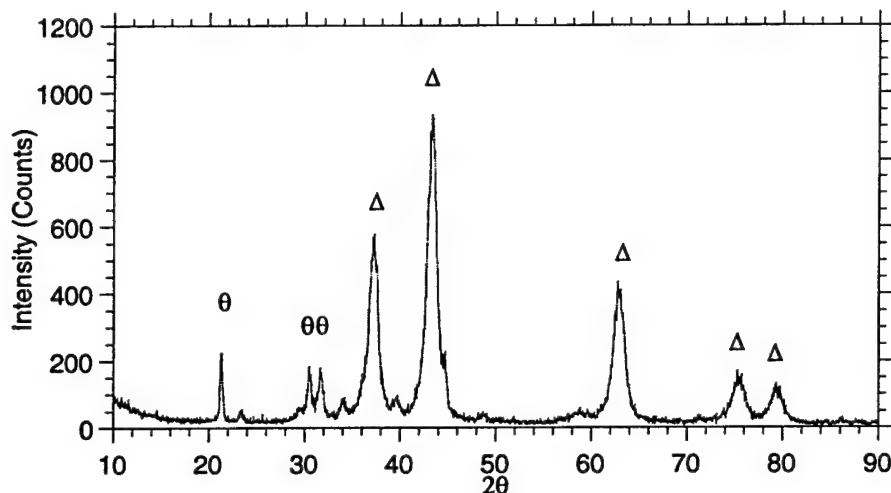
Figure 5-2. XRD data of LiNiO$_2$ xerogels heat treated at 300°C for 5 hours.(-Δ-)NiO phase (-θ-)Li$_2$CO$_3$ phase.

(a) *Rotary evaporation:*

$$\text{LiOH}\cdot\text{H}_2\text{O} + \text{Ni(OAc)}_2\cdot 4\text{H}_2\text{O} \text{ ------------>} x\text{LiOH} + (1-x)/2 \text{ Ni(OH)}_2 +$$

$$(1-x)\text{LiOAc} + (1+x)/2 \text{ Ni(OAc)}_2 + 5 \text{ H}_2\text{O}_{(g)} \quad (5.1)$$

31% weight loss (Calculated)

(b) *Heat treatment:*

$$x\text{LiOH} + (1-x)/2 \text{ Ni(OH)}_2 +$$

$$(1-x)\text{LiOAc} + (1+x)/2 \text{ Ni(OAc)}_2 \text{ -------------->} 1/2 \text{ Li}_2\text{CO}_3 + \text{NiO} + \text{gases} \quad (5.2)$$

44.2% weight loss (Calculated)
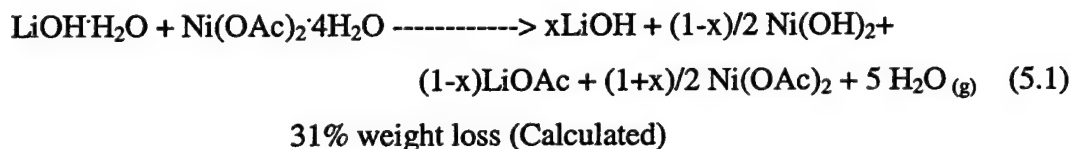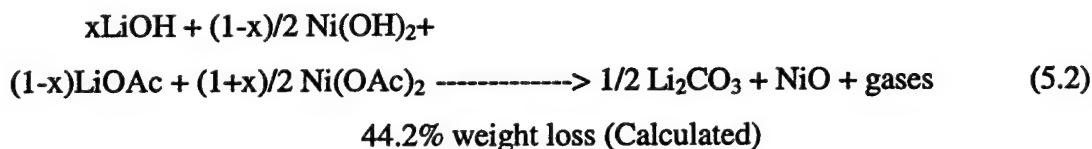
FTIR was also used to examine the composition of the xerogel generated according to the proposed reaction in equation (5.1). This was done by collecting an FTIR spectra of the xerogel and comparing it with those of commercial Ni(OH)$_2$, LiOH, LiOAc and Ni(OAc)$_2$. In the case of the latter three compounds, the salts were dissolved in water and subjected to rotary evaporation similar to the xerogels prior to collection of the spectra. This was done to replicate the physical form and state of the starting materials similar to the xerogel, and also to eliminate any structural variations.

58

Furthermore, this would provide a more realistic and scientific bases to compare and analyze the structure of the xerogel. The IR spectra obtained on commercial $Ni(OH)_2$, and the dehydrated LiOH, LiOAc and $Ni(OAc)_2$ salts derived by rotary evaporation are shown in Fig. 5-3(a) and (b). By superimposing the IR spectra of commercial $Ni(OH)_2$ and dehydrated LiOH, LiOAc and $Ni(OAc)_2$ as shown in Fig. 5-3(c), it is seen that some absorption peaks may disappear because of the overlap of the peaks. The infrared spectrum corresponding to the xerogel powder of $LiNiO_2$ is shown in Fig. 5-3(d).

A comparison of the spectrum obtained on the xerogel and the superimposed spectra for the dehydrated salts shows that all the resolved vibrational peaks seen in the superimposed spectrum are present in the xerogel sample. This therefore suggests that the xerogel could be composed of an intricate mixture of $Ni(OH)_2$ and dehydrated LiOH, LiOAc and $Ni(OAc)_2$. Two sharp absorption peaks shown in the IR spectrum of the xerogel in the 3500 to 3700 cm^{-1} region can be identified as OH stretching modes which represent the OH groups bonded to Li and Ni respectively. The existence of LiOH in the xerogels is indicative of the presence of the unreacted hydroxide in the xerogel powders remaining trapped in the solid during rotary evaporation. This amount however can be expected to be negligible under the present experimental conditions. The other two important peaks seen in the region of 1400 to 1600cm^{-1} are the characteristic vibration modes corresponding to symmetric and asymmetric COO stretching [1-8] arising from the acetate groups, which cannot be categorically resolved as being bonded to Li or Ni.

Based on the IR, XRD and thermal analyses, it is clear that the xerogel is a mixture of hydroxides and acetates. However, it is also possible that there may be hydroxy-acetate species of Ni such as Ni(OH)(OAc). The formation of such a species due to the partial hydrolysis of $Ni(OAc)_2$ is quite probable particularly in the presence of stoichiometric LiOH necessary to form $LiNiO_2$ that is insufficient to completely hydrolyze $Ni(OAc)_2$. In order to identify the presence of this complex in the xerogel with complete confidence, it was decided to disperse the xerogel in water and analyze the solid and liquid components corresponding to the dissolved and insoluble fractions. The freshly prepared xerogel was therefore dispersed in water and collected after separation from the liquid by centrifugation. The clear supernatant liquid extracted after centrifugation was dried to

(a)

(b)

60
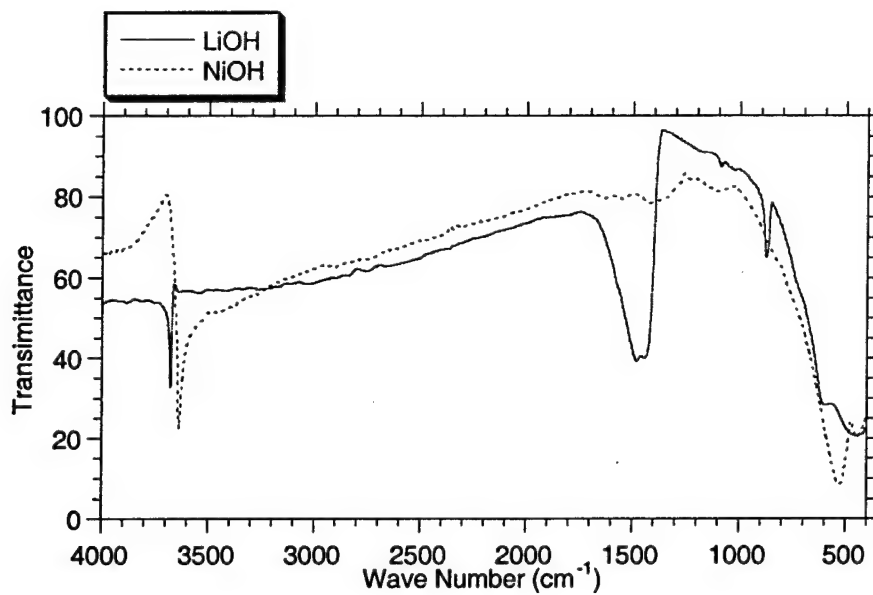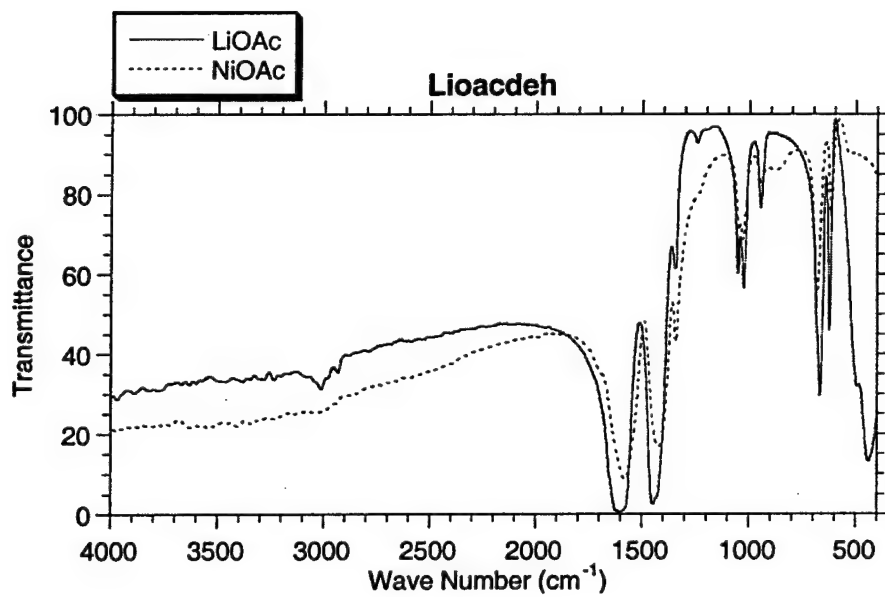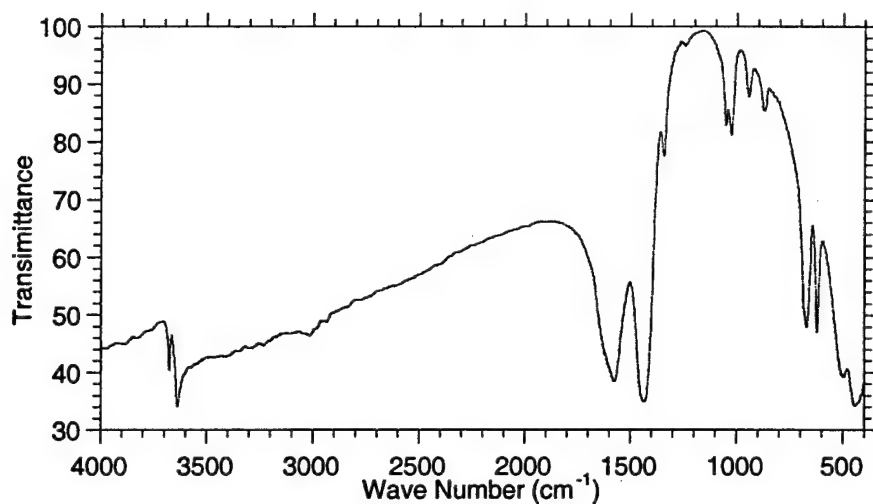
(c)
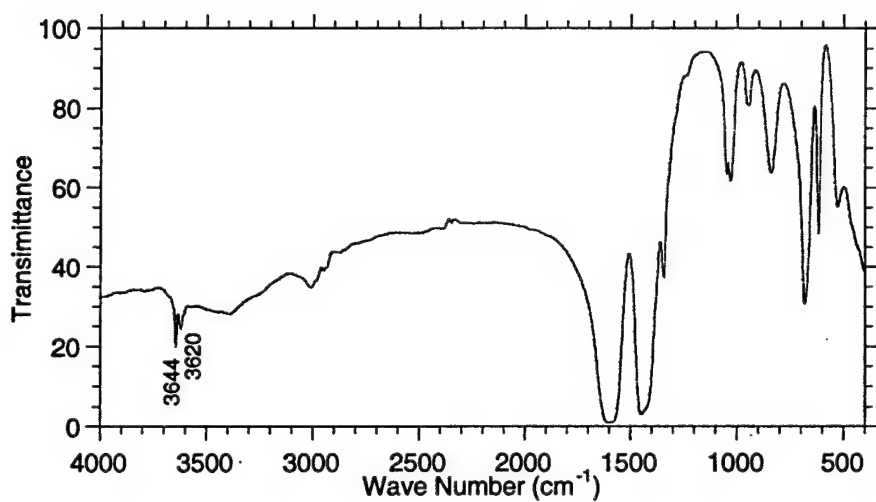
(d)

Figure 5-3. The infrared spectra of (a)commercial Ni(OH)$_2$ and dehydrated LiOH, (b)Ni(OAc)$_2$ and LiOAc. The superimposed infrared spectrum of commercial Ni(OH)$_2$ and dehydrated LiOH, LiOAc and Ni(OAc)$_2$ is shown in (c). The infrared spectrum corresponding to the xerogel powder of LiNiO$_2$ is shown (d).

collect the dissolved products. Thus, the solid precipitate and the resultant powders obtained by drying the clear solution after centrifugation were both investigated again using FTIR, the plots for which are shown in Fig. 5-4(a) and 5-4(b) respectively.

It can be seen that the powders obtained by drying the clear solution does not contain any OH vibrations which indicates that all of the OH groups are precipitated during dispersion of the xerogel in water. On the other hand, the powders derived from the precipitates show only one OH stretching band instead of two observed in the unwashed xerogel (see Fig. 5-3(d)). The OH stretching vibration which was seen at $3620cm^{-1}$ previously in the unwashed xerogel disappears, indicating the complete reaction of LiOH with nickel acetate during dispersion of the xerogel in water. In comparison to the vibrations characteristic of the dehydrated LiOH, the position of the OH stretching peak corresponding to LiOH in the xerogel is observed to shift to lower frequencies (from $3678cm^{-1}$ to $3620cm^{-1}$). This could be attributed to hydrogen bonding between OH groups and the residual water molecules in the xerogel sample [9]. The IR spectrum of the precipitates collected after centrifugation also shows distinct absorption peaks at $1618 cm^{-1}$, $1435cm^{-1}$ and 1373 and $1312cm^{-1}$ which are not characteristic of the vibrations corresponding to nickel hydroxide shown in Fig. 5-3(a) and could arise from vibrations related to acetate ligands. This therefore suggests the possibility of the existence of a nickel hydroxy acetate in the precursor which is insoluble in water.

It is known that both LiOAc and $Ni(OAc)_2$ are soluble in water, while $Ni(OH)_2$ is insoluble. If Ni(OH)(OAc) were to exist, it should be insoluble in water since the spectrum collected on the solid obtained after drying the liquid portion separated by centrifugation (see Fig. 5-4(a)) shows no OH vibrations. If the Li to Ni ratio in the sample which is soluble in water is known, the amount of acetates soluble in water can also be determined and therefore the amount of acetate which is insoluble in water can be obtained by mass balance confirming the existence of Ni(OH)(OAc). In order to validate this analysis and verify the presence of Ni(OH)(OAc), chemical analysis was conducted on the sample derived by drying the liquid portion separated by centrifugation. The results of the chemical analysis are shown in Table 5-1.

From the chemical analysis, two conclusions can be made as follows:
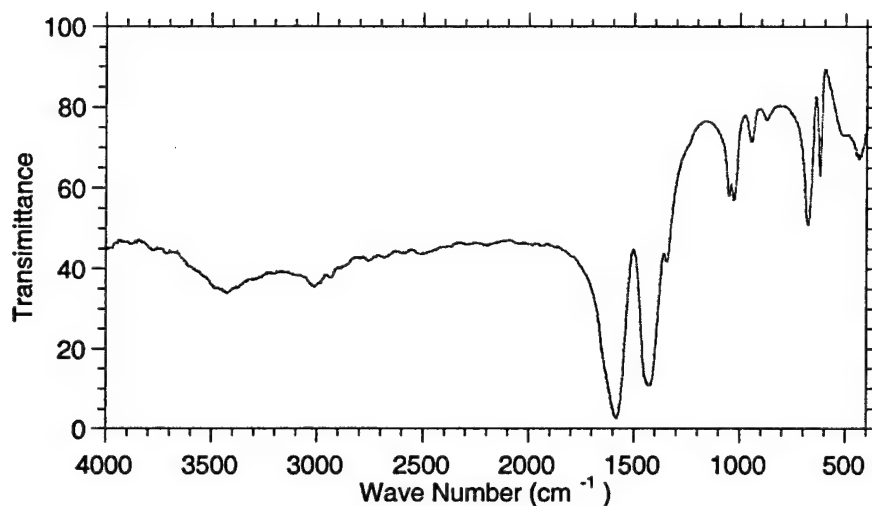
(a)
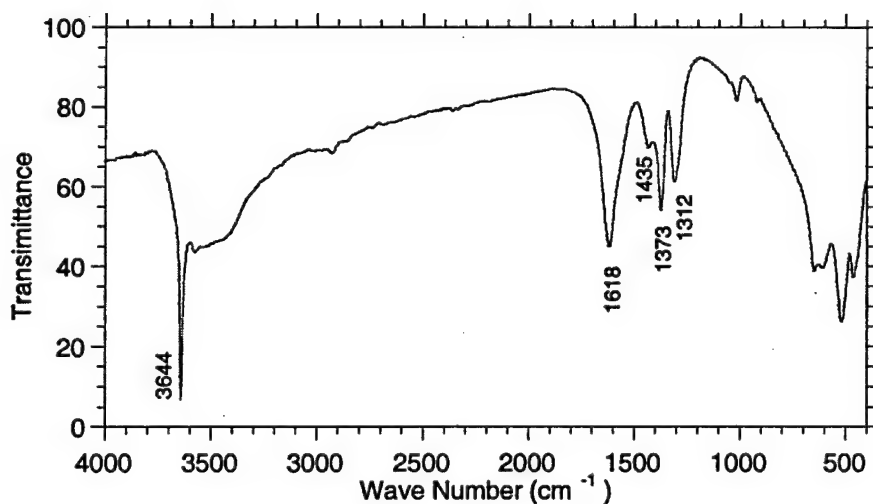
(b)

Figure 5-4. IR analysis is of the precipitate and the clear solution separated after centrifugation. (a) The IR data for the powders obtained from the clear solution after drying. (b) The IR data for the precipitate.

Table 5-1. The results of chemical analysis of the sample obtained by drying the liquid portion collected after centrifugation.

Element	Weight Percent (%)	Stoichiometric Molar Ratio
Lithium	5.14	1.000
Nickel	15.54	0.358

1. LiOAc and $Ni(OAc)_2$ are the only species that are present in the sample which is soluble in water with a stoichiometric ratio of LiOAc : $Ni(OAc)_2$ = 1 : 0.358. This conclusion is arrived at by considering the fact that the weight percent of Li and Ni calculated by assuming a stoichiometric ratio of Li: Ni: (OAc) = 1: 0.358: (1+ 0.358×2) is in agreement with the weight percent of Li and Ni observed from chemical analysis. Thus the balance of the acetate groups can be assumed to remain in the centrifuged solid.

2. By assuming a molar ratio of Li: Ni: (OAc) = 1: 1: 2 in the xerogel, the sample which is insoluble in water should contain 0.284 mole of acetate groups which are present as nickel hydroxy acetate and 0.358 mole of nickel hydroxide which corresponds to a 19.1 weight % and 16.6 weight % of the xerogel respectively. It should be mentioned that the assumption of a molar ratio of Li: Ni: OAc = 1: 1: 2 is valid because this is the nominal composition of the starting materials and is the expected ratio in the solid xerogel. Furthermore, since the acetate groups can not react with the alcohol present in the solution to form an ester without the presence of protons during the preparation of the xerogel, no loss of acetate groups can be expected.

Therefore, the vibrations at 1618, 1435, 1373 and 1312 cm^{-1} in the solid precipitate collected after centrifugation can be attributed to the presence of Ni(OH)(OAc). These vibrations have been clearly isolated during dissolution and centrifugation, suggesting its major presence in the original xerogel. The FTIR analysis of the xerogel however, does not clearly indicate the presence of hydroxy acetate due to

the strong overlap of the acetate vibrations in the region of 1400-1600cm^{-1}. This makes the characteristic vibrations of the hydroxy acetate groups difficult to resolve.

From the analyses and results shown above, it can be concluded that the xerogel is mainly composed of not only LiOH, Ni(OH)$_2$, LiOAc and Ni(OAc)$_2$ but also Ni(OH)(OAc), the existence of which has been confirmed by a combination of IR and chemical analyses. The two reactions proposed earlier can now accordingly be modified as follows:

<div align="center">rotary evaporation</div>

$$\text{LiOH·H}_2\text{O} + \text{Ni(OAc)}_2\text{·4H}_2\text{O} \text{ ------------> } x\text{LiOH} + (1\text{-}x\text{-}y)/2 \text{ Ni(OH)}_2 +$$

$$(1\text{-}x)\text{LiOAc} + (1\text{+}x\text{-}y)/2 \text{ Ni(OAc)}_2 + y \text{ Ni(OH)(OAc)} + 5 \text{ H}_2\text{O}_{(g)}$$

<div align="center">After heat treatment</div>

$$\text{ ------------> } 1/2 \text{ Li}_2\text{CO}_3 + \text{NiO} + \text{gases} \qquad (5.3)$$
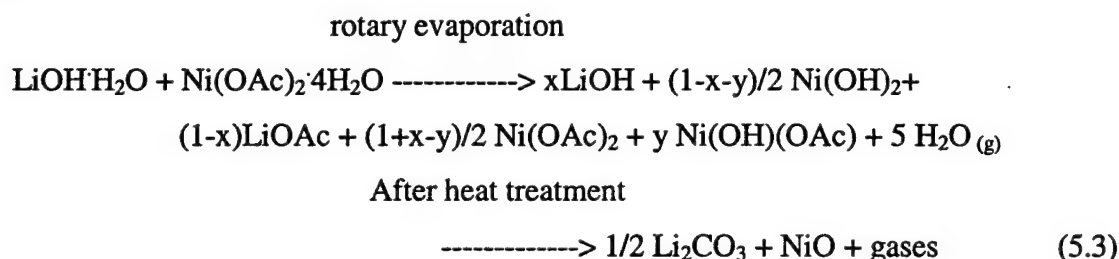
Differential thermal analysis results shown in Fig. 5-5 demonstrate the homogeneity of the xerogel. This can be stated with conviction by comparing the DTA analysis of the xerogel and the sample prepared by mixing Ni(OH)$_2$, Ni(OAc)$_2$ and LiOAc in the ratio of Ni(OH)$_2$: Ni(OAc)$_2$: LiOAc = 0.5 : 0.5 : 1. This ratio was chosen to approximately replicate the composition of the xerogel. The DTA analysis of the xerogel shows a broad endotherm $\approx$230°C probably corresponding to the T$_g$ of the amorphous xerogel and a broad exothermic peak at $\approx$270°C with a shoulder owing to the crystallization of NiO and Li$_2$CO$_3$ as confirmed by XRD. On the other hand, the DTA analysis of the mixed precursor prepared by solid state methods shows several exothermic peaks at $\approx$270°C, 320°C and 340°C. These peaks possibly correspond to the decomposition of Ni(OH)$_2$, Ni(OAc)$_2$ and LiOAc. These differences in the thermal behavior of the xerogel and the solid state precursors, and the occurrence of a single exothermic peak in the DTA analysis of the xerogel is therefore a reflection of the molecular homogeneity of the xerogel. Nevertheless, although the precursor could be considered to be well mixed, the mechanism of formation of NiO and Li$_2$CO$_3$ is still unclear.
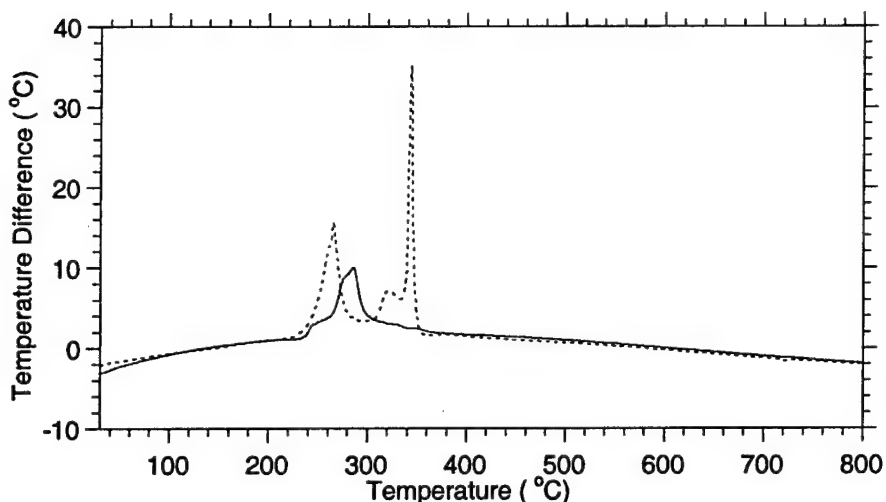
Figure 5-5. The homogeneity of the xerogel is demonstrated by the DTA analysis of the xerogel and the sample which is prepared by mixing a ratio of $Ni(OH)_2$: $Ni(OAc)_2$: $LiOAc$ = ½ : ½ : 1. A single exothermic peak of the xerogel sample is observed (---) compared to several exothermic peaks associated with the solid state processed sample (---).

5.2 Xerogel generated using the spray drying process:

The as-prepared powders employed for synthesizing $LiNiO_2$ and $LiNi_{0.75}Co_{0.25}O_2$, derived by the spray drying process were also characterized using TGA, XRD and FTIR. The FTIR data collected on both $LiNiO_2$ and $LiNi_{0.75}Co_{0.25}O_2$ xerogels generated by this process are shown in Fig. 5-6. Since the results of the analyses of the xerogel powder are very similar for both $LiNiO_2$ and $LiNi_{0.75}Co_{0.25}O_2$, only the results of the as-prepared powders used for synthesizing $LiNiO_2$ are discussed in this section. In Fig. 5-6, no sharp O-H stretching bands are observed around 3500~3700 cm^{-1} which implies the absence of either lithium hydroxide or nickel hydroxide. By comparing the infrared spectra obtained for both dehydrated nickel acetate and lithium acetate as shown in Fig. 5-7, one can assign the absorption bands belonging to the acetate groups. The dehydrated acetates were generated by rotary evaporation of the dissolved salts in water using a rotary
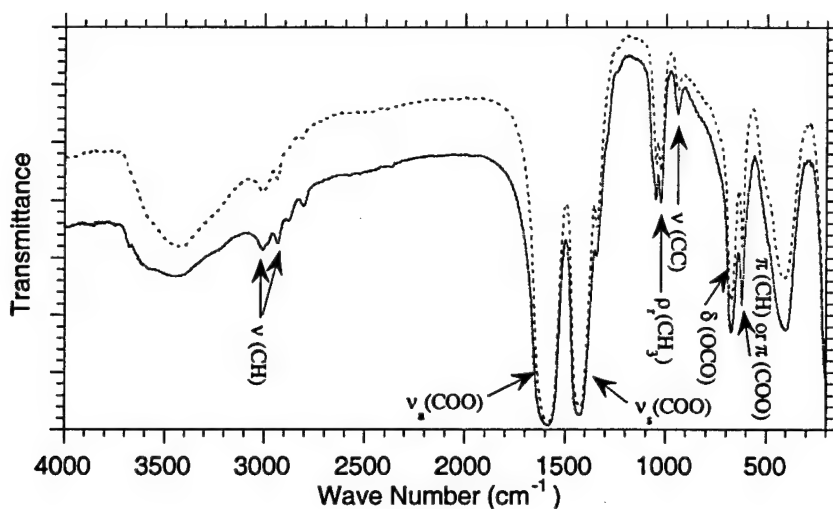
Figure 5-6. The FTIR data of LiNiO$_2$ (represented by ⋯⋯) and LiNi$_{0.75}$Co$_{0.25}$O$_2$(represented by ——) xerogels generated by the spray drying process.
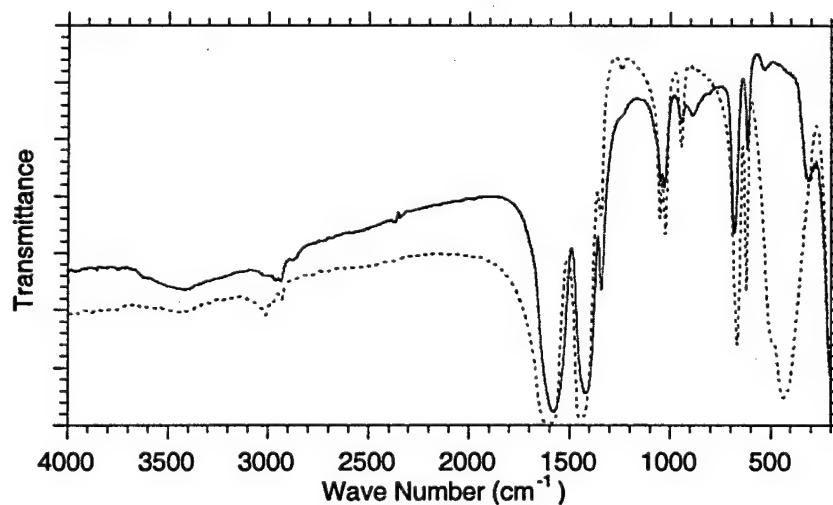
Figure 5-7. The IR data of the dehydrated lithium acetate (represented by ⋯⋯) and nickel acetate (represented by ——). By comparing the IR data of the xerogel and the data obtained from the dehydrated lithium acetate and nickel acetate, it is possible to identify the vibrational bands belonging to the acetate groups.

evaporator (Buchi). According to Nakamoto and Ito et. al [1, 2], bands observed at 3008 and 2931 cm^{-1} can be assigned to $\nu(CH)$, and bands seen at 1587 and 1425 cm^{-1} can be assigned to $\nu_a(COO)$ and $\nu_s(COO)$, respectively. Furthermore, the presence of a strong absorption band below 500 cm^{-1} in the xerogel sample corresponding to the absorption of lithium acetate confirms its existence in the xerogel. Since there is no distinct absorption band characteristic of nickel acetate, its existence from the infrared spectra may not be confirmed. Some other bands observed at 2881 and 2803 cm^{-1} which can not be assigned to acetate groups could be attributed to the CH_3 vibrations of the methoxy group which will be discussed later.

The TGA/DTA data is shown in Fig.5-8. The heating rate utilized in this case is 5°C/min to 800°C. A one step weight loss of 41.6% occurring between 230°C and 300°C corresponding to the two broad exothermic reactions. According to the XRD analysis of the xerogel heat treated at 300°C for 5 h as shown in Fig. 5-9, a mixture of NiO and Li_2CO_3 are observed to be the major products of the decomposition reaction. The results of the IR and thermal analyses of the xerogel however, do not provide sufficient information to conclusively predict its structure and analyze the reactions responsible for the formation of the xerogel. In order to comment on the reaction mechanisms, it was decided to conduct FTIR analysis on an additional sample. This sample was prepared by dissolving lithium hydroxide in methanol and then recovering the powder by evaporating the solvent in a rotary evaporator. The results of the infrared spectra collected on this sample is shown in Fig. 5-10. It can be seen from Fig. 5-10 that a mixture of lithium hydroxide and lithium methoxide are formed after dissolving the hydroxide in methanol. The characteristic CH stretching bands reported at 2790, 2850 and 2920 cm^{-1} [10] correspond to 2771, 2836 and 2928 cm^{-1} in the present study which confirms the existence of lithium methoxide. Similar analysis conducted on a nickel acetate-methanol solution shows no perceivable reaction as expected. Based on the results of the infrared and TGA analyses described above, it is possible to discuss the reactions that occur leading to the formation of the xerogels. At the same time, it is also possible to analyze the structure of the xerogel. These results can be summarized as follows:

1. The dissolution of lithium hydroxide in methanol leads to the formation of some lithium methoxide, LiOMe (Me = methyl group).
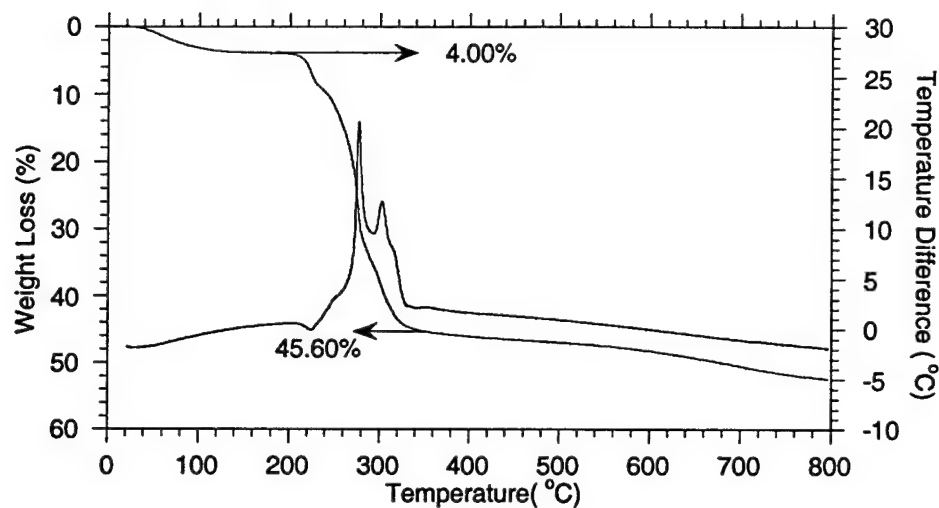
Figure 5-8. The TGA/DTA analysis of the LiNiO$_2$ xerogel. A characteristic one step weight loss (41.60%) is observed.
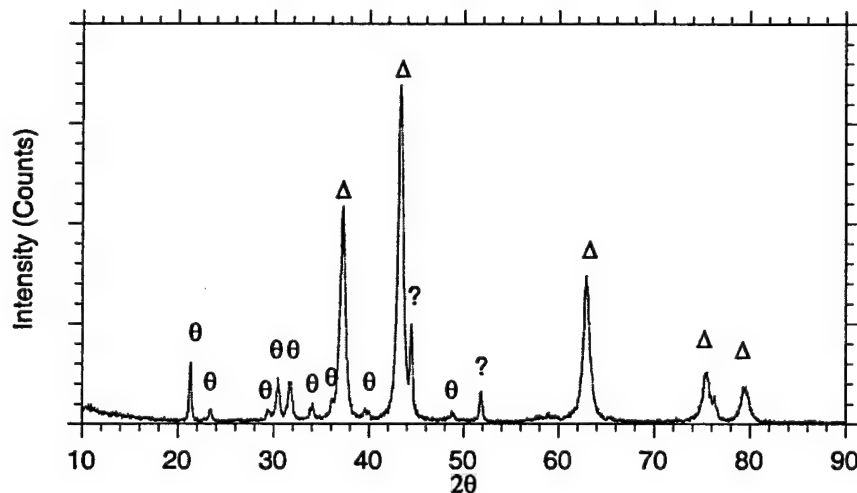
Figure 5-9. XRD pattern of the xerogel sample heat treated at 300°C for 5 hours indicating a mixture of NiO and Li$_2$CO$_3$ as the major phases in the intermediate products obtained after the decomposition reaction.
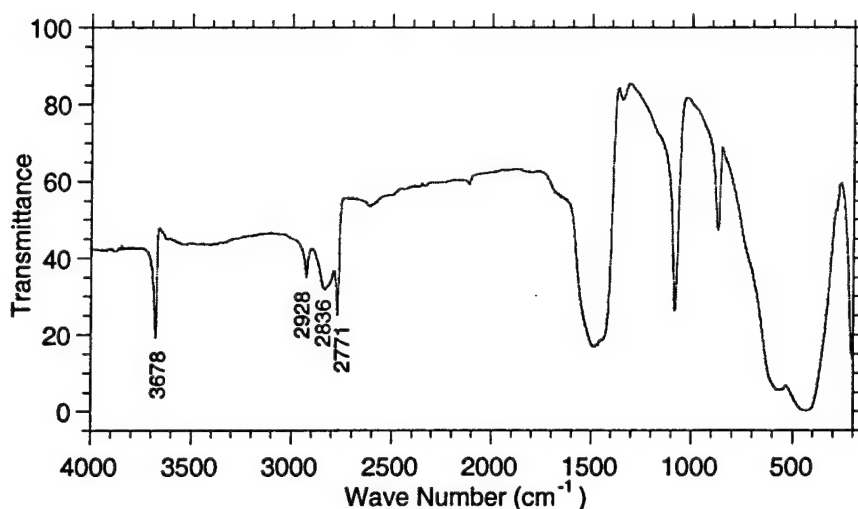
Figure 5-10. The results of the IR analyses on the precipitates obtained from drying the solution by dissolving lithium hydroxide monohydrate in methanol.

2. Since OH⁻ and OMe⁻ are strong nucleophiles, the addition of lithium hydroxide-methanol solution to the nickel acetate-methanol solution can lead to the formation of either Ni(OH)(OAc) or Ni(OMe)(OAc) and Li(OAc). The formation of nickel hydroxy acetate has already been identified and reported by us in section 5.1. This partially substituted hydroxide is insoluble in water and if it had occurred in the present case, should precipitate out as soon as the lithium hydroxide-methanol solution was transferred to the nickel acetate-methanol solution. In the present work, although precipitation is observed, the precipitates appear to redissolve back into the methanol solution which could imply initially the formation of Ni(OH)(OAc) during the addition of the lithium hydroxide-methanol solution to the solution of nickel acetate in methanol. This initially precipitated hydroxy-acetate complex then redissolves back in excess methanol, due to the possible OMe ↔ OH exchange reaction.

3. Since no characteristic OH vibration is observed in the xerogel and the possibility of the loss of acetate groups during drying is low (because of the lack of proton to assist the formation of ester), it can therefore be assumed that the xerogel is largely composed of Ni(OMe)(OAc) and LiOAc in a stoichiometric ratio of

70

lithium : nickel : methoxy groups : acetate groups = 1 : 1 : 1 : 2. Based on the knowledge that the phases present after the decomposition reaction are primarily nickel oxide and lithium carbonate (see Fig. 5-9), the percent weight loss of the reaction can be expected to be 47.90%, which is however much higher than the weight loss observed from the TGA analysis (41.6%). A possible explanation for this deviation could be the condensation of methoxy groups attached to nickel atoms with the OH⁻ groups contributed by lithium hydroxide (source of OH⁻ groups) or by the hydrolysis of methoxy groups initiated by the addition of water and the subsequent condensation of hydroxy groups during the spray drying process at approximately 200°C. The possible formation of Ni-O-Ni linkages due to condensation could lower the molecular weight of the xerogel thereby resulting in a lower percentage of weight loss as observed in the TGA analysis. This assumption is further supported by the absence of OH vibrations observed in the FTIR analysis of the xerogel. This mechanism is very likely since we have also observed the formation of a gel by aging the solution prepared for spray drying. The kinetics of the gelation reaction is very much dependent on the concentration of water. The presence of such condensed species in the xerogel could be confirmed by observing the Ni-O vibrations in the xerogel. It should be mentioned that the Ni-O vibration attributed to the Ni-O-Ni linkages may not be easily identified in the FTIR analysis of the xerogel. This is because of the strong absorption band below 500 cm⁻¹, characteristic of lithium acetate which occurs in the same frequency range as the Ni-O stretching vibration normally observed at 425 and 375 cm⁻¹ [11].

4. In conclusion, therefore the reactions responsible for the formation of the xerogel during the different stages, can be summarized as follows:

A) <u>Formation of lithium methoxide:</u> The dissolution of LiOH in methanol leads to formation of some LiOMe

$$LiOH \cdot H_2O \quad \rightarrow \quad x\, LiOH + (1-x)\, LiOMe \qquad\qquad (5.4)$$

B) Precipitation of Ni(OH)(OAc): The mixing of the LiOH-MeOH solution and the Ni(OAc)$_2$·4H$_2$O-MeOH solution leads to precipitation:

$$x \text{ LiOH} + (1-x) \text{ LiOMe} + \text{Ni(OAc)}_2 \cdot 4\text{H}_2\text{O} \rightarrow \text{LiOAc} +$$

$$x \text{ Ni(OH)(OAc)}_{ppt} + (1-x) \text{ Ni(OMe)(OAc)} + 4 \text{ H}_2\text{O} \qquad (5.5)$$
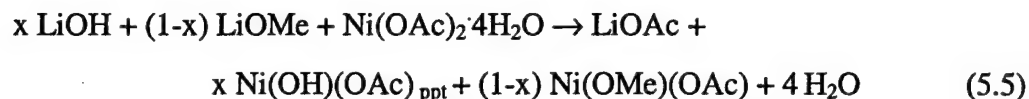
C) Redissolution leading to OH ↔ OMe:

$$\text{Ni(OH)(OAc)} + \text{MeOH} \rightarrow \text{Ni (OMe)(OAc)} + \text{H}_2\text{O} \qquad (5.6)$$

D) Dilution with water leading to hydrolysis and condensation during spray drying:

$$n \text{ Ni(OMe)(OAc)} + (n-y)/2 \text{ H}_2\text{O} \rightarrow \text{Ni}_n\text{O}_{(n-y)/2}(\text{OMe})_y(\text{OAc})_n + (n-y) \text{ MeOH} \qquad (5.7)$$
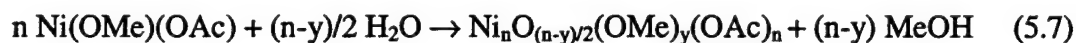
5. The two exothermic peaks observed in the DTA analysis may represent the decomposition of the nickel species and the lithium acetate formed by virtue of the reactions shown above, which however has not been confirmed at this stage.

5.3 Xerogel generated using the gelation process:

As was described and discussed earlier in section 5.2, the methanol solution which contains stoichiometric amounts of lithium hydroxide and nickel acetate (or stoichiometric amounts of nickel acetate and cobalt acetate) could gel if water is added. This phenomena was studied further by conducting the following two sets of experiments. For convenience, the experimental procedures are outlined below:

72

First set of experiment:

Two trial experiments were outlined as follows:

1. 0.1 mole of nickel acetate and 0.1 mole of lithium hydroxide were dissolved separately in 150ml methanol and 30ml de-ionized water respectively. After complete dissolution of these inorganic salts in the respective solvents, the lithium hydroxide-water solution was transferred to the nickel acetate-methanol solution. This resulted in immediate precipitation. The precipitates , however, **did not dissolve** back into the solution after stirring.

2. In the second experiment, 0.1 mole of nickel acetate and 0.1 mole of lithium hydroxide were separately dissolved in 150ml water and 50ml methanol respectively. Precipitates were seem to form as soon as the lithium hydroxide-methanol solution was transferred to the nickel acetate-water solution. The resultant precipitates, however, **redissolved** back into the solution after stirring.

Based on this observation, a second set of experiment was conducted.

Second set of experiment:

Two detailed systematic experiments were conducted as follows:

1. 0.1mole of nickel acetate and 0.1mole of lithium hydroxide were dissolved separately in 120ml and 50ml methanol respectively. After complete dissolution of these inorganic salts, the lithium hydroxide-methanol solution was transferred to the nickel acetate-methanol solution. 100ml DI water was then added to the mixture solution. Similarly, two more methanol solution mixtures containing identical concentrations of nickel and lithium salts were prepared to which 200 and 300ml DI water were added separately. All the three as-prepared solutions were then sealed in the beakers by covering the top with parafilm.

2. 0.1mole of nickel acetate and 0.1mole of lithium hydroxide were dissolved in 150ml DI water and 50ml methanol separately. After complete dissolution, the lithium hydroxide-methanol solution was transferred to the nickel acetate-water solution. This resulted in the formation of precipitates initially, which redissolved back into the solution after stirring. The as-prepared solution was then sealed by covering the beaker with parafilm.

73

The above experiments indicated show that the solution prepared in 2 in the second set of experiment gelled in 24 hours. Furthermore, the solutions prepared in 1 which contained 200 and 300ml of added water gelled in 2 to 4 days. In comparison, the solution which contained only 100ml water did not gel even after 7 days.

Two conclusions can be drawn from the observation of these two sets of experiments. First, the formation and redissolution of the precipitates is related to the dissolution and reaction of lithium hydroxide in methanol. This implies that the gelation reaction is dependent on the formation of lithium methoxide that is generated during the dissolution of LiOH in methanol. This is true since only precipitation is observed instead of gelation if lithium hydroxide is dissolved in water. Second, the kinetics of the gelation reaction is strongly dependent on the concentration of water. The conclusions drawn from above reflect the possibility of the formation of Ni-O-Ni linkages generated by the formation nickel methoxide as an intermediate product that undergoes hydrolysis and condensation initiated by the addition of water. This intricate interplay of the role of methanol and water with the use of transition metal acetates is the fundamental basis of the particulate sol-gel process.

5.4 Characteristics of the spray decomposition process:

The solution prepared for the spray decomposition process is actually identical to that used for the spray drying process. Since the xerogel produced from the spray drier is directly led into the furnace, this process leads to the final oxide in a one step process. The spray decomposition process therefore has the potential ability to generate powders on a large scale with possibly improved electrochemical properties. This process may thus offer several advantages: (a) It is a continuous one-step process as opposed to a "batch" process and (b) It reduces problems due to the "batch-size" that generally occur in other processes normally caused by a change in the atmosphere and the partial pressure of the gases in the furnace due to the products released during decomposition. Incomplete decomposition and formation of undesired intermediate products that are characteristic of the small size of the batch are minimized due to the decomposition step following spray drying. (c) Since the heat treatment time is short compared to the "batch" processes, it is possible to obtain powders with smaller crystallite and particle sizes and therefore high

74

surface area. (d) Narrower distribution of particle size is also expected for the powders generated from this process owing to a more uniform temperature distribution thereby favoring homogeneous nucleation and growth of the desired phase. (e) Good control of composition and stoichiometry can be attained due to faster kinetics brought about by the reduced diffusion distances of the different species in the atomized droplets.

Part II.   *Phase evolution, morphology and surface area characterization*

5.5   Phase evolution of $LiNiO_2$ during heat treatment:

This was done to determine the heat treatment temperature and the mechanisms responsible for the formation of $LiNiO_2$ and $LiNi_{0.75}Co_{0.25}O_2$. X-ray diffraction was used to investigate the phase evolution behavior of $LiNiO_2$ and $LiNi_{0.75}Co_{0.25}O_2$ with heat treatment. The phase evolution pathways of $LiNiO_2$ using the xerogels obtained from rotary evaporation, spray drying and the gelation processes are shown in Figure 5-11, 5-12 and 5-13 respectively. In all these three processes, a common feature is that no progressive reaction between nickel oxide and lithium carbonate, formed at 300°C, is seen to occur until the temperature of 600°C is reached. At 600°C, some lithium deficient $LiNiO_2$ is formed. Phase pure $LiNiO_2$ can be obtained however only when the precursors are heat treated beyond 700°C. An interesting and important aspect to be noticed is that the xerogel which is generated using the spray drying process shows a larger amount of the $LiNiO_2$ phase at 600°C in comparison to the xerogels prepared by both rotary evaporation and the gelation processes heat treated at the same temperature. This can be stated with conviction since the plots shown for the phase evolution study are all stacked up using identical scales for the intensity. The formation of a larger amount of $LiNiO_2$ at 600°C could be related to the distribution, particle size and morphology of lithium carbonate and nickel oxide formed after the decomposition of the xerogel at temperatures below 300°C. These aspects also affect the kinetics of the reaction leading to the formation of stoichiometric $LiNiO_2$ with minimum defect concentration. The influence of these factors on the formation of stoichiometric $LiNiO_2$ will be clarified in the sections to follow.

The x-ray diffraction pattern of the spray decomposed xerogel is shown in Figure 5-14. It could be expected that $LiNiO_2$ is the only major phase revealed in the X-ray diffraction analysis. Unfortunately, similar to the other processes, lithium carbonate and nickel oxide are again found to be the major phases present in the spray decomposed sample. The decomposed xerogel was therefore heat treated in order to obtain $LiNiO_2$ and understand its properties and electrochemical response. The evolution of the phases upon heat treatment of the spray decomposed powders is shown in Figure 5-15. More $LiNiO_2$ begins to evolve only at 700°C as opposed to 600°C in the spray drying process. Further heat treatments at 800°C although for a short time of 2 h are needed to obtain fully crystalline single phase $LiNiO_2$. Since no $LiNiO_2$ phase is seen in the X-ray analysis of the spray decomposed powders, there is a need to modify the parameters in future in order to obtain phase pure $LiNiO_2$ in one step as proposed before. The parameters to be modified will include (a) dilution of the solution concentration. (b) decrease of the aspiration rate or increase of the length of the decomposition zone in order to facilitate decomposition of the powder and promote the formation of $LiNiO_2$. This will form the basis of the studies to be conducted in the future.

Figure 5-11. Phase evolution of LiNiO$_2$ xerogel generated using the rotary evaporation process. All peaks at 800°C correspond to LiNiO$_2$. (-θ-) Li$_2$CO$_3$ phase. (-Δ-) NiO phase. (-o-) LiNiO$_2$ phase. All heat treatments were conducted in air for 5 hours except the sample at 800°C which was obtained after heat treatment in air for 8 hours. Note that the scales for the peak intensity are identical for all the plots.
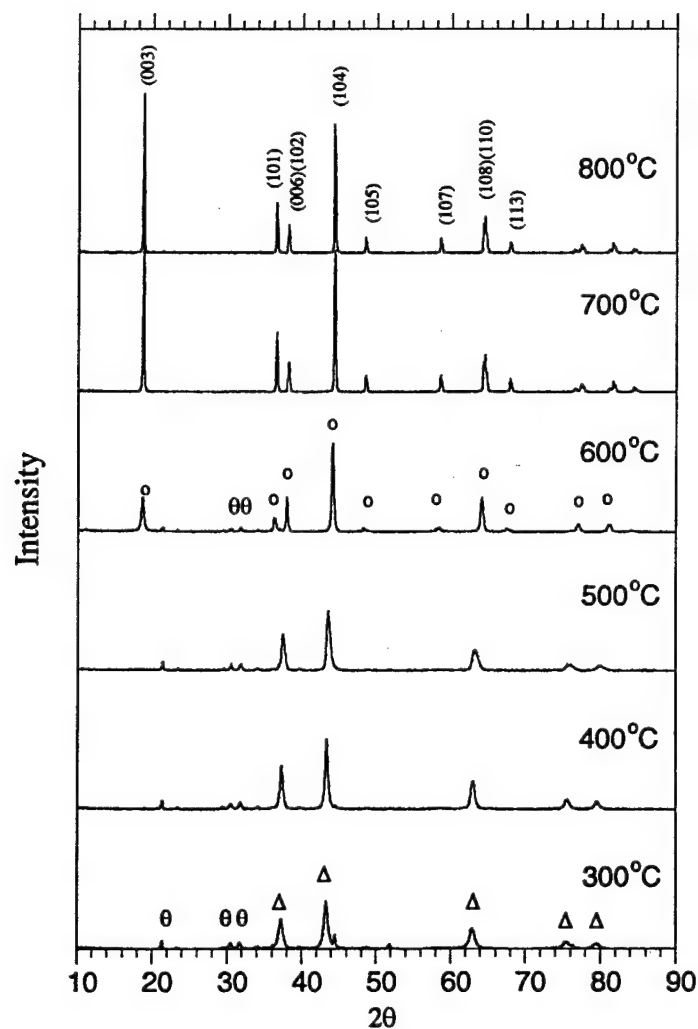
Figure 5-12. Phase evolution of $LiNiO_2$ xerogel generated using the spray drying process. All peaks at 800°C correspond to $LiNiO_2$. (-θ-) Li_2CO_3 phase. (-Δ-) NiO phase. (-o-) $LiNiO_2$ phase. All heat treatments were conducted in air for 5 hours. Note that the scales for the peak intensity are identical for all the plots.
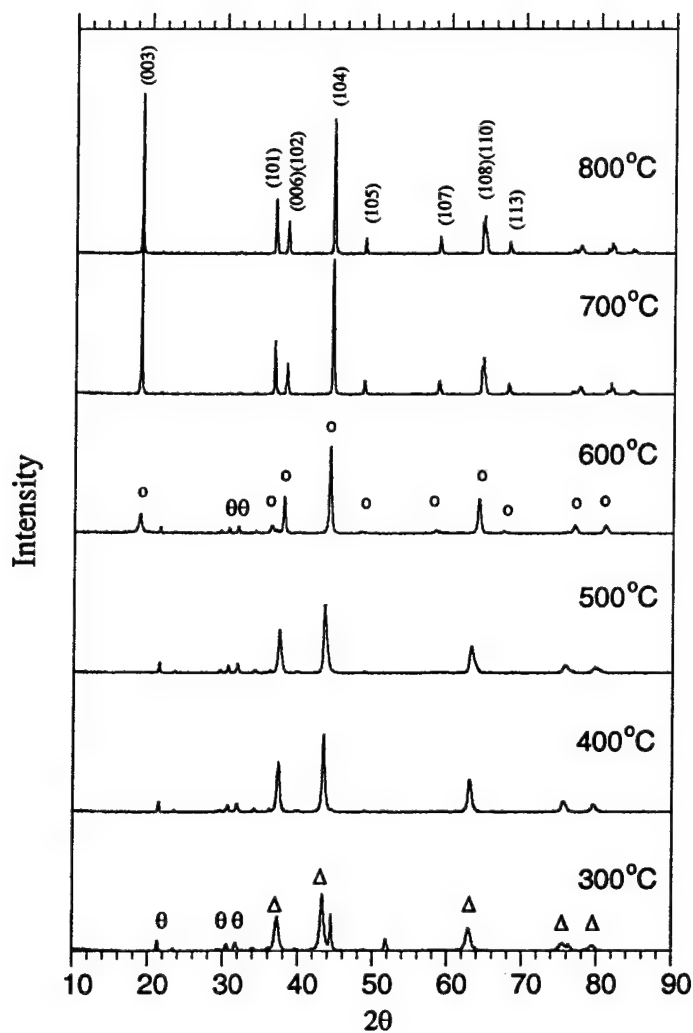
Figure 5-13. Phase evolution of $LiNiO_2$ xerogel generated using the gelation process. All peaks at $800^{\circ}C$ correspond to $LiNiO_2$. (-θ-) Li_2CO_3 phase. (-Δ-) NiO phase. (-o-) $LiNiO_2$ phase. All heat treatments were conducted in air for 5 hours. Note that the scales for the peak intensity are identical for all the plots.
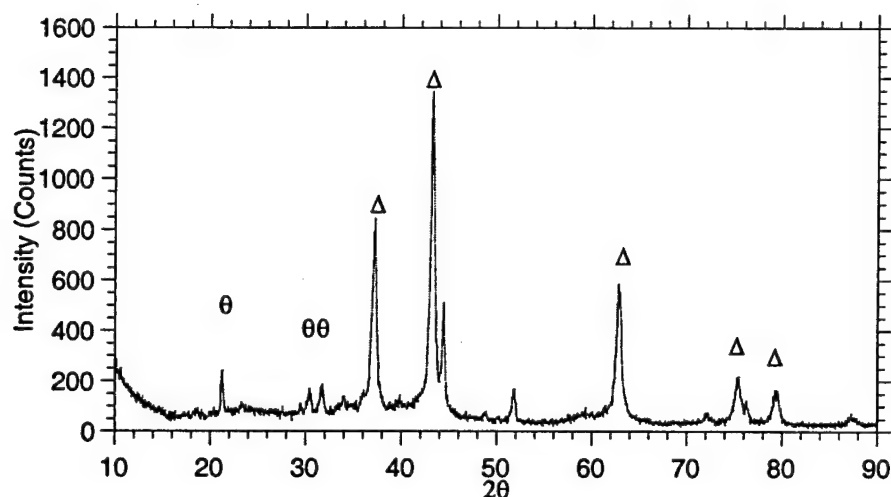
Figure 5-14. XRD data of the spray decomposed sample. (-Δ-) represents the NiO phase and (-θ-) represents the Li_2CO_3 phase.
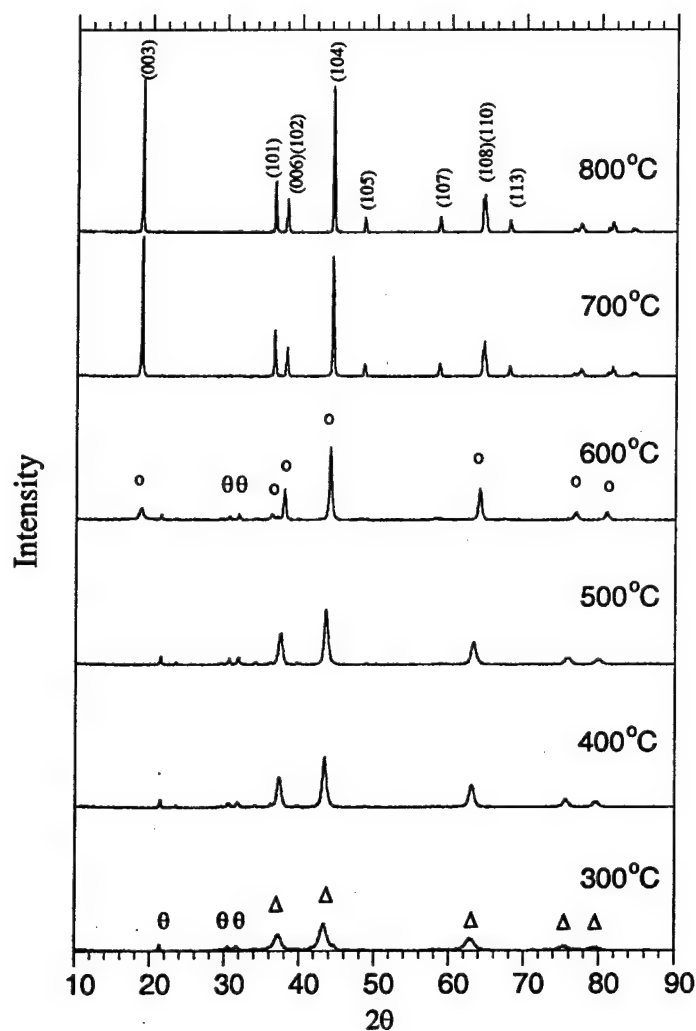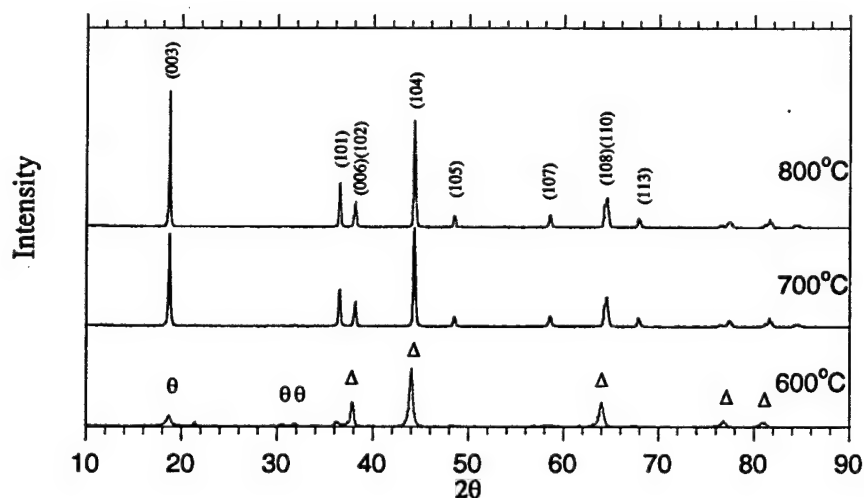

Figure 5-15. Phase evolution of $LiNiO_2$ xerogel generated using the spray decomposition process. All peaks at 800°C correspond to $LiNiO_2$. (-θ-) Li_2CO_3 phase. (-Δ-) NiO phase. All heat treatments were conducted for 5 hours in air except the sample at 800°C which was heat treated for 2 hours. Note that the scales for the peak intensity are identical for all the XRD patterns.

5.6   Phase evolution of LiNi$_{0.75}$Co$_{0.25}$O$_2$ during heat treatment:

X-ray diffraction was also used to observe the phase evolution of LiNi$_{0.75}$Co$_{0.25}$O$_2$ with heat treatment temperature. All the heat treatments were conducted in an air atmosphere in the temperature range of 300 to 800°C for 5h except the sample heat treated at 800°C which was held for only 2h. The phase evolution of LiNi$_{0.75}$Co$_{0.25}$O$_2$ using xerogels obtained from the rotary evaporation and spray drying processes are shown in Figure 5-16, 5-17 respectively. It can be seen that the phase evolution behavior in very similar to that of LiNiO$_2$. The mixed oxide is formed by the reaction of Li$_2$CO$_3$ with (NiCo) oxide. In comparison to the phase evolution behavior of LiNiO$_2$, however, it can be seen that substitution of 25 mol% cobalt for nickel renders the compound readily oxidizable. Thus peaks characteristic of the low temperature phase of LiNi$_{0.75}$Co$_{0.25}$O$_2$ corresponding to LT- LiNi$_{0.75}$Co$_{0.25}$O$_2$ reported in the literature [12, 13] are seen at a temperature as low as 400°C. Furthermore, the broad nature of the X-ray peaks clearly reflects the smaller crystallite size of nickel cobalt oxide in comparison to that of nickel oxide. The kinetics of the decomposition of lithium carbonate in the case of LiNi$_{0.75}$Co$_{0.25}$O$_2$ can therefore be expected to be faster in contrast to LiNiO$_2$. This can be seen from the fact that at 600°C the LiNi$_{0.75}$Co$_{0.25}$O$_2$ phase is almost free of lithium carbonate and at 700°C itself, phase pure LiNi$_{0.75}$Co$_{0.25}$O$_2$ is obtained unlike the case for LiNiO$_2$.

In the case of LiNiO$_2$, even prolonged heat treatment at 800°C is not sufficient for completely eliminating the carbonate phase. The faster kinetics of lithium carbonate decomposition in the case of LiNi$_{0.75}$Co$_{0.25}$O$_2$ could be attributed to the smaller crystallite size of the intermediate products formed as a result of decomposition of the xerogels. Furthermore, the introduction of Co and formation of the (Ni,Co) oxide renders the interphase of Li$_2$CO$_3$ and the mixed oxide more unstable favoring the reactions at a lower temperature. In addition, the ease of formation of LiNi$_{0.75}$Co$_{0.25}$O$_2$ with reduced defect concentration is probably due to the electronic configuration of the (Ni,Co) oxide being closer to the low spin state of d^6(t$_{2g}^6$e$_g^0$) which is much more stable in an octahedral ligand field of oxygen. The influence of the residual lithium carbonate on the electrochemical response of LiNiO$_2$ will be discussed in detail in the later section.

81
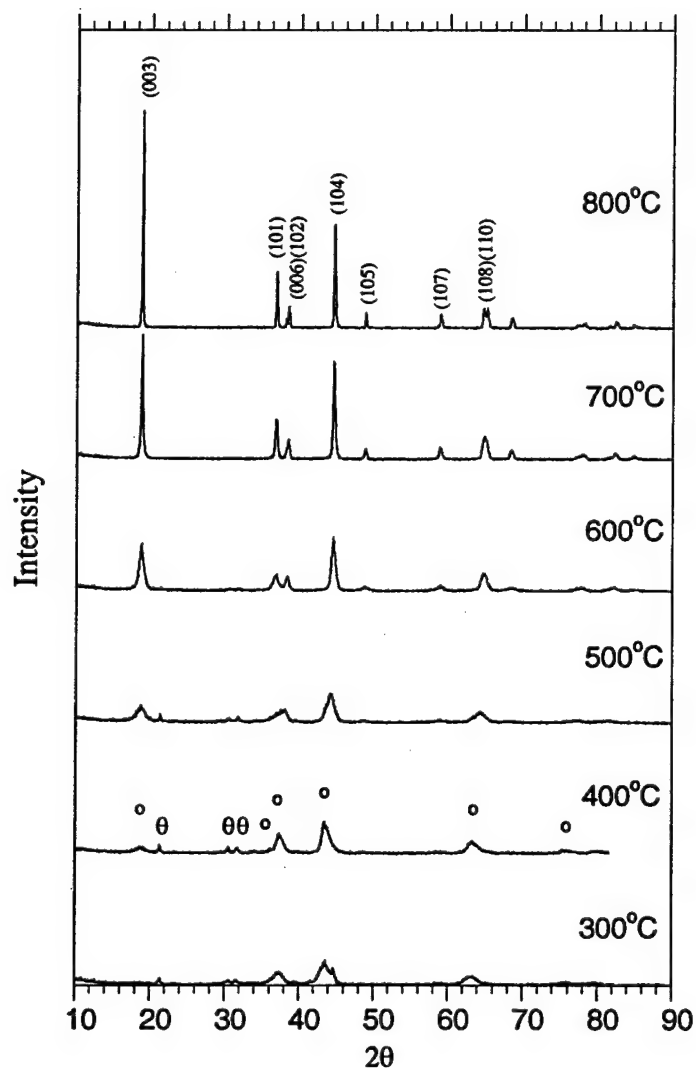
Figure 5-16. XRD results showing the phase evolution of $LiN_{0.25}Co_{0.75}O_2$ with heat treatment in the temperature range from 300°C to 800°C respectively using the xerogel generated by the rotary evaporation process. All the heat treatments were conducted in air for 5 hours except the sample heat treated at 800°C which was held for only 2 hours. (-θ-) represents the Li_2CO_3 phase and (-o-) represents the $LiNiO_2$ phase.
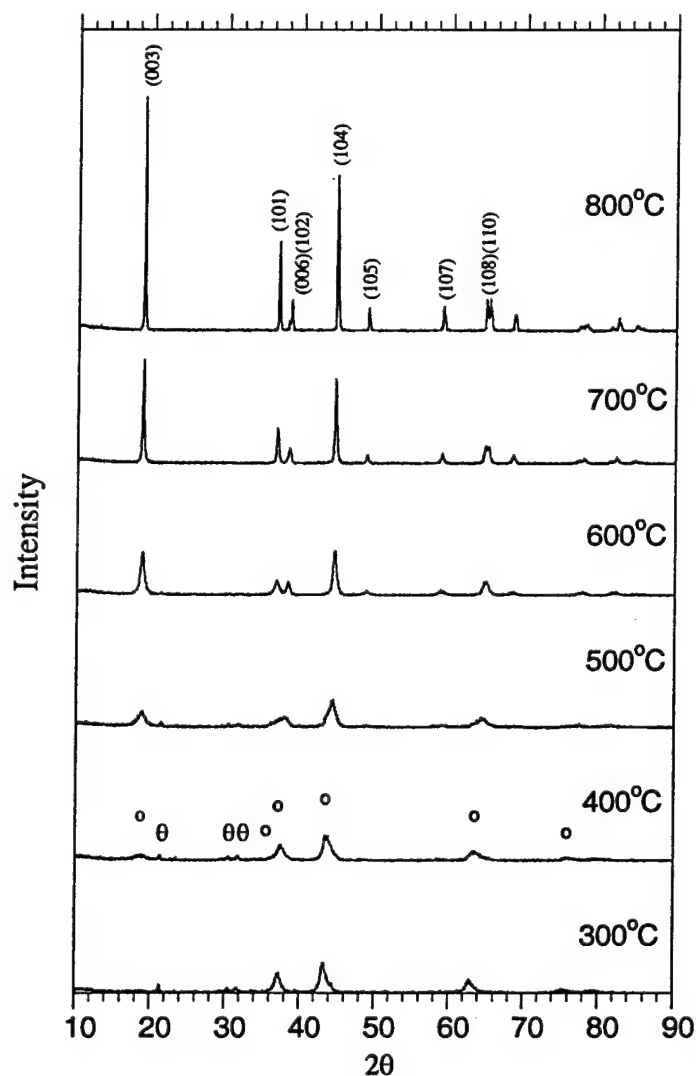
Figure 5-17. XRD results showing the phase evolution of $LiNi_{0.25}Co_{0.75}O_2$ with heat treatment in the temperature range of 300°C to 800°C respectively using the xerogel generated by the spray drying process. All the heat treatments were conducted in air for 5 hours except the sample heat treated at 800°C which was held for only 2 hours. (-θ-) represents the Li_2CO_3 phase and (-o-) represents the $LiNiO_2$ phase.

83

5.7 Characterization of morphology and specific surface area of $LiNiO_2$ and $LiNi_{0.75}Co_{0.25}O_2$:

Characterization of morphology of $LiNiO_2$ and $LiNi_{0.75}Co_{0.25}O_2$ Powders:

The morphology of the as-prepared xerogels of $LiNiO_2$ generated using the rotary evaporation and spray drying processes are shown in Figure 5-18. A flocculated, sponge-like morphology is seen for the xerogels generated by the rotary evaporation process. In comparison to this, the spray dried xerogel shows a distinct fractured hollow spherical morphology. The morphology, particle size as well as the crystallite size distribution of the resultant $LiNiO_2$ are actually influenced by the structure and reactivity of the xerogels which is controlled by the drying process. This is very clear from the morphology of the resultant $LiNiO_2$ powders generated from these two processes which are shown in Figures 5-19, 5-20 respectively. The powders were observed at a magnification of 30X, 1kX and 10kX.

At a magnification of 30X, the powders generated by the spray drying process exhibit a wide particle size distribution ($\approx 15\sim100\mu m$) although narrower than that seen in the rotary evaporation process ($< 10\sim150\mu m$). A characteristic feature of the spray dried powders is that each particle represents a collection of agglomerated crystallites. When the powders are observed at a higher magnification (10kX), faceted crystallites (approximately $1\mu m$) characteristic of the trigonal $R\bar{3}m$ symmetry are observed. In comparison, powders generated by the rotary evaporation process show more random morphologies devoid of any faceting. The powder clusters exhibit a wider crystallite size distribution and range from individual crystallites $\approx 0.2\mu m$ to agglomerates several microns in size. Similar morphology is also exhibited by the $LiNi_{0.75}Co_{0.25}O_2$ powders.

The morphology of the $LiNi_{0.75}Co_{0.25}O_2$ powders synthesized using the xerogel generated by the rotary evaporation and spray drying processes are shown in Figure 5-21 and 5-22. Once again, the primary particle several microns in size is comprised of a collection of agglomerates of crystallites ≤ 1 μm in size. A more uniform platelet-type morphology is again seen for the rotary evaporation processed powders. The spray dried powder particles clearly exhibit individual crystallites (≤ 1 μm). The similarity in the morphology of the $LiNiO_2$ and $LiNi_{0.75}Co_{0.25}O_2$, generated by the two processes implies

84

that the resultant oxide morphology is controlled by the structure of the xerogel and the kinetics of the reaction leading to the oxide. This aspect is also illustrated by observation of the morphology of the resultant $LiNiO_2$ powders generated by
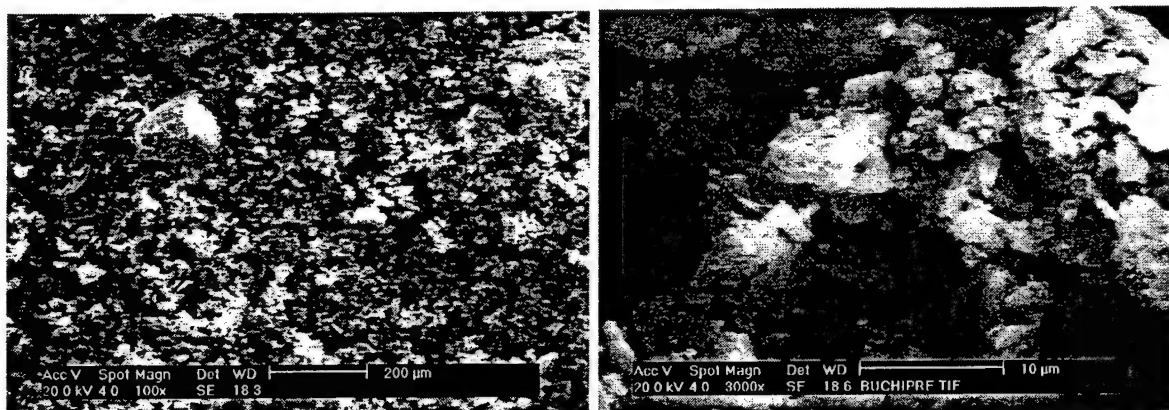
(a)
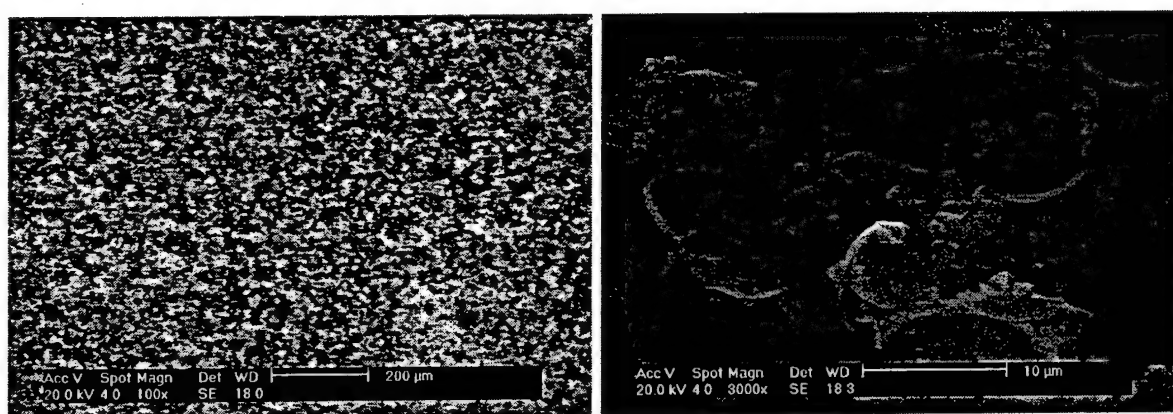
(b)

Figure 5-18. The morphology of the $LiNiO_2$ xerogels generated using the (a) rotary evaporation and (b) spray drying processes.
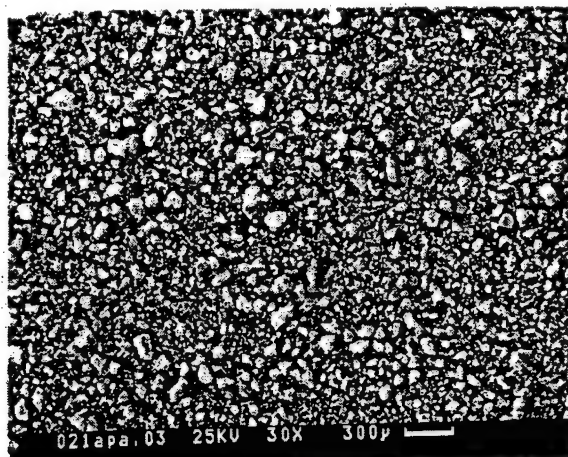
(a)
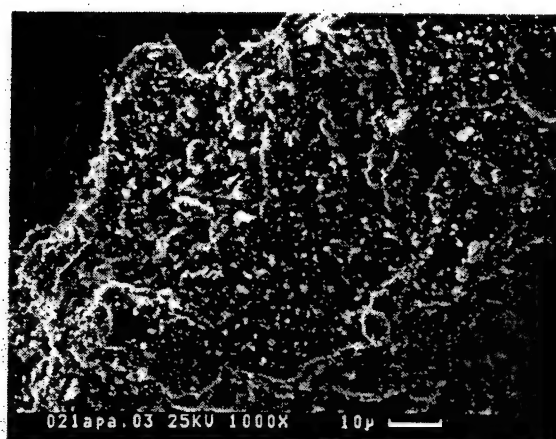
(b)

(c)

Figure 5-19. The morphology of LiNiO$_2$ powders generated by the rotary evaporation process observed at a magnification of (a) 30X, (b) 1000X and (c) 10000X respectively.
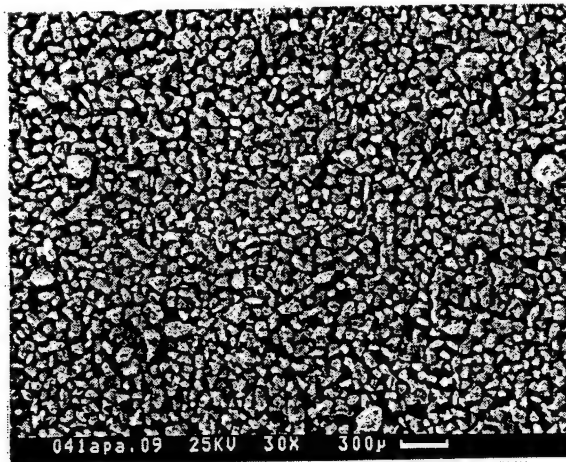
(a)
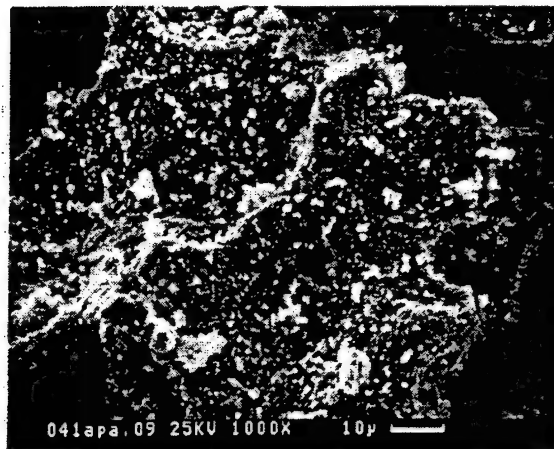
(b)
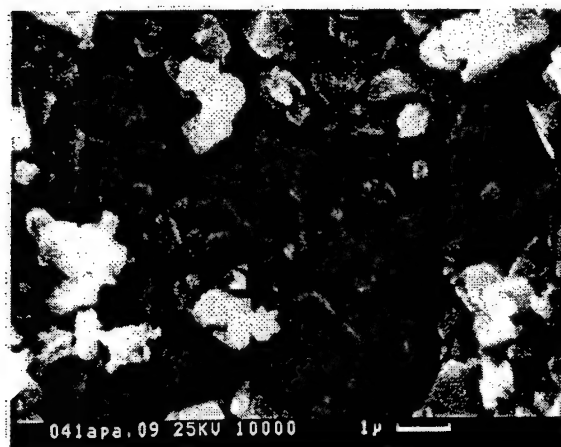
(c)

Figure 5-20. The morphology of LiNiO$_2$ powders generated by the spray drying process observed at a magnification of (a) 30X, (b) 1000X and (c) 10000X respectively.
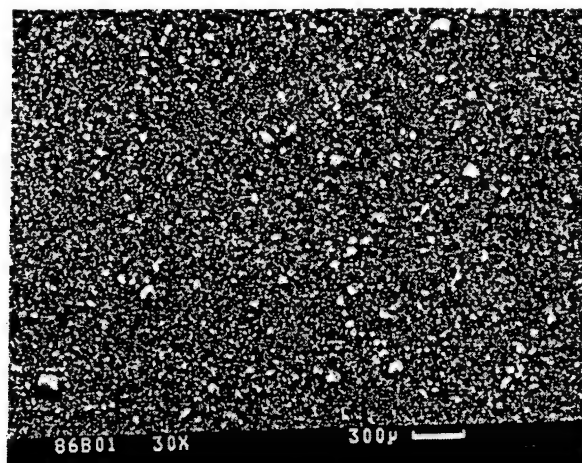
(a)
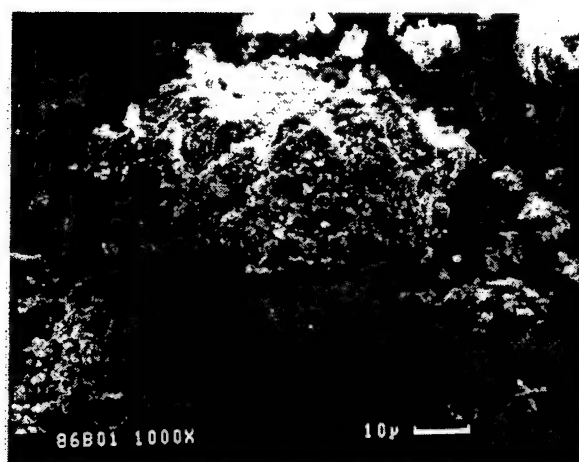
(b)
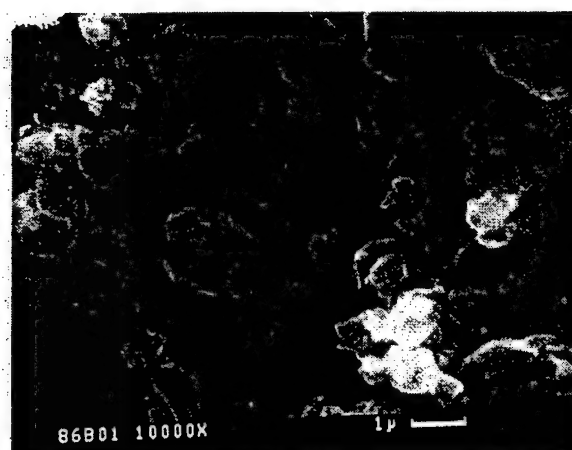
(c)

Figure 5-21. The morphology of $LiNi_{0.75}Co_{0.25}O_2$ powders generated by the rotary evaporation process observed at a magnification of (a) 30X, (b) 1000X and (c) 10000X respectively.
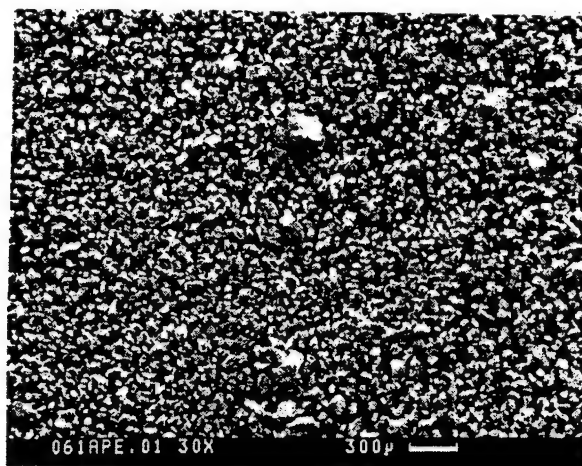
(a)
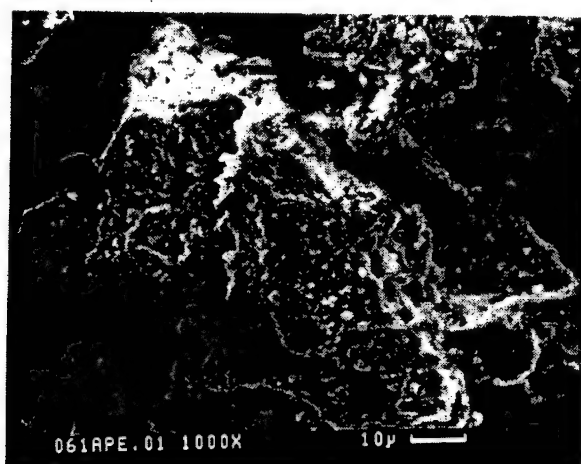
(b)

(c)

Figure 5-22. The morphology of $LiNi_{0.75}Co_{0.25}O_2$ powders generated by the spray drying process observed at a magnification of (a) 30X, (b) 1000X and (c) 10000X respectively.
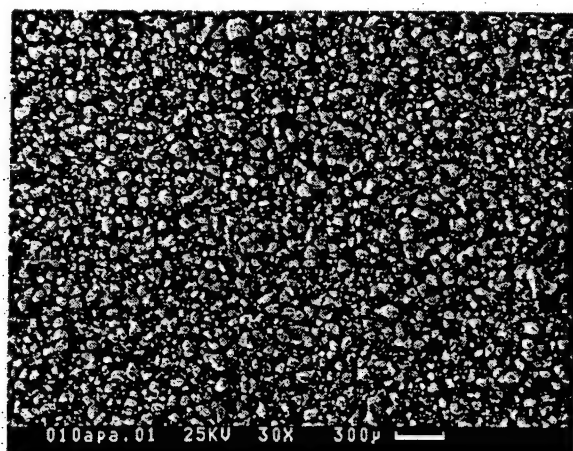
(a)
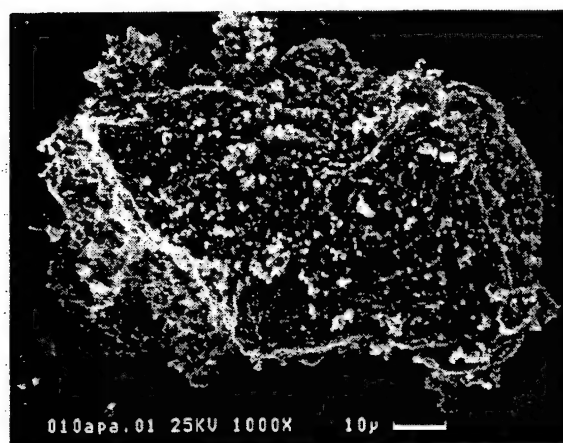
(b)
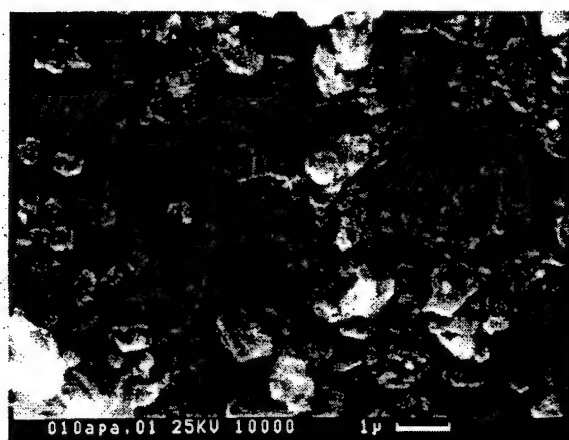
(c)

Figure 5-23. The morphology of $LiNiO_2$ powders generated by the gelation process observed at a magnification of (a) 30X, (b) 1000X and (c) 10000X respectively.

the gelation process. It should be remembered that rotary evaporation was used for drying the gel resulting from the gelation process. The morphology of the resultant powders shown in Figure 5-23 are therefore very similar to the rotary evaporation processed oxide powders. A wide particle size as well as crystallite size distribution is observed. In conclusion, powders generated by heat treatment of the xerogel produced by the spray drying process show a narrower particle size and crystallite size distribution in comparison to the powders generated using the rotary evaporation processes.

Specific surface area of LiNiO$_2$ and LiNi$_{0.75}$Co$_{0.25}$O$_2$ powders:

The specific surface area of the xerogel as well as the heat treated powders generated by the rotary evaporation and spray drying processes are shown in Table 5-2.

Table 5-2. The specific surface area of LiNiO$_2$ powders generated using different processes.

Process	Xerogel (m^2/g)	Resultant LiNiO$_2$ (m^2/g)
Rotary evaporation	0.99	0.32 ~ 0.67
Spray drying	4.74	0.42 ~ 1.14

The specific surface area was measured on the oxide powders obtained after heat treating the as-prepared xerogels at 800°C for 2-8 hours respectively. From Table 5-2, it can be seen that the specific surface area of both rotary evaporated and spray dried xerogels are very low. However, still the general trend in the specific surface area can be easily seen. The powders obtained using the spray dried precursor in general exhibit a higher specific surface area in comparison to the one obtained using the rotary evaporated precursor. This is probably due to the atomized droplets that result in hollow spherical particles. The porous nature and the fine sizes could contribute to the relatively higher specific surface area. Upon heat treatment, however, there is a drop in the surface area as expected. This is clearly due to the sintering of the crystallites as is also evident in the SEM images (see Figure 5-20(c)). Similar results are observed for LiNi$_{0.75}$Co$_{0.25}$O$_2$ powders obtained by rotary evaporation and spray drying processes. The specific surface area of the xerogel

powders and the heat treated powders generated by the rotary evaporation and spray drying processes are shown in Table 5-3.

Table 5-3. The specific surface area of $LiNi_{0.75}Co_{0.25}O_2$ powders generated using different processes.

Processes	Xerogel (m^2/g)	Resultant $LiNi_{0.75}Co_{0.25}O_2$ (m^2/g)
Rotary evaporation	1.73	2.03
Spray drying	4.18	1.31

The specific surface area of the heat treated powders were measured after heat treatment of the as-prepared xerogels at 800°C for 2 hours.

Part III. *Electrochemical characterization*

5.8 Electrochemical characterization of the synthesized $LiNiO_2$ powders:

As mentioned and described in Chapter 2, the possible loss of Li during heat treatment causes the disorder of Ni on the Li sites which consequently degrades the electrochemical activity of the synthesized materials. In order to alleviate this problem, $LiNiO_2$ was obtained by adjusting the ratio of Li to Ni in the initial mixture and the subsequent heat treatment time to facilitate the formation of the materials with stoichiometry closer to unity. The electrochemical properties of $LiNiO_2$ synthesized from different xerogels generated by the rotary evaporation, spray drying and gelation processes varying the above parameters are summarized in Table 5-4, 5-5 and 5-6. The oxide generated by heat treatment of the spray decomposed powders did not show any electrochemical activity suggesting the defective nature of the oxide. Modification of the spray decomposition process would be necessary along the lines discussed in section 5.5 to make this process feasible. This will form the basis for future studies in this system. The highest first discharge capacity of $LiNiO_2$ corresponding to these three processes are 100, 135 and 125 mAh/g respectively.

Table 5-4. Discharge capacity of $LiNiO_2$ and the experimental parameters used to obtain the oxide from xerogels generated by the rotary evaporation process.

File name	Nominal Stoichiometry	Dwell Time[#]	Peak Ratio (X-ray)	Lithium Content*	Discharge Cap. (mAh/g)
021apa.03	1 : 1	2h	0.766	0.911	No Capacity
021apa.02	1 : 1	5h	0.834	0.900	No Capacity
021apa.01	1 : 1	8h	0.952	0.883	No Capacity
022apa.03	1 : 1.05	2h	0.727	0.918	No Capacity
022apa.02	1 : 1.05	5h	0.676	0.928	~ 90
022apa.01	1 : 1.05	8h	0.806	0.904	~ 100
023apa.03	1 : 1.08	2h	0.776	0.909	~ 80
023apa.02	1 : 1.08	5h	0.682	0.927	~ 80
023apa.01	1 : 1.08	8h	0.695	0.924	~ 65

[#] 800°C   *Calculated from Dahn's method [14]

Table 5-5. Discharge capacity of $LiNiO_2$ and the experimental parameters used to obtain the oxide from xerogels generated by the spray drying process.

File name	Nominal Stoichiometry	Dwell Time	Peak Ratio (X-ray)	Lithium Content*	Discharge Cap. (mAh/g)
041apa.09	1 : 1	2h	0.895	0.891	No Capacity
041apa.10	1 : 1	5h	0.740	0.916	~ 50
041apa.11	1 : 1	8h	0.815	0.903	~ 35
045apa.01	1 : 1.05	2h	0.936	0.885	No Capacity
045apa.02	1 : 1.05	5h	0.710	0.921	~ 135
045apa.03	1 : 1.05	8h	0.738	0.916	~ 100
049apa.01	1 : 1.08	2h	0.855	0.897	~ 70
049apa.02	1 : 1.08	5h	0.721	0.919	~ 125
049apa.03	1 : 1.08	8h	0.741	0.915	~ 100

[#] 800°C   *Calculated from Dahn's method [14]

Table 5-6. Discharge capacity of $LiNiO_2$ and the experimental parameters used to obtain the oxide from xerogels generated by the gelation process.

File name	Nominal Stoichiometry	Dwell Time	Peak Ratio (X-ray)	Lithium Content*	Discharge Cap. (mAh/g)
010apa.01	1 : 1	2h	0.975	0.880	No Capacity
009apa.02	1 : 1	5h	0.766	0.911	~ 50
009apa.03	1 : 1	8h	0.847	0.898	~ 45
011apa.01	1 : 1.05	2h	0.884	0.893	No Capacity
011apa.02	1 : 1.05	5h	0.722	0.919	~ 125
011apa03	1 : 1.05	8h	0.715	0.920	~ 110
013apa.01	1 : 1.08	2h	0.891	0.892	~ 65
013apa.02	1 : 1.08	5h	0.734	0.917	~ 115
013apa.03	1 : 1.08	8h	0.709	0.921	~ 100

[#] 800°C   *Calculated from Dahn's method [14]

The integrated peak intensity ratio $I(003)/I(104)$ determined from the x-ray diffraction pattern was used for monitoring the lithium content following the guidelines published by Dahn et al. [14-17]. This was used as an indicator for ascertaining the disorder of nickel atoms on lithium sites. By controlling the stoichiometry (Ni to Li ratio) and heat treatment time, the final lithium content can therefore be altered which affects the discharge capacity of the synthesized $LiNiO_2$. However, some inconsistencies were observed between the calculated Li content in the material and the discharge capacity which will be discussed later in this section. Based on the information listed in Table 5-4, 5-5 and 5-6, several general trends can be summarized. These are: (a) It is difficult to obtain stoichiometric $LiNiO_2$ utilizing the PSG processes developed so far. This can be seen from the fact that the adjustment of the Ni to Li ratio in the starting materials and controlling heat treatment time fails to obtain stoichiometric $LiNiO_2$. The reason for this could be attributed to the competition between the decomposition of $LiNiO_2$ which causes loss of Li during the prolonged heat treatments at high temperature ($800^{\circ}C$) as reported in the literature [16, 18], and the decomposition of Li_2CO_3 which is the source of Li in the resultant $LiNiO_2$. (b) Addition of excess Li during the synthesis can actually function as a reservoir for supplying Li to promote the formation of $LiNiO_2$ and therefore improve the electrochemical property. This aspect can be seen by comparing the Li content and the heat treatment time for the different nominal compositions of the starting precursors. Continued loss of lithium in the oxide is seen with varying heat treatment time when the starting Ni to Li ratio is 1:1. However, an increase in the Li content in the oxide is observed with heat treatment time when excess lithium is used to synthesize the precursors. (c) Nevertheless, still a large excess of lithium contained in the xerogel does not help to improve the discharge capacity of the synthesized $LiNiO_2$. Instead, it decreases the discharge capacity of the material as shown in the table.

The observations (a) and (b) are related to the kinetics of lithium carbonate decomposition and the formation of lithium nickel oxide which will be discussed later. Conclusion (c) is related to the influence of electrochemical property caused by the presence of lithium carbonate since it is the only major impurity phase observed in the synthesis of these oxides.

94
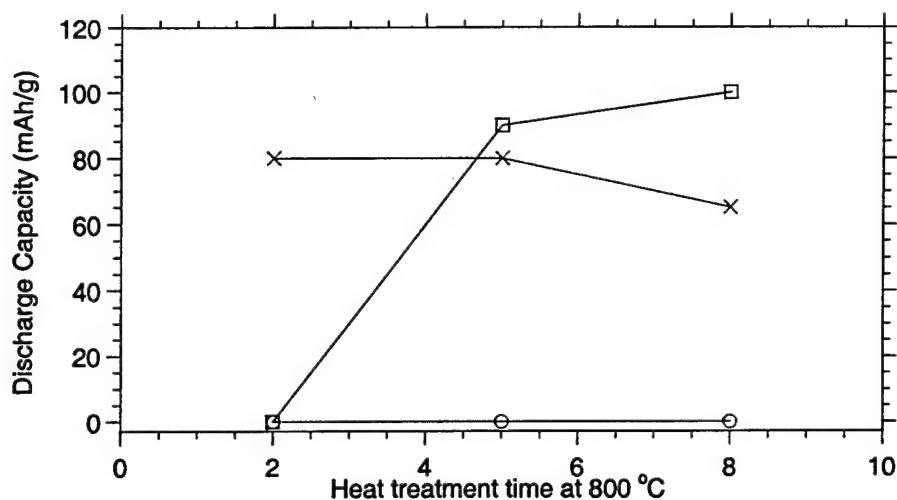
Figure 5-24. Plot of the heat treatment time versus first discharge capacity using different starting Li to Ni ratios in the precursor. Li : Ni = 1 : 1 is represented by (-o-), 1.05 : 1 and 1.08 : 1 are represented by (-□-) and (-×-) respectively.
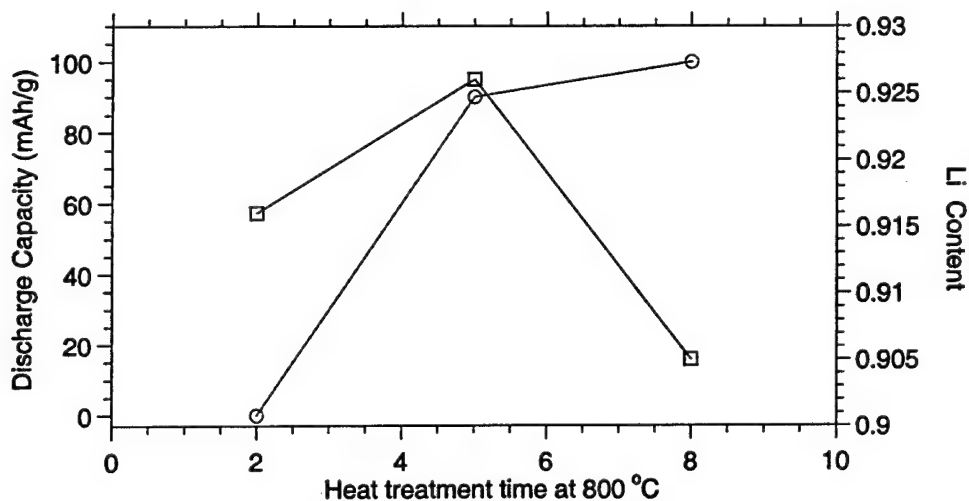
Figure 5-25. A demonstration of the effect of Li_2CO_3 on the electrochemical property of the oxide. (-o-) represents the variation capacity with heat treatment time using a starting ratio of Li: Ni = 1.05 : 1 in the precursor. The lithium content of the material versus heat treatment time using the experimental formula concluded by Dahn. et al. is represented by (-□-), which is used as an indicator for Ni disorder.

According to the information given in Table 5-4, for the oxide generated by the rotary evaporation processes, variation of the first discharge capacity using different initial ratio of Li to Ni in the precursor with respect to heat treatment time is plotted in Fig. 5-24. From the figure it can be seen that the capacity of the material generally increases with the addition of excess Li. However, the incorporation of a large excess of Li is seen to induce a loss in capacity of the synthesized material. The best first discharge capacity of 100mAh/g has been exhibited by the $LiNiO_2$ powders synthesized using a Li to Ni ratio of 1.05 after heat treatment of the xerogels at $800^{\circ}C$ for 8 hours. This loss in capacity of the oxide generated by the addition of excess Li is primarily due to Li_2CO_3, present as the main impurity in the synthesized oxide. This deleterious influence caused by the presence of Li_2CO_3 is also seen from the plot of capacity with heat treatment time for the oxide synthesized using a Li to Ni ratio of 1.05 in the starting precursor dried by rotary evaporation, shown in Fig. 5-25. In the same plot, the variation of the lithium content in the material with heat treatment time is also presented. The lithium content shown in Fig. 5-25 is determined using the experimental formula deduced by Dahn. et al.[14], which is also used as an indicator for the disorder of Ni. From Fig. 5-25 it can be seen that although the lithium content in the oxide which is heat treated at $800^{\circ}C$ for 8 hours is much less compared to the sample heat treated for 5 hours, the capacity of the oxide increases with heat treatment time. The decrease in the Li content could be attributed to the decomposition of $LiNiO_2$ which results in an increase in the misposition of Ni [15, 18]. The increase in capacity suggests that the electrochemical property of the synthesized material is not only determined by the lithium content (which is used as an indicator of the disorder) of the oxide, but is also influenced by the existence of lithium carbonate. The presence of lithium carbonate can influence the capacity of material not only by reducing the active weight of the oxide, but also contributing significantly to the polarization of the cathode.

In order to demonstrate this deleterious influence of Li_2CO_3, a plot of the voltage versus Li content for the first 2 cycles of the two samples synthesized by rotary evaporation using a ratio of Li : Ni = 1.05 : 1 and heat treated at $800^{\circ}C$ for 5 and 8 hours respectively is presented in Fig. 5-26(a) and 5-26(b).

96
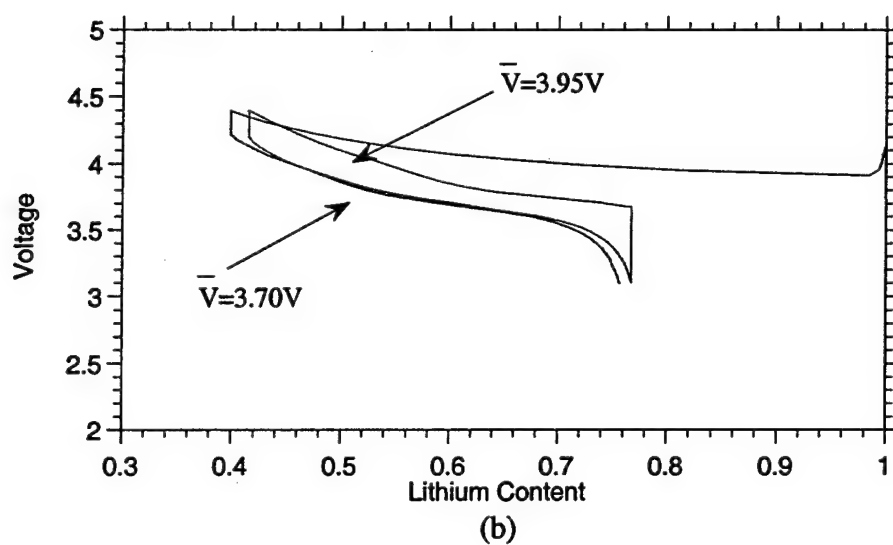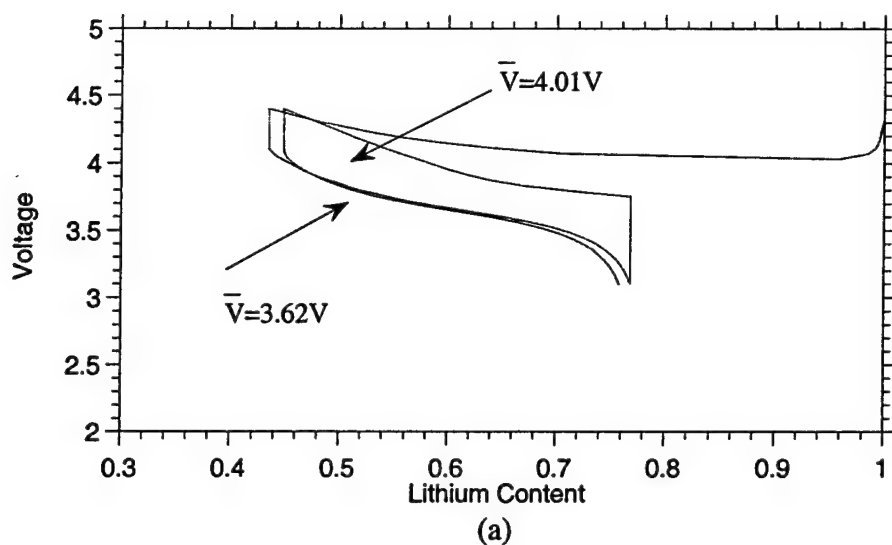
Figure 5-26. Plot of the voltage versus Li content for the first 2 cycles of the two samples synthesized using a Li to Ni ratio of 1.05 : 1. (a) The sample heat treated at 800°C for 5 hours and (b) the sample which is heat treated at 800°C for 8 hours.

The average voltage of the second cycle for each sample (first cycle may not be accurate because of the instability of the test cell) during charge and discharge is calculated using the formula:

$$\overline{V} = (\int_{Q_1}^{Q_2} VdQ) / Q_{sum} \qquad (5.8)$$

where '$\overline{V}$' is the average voltage and 'Q' is the variation in charge, i.e. Coulombs. In the case of the sample heat treated for 5 hours, the average voltages for the second charge and discharge cycles are obtained as 4.01V and 3.62V in comparison to 3.95, 3.70V for the sample which is heat treated for 8 hours. From the calculation of the average voltage, it is clearly seen that the increase in the specific capacity of the sample which is heat treated for 8 hours is not due to the weight loss caused by the decomposition of Li_2CO_3. Instead, it is because of a decrease in the average voltage (decrease of polarization) that causes the increase in capacity. From the results shown above, the exact reason for the influence of variation in the electrochemical behavior caused by the presence of lithium carbonate could be attributed to the distribution of lithium carbonate in the heat treated materials. It is possible that presence of trace amounts of Li_2CO_3 as a secondary phase in the oxide may increase the polarization by forming a film over the oxide surface and therefore retard the diffusion of lithium into the electrolyte. Hence, it is possible that the oxide obtained after heat treatment at 800°C for 5 hours shows a lower capacity in comparison to the oxide obtained after 8 hours (see Fig. 5-24).

In order to clarify this aspect, it was decided to analyze the morphology of the lithium carbonate phase present in the synthesized oxide. The sample which was synthesized using a ratio of Li:Ni=1.08:1 in the starting material followed by a 2 hour heat treatment at 800°C was used for the TEM and STEM analysis in order to observe the morphology of the Li_2CO_3 present in the oxide. This particular composition was selected for the TEM and STEM analysis since it would be easier to observe the morphology of the undecomposed Li_2CO_3 in a sample containing a large excess of lithium.

The TEM bright field images shown in Fig. 5-27(a) and 5-27(b) at different magnifications reveal the morphology of the oxide as well as the carbonate. As shown in the figures, two phases with distinct compositional contrast can be seen. The images show dark faceted particles (< 1μm) surrounded by a secondary phase light in color. The

secondary phase appears to be non-uniformly distributed around the dark faceted particles forming a coating of random thickness. It was therefore decided to analyze the compositional variation in the two phases. Spots 'α ' and 'β ' were selected as the representative sites for EDX analysis in the powders corresponding to the light and dark regions.

(a)
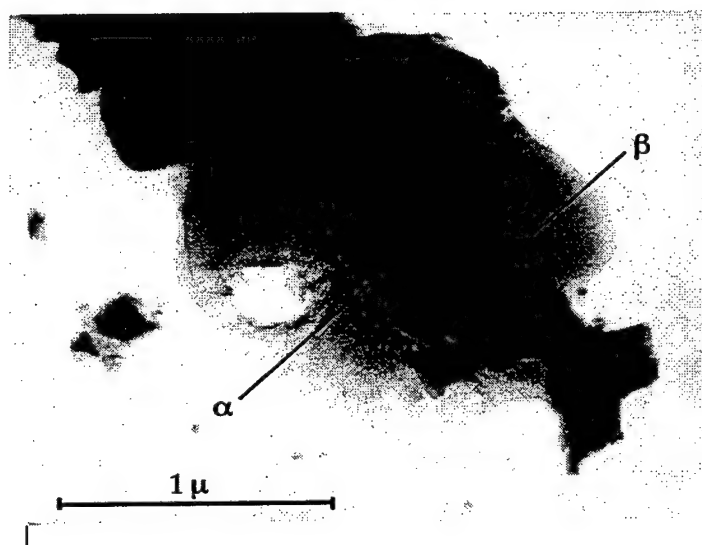
(b)
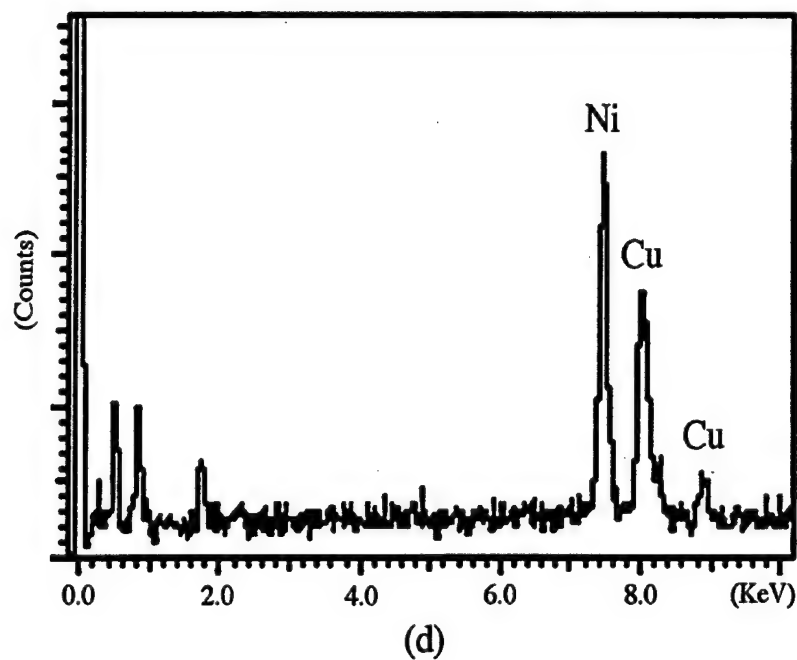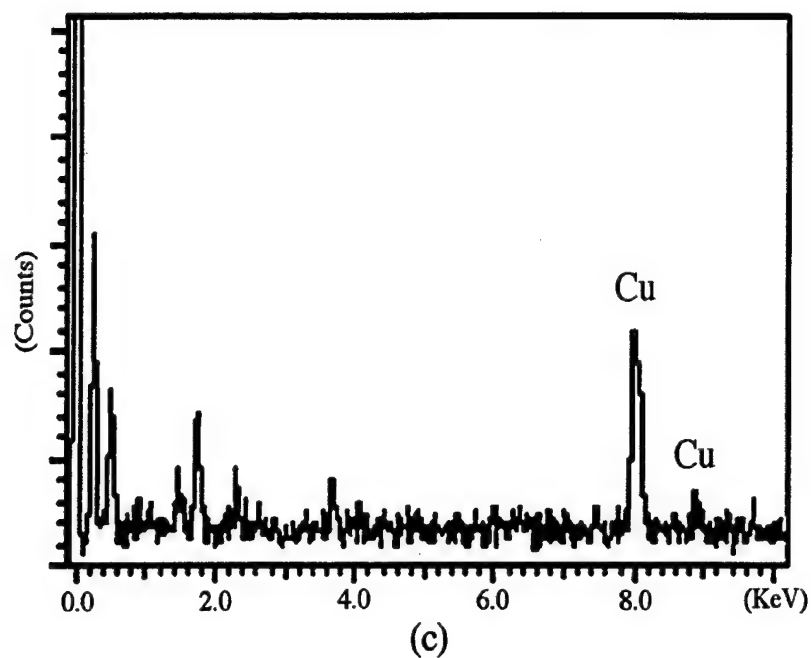
Figure 5-27. The TEM bright field images showing the morphology of the materials (a) at a magnification of 13500X and (b) 36000X respectively. The EDX data which corresponds to the spots "α" and "β" indicated in (b) are shown in (c) and (d) respectively, for the purpose of distinguishing the $LiNiO_2$ and Li_2CO_3 phases.

(a)
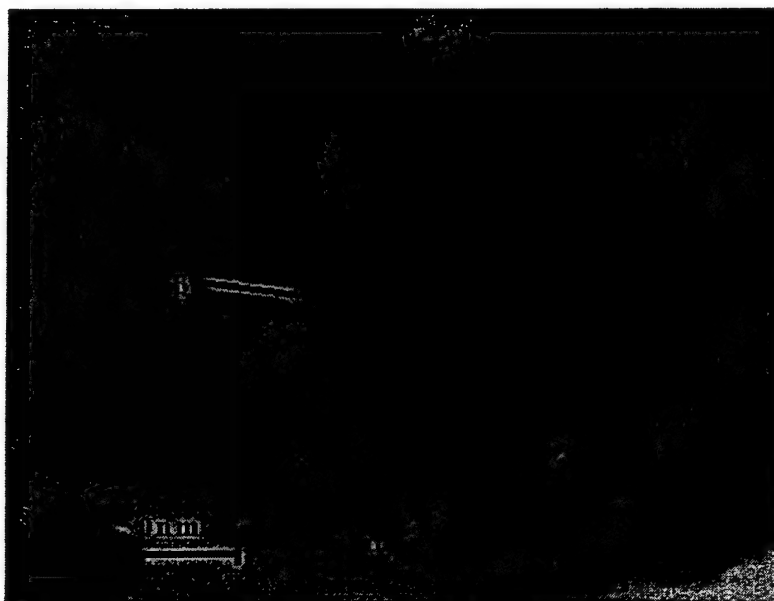
(b)
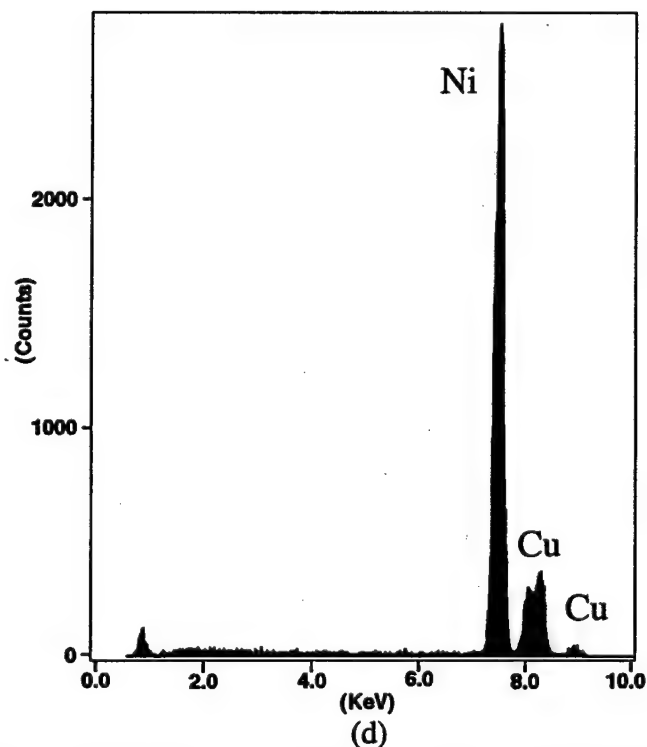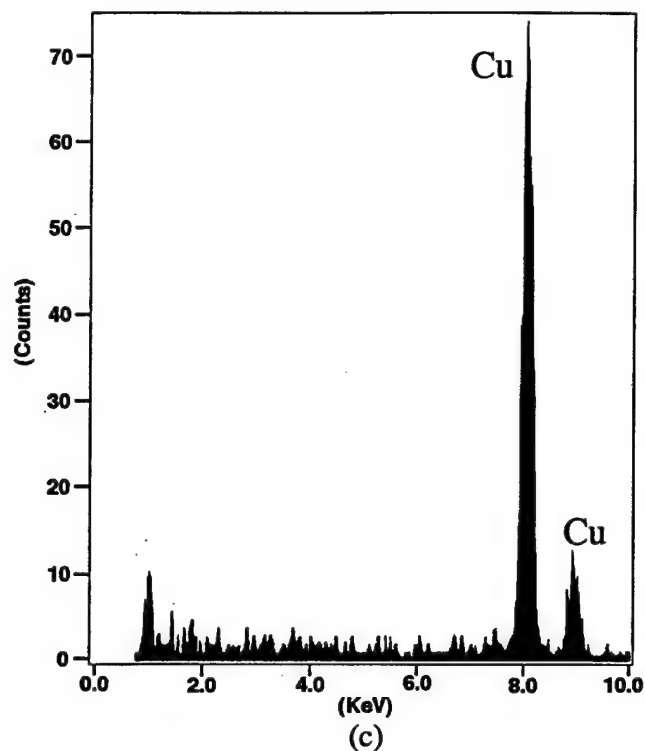
Figure 5-28. The morphology of Li_2CO_3 is also investigated using STEM. (a) morphology at a magnification of 200kX and (b) 500kX. The EDX data which corresponds to the spots "α" and "β" indicated in (b) are shown in (c) and (d) respectively. The light colored phase corresponding to Li_2CO_3 actually surrounds the $LiNiO_2$ particles.

102

The results of the EDX analysis are shown in Fig. 5-27(c) and 5-27(d) respectively. The results of EDX analysis on the two spots show clearly the presence of Ni only in region marked 'β'. The peaks for copper are mainly from the grids used for mounting the sample. This therefore suggests that region 'α' is the Li_2CO_3 phase and the region 'β' is the $LiNiO_2$ phase. Thus, the TEM analysis of the oxide shows that some of the $LiNiO_2$ particles are actually surrounded by Li_2CO_3. Similarly, STEM analysis was used to supplement the results of TEM and verify the nature of the light colored phase surrounding the oxide particles.

The morphology of the oxide and the morphology of Li_2CO_3 are shown in Fig. 5-28(a) and 5-28(b) respectively. Similar to the TEM results, the STEM micrographs also show the presence of dark and light regions (see Fig. 5-28). Once again EDX analysis was used to identify the light and dark regions. The analysis was conducted on region 'α' corresponding to the light phase and 'β' corresponding to the dark phase. Similar to the TEM results, the pale light colored region corresponds to the Li_2CO_3 phase as indicated by the EDX results shown in Fig. 5-28(c). Lithium carbonate therefore appears to more or less surround the $LiNiO_2$ particles as indicated by both TEM and STEM analysis of the heat treated powder. The existence of Li_2CO_3 which covers the $LiNiO_2$ particles could retard the diffusion of Li during cycling which causes an increase in the impedance of the cathode.

It is known that the measured voltage ($V_{measured}$) is a sum of the open circuit voltage and the voltage due to the internal resistance of the material given as :

$$V_{measured} = V_{open\ circuit} + V_{IR} \qquad (5.9)$$

Thus in the case of the oxide synthesized using a Li to Ni ratio of 1.05:1 and heat treated at 800°C for 5 hours, a higher resistance is seen due to the presence of the film of Li_2CO_3 causing an increase in the measured voltage '$V_{measured}$'. During charging at a given Li content, therefore, the cell would exhibit a higher voltage corresponding to the pre-set cut-off voltage thereby lowering the capacity as indicated in Figures 5-26. However upon heat treatment at 800°C for a longer time of 8 hours, decomposition of Li_2CO_3 occurs causing a reduction in the polarization and therefore the measured voltage '$V_{measured}$'

leading to a higher discharge capacity. Similarly, increasing the lithium content by addition of large excess Li leads to the formation of a larger amount of Li_2CO_3 covering the surface of the $LiNiO_2$ particles. As a result, longer heat treatments are essential at $800^{\circ}C$ in order to enhance the decomposition of the carbonate phase and facilitate the formation of the stoichiometric oxide. This is however limited due to the subsequent decomposition of the oxide at $800^{\circ}C$ (see Fig. 5-24) thereby lowering the capacity. Thus, the decomposition of the carbonate should be initiated at a lower temperature and the kinetics of the reaction should be accelerated in order to improve the capacity. According to the results shown above, a simple reaction mechanism is proposed. The proposed mechanism is illustrated by a schematic figure as shown in Figure 5-29.
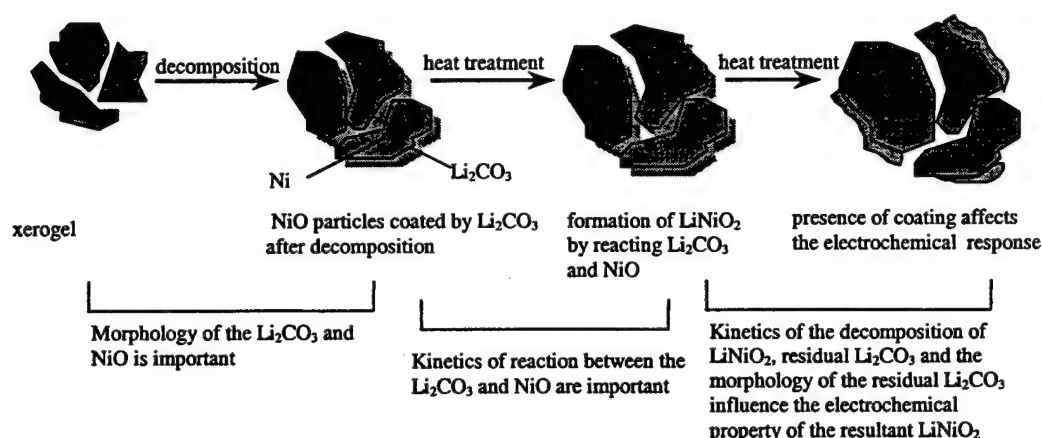
Figure 5-29. Proposed reaction mechanism illustrating the formation of $LiNiO_2$ from the xerogels derived by rotary evaporation.

Based on the schematic above illustrating the proposed reaction mechanism, enhancement of lithium carbonate decomposition as well as the prevention of the decomposition reaction at high temperatures should be the key factors responsible for synthesizing stoichiometric and electrochemically active materials in all the four processes. This aspect will be further clarified in section 5.10. It should be mentioned that this is also one of the main factors contributing to the inactivity of the $LiNiO_2$ obtained by spray decomposition. The reaction mechanisms and kinetic studies that will be

described in section 5.10 will also be important in outlining improvements to the spray decomposition process in the future.

The cycling behavior (capacity versus cycle number) and voltage profile (voltage versus composition of Li) of $LiNiO_2$ synthesized using xerogels generated by rotary evaporation, spray drying and the gelation processes are displayed in Figure 5-30 and Figure 5-31. These plots were obtained from test batteries comprising of cathodes of materials derived from each of the three processes exhibiting the highest capacities. The X-ray diffraction patterns of these samples are also shown in Figure 5-32. The differential capacity, dQ/dV versus voltage, V plot of the second cycle for these samples are also shown in Figure 5-33. By comparing the dQ/dV plot of the $LiNiO_2$ synthesized in this study and the commercial $LiNiO_2$ powders obtained from FMC shown in Figure A-8 (Appendix A), one can conclude that the phase transformation reactions during cycling are suppressed. Similar observation is also reported earlier by Hirano et al. [19] which is attributed to the observation of the fact that the suppression of phase transformation is induced by the misposition of Ni^{2+} ions on the Li sites thereby acting as "Pillaring" agents. The reason of this delay or suppression of phase transformation is more appropriately explained by the minimization of the well-known Jahn-Teller distortion [20, 21] caused by the induction of divalent cations on the transition metal sites. Owing to this observation, a more complete study on the function as well as effects of divalent cations on the transition metal sites was conducted which is included in Appendix C and D.
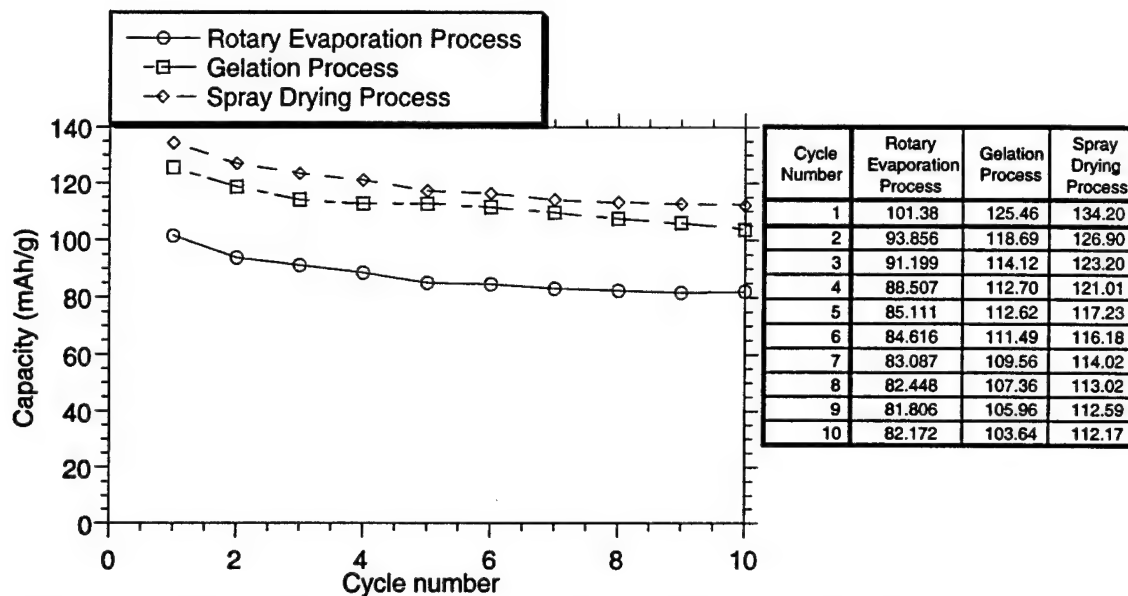
Figure 5-30. The capacity versus cycle number of $LiNiO_2$ synthesized using xerogels generated by the rotary evaporation, gelation and spray drying processes. The plots represent the highest capacities of the materials synthesized using the three processes.

Cycle Number	Rotary Evaporation Process	Gelation Process	Spray Drying Process
1	101.38	125.46	134.20
2	93.856	118.69	126.90
3	91.199	114.12	123.20
4	88.507	112.70	121.01
5	85.111	112.62	117.23
6	84.616	111.49	116.18
7	83.087	109.56	114.02
8	82.448	107.36	113.02
9	81.806	105.96	112.59
10	82.172	103.64	112.17
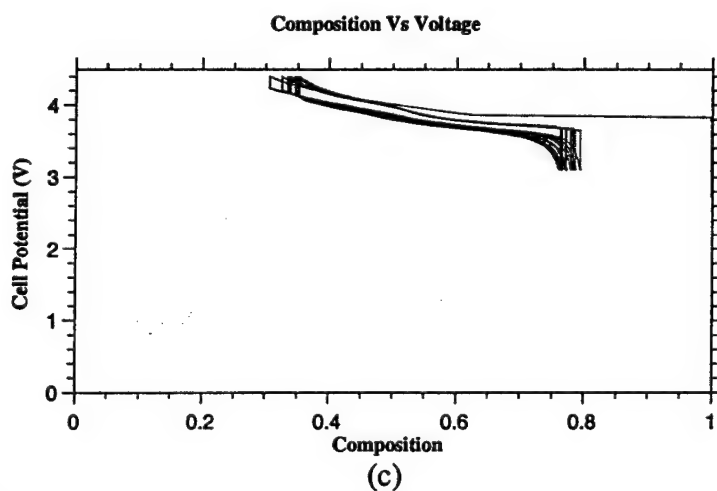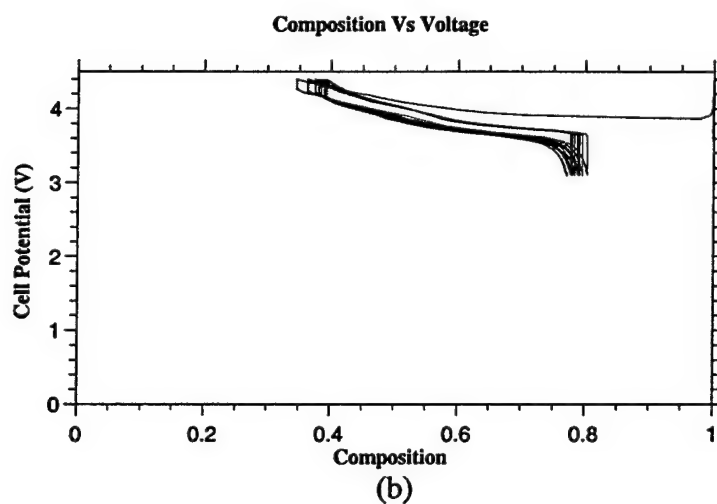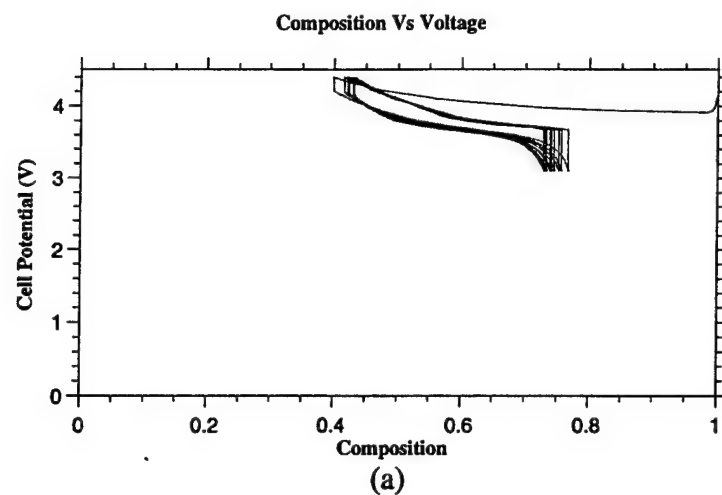
Figure 5-31. Voltage versus composition of $LiNiO_2$ synthesized using xerogels generated by (a)rotary evaporation, (b)gelation and (c)spray drying processes. These plots are representative of the materials which show the highest capacities.

Peak	Relative intensity
(003)	87.73
(101)	33.25
(006)+(102)	26.81
(104)	100

(003)/(104)	((006)+(102))/(101)	Lithium Content
0.877	0.806	0.904

File name: 022apa.01
Starting Ni:Li = 1:1.05
Heat Treatment Conditions:

800°C, 8hrs

(a)

Peak	Relative intensity
(003)	93.31
(101)	35.21
(006)+(102)	25.44
(104)	100

(003)/(104)	((006)+(102))/(101)	Lithium Content
0.933	0.722	0.919

File name: 011apa.02
Starting Ni:Li = 1:1.05
Heat Treatment Conditions:

800°C, 5hrs

(b)

Peak	Relative intensity
(003)	93.91
(101)	35.05
(006)+(102)	24.88
(104)	100

(003)/(104)	((006)+(102))/(101)	Lithium Content
0.939	0.710	0.921

File name: 045apa.02
Starting Ni:Li = 1:1.05
Heat Treatment Conditions:

800°C, 5hrs

(c)

Figure 5-32. X-ray diffraction patterns of $LiNiO_2$ synthesized using xerogels generated by (a)rotary evaporation, (b)gelation and (c)spray drying processes. The patterns are representative of the materials which display the highest capacities.

108
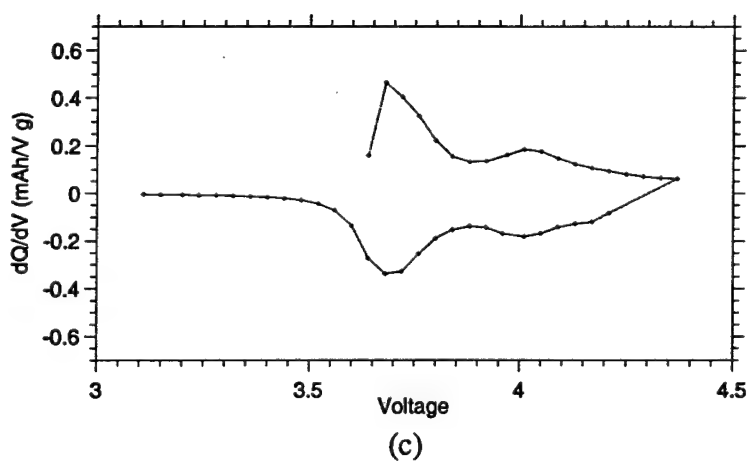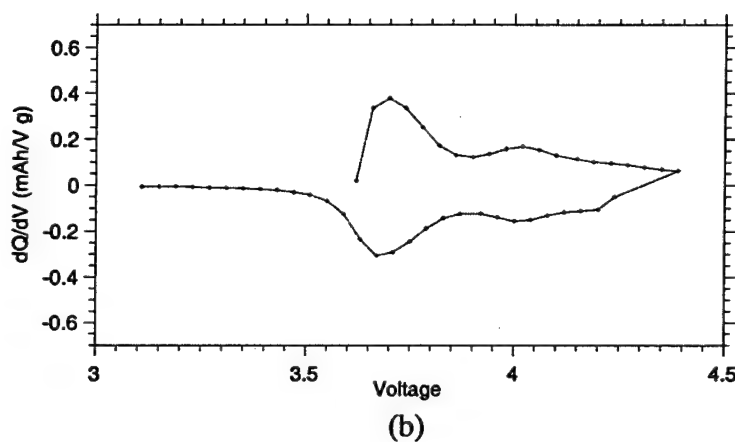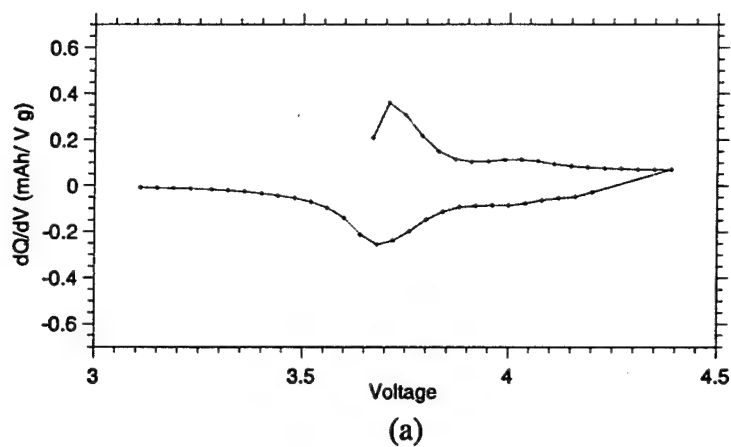
Figure 5-33. Plot showing the variation of differential capacity, dQ/dV and voltage, V of the second cycle for LiNiO$_2$ synthesized using xerogels generated by (a)rotary evaporation, (b)gelation and (c)spray drying processes.

5.9 Electrochemical characterization of the synthesized LiNi$_{0.75}$Co$_{0.25}$O$_2$ powders:

In comparison to the electrochemical response of the PSG derived LiNiO$_2$, the mixed oxide, LiNi$_{0.75}$Co$_{0.25}$O$_2$ shows a much better capacity. This could be attributed to the decrease in disorder of Ni^{2+} on Li sites observed for the resultant LiNi$_{0.75}$Co$_{0.25}$O$_2$. Furthermore, the recurring problem of lithium carbonate is much less severe compared to that seen for LiNiO$_2$. As was pointed out in the section on phase evolution, the LiNi$_{0.75}$Co$_{0.25}$O$_2$ obtained at the temperature of 600°C is almost free of lithium carbonate. The plot of capacity versus cycle number for LiNi$_{0.75}$Co$_{0.25}$O$_2$ synthesized using the rotary evaporation and spray drying processes are shown in Figure 5-34. It should be mentioned that the capacity of LiNi$_{0.75}$Co$_{0.25}$O$_2$ generated by the rotary evaporation process shows a discharge capacity of 168mAh/g for the first cycle. A discharge capacity of 180mAh/g was however obtained for LiNi$_{0.75}$Co$_{0.25}$O$_2$ generated by the spray drying process. The capacity of the materials presented here are comparable or even better than those reported in the literature for materials with the same composition [7]. Figure 5-35 shows the voltage versus composition plot of those LiNi$_{0.75}$Co$_{0.25}$O$_2$ synthesized using xerogels generated by rotary evaporation and spray drying processes. X-ray diffraction patterns of these samples are also shown in Figure 5-36. By comparing the peak ratio of (003)/(104) obtained for LiNi$_{0.75}$Co$_{0.25}$O$_2$ and the peak ratio obtained for LiNiO$_2$ shown earlier in Figure 5-32, one can conclude that the defect concentration is minimized by substituting 25% of Ni by Co. Finally, the differential capacity dQ/dV versus voltage V plots are also shown in Figure 5-37. A single peak is observed in the charge and discharge cycle of LiNi$_{0.75}$Co$_{0.25}$O$_2$ implying that no phase transformation is seen during cycling.

Cycle Number	Rotary Evaporation Process	Spray Drying Process
1	167.83	182.02
2	167.19	180.83
3	167.18	178.86
4	166.31	177.63
5	165.12	176.52
6	163.16	175.05
7	162.02	173.36
8	160.82	171.35
9	159.36	169.70
10	158.29	168.39
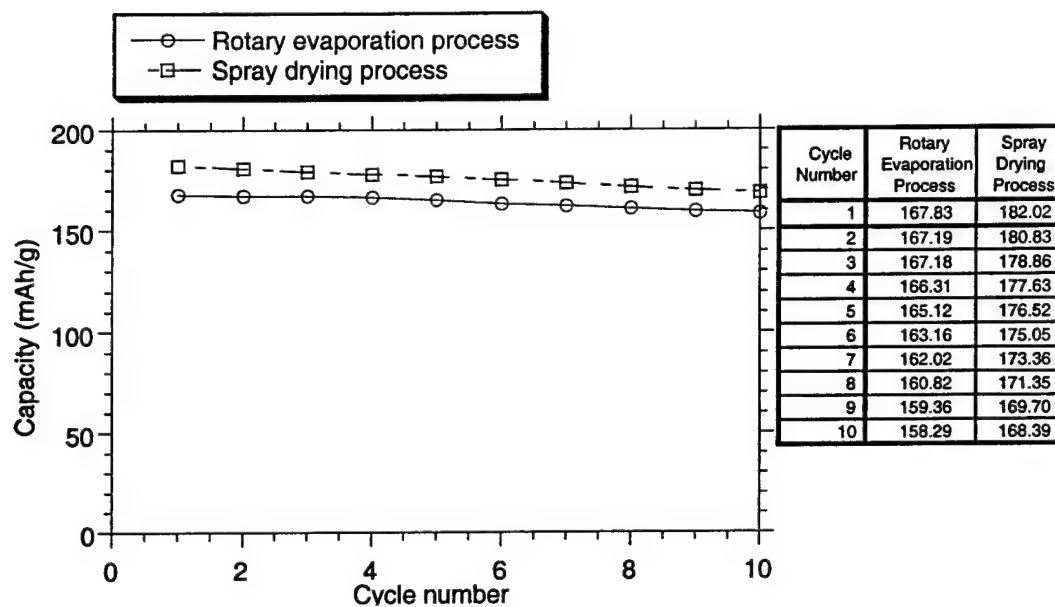
Figure 5-34. Plot showing the variation of capacity versus cycle number of $LiNi_{0.75}Co_{0.25}O_2$ synthesized from xerogels generated by the rotary evaporation and spray drying processes. Those plots are representative of materials which show the highest capacities.

Composition Vs Voltage

(a)

Composition Vs Voltage

(b)
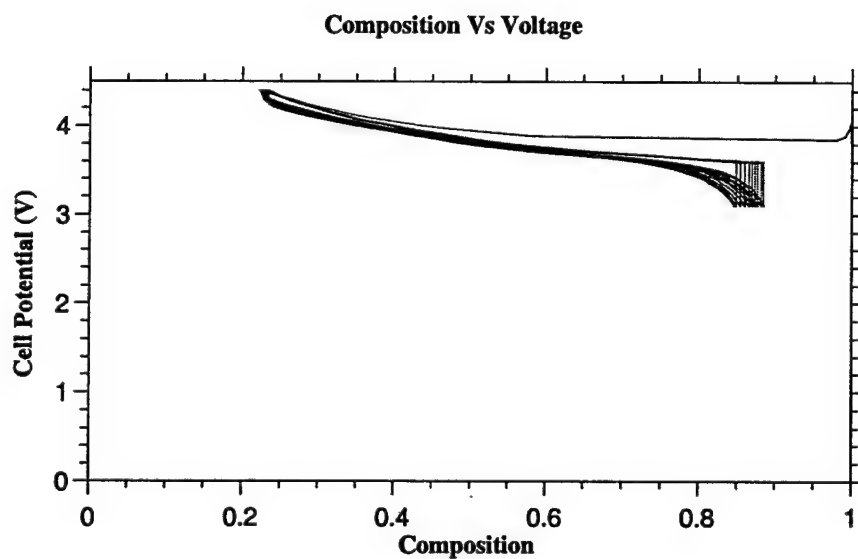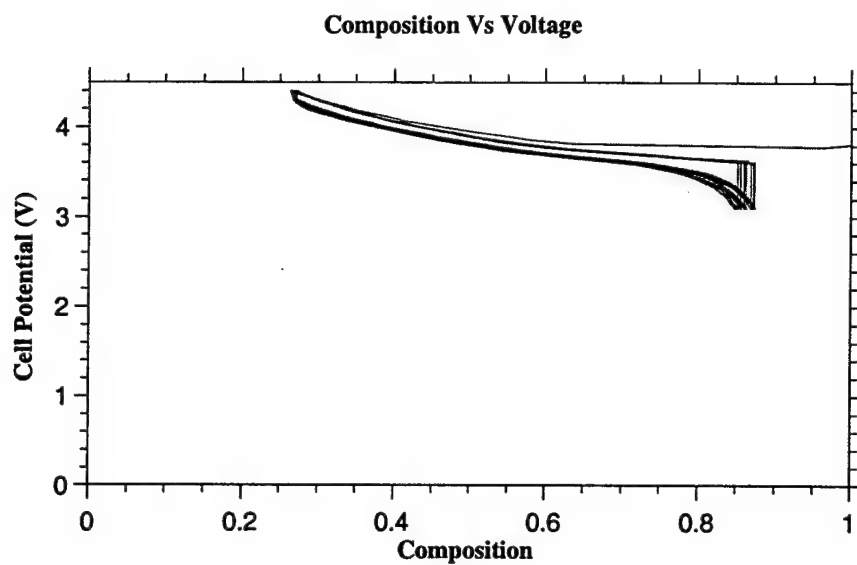
Figure 5-35. Plot of voltage versus composition of the cathodes made from $LiNi_{0.75}Co_{0.25}O_2$ synthesized using xerogels generated by (a)rotary evaporation and (b)spray drying processes. The plots represent the materials which show the highest capacities.

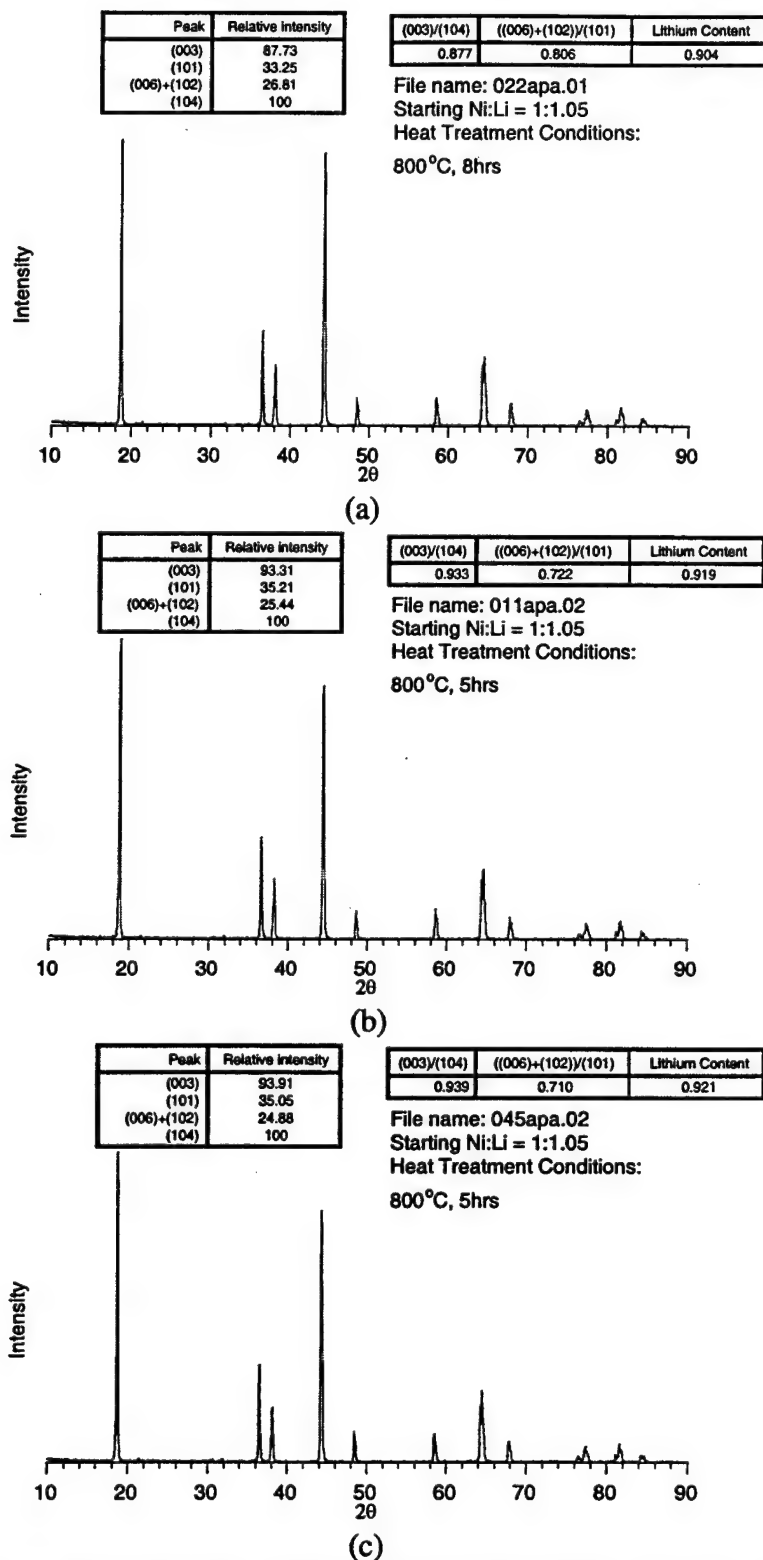| Peak	Relative intensity
(003)	100
(101)	32.28
(006)+(102)	16.61
(104)	72.44

Filename: 086apb.01
Starting Ni:Li =1:1
Heat Treatment Conditions:

800 °C, 2hrs

(a)

Peak	Relative intensity
(003)	100
(101)	39.59
(006)+(102)	19.56
(104)	82.35

Filename: 061ape.01
Starting Ni:Li =1:1
Heat Treatment Conditions:

800 °C, 2hrs

(b)
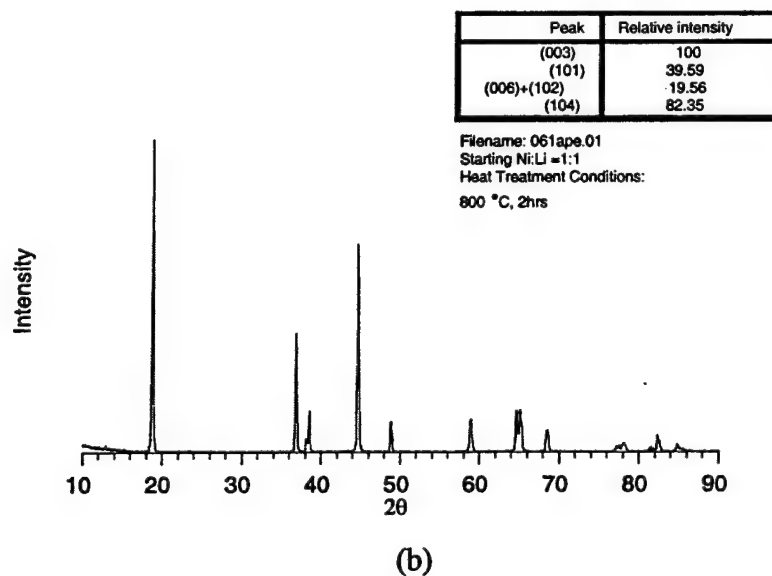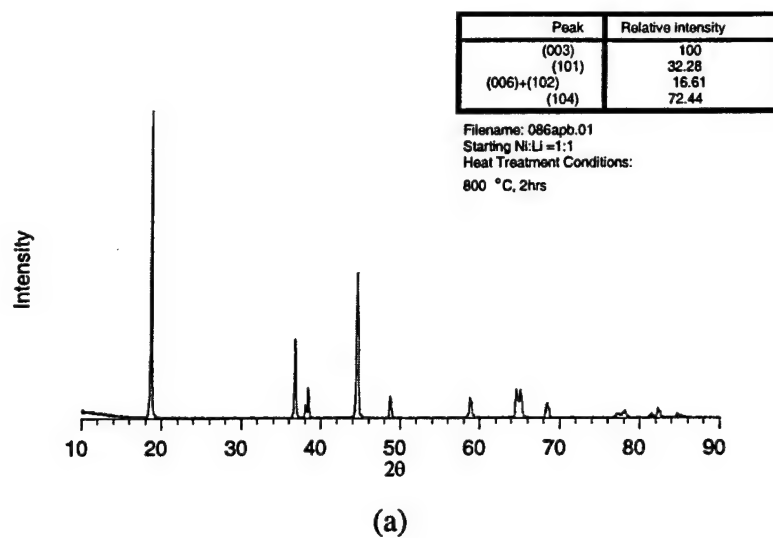
Figure 5-36. The X-ray diffraction patterns of $LiNi_{0.75}Co_{0.25}O_2$ powders synthesized using the xerogels generated by (a) rotary evaporation and (b) spray drying processes. The patterns correspond to the materials which exhibit the highest capacities.

113
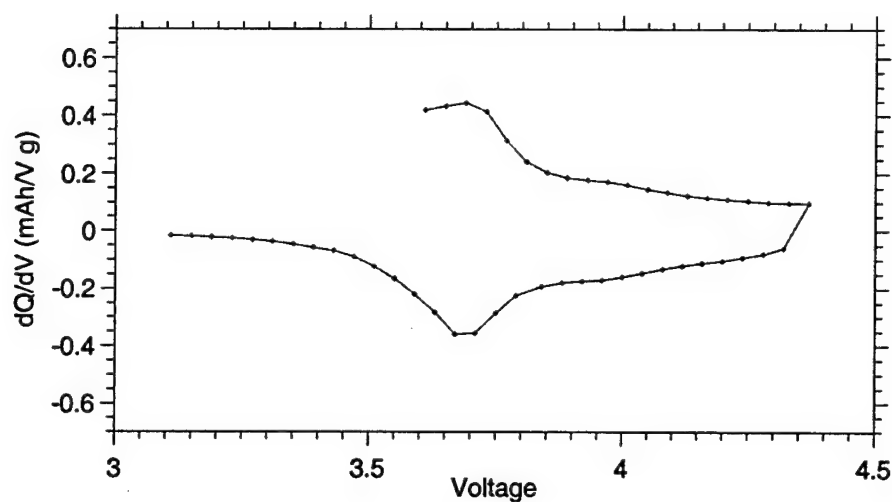
(a)
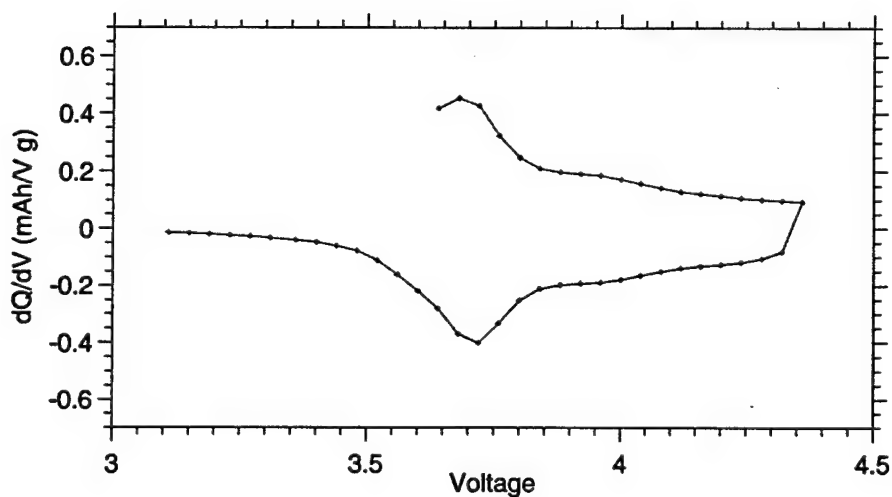
(b)

Figure 5-37. Plot showing the changes in the differential capacity, dQ/dV with voltage, V plots for $LiNi_{0.75}Co_{0.25}O_2$ synthesized using xerogels generated by (a)rotary evaporation and (b)spray drying processes. The plots represent the materials which show the highest capacities.

Part IV.   Investigation of the mechanisms and kinetics of formatin of stoichiometric LiNiO₂ using the particulate sol-gel approach

5.10   Synthesis of stoichiometric LiNiO₂:

According to the proposed mechanism outlined in section 5.8, it is clear that in all the processes described the prevention of decomposition of $LiNiO_2$ and loss of lithium at high temperature is the key to the synthesis of stoichiometric $LiNiO_2$. This is because with the prevention of the decomposition of the oxide, the kinetics of the reaction between lithium carbonate and nickel oxide is the only factor that would govern the formation of stoichiometric $LiNiO_2$, which is time dependent. In order to identify the proper temperature and atmosphere for synthesizing stoichiometric $LiNiO_2$, commercial $LiNiO_2$ procured from FMC is utilized for investigating the decomposition of $LiNiO_2$ at various temperatures in different atmospheres. Results of simultaneous TGA/DTA
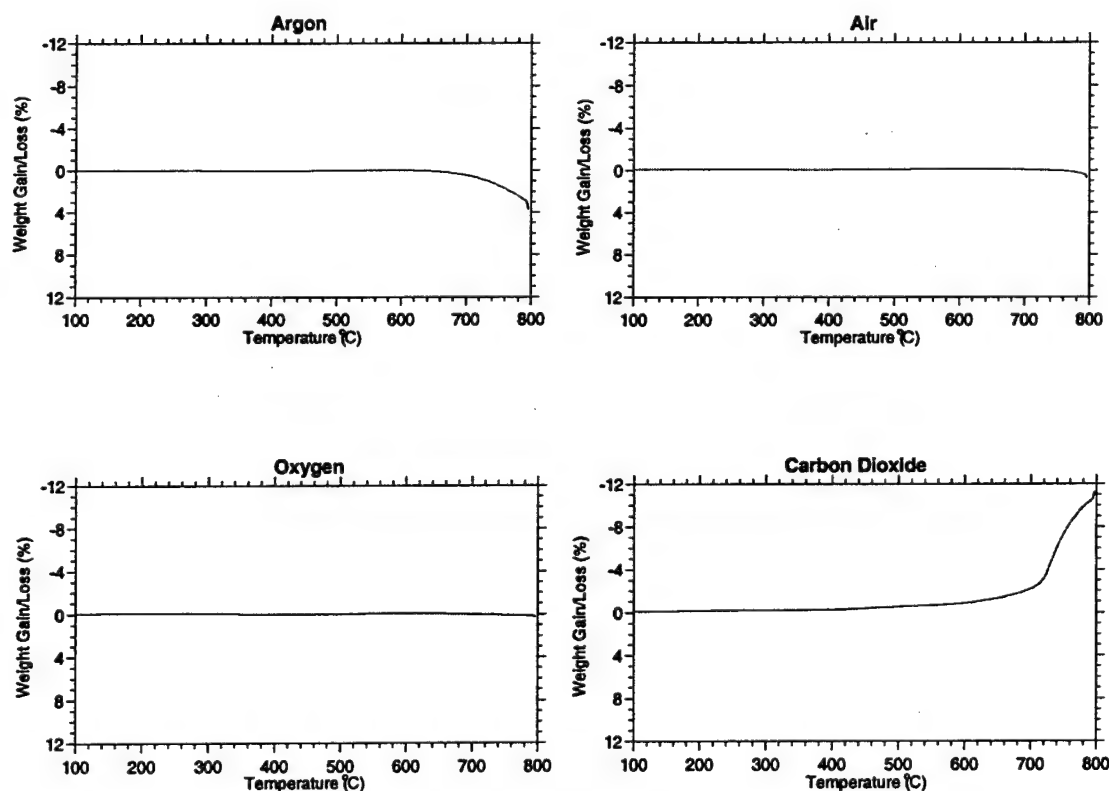
Fig. 5-38. The result of simultaneous TGA/DTA analysis on the FMC $LiNiO_2$ conducted under argon, air, oxygen and carbon dioxide atmospheres. A heating rate of $10^{\circ}C/min$ to $800^{\circ}C$ is the heat treatment schedule utilized for this TGA analysis. All figures are shown using the same scale for comparison.

analysis conducted on the FMC procured $LiNiO_2$ heat treated in argon, air, oxygen and carbon dioxide is shown in Fig. 5-38. A heating rate of $10^\circ C/min$ from room temperature to $800^\circ C$ is the heat treatment schedule utilized for all the TGA analysis. From Fig.5-38 it can be seen that weight loss occurs when $LiNiO_2$ is heat treated in argon, air and oxygen. In contrast, a weight gain is observed for the sample heat treated in carbon dioxide. The weight loss of $LiNiO_2$ heat treated under argon, air and oxygen can be attributed to the occurrence of the following reaction:

$$LiNiO_2 \xrightarrow{\hspace{1cm}} 1/(2\text{-}x)\ Li_xNi_{2\text{-}x}O_2 + (1\text{-}x)/(2\text{-}x)\ Li_2O + (1\text{-}x)/2(2\text{-}x)\ O_{2(g)}\uparrow \quad (5.10)$$
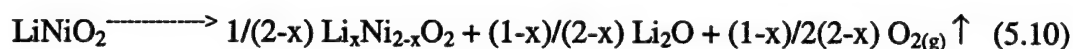
Initial: 1 mole

Final: 0 mole $+1/(2\text{-}x)$ mole $+(1\text{-}x)/(2\text{-}x)$ mole $+(1\text{-}x)/2(2\text{-}x)$ mole

% **weight loss** observed $= [(1\text{-}x)/2(2\text{-}x)] \times 32\ /\ 98 \times 100\%$

Similarly, the weight gain of $LiNiO_2$ heat treated in carbon dioxide can be expressed utilizing the following equation:

$$LiNiO_2 + (1\text{-}x)/(2\text{-}x)\ CO_{2(g)} \xrightarrow{\hspace{1cm}} 1/(2\text{-}x)\ Li_xNi_{2\text{-}x}O_2 +$$
$$(1\text{-}x)/(2\text{-}x)\ Li_2CO_3 + (1\text{-}x)/2(2\text{-}x)\ O_{2(g)}\uparrow \quad (5.11)$$
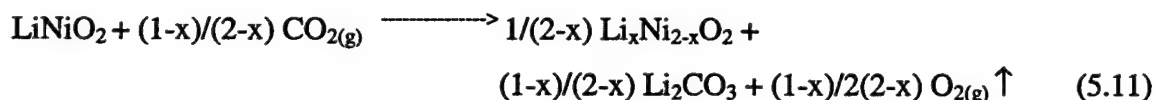
% **weight gain** observed $= \{[(1\text{-}x)/(2\text{-}x)]\times44-[(1\text{-}x)/2(2\text{-}x)]\times32\}/\ 98 \times 100\%$

Since the subscript 'x' can be measured from the weight change, furthermore 'x' is an indication of the misposition of Ni on Li site, one can therefore obtain the concentration of defects (disorder of Ni on Li site) from the weight change measured by TGA.

The temperature of on-set of the weight change, the net weight change between room temperature and $800^\circ C$, and the calculated defect concentration for $LiNiO_2$ heat treated in argon, air, oxygen and carbon dioxide are summarized in Table 5-7. Since the goal of the study is to synthesize stoichiometric $LiNiO_2$, the data obtained for stoichiometric $LiNiO_2$ heat treated in air and oxygen are especially important since the presence of oxygen is necessary for the formation of stoichiometric $LiNiO_2$ as can be seen from the reaction shown below:

$$NiO + 1/2\ Li_2CO_3 + 1/4\ O_{2(g)} \text{----------} > LiNiO_2 + 1/2\ CO_{2(g)} \uparrow \qquad (5.12)$$

Furthermore, in an air or oxygen atmosphere, the weight change on-set temperature gives an indication of the maximum heat treatment temperature that can be employed for synthesizing stoichiometric $LiNiO_2$. The net weight change at a specific temperature (e.g. at 800°C) also gives an indication for the loss of Li that is related to the concentration of disorder (misposition of Ni on Li site).

Table 5-7. The starting temperature of weight change, the net weight change between room temperature and 800°C, and the calculated defect concentration for $LiNiO_2$ heat treated in argon, air, oxygen and carbon dioxide.

	Argon	Air	Oxygen	Carbon dioxide
Weight change starting temperature	645°C	705°C	790°C	240°C
Net weight change between room temperature and 800°C	-3.06%	-0.64%	-0.13%	+11.23%
x value of $Li_xNi_{2-x}O_2$	0.7693	0.9592	0.9920	0.3524
Calculated defect concentration at 800°C	23%	4%	0.8%	65%

Based on the information obtained from Table 5-7, it can be seen that oxygen is the most preferred environment for synthesizing stoichiometric $LiNiO_2$ which would yield the optimum electrochemical response. In this sense, this heat treatment would result in the best quality oxide. This is because of the highest decomposition temperature implying maximum stability as well as minimum defect concentration expected when heat treating the synthesized oxide under oxygen. Heat treatment in air does render the oxide to be unstable beyond 800°C. A combination of air and oxygen treatments at certain preferred temperatures would be most suitable for synthesizing optimal quality $LiNiO_2$. The best quality $LiNiO_2$, with lowest defect concentration and highest electrochemical activity, is therefore synthesized by heat treating the as-prepared powders in air at 700°C for 2 hours followed by a second heat treatment in oxygen at 750°C for 5 hours. The first heat treatment is conducted in a box furnace that is directed towards removal of most of the undesirable carbon species during the decomposition

reaction of the as-prepared powders. The second step heat treatment cycle is utilized for the minimization of the defect concentration. The XRD pattern obtained on the best quality $LiNiO_2$ is shown in Fig. 5-39. This sample was synthesized utilizing the as-prepared powders derived by the rotary evaporation process followed by employing the modified refined heat treatment schedule. From Fig. 5-39, it can be seen that the intensity ratio of the (003) and (104) peaks is maximized which is an indication of the minimization of the defect concentration.
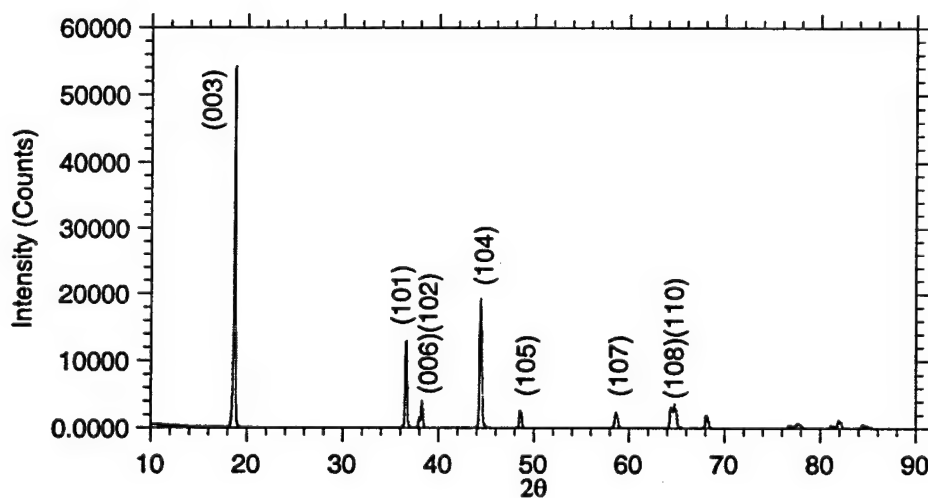
Fig. 5-39. The XRD pattern of the best quality $LiNiO_2$ with minimum defect concentration. This sample was synthesized utilizing the as-prepared powders derived by the rotary evaporation process subjected to the refined heat treatment schedule. From Fig. 5-39, it can be seen that the intensity ratio between the peaks (003) and (104) is maximized which is an indication of the minimization of defect concentration.
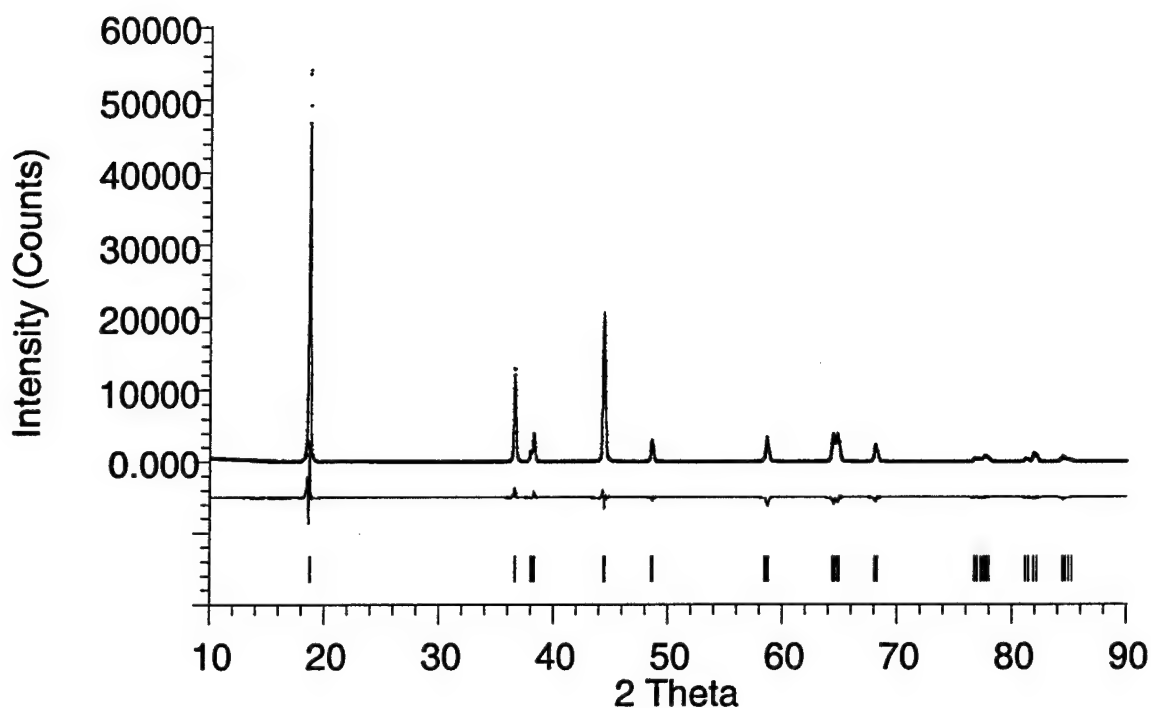
Fig. 5-40. The Results of the Rietveld refinement of the X-ray diffraction pattern obtained for LiNiO$_2$. The '+' sign indicate the observed pattern and the solid line indicate the calculated pattern. The differences between the observed and the calculated values are represented by the second solid line on the bottom of the plot. The tic marks indicate the allowed Bragg reflections.

Table 5-8. The detailed information of the Rietveld refinement conducted on the XRD pattern of LiNiO₂.

Bravais lattice	Hexagonal
Space group	$R\bar{3}m$
Atom positions	
Li (3a)	(0, 0, 0)
Ni (3b)	(0, 0, ½)
O (6c)	(0, 0, z) z=0.2417
Site occupancy	
O	1.0000
Ni	1.0000
Li	0.9899
Ni on Li site	0.0101
Lattice parameters	
$a\,(\overset{o}{A})$	2.87562
$c\,(\overset{o}{A})$	14.20137
Cell volume ($\overset{o}{A}{}^3$)	101.7007
Refinement quality indicator	
R_{wp}	12.48
R_p	9.11
R_e	5.88
S	2.12
d	0.5128
R_I	6.48
R_F	3.37

$$R_{wp} = \left\{ \frac{\sum w_i (y_i(obs) - y_i(calc))^2}{\sum w_i (y_i(obs))^2} \right\}^{1/2} \qquad \text{(R-weighted pattern)}$$

$$R_p = \frac{\sum |y_i(obs) - y_i(calc)|}{\sum y_i(obs)} \qquad \text{(R-pattern)}$$

$$R_e = [(N - P) / \sum w_i y_i(obs)^2]^{1/2} \qquad \text{(R-expected)}$$

$$S = [S_y / (N - P)]^{1/2} = R_{wp} / R_e \qquad \text{(Goodness-of-fit)}$$

The Dubin-Watson statistic,

$$d = \sum_{i=2}^{N} (\Delta y_i - \Delta y_{i-1})^2 / \Delta (\prod_{i=1}^{N} y_i)^2 \qquad \text{Where } \Delta y_i = y_i(obs) - y_i(calc)$$

$$R_I = \frac{\sum \left| I_k('obs') - I_k(calc) \right|}{\sum I_k('obs')} \qquad \text{(R-Bragg factor)}$$

$$R_F = \frac{\sum \left| (I_k('obs'))^{1/2} - (I_k(calc))^{1/2} \right|}{\sum (I_k('obs'))^{1/2}} \qquad \text{(R-structure factor)}$$

"obs" = observed
"calc" = calculated
$w_i = 1/y_i(obs)$
y_i = intensity at the i th step
$S_y = \sum_i w_i (y_i(obs) - y_i(calc))^2$ = Termed "residual", the quantity minimized in the
    least-square refinement
I_k = the intensity assigned to the k th Bragg reflection at the end of the
    refinement cycles
N = number of observations
P = the number of parameters adjusted

A more accurate value of the defect concentration is obtained using the Rietveld refinement technique. The results of the Rietveld refinement are shown in Fig. 5-40 and the detailed necessary information about the refinement obtained is also shown in Table 5-8. The RIETAN94 [22] software was used to simulate the XRD pattern for $LiNiO_2$. It should be noticed that the refinement result is obtained by assuming the occupancy of Li + (Ni on Li site) to be unity. From the results shown in Table 5-8, it can be seen that the defect concentration is very small (~1% of nickel misposition on lithium site) which is comparable with the minimum value obtained so far as reported by Dahn et al [15].

The electrochemical activity of this nearly stoichiometric low defect concentration $LiNiO_2$ is more superior in comparison to the $LiNiO_2$ synthesized earlier. This can be seen from the capacity versus cycle plot for the first 30 cycles as shown in Fig. 5-41. A high capacity of 205 mAh/g is obtained for the first cycle when the material is charged and discharged using a current density of $500\mu A/cm^2$, which corresponds to a C-rate of approximately C/2. However, the capacity fade is still high (0.71%/cycle) although the capacity has been increased. The reason for this high fade arises from the

decomposition of the material when charged to high voltages as has been discussed in the previous publication that is shown in Appendix B and C.

The first cycle voltage versus Li content plot for this low defect concentration $LiNiO_2$ is shown in Fig. 5-42. A very small current density of $10\mu A/cm^2$ which corresponds to a C-rate of ~C/100 is utilized for this test electrode. Several small plateaus are observed which corresponds to several sharp peaks observed in the dQ/dV versus V plot as shown in Fig. 5-43. The sharp peaks observed in the dQ/dV versus V plot can be attributed to the first order phase transformation of the material during charging or discharging [23]. The peaks observed at 3.65V, 4.03V and 4.18V can be assigned to the coexistence of the first hexagonal phase and the monoclinic phase (H_1+M), the monoclinic phase and the second hexagonal phase (M+H_2), and the second hexagonal phase along with the third hexagonal phase (H_2+H_3) respectively as reported in the literature [21,24-26]. By comparing the dQ/dV versus V plots of the low defect concentration $LiNiO_2$ and a high defect concentration $LiNiO_2$ reported earlier (in section 5.8), the misposition of Ni on Li site is obvious. The high defect concentration $LiNiO_2$ thus did not exhibit the characteristic phase transformations (see Fig. 5-33) due to the pillaring effect of Ni^{2+} on Li^+ sites as discussed earlier.
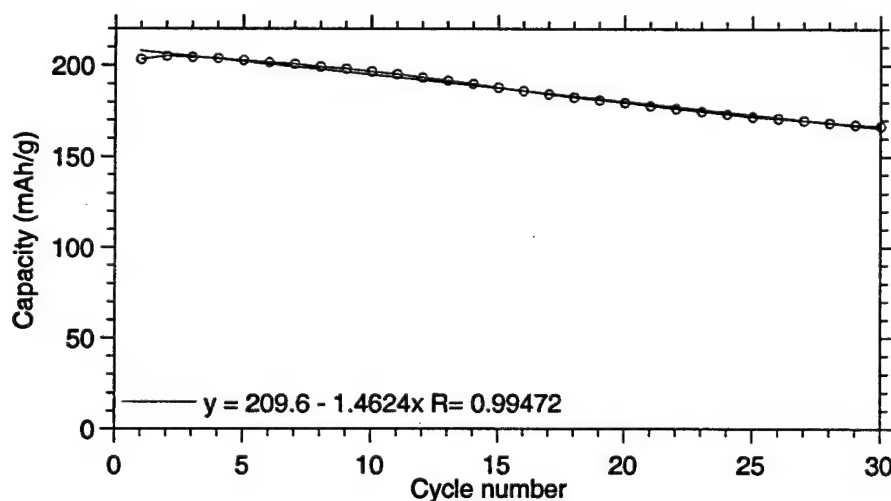
Fig. 5-41. The capacity versus cycle plot of the first 30 cycles for $LiNiO_2$ synthesized using the xerogel generated by the rotary evaporation process.
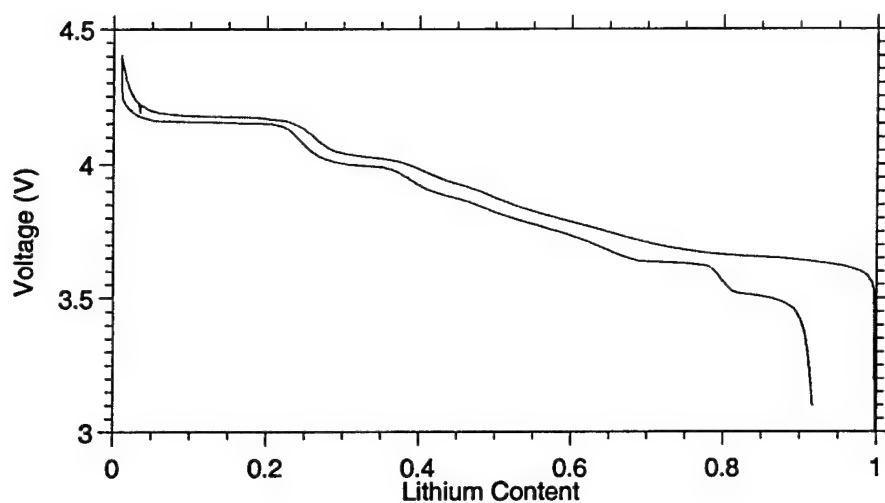
Fig. 5-42. The first cycle voltage versus Li content plot for the low defect concentration LiNiO$_2$. A very small current density of $10\mu A/cm^2$ which corresponds to a C-rate of ~C/100 was utilized for this test electrode.
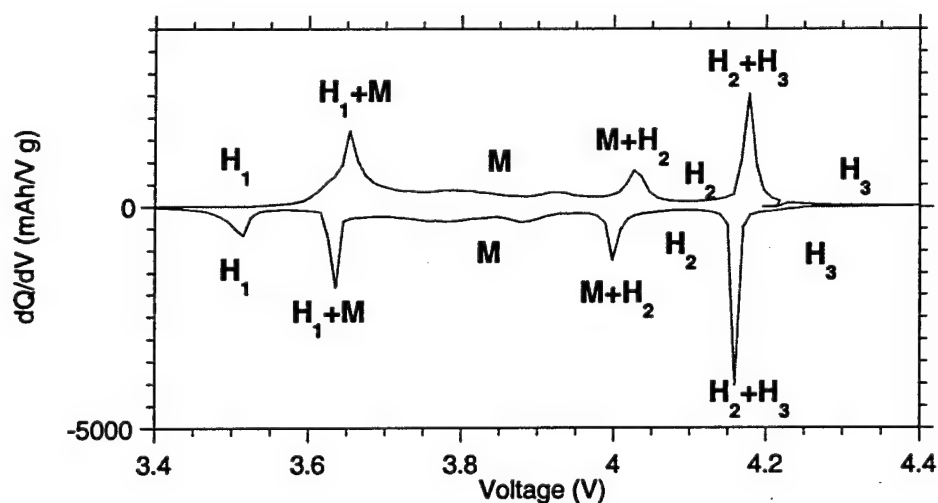
Fig. 5-43. The differential capacity dQ/dV versus V plot for the same battery tested above in Fig. 5-42. Sharp peaks observed in the figure can be attributed to the characteristic first order phase transition of the material during cycling.

123

5.11 Rate capability of defect free LiNiO$_2$ versus the heat treatment time:

The results so far have discussed the influence of defect concentration and residual lithium carbonate on the electrochemical property of the synthesized LiNiO$_2$. However, the electrochemical response is also dependent on the microstructure of the synthesized oxide. Thus, morphology, specific surface area, crystallite size, particle size distribution and impurities can also be important in governing the performance of the material. These aspects though important are only secondary in nature and become relevant only when the desired stoichiometry, point defect and crystal structure is attained. The previous section discussed the methodology developed to synthesize phase pure LiNiO$_2$ with minimum defect concentration. In the following section, the influence of crystallite size on the electrochemical activity has been elucidated.

One of the most important properties of the LiMO$_2$ (M=Co, Ni, Ni$_x$Co$_{1-x}$...etc.) type oxides that directly limits its practical application is their rate capability. This is particularly important for obtaining the high power output desired for their application in electric vehicles. As discussed earlier in the background section, the size of crystallites potentially influence the rate capability of the material due to the slow diffusion of lithium in the bulk. Solid state processes involve prolonged heat treatments at high temperature that favor growth of large crystallites. The PSG process studied here allows the flexibility to have some control over the growth of the crystallites due to the controlled variation of the heat treatment time. An added advantage is the ability to achieve stoichiometric LiNiO$_2$ with minimum defect concentration in significantly shorter periods of time as opposed to conventional solid state methods. Thus better control on growth of the crystallites can be achieved. In order to identify the effect of crystallite size on the rate capability of the materials, a set of experiments were conducted to only vary the size of the crystallites while controlling the following factors:

1. Constant defect concentration
2. Minimization of phase impurities such as lithium carbonate
3. Constant particle size
4. Maintaining a constant surface area of the powders
5. Maintaining a constant powder morphology

In order to control all these factors, $LiNiO_2$ powders were synthesized using the following synthetic protocol. The as-prepared powders generated from the rotary evaporation process (starting Li:Ni= 1.05:1) were first decomposed in the box furnace in air at 700°C for 2 hours. The decomposed powders were then separated into three batches that were heat treated again separately in the tube furnace under flowing oxygen for 5, 15 and 30 hours at 750°C. All these heat treatments were conducted on the same batch of as-prepared powders. This was done in order to maintain constant reaction kinetics of formation of $LiNiO_2$ and a constant particle morphology of the oxide. Heat treatments were conducted in oxygen in order to control the defect concentration as well as the phase purity. The synthesized powders were all sieved through a 300-mesh screen before electrochemical characterization in order to maintain an identical or similar particle size distribution. The surface area of these powders was all within $1m^2/g$ as shown by the BET surface area measurements. All these factors were thus controlled leaving the crystallite size to be the only variant that was altered by varying the heat treatment time.

The phase purity as well as the defect concentration of the powders that were heat treated in oxygen for 5, 15 and 30 hours was first analyzed using XRD. The results of Rietveld refinement on the X-ray diffraction patterns of these heat treated powders are shown in Fig. 5-44 and Table 5-9 respectively. From Table 5-9 it is clear that the defect concentrations of these three samples are quite small (< 2%). However, the sample that was heat treated for 5 hours only shows a slightly higher defect concentration in comparison to the samples that were heat treated for 15 and 30 hours. It should be noted that the lattice parameters and unit cell volume increase with increase in the defect concentration. This observation is consistent with the results reported in the literature and thus justifies the accuracy of the present refinement result. The result can also be rationalized on the basis that the insertion of more Li atoms between the NiO_2^- slabs (less defect concentration), causes the formation of more Ni^{3+} cations leading to a decrease in the lattice parameters.

The morphology of the samples heat treated for 5, 15 and 30 hours is shown in Fig. 5-45. All micrographs were taken at the same magnification for comparison.
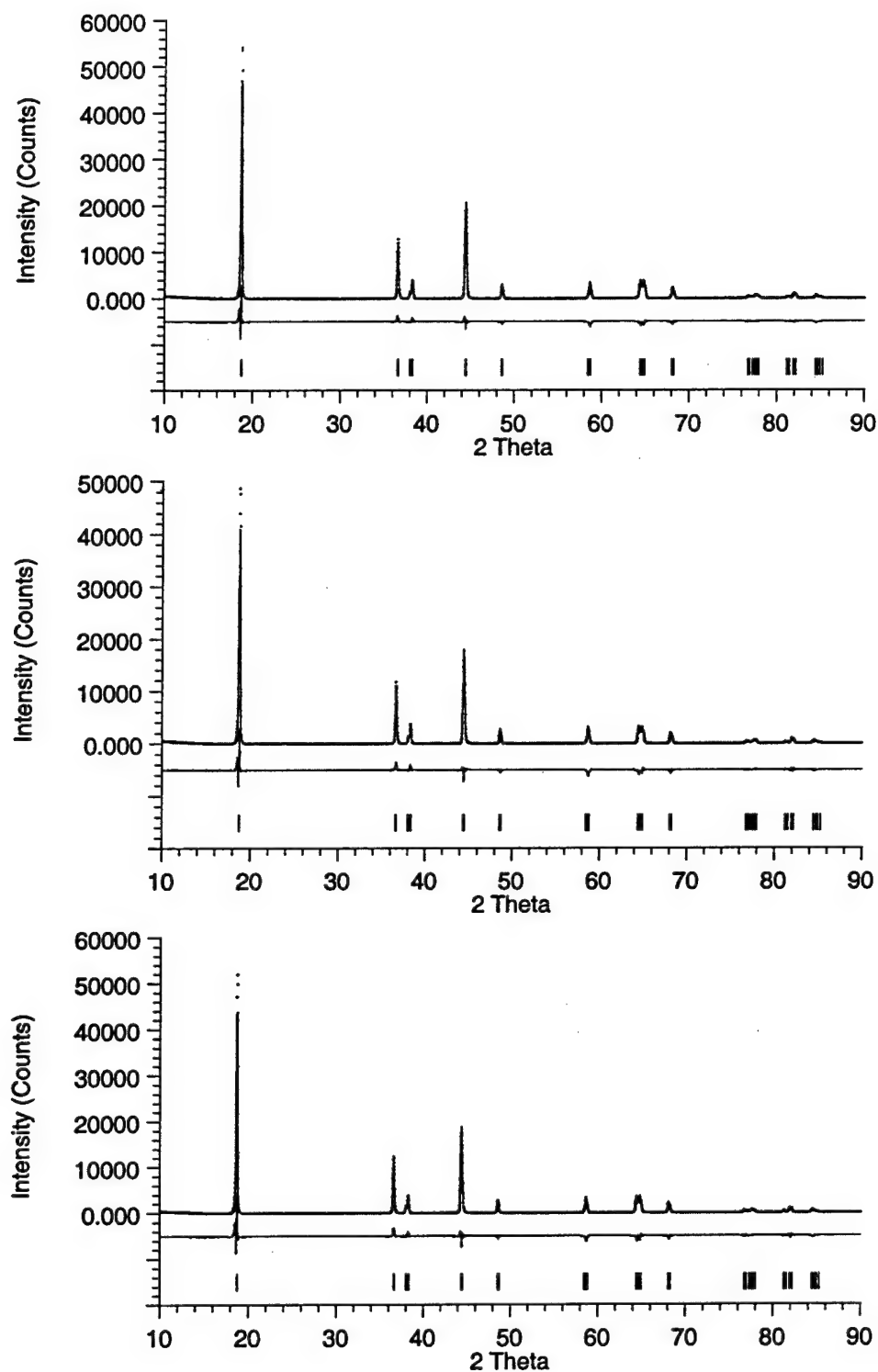
Fig. 5-44. The results of Rietveld refinement conducted on the X-ray diffraction patterns of the powders that were heat treated in oxygen for 5, 15 and 30 hours under oxygen atmosphere.

126

Table 5-9. A summary of the Rietveld refinement results obtained for the powders that were heat treated under oxygen for 5, 15 and 30 hours.

5 hours	Site occupancy	
	O	1.0000
	Ni	1.0000
	Li	0.9899
	Ni on Li site	0.0101
	Lattice parameters	
	$a\,(\overset{o}{A})$	2.87562
	$c\,(\overset{o}{A})$	14.20137
	Cell volume $(\overset{o}{A}^3)$	101.7007
	Refinement quality indicator	
	Rwp%	12.48
15 hours	Site occupancy	
	O	1.0000
	Ni	1.0000
	Li	0.9945
	Ni on Li site	0.0055
	Lattice parameters	
	$a\,(\overset{o}{A})$	2.87407
	$c\,(\overset{o}{A})$	14.19044
	Cell volume $(\overset{o}{A}^3)$	101.5129
	Refinement quality indicator	
	Rwp%	14.74
30 hours	Site occupancy	
	O	1.0000
	Ni	1.0000
	Li	0.9943
	Ni on Li site	0.0057
	Lattice parameters	
	$a\,(\overset{o}{A})$	2.87615
	$c\,(\overset{o}{A})$	14.19559
	Cell volume $(\overset{o}{A}^3)$	101.6968
	Refinement quality indicator	
	Rwp%	15.73

(a)

(b)

(c)

128
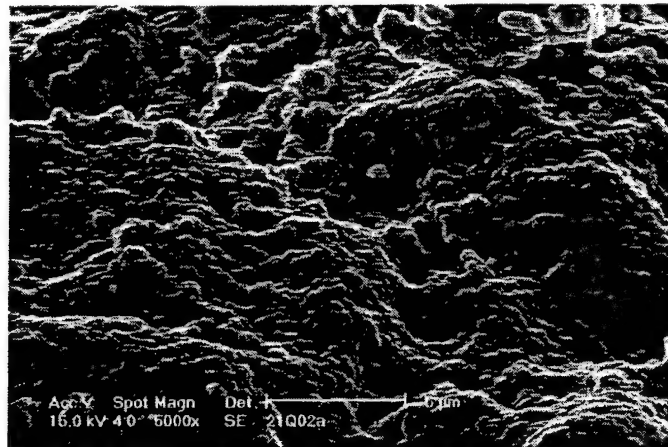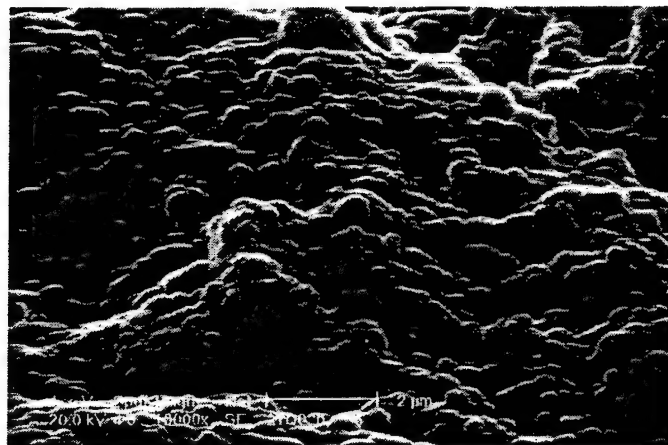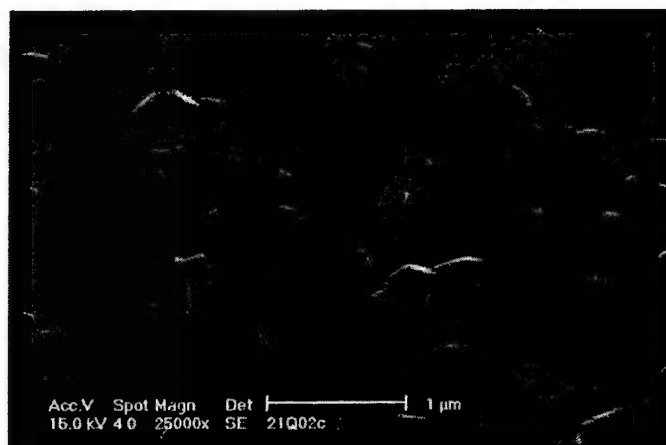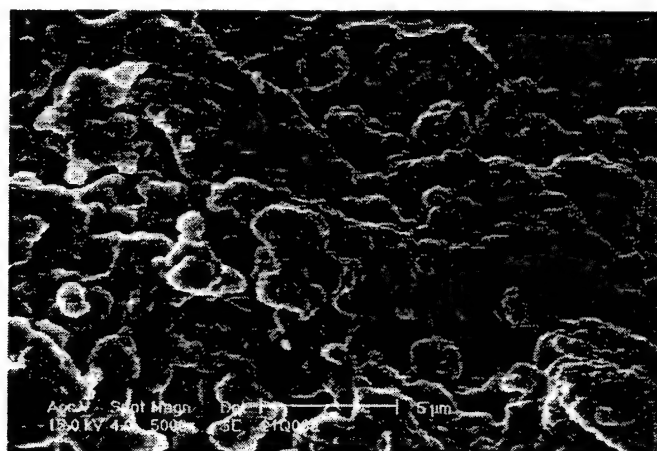
(d)
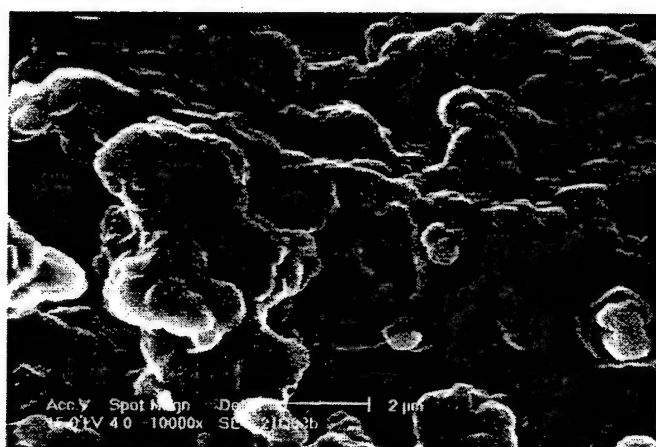
(e)
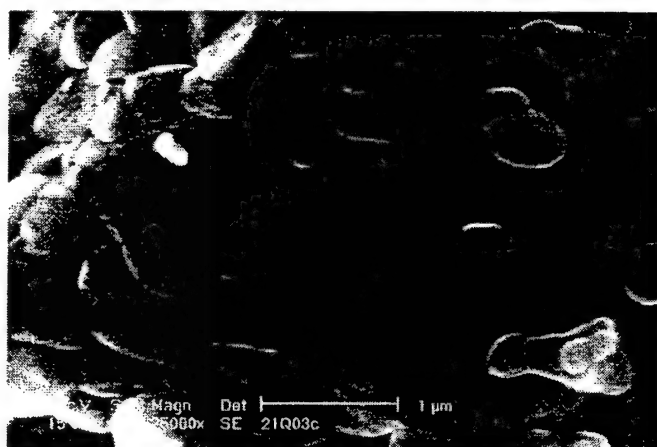
(f)
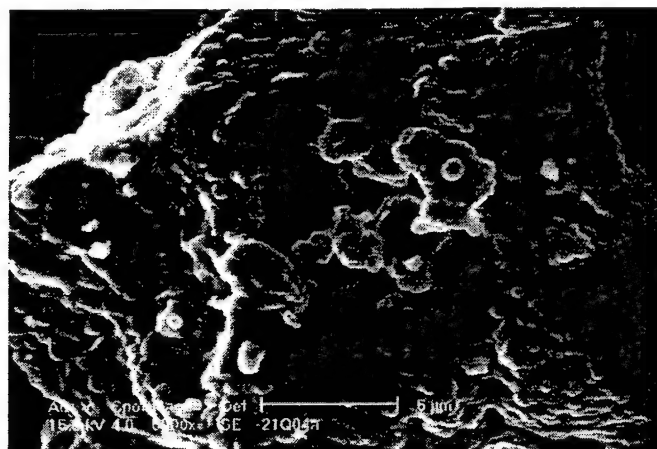
(g)

(h)
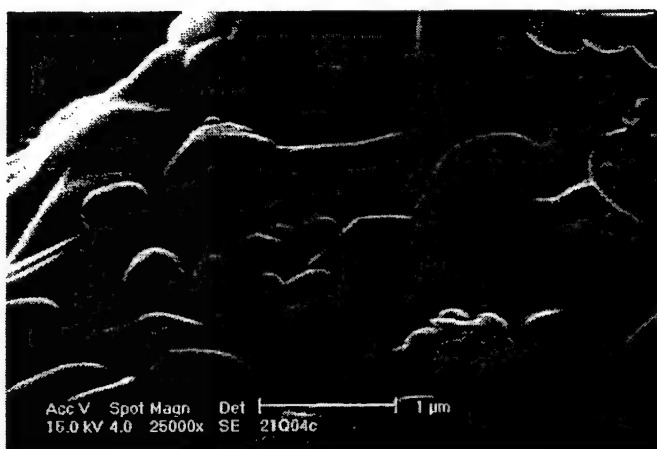
(i)

Fig. 5-45. The morphology of the samples heat treated for 5h ((a)~(c)), 15h ((d)~(f)) and 30h ((g)~(I)). Each set of micrographs represent a magnification of 5k, 10k and 25k respectively. All micrographs were taken at the same magnification for comparison.

130

It is clear that the size of the crystallites increase with the increase of heat treatment time. The size of the crystallites increase from ~0.5μm for the sample heat treated for 5 hours to ~2μm for the sample heat treated for 30 hours. A more accurate measurement of the average crystallite size of materials heat treated for different period of time was conducted by using the SEM images from 4 different regions for each material at the same magnification (20kX). For each SEM image, the average crystallite size was measured using the following equation [27]:

$$D = \Sigma L / N \tag{5.13}$$

Where 'D' is the average crystallite size, 'L' is the total length of the segment intersecting the grains (usually 4 lines were employed for each picture) and N is the number of crystallites intersected by the line. The overall average crystallite size is finally obtained by averaging the average sizes obtained from the four SEM pictures taken for the oxide after each heat treatment time. Thus, a total of 16 lines spanning (~200 grains) for each heat treatment time used was utilized for obtaining the average crystallite size. The resultant plot of the crystallite size versus heat treatment time is therefore shown in Fig. 5-46. The influence of increase in the crystallite size on the electrochemical property will be discussed in the following section.

The electrochemical property of the materials that were heat treated for 5, 15 and 30 hours was evaluated using different current densities ranges from 10 μA/cm^2 to 5 mA/cm^2. All the test electrodes were chosen to have very similar weight (0.0055g ± 0.0001g) to avoid different extents of polarization caused by differences in the weight of the electrode. Fig. 5-47 shows the capacity versus current density for the three sets of materials that were heat treated at 750°C for 5, 15 and 30 hours respectively. It can be clearly seen that the capacity of each set of materials drops with an increase in the current density owing to the increase in polarization. Furthermore, at the same current density, the materials heat treated for a longer time always show lower capacities (~10% drop in capacity of the sample heat treated for 30 hours for each current density compared to the material heat treated for 5 hours). This general trend is reflected even more clearly in the plot of the capacity versus heat treatment time shown in Fig. 5-48. The drop in capacity can be attributed to the increase in the crystallite size and the corresponding diffusional distances that is proportional to the heat treatment time.
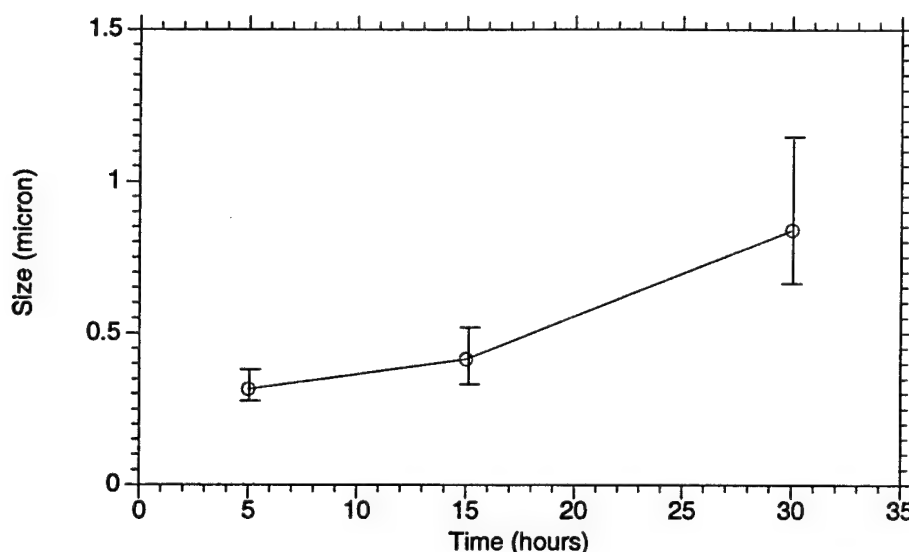
Fig. 5-46. Plot of crystallite size with heat treatment time showing a growth in the crystallite with heat treatment time. The crystallites grow from ~0.4μm size for the sample heat treated for 5 hours to ~1μm for the sample heat treated for 30 hours.

Fig. 5-49 shows the differential capacity dQ/dV versus V curves for the second cycle obtained for the three sets of samples that were heat treated for the three different time periods. A current density of 0.5mA/cm^2 corresponding to a C-rate of C/2 was utilized for the battery test. Apparently, all these three samples show very similar behavior. This can be attributed to the relatively small capacity difference in the three materials (~10% capacity difference). However, there is still a general trend that can be observed. At most of the voltages corresponding to the phase transitions, the sample heat treated for 5 hours shows a slightly higher peak intensity than the sample heat treated for 15 and 30 hours respectively. The slightly higher peak intensity for only the sample heat treated for 5 hours compared to those heat treated for 15 and 30 hours actually suggests an increase in the polarization caused by an increment in the crystallite size. The reduction in capacity with the increase in the crystallite size can be attributed to a decrease in the grain boundary surface area with the increase in heat treatment time thus increasing the diffusion distances. Thus the diffusion distance for lithium in the samples heat treated for 30 hours is much larger than the samples heat treated for 5 hours resulting in higher capacity for the same current settings.
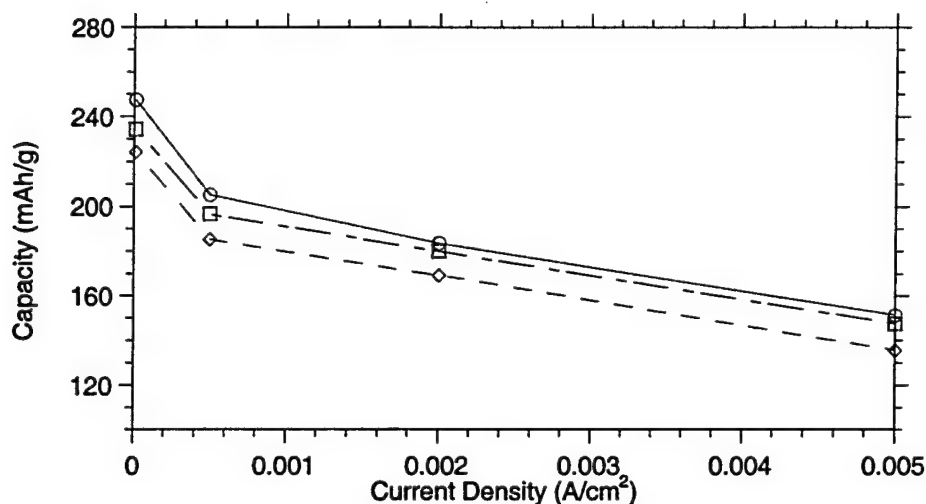
Fig. 5-47. Plot showing the variation of the capacity versus current density for the three sets of materials that were heat treated at 750°C for 5 (o), 15 (□) and 30 (◊) hours respectively.
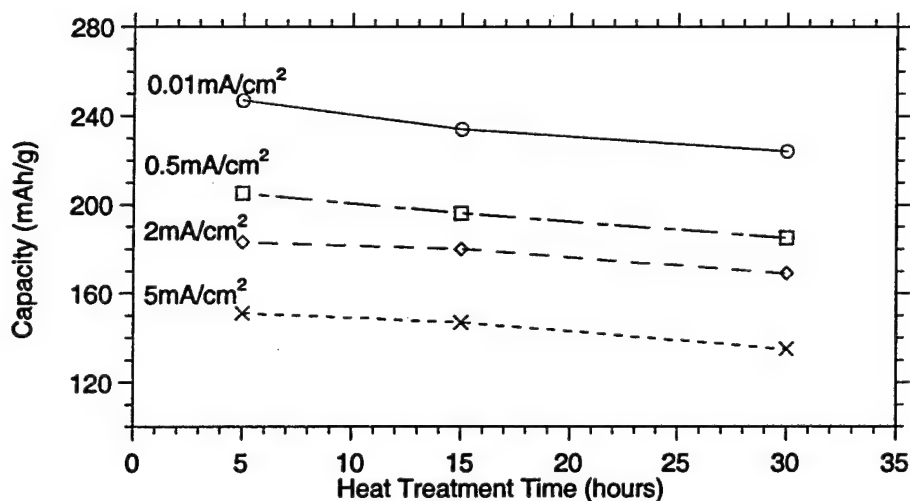
Fig. 5-48. Plot of the capacity versus heat treatment time. Four different current densities ($10\mu A/cm^2$, $500\mu A/cm^2$, $2mA/cm^2$, $5mA/cm^2$) were used for the battery tests. The drop in capacity can be attributed to the increase in crystallite size that is proportional to the heat treatment time.
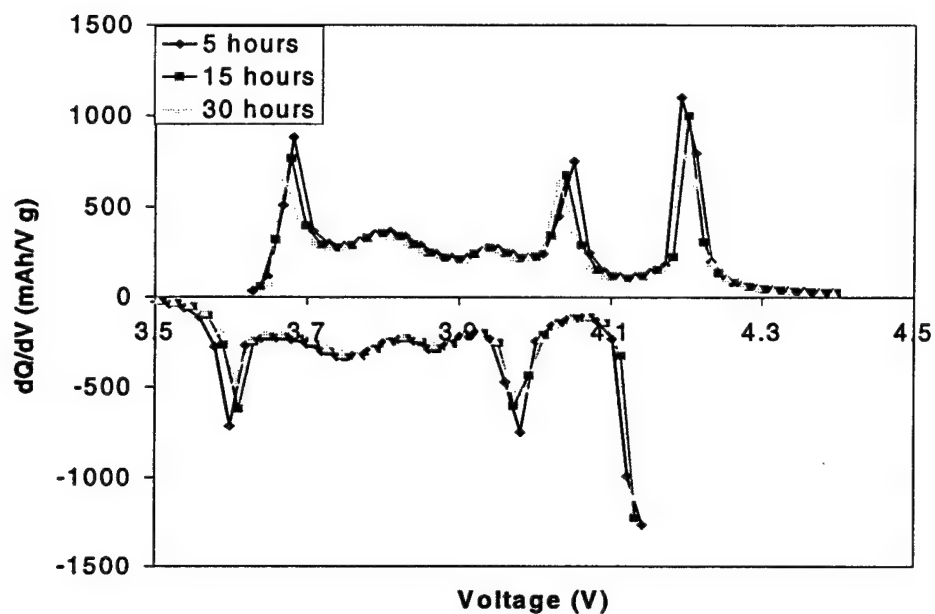
Fig. 5-49. The first cycle differential capacity dQ/dV versus V curves for the three sets of samples that were heat treated for the three different time periods. A current density of 0.5mA/cm^2 corresponding to a C-rate of C/2 was utilized for the battery tests.

5.12 Factors that influence the electrochemical property of the batteries comprising the $LiMO_2$ (M = Ni, $Ni_{0.75}Co_{0.25}$) cathode materials:

The entire electrochemical tests reported so far were based on the cut off voltages for each cycle of the test batteries being set at 4.4 and 3.1V versus lithium. Furthermore, the observed voltage is a summation of the open circuit voltage (equilibrium voltage) and the excess voltage arising from the internal resistance of the cathode shown by the following equation:

$$V_{measured} = V_{open\ circuit} + V_{IR} \qquad (5.9)$$

Based on the results so far, it is possible to discuss the important factors influencing the electrochemical property of the cathode materials. These factors can actually be tested as those that contribute to the internal resistance of the battery owing to the cathode materials.

According to the analysis so far, the contributions of each factor discussed earlier can be ranked based on their ability to increase the internal resistance of the cathode. In this regard, the effect of defect concentration would be the most important factor. If the material has a high defect concentration, it will no longer be electrochemically active. The second important factor contributing to the internal resistance is the phase impurity. The existence of impurity phase such as lithium carbonate can not only decrease the capacity of the material owing to its mass, but also interfere with the diffusion of Li into the electrolyte thereby increasing the polarization loss. Finally, the size of crystallites can also influence the electrochemical property of the material owing to its contribution to polarization as a result of the large diffusion distances with the increase in crystallite size. This aspect thus justifies the motivation for developing more efficient precursors for synthesizing $LiMO_2$ compounds in short time.

5.13 Mechanism of formation of LiNiO$_2$:

1. *Formation of lithium carbonate and nickel oxide after decomposition:*

This section discusses the reaction mechanisms involved in the formation of LiNiO$_2$. The structural and thermal analysis of the xerogels had indicated that the xerogels decompose on heat treatment at 300°C to yield Li$_2$CO$_3$ and NiO. However, the exact mechanism of this reaction is unclear. This section will highlight the details of this study. From the XRD data of the xerogels prepared by rotary evaporation and spray drying processes heat treated at 300°C for 5 hours as shown in Fig. 5-2 and 5-9, lithium carbonate and nickel oxide are the only products formed after the decomposition reaction. Since the XRD data was not obtained under dynamic conditions, formation of LiNiO$_2$ via the reaction between lithium carbonate and nickel oxide would have to be further examined and confirmed. The following evidences and experiments are used to confirm the formation of LiNiO$_2$ via the reaction between lithium carbonate and nickel oxide after the decomposition of xerogel is completed.

The first evidence comes from the weight loss observed from the TGA analysis. Recall the reaction shown by equation 5.2 in section 5.1:

$$xLiOH + (1-x)/2\ Ni(OH)_2 +$$

$$(1-x)LiOAc + (1+x)/2\ Ni(OAc)_2 \xrightarrow{\hspace{1.5cm}} 1/2\ Li_2CO_3 + NiO + gases \qquad (5.2)$$

$$44.2\%\ \text{weight loss (Calculated)}$$
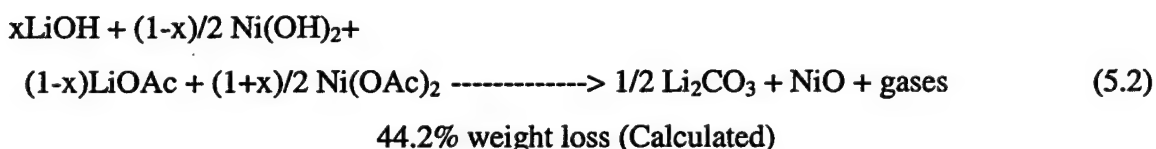
If the formation of LiNiO$_2$ proceeds via the subsequent reaction between Li$_2$CO$_3$ and NiO obtained after decomposition, the weight loss observed for this latter reaction can be calculated as:

$$NiO + 1/2\ Li_2CO_3 + 1/4\ O_{2(g)} \xrightarrow{\hspace{1cm}} LiNiO_2 + 1/2\ CO_{2(g)} \uparrow \qquad (5.12)$$

$$7.0\ \%\ \text{weight loss (Calculated)}$$
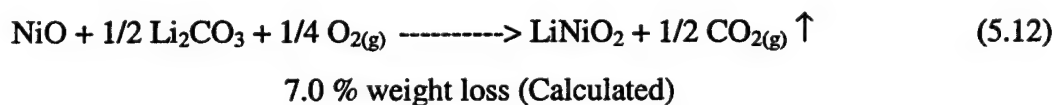
This percentage weight loss is calculated based on the original weight of the xerogel. By comparing the calculated weight loss (7.0%) and the observed weight loss (7.9%, at 800°C) measured by the TGA shown in Fig. 5-1, it is obvious that the decomposition products of the xerogel are indeed lithium carbonate and nickel oxide. It should be mentioned that the observed weight loss is slightly more than the calculated weight loss.

136

This could be attributed to the decomposition of LiNiO$_2$ as has been discussed earlier in section 5.10.

The second evidence comes from the in-situ evolved gas analysis conducted using the TG/MASS spectrometer. The evolution of carbon dioxide during heat treatment detected by the mass spectrometer is shown in Fig. 5-50.
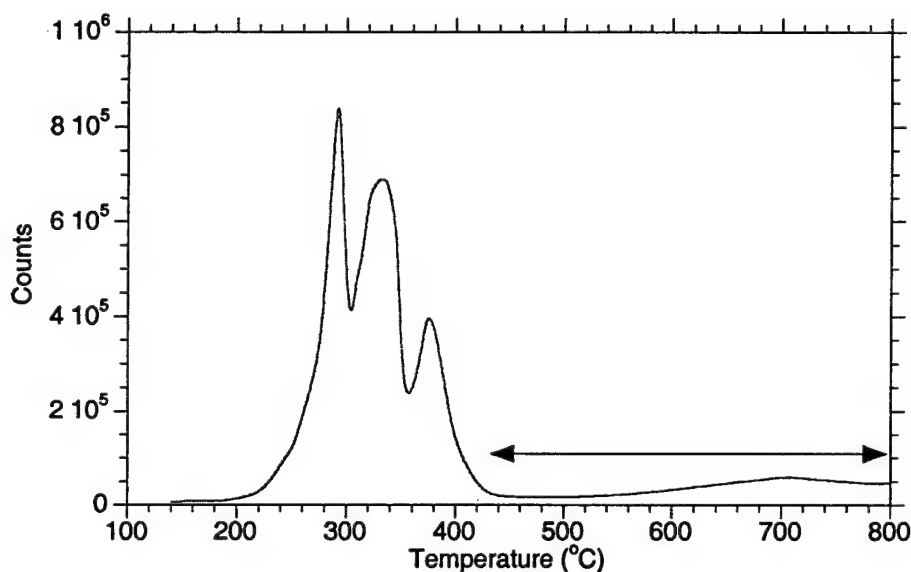
Fig. 5-50. The evolution of carbon dioxide during heat treatment detected by the mass spectrum.

A continuous evolution of carbon dioxide is observed even after decomposition. This observation is a confirmation of LiNiO$_2$ formation proceeding via the reaction between lithium carbonate and nickel oxide with the evolution of carbon dioxide. Thus, the reaction between the porducts of decomposition of the xerogel seen in the XRD patterns (refer to Fig. 5.2) is confirmed.

2. *Does lithium nickel oxide form via direct single step or a multi-step reaction?*

According to the conclusion of the earlier section, the overall reaction between lithium carbonate and nickel oxide to form lithium nickel oxide can always be written as:

$$2NiO + Li_2CO_3 + 1/2\ O_{2(g)} \text{-----------> } 2LiNiO_2 + CO_{2(g)} \uparrow \qquad (5.14)$$

137
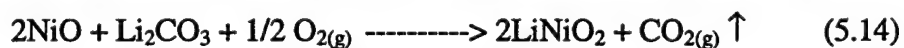
However, it is also possible for the above reaction to proceed via two steps:

$$Li_2CO_3 \longrightarrow Li_2O + CO_{2(g)}\uparrow \qquad (5.15)$$

$$1/2\ O_{2(g)} + Li_2O + 2\ NiO \longrightarrow 2\ LiNiO_2 \qquad (5.16)$$
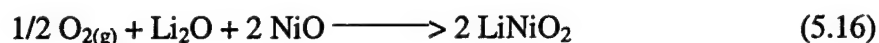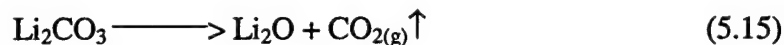
The major factor distinguishing the "direct" and "multi-step" reaction is whether the decomposition of lithium carbonate occurs before its reaction with nickel oxide or during its reaction with nickel oxide. Before investigating the exact mechanism of the reaction between lithium carbonate and nickel oxide formed after decomposition of the xerogel, to form lithium nickel oxide, it would be necessary to determine the feasibility of a 'direct' or a 'multi-step' reaction for the formation of lithium nickel oxide.

In order to answer this question, it is necessary to examine the validity of the separate reactions proposed above. The decomposition of lithium carbonate to form lithium oxide with the evolution of carbon dioxide was monitored by the TGA/Mass Spectrometer. Commercially obtained lithium carbonate was heat treated in the TGA/MS unit in air using a heating rate of $10^\circ C/min$. Fig. 5-51 shows the weight loss of lithium carbonate measured by TGA along with the evolution of carbon dioxide detected by the mass spectrometer. This result confirms the decomposition of Li_2CO_3 at $\approx 725^\circ C$ to form lithium oxide with the evolution of carbon dioxide (Details can be referred to Appendix B).

The possibility of direct reaction between Li_2O and NiO to form $LiNiO_2$ is also examined using TGA. Nickel oxide was synthesized by heat treating commercially obtained nickel hydroxide in air at $800^\circ C$ for 2 hours. The details of the synthesis protocols are shown in Appendix B. The as-synthesized nickel oxide was mixed with stoichiometric amount of commercially obtained lithium oxide (Aldrich, 98%) using mortar and pestle. The TGA analysis of this Li_2O-NiO mixture is shown in Fig. 5-52. The on-set of weight gain is seen at $\sim 450^\circ C$ suggesting that the direct reaction between lithium oxide and nickel oxide is possible. Based on this, it can be concluded that it is possible to form lithium nickel oxide via the reaction between nickel oxide and lithium oxide obtained from the decomposition of lithium carbonate.

Fig. 5-51. The weight loss of lithium carbonate measured by TGA with the evolution of carbon dioxide detected by the mass spectrum.
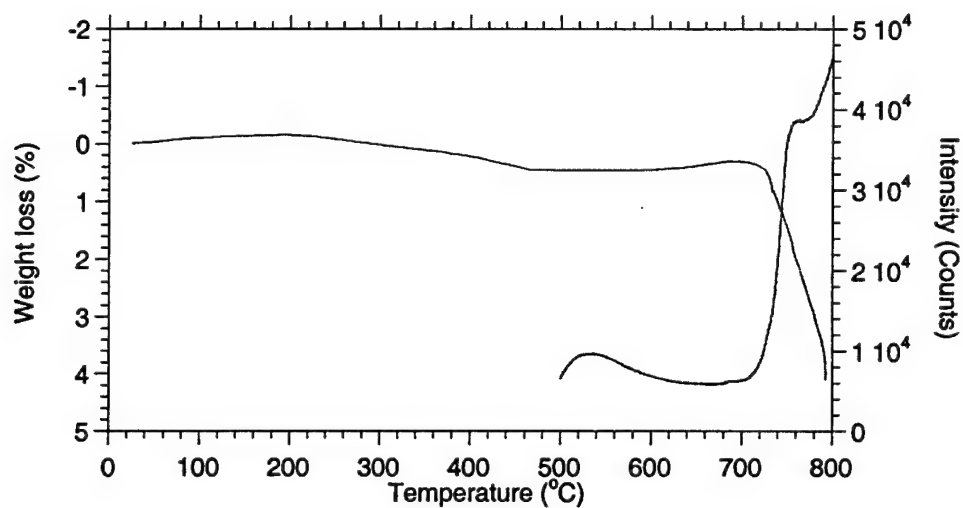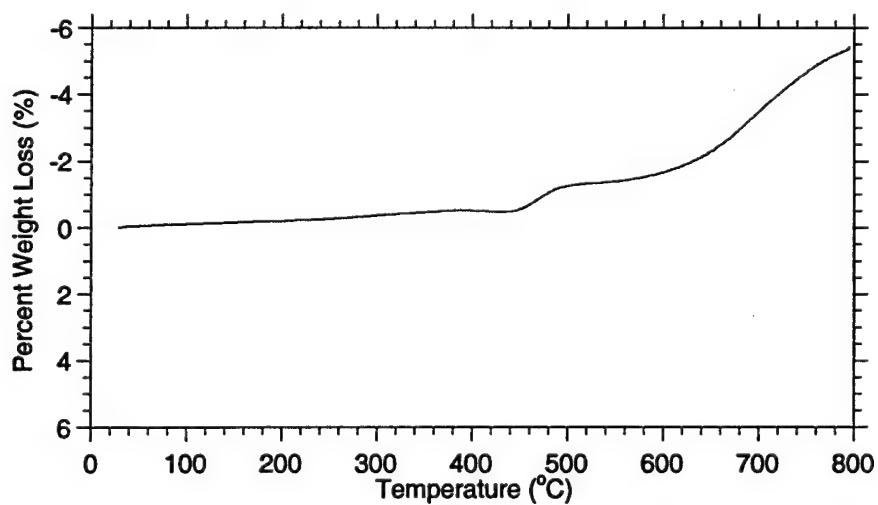

Fig. 5-52. The TGA analysis conducted on the Li_2O-NiO mixture. A weight gain started at ~450°C suggests that direct reaction between lithium oxide and nickel oxide is possible.

Another set of experiments were also designed to be executed in the TGA unit for the purpose of understanding whether lithium carbonate can directly react with nickel oxide. The proposed concept is that if the reaction between lithium carbonate and nickel oxide should proceed via the formation of lithium oxide, the amount of lithium nickel oxide formed would depend on the formation of lithium oxide. In other words, if the kinetics of consumption observed of lithium carbonate is larger in the case of Li_2CO_3+NiO mixture, we can conclude that the direct reaction between lithium carbonate and nickel oxide is possible. The analytical basis for identifying this mechanism is shown below:

The decomposition of lithium carbonate can be written as:

Li_2CO_3------------> Li_2O + CO_2

-dm/dt   +dm/dt   +dm'/dt

$dW\%/dt = \{-74 \times [dm/dt] + 30 \times [dm/dt]\} / Wi \times 100\%$
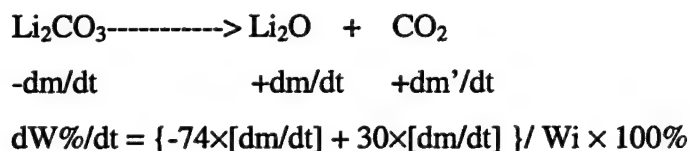
Rearrangement of this equation, gives:

$dm/dt = -(100\% \times Wi \times dW\%/dt)/44$

"m" represents mole, "t" represents time, Wi and W% represent initial sample weight and percent weight change respectively. Similarly, the reaction of lithium carbonate and nickel oxide can be written as:

$1/2\ Li_2CO_3$ + NiO + $1/4\ O_2$ ------------> $LiNiO_2$ + $1/2\ CO_2$

-1/2[dm'/dt]   -dm'/dt   -1/4[dm'/dt]   +dm'/dt   +dm'/dt

$dW'\%/dt = \{-37 \times [dm'/dt] - 75 \times [dm'/dt] - 8 \times [dm'/dt] + 98 \times [dm'/dt]\} / Wi' \times 100\%$
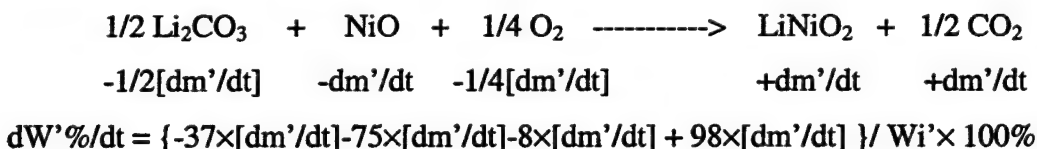
Rearrangement of this equation, gives:

$dm/dt = -(100\% \times Wi' \times dW'\%/dt)/22$

The TGA analysis of lithium carbonate decomposition is shown in Fig. 5-53(a). At the same time, the TGA analysis of the lithium carbonate-nickel oxide mixture is shown in Fig. 5-53(b). In order to compare the two reactions, the rates dm/dt and ½(dm'/dt) were determined. The corresponding dm/dt and ½(dm'/dt) plots are shown in Fig. 5-53(c). It should be noticed that the TGA analysis is conducted in air using a constant heating rate of 10°C/min to 800°C. By comparing dm/dt and ½(dm'/dt), it is obvious that the kinetics of lithium carbonate decomposition is faster in the case of the Li_2CO_3-NiO mixture. It is also possible based on the above data that the enhanced

140
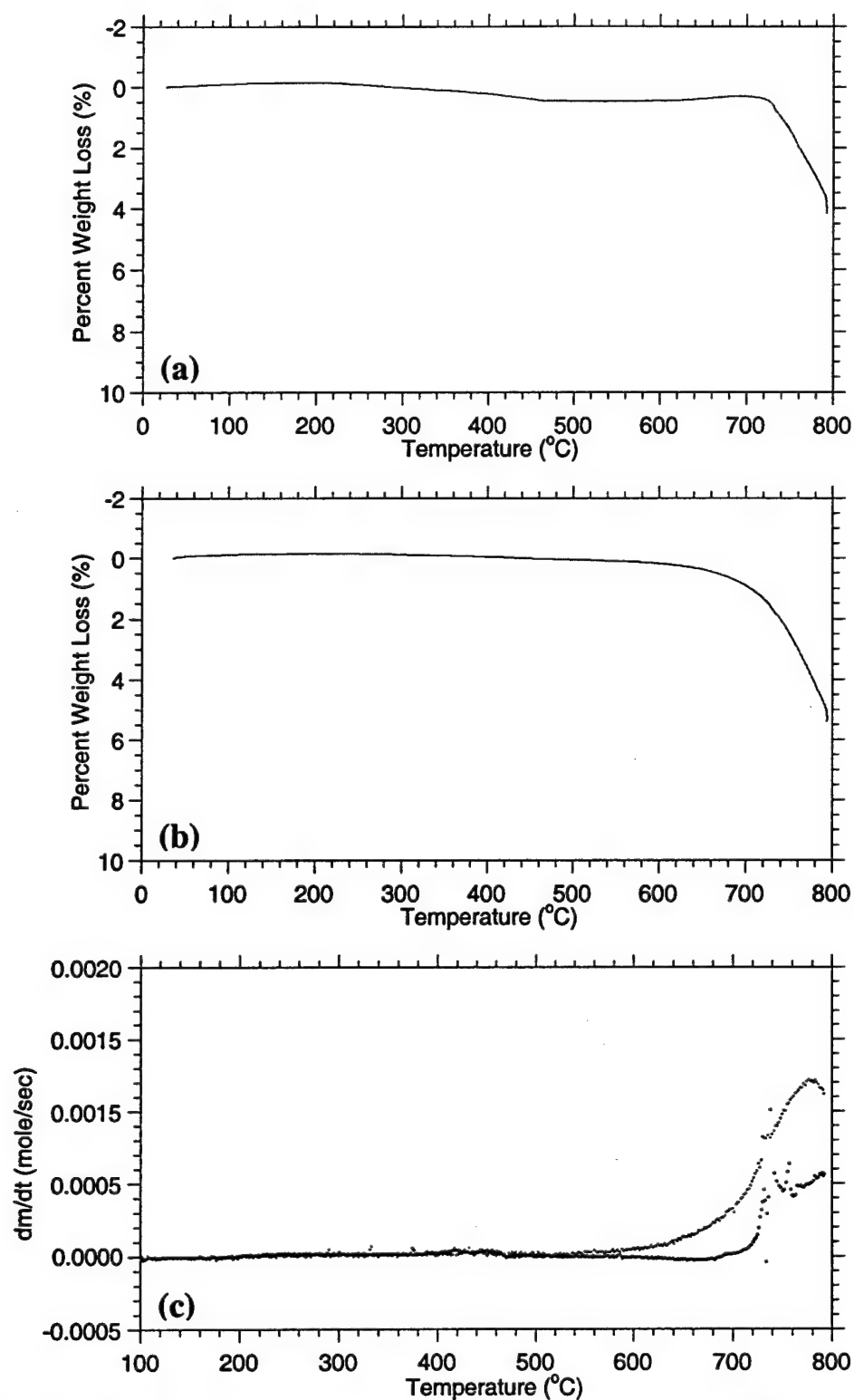
Fig. 5-53. (a) The TGA analysis of lithium carbonate decomposition. At the same time, the TGA analysis of lithium carbonate-nickel oxide mixture is also shown in (b). The corresponding ½(dm'/dt) (the top curve) and dm/dt (the bottom curve) is shown in (c).

141

decomposition of lithium carbonate to form Li_2O could be catalyzed by the presence of nickel oxide. However, if we consider the direct reaction between lithium oxide and nickel oxide as shown in Fig. 5-52, the reaction appears to begin at a temperature of ~450°C which is much lower than the temperature at which the reaction occurs in the Li_2CO_3-NiO mixture (>550°C). Thus, it is highly improbable that lithium oxide could form initially and remain stable without reacting with nickel oxide. Based on this argument one can conclude that lithium carbonate directly reacts with nickel oxide.

3. *Exact mechanism responsible for the formation of LiNiO₂ via the reaction of lithium carbonate and nickel oxide obtained by decomposing the xerogel derived by the rotary evaporation process:*

The experiments conducted so far on commercial Li_2CO_3, $NiO+Li_2O$, $NiO+Li_2CO_3$ mixtures suggest that a direct reaction between lithium 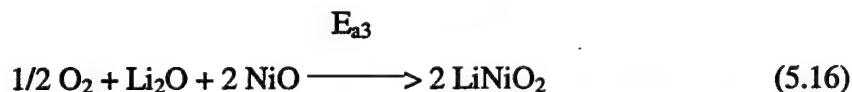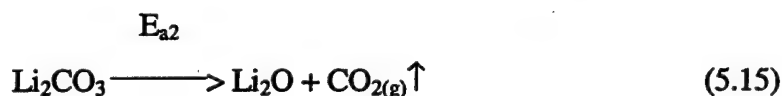carbonate and nickel oxide is possible. The question now however, is to provide direct quantitative evidence for a similar reaction between lithium carbonate and nickel oxide formed after decomposition of the xerogel. In order to answer this question, the reactions need to be examined more closely. Recall equations (5.14), (5.15) and (5.16):

$$E_{a1}$$
$$Li_2CO_3 + 2NiO + 1/2\ O_2 \ \text{------------->}\ 2LiNiO_2 + CO_{2(g)}\uparrow \qquad (5.14)$$

$$E_{a2}$$
$$Li_2CO_3 \longrightarrow Li_2O + CO_{2(g)}\uparrow \qquad (5.15)$$

$$E_{a3}$$
$$1/2\ O_2 + Li_2O + 2\ NiO \longrightarrow 2\ LiNiO_2 \qquad (5.16)$$
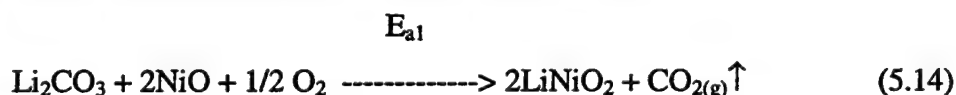
In the case of reaction (5.15), a weight loss should be observed while the reaction proceeds. As a result, the differential weight change (dM/dT, 'M' represents mass and 'T' represents temperature) of reaction (5.15) should possess a peak that is negative in sign as the reaction progresses. For similar reason, the differential weight change of reaction (5.16) should exhibit a peak that is positive in sign but smaller in the magnitude than reaction (5.15) as the reaction progresses. If the differential weight change of these two reactions between lithium carbonate and nickel oxide possesses two distinguishable

peaks, the negative peak can always be attributed to reaction (5.15) and the positive peak to reaction (5.16). However, if the differential weight change between lithium carbonate and nickel oxide exhibits only one peak, then it is clearly indicative of reaction (5.15) and reaction (5.16) occurring at the same time. This is because the superposition of the negative and the positive peaks occurring at the same time (temperature) would reflect a single peak in the differential weight loss plot. Based on this analysis, the reaction between lithium carbonate and nickel oxide produced from the decomposition of the xerogel can be analyzed to identify whether a direct or multi-step reaction is responsible for the formation of lithium nickel oxide.

The differential weight change of the xerogel heat treated in TGA in air using a heating rate of 10°C/min up to 800°C is shown in Fig. 5-54. Only one single symmetric peak is observed in this case. This result clearly implies that lithium carbonate and nickel oxide decomposed from the xerogel undergo a direct reaction leading to the formation of $LiNiO_2$. The term 'direct' reaction used here gives a mechanistic picture of the reaction between nickel oxide and lithium carbonate that react at the same time with the evolution of carbon dioxide. The activation energy of the overall direct reaction will be discussed later in section 5.14.
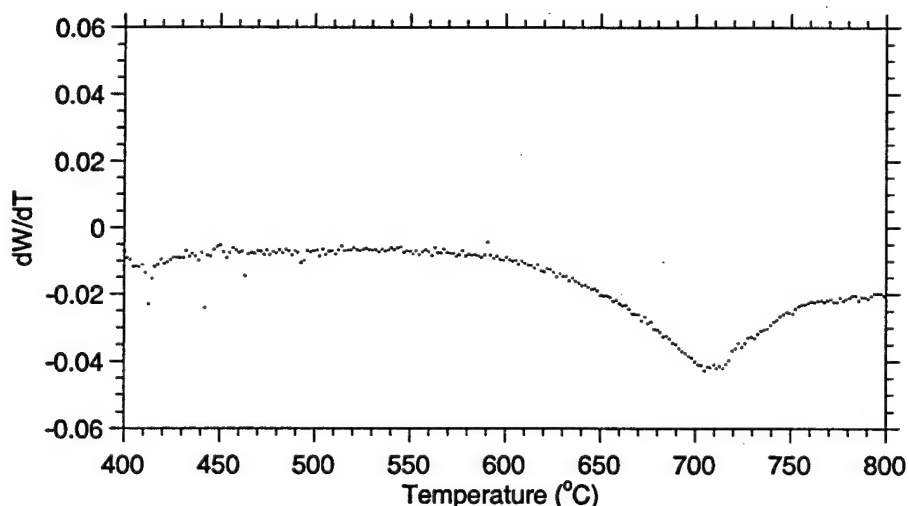

Fig. 5-54. The differential weight change of the xerogel heat treated in TGA unit in air using a heating rate of 10°C/min up to 800°C.

143

4. _Proposed microscopic reaction mechanism for the direct reaction:_

In the present section, the microscopic mechanisms involved in the reaction of lithium carbonate and lithium oxide with nickel oxide will be discussed. This will however require a proper insight into the possible microscopic reaction mechanisms.

Diffusion is one of the key aspects extremely important for any chemical reaction to occur and undergo completion. There are however several diffusional pathways for ion and mass transport to occur. Many reactions proceed via diffusion of lattice defects [28-30]. In other words, the formation of point defects is important for the formation of these compounds. In the case of lithium oxide or lithium carbonate, the chemical species namely, Li_2O, Li_2CO_3 and CO_2 are all rigid valent species whose diffusivities are higher than Ni (because of low atomic or molecular weight). Therefore, the reaction between nickel oxide and lithium oxide (or lithium carbonate) should most likely proceed via diffusion of the lighter chemical species into the heavier nickel oxide. The problem however is to understand how these chemical species enter the nickel oxide lattice?

If the reaction proceeds through the lattice defect of nickel oxide, the reaction kinetics should be proportional to the concentration of lattice defect in nickel oxide. In order to verify the type of defects in nickel oxide, the oxide was first synthesized by decomposing commercially obtained nickel hydroxide in air at 800°C for 2 hours. The results of the characterization of the synthesized nickel oxide and simulation of the structure is shown in Appendix B. From the results of the Rietveld refinement conducted on the synthesized nickel oxide, it is clear that oxygen occupancy is one with a small amount of nickel vacancies suggesting that the synthesized NiO is nearly stoichiometric with 2% Ni vacancies. In order to verify the influence of reaction gas on the defect concentration of nickel oxide, the synthesized nickel oxide was then again heat treated separately in oxygen as well as argon atmosphere at 800°C for 5 hours. The XRD patterns of nickel oxide that was heat treated separately in oxygen and argon are shown in Fig. 5-55 and 5-56 respectively. By inspecting the observed peak intensity and lattice parameter, it is clear that the defect concentration of nickel oxide is independent of the reaction atmosphere. Since the formation of lithium nickel oxide is dependent on the oxygen partial pressure and the lattice defect formation of nickel oxide is independent of oxygen

partial pressure, it is clear that the mechanism of the nickel oxide formation should not rely on the defect concentration (or defect formation) of nickel oxide.
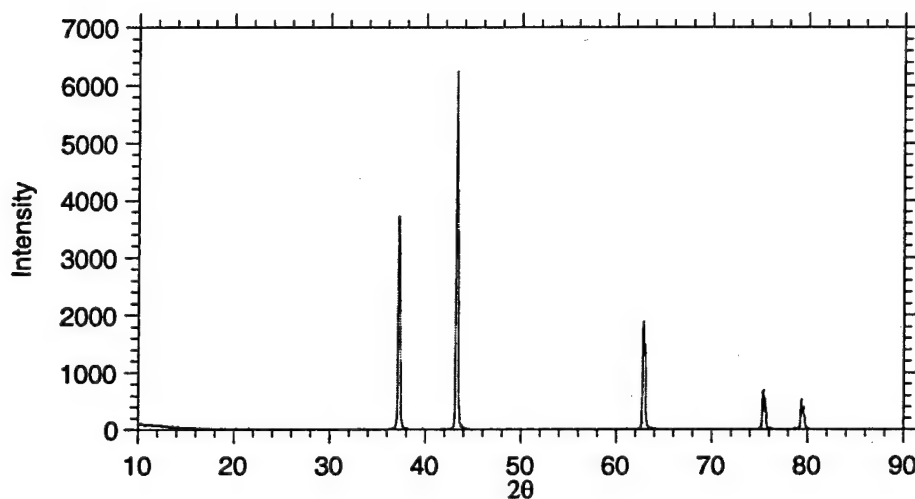

Fig. 5-55. The XRD patterns of nickel oxide that was heat treated in oxygen at 800°C for 5 hours.
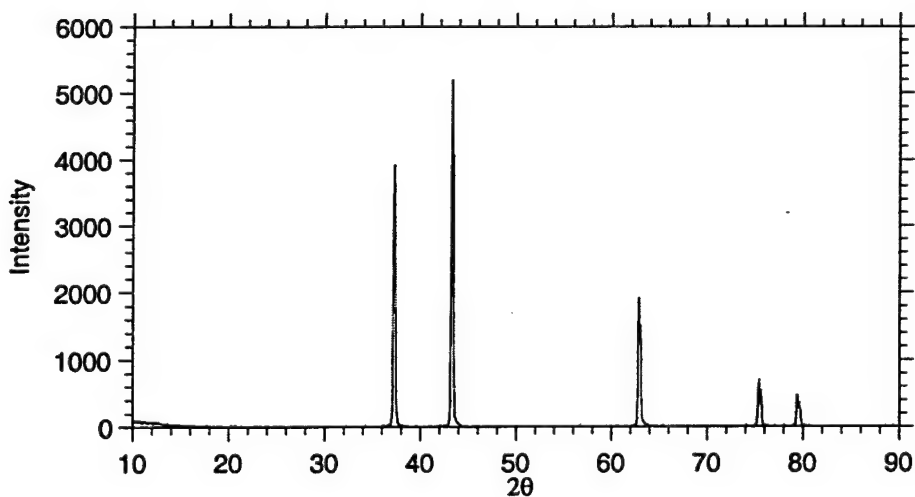
Fig. 5-56. The XRD patterns of nickel oxide that was heat treated in Argon at 800°C for 5 hours.

145

Based on the above arguments, the most plausible reaction mechanism for the formation of lithium nickel oxide via the reaction between nickel oxide and lithium oxide (or lithium carbonate) is the insertion of lithium oxide into the nickel oxide host lattice that is favored by oxygen. Fig. 5-57 shows the crystallographic representation of the most plausible reaction mechanism responsible for the reaction of nickel oxide and lithium oxide to form lithium nickel oxide.
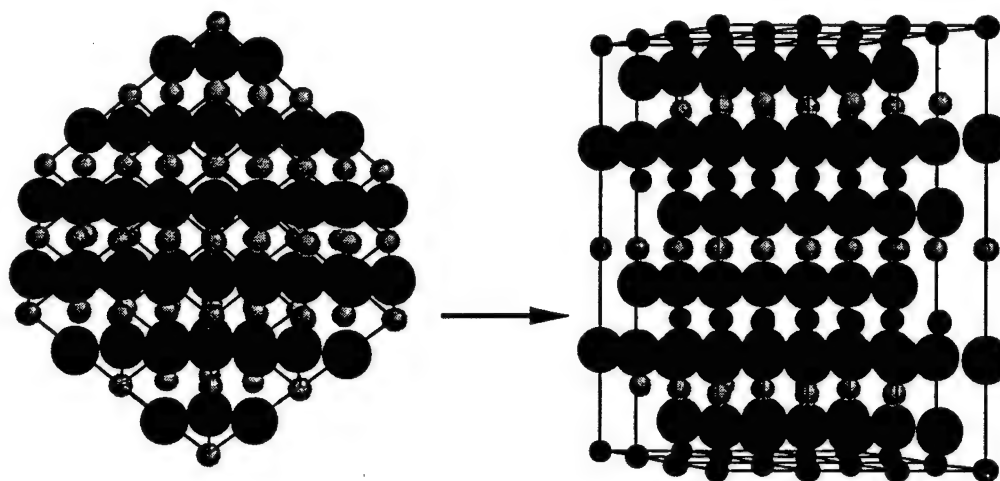
Fig. 5-57. Crystallographic representation showing the most plausible reaction mechanism for the reaction of nickel oxide and lithium oxide to form lithium nickel oxide.

In this sense, it is reactive insertion of lithium oxide into nickel oxide in the presence of oxygen. In Fig. 5-57, the nickel oxide is aligned along the [111] direction at the same time the lithium nickel oxide is also aligned along the [0001] direction. It should be noticed that the stacking sequence of lithium nickel oxide is -O-Li-O-Ni-O-Li-O-Ni-O-Li-O-Ni-O- and the stacking sequence of nickel oxide is -O-Ni-O-Ni-O-Ni-O-Ni-O-. The stacking sequence is important because addition of the Li-O layer in between the Ni-O layers results in $LiNiO_2$. This is the first plausible reason why intercalation of lithium oxide into nickel oxide yields lithium nickel oxide. The second reason proposed here is based on the defect formation in nickel oxide. Since the defect concentrations in nickel oxide are not sensitive to the atmospheric environment but the reaction kinetics of lithium

nickel oxide formation is dependent and sensitive to the oxygen partial pressure, the intercalation process is therefore again the most possible pathway for the reaction to proceed. This is because the intercalation process is independent of the lattice defects. The third reason is based on the characteristics of the intercalation process. Usually the intercalation process begins with the insertion of the intercalants into the possible channels separated at a miximum distance. Other empty channels at a lesser distance of separation from the intercalated channels are then filled up later on. This can be visualized from Fig. 5-58 which schematically shows the intercalation process [31]. Extending this characteristic of the intercalation process to the intercalation of lithium oxide into nickel oxide, it is clear that the disordered lithium nickel oxide can form before all the lithium layers are filled up (as shown schematically in Fig. 5-59). In addition, no distinct nickel oxide and lithium nickel oxide interface can be observed during the reaction process. These two aspects correlate very well with what is reported in the literature. In fact, Dahn et. al. [15,16] have reported that a transition of disordered rock salt structure of non-stoichiometric lithium nickel to hexagonal structure occurs at $x = 0.62$ (lithium content). However, no microscopic evidence of the existence of the reaction interfaces between nickel oxide and lithium oxide has been reported yet so far. This is probably because of the fine polycrystalline nature of the powders. A systematic study of this structural alteration using single crystals can provide good insight into this proposed mechanism.
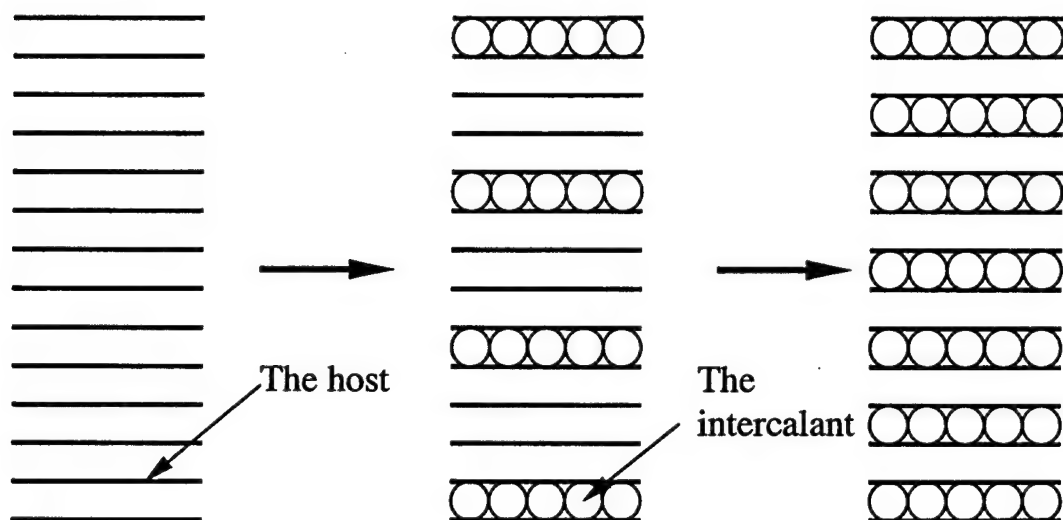
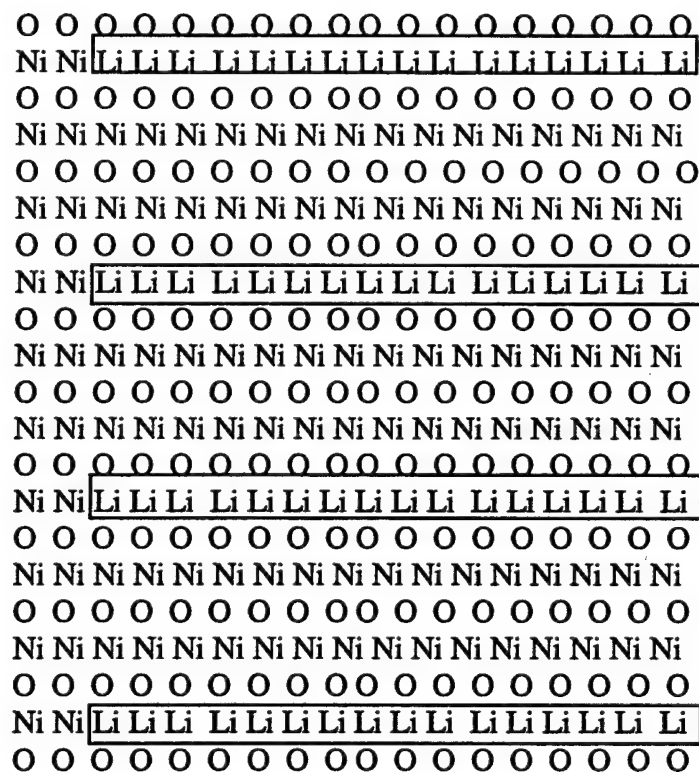Fig. 5-58. A schematic representation of the intercalation process [32].

Fig. 5-59. A schematic representation of the disordered (lithium) nickel oxide. The disordered nickel oxide forms prior to filling up of all the lithium layers.

148

5.14 Activation energy (E_a) of formation of LiNiO$_2$ via reaction of Li$_2$CO$_3$ and NiO – obtained from the decomposition of the xerogel generated by the rotary evaporation process:

The earlier sections discussed the mechanism of formation of LiNiO$_2$. It was shown that lithium carbonate indeed directly reacts with nickel oxide to form LiNiO$_2$. In the present section, Kissinger's method [33-39] is utilized for estimating the activation energy of formation of LiNiO$_2$ via the reaction between Li$_2$CO$_3$ and NiO obtained by decomposition of the xerogel generated by the rotary evaporation process. The major advantage of utilizing Kissinger's method for estimating the activation energy is that it is possible to obtain the activation energy of the reaction without requiring any detailed information of the reaction mechanism. This section will begin with the introduction of the principles of the Kissinger's method, followed by the experimental procedures, results and discussion.

1. *Principle of the Kissinger's method for the estimation of activation energy:*

One of the most important characteristics of the Kissinger's method is that it is a non-isothermal method for estimation of the activation energy. The meaning of "non-isothermal" implies an investigation of reaction kinetics under constant change of heating temperature (i.e. constant heating rate) instead of constant temperature. If we define the extent of reaction to be α, which can be represented as:

$$\alpha = (Wi-W)/(Wi-Wf) \qquad (5.17)$$

Where Wi, W and Wf represent the initial weight, weight during reaction and the final weight (at completion of reaction) of the sample. The change in the extent of reaction versus time can now be expressed as:

$$d\alpha/dt = f(\alpha)k(T) \qquad (5.18)$$

Where $f(\alpha)$ represents the reaction mechanism, $k(T)$ represents the rate constant of the reaction at temperature T. It is known that the rate constant of the reaction can be expressed in the Arrhenius form as:

$$k(T)= Aexp(-Ea/RT) \qquad (5.19)$$

Where A is the frequency factor and Ea is the activation energy of the reaction. As a result, equation (5.17) can be rearranged to yield:

$$d\alpha/dt = f(\alpha)A\exp(-Ea/RT) \tag{5.20}$$

When the reaction kinetics reaches a maximum, $d(d\alpha/dt)/dt = 0$. Thus

$$d(d\alpha/dt)/dt = f'(\alpha)d\alpha/dt\, A\, \exp(-Ea/RT) +$$

$$f(\alpha)\, A\, (Ea/RT^2)\, (dT/dt)\, \exp(-Ea/RT) = 0 \tag{5.21}$$

Rearrangement of equation (5.21), gives:

$$f'(\alpha_M)d\alpha/dt = -f(\alpha_M)\, (Ea/RT_M{}^2)\, (dT/dt) \tag{5.22}$$

Where the subscript "M" represents reaction maximum. At this point, substitution of equation (5.20) into equation (5.22), gives:

$$f'(\alpha_M)A\exp(-Ea/RT_M) = (Ea/RT_M{}^2)\, (dT/dt) \tag{5.23}$$

By taking natural logarithm on both sides of equation (5.23) and rearranging gives the useful form of the Kissinger's equation:

$$\ln[(dT/dt)/T_M{}^2] = [\ln f'(\alpha_M)AR/Ea] - Ea/RT_M$$

$$\boxed{\ln[(dT/dt)/T_M{}^2] = \text{Constant} - Ea/RT_M} \tag{5.24}$$

This analytical representation suggests that the knowledge of reaction maximum (i.e. maximum kinetics) at different heating rates, should yield the reaction activation energy. The activation energy (Ea) is obtained from the slope of the regression line of $\ln[(dT/dt)/T_M{}^2]$ versus $1/T_M$. This final condensed equation is known as the "Kissinger's equation".

2. *The activation energy of formation of LiNiO$_2$ via the reaction between Li$_2$CO$_3$ and NiO obtained by decomposition of the xerogel generated by the rotary evaporation process:*

In order to determine the activation energy (Ea) for the formation of LiNiO$_2$ via the reaction of Li$_2$CO$_3$+NiO derived by decomposition of the rotary evaporated xerogel, the following method was employed. Five heating rates were chosen for heat treating the xerogel sample in air utilizing TGA. The 5 different heating rates chosen for heat treating

150

the samples from room temperature to 900°C are 5, 10, 20, 30 and 40°C/min respectively. The results of the TGA the analysis is shown in Fig. 5-60.
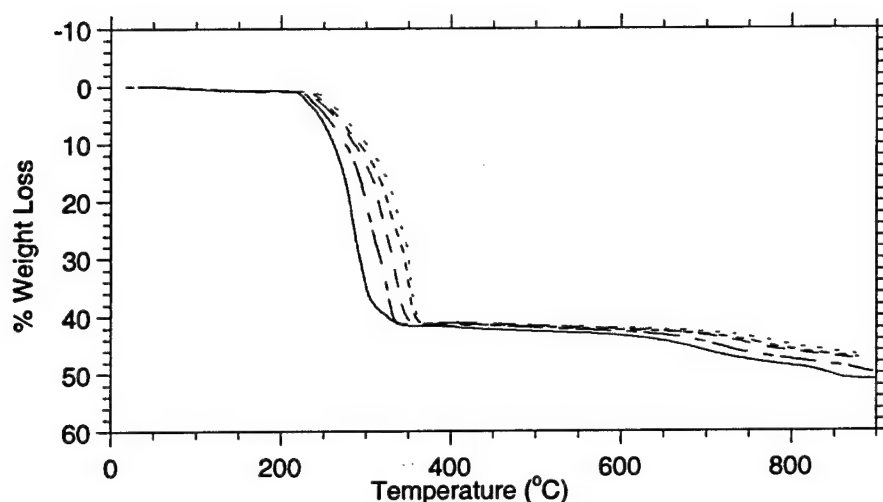

Fig. 5-60. The results of the TGA the analysis for the 5 different heating rates chosen for heat treating the samples up to 900°C in air. The heating rates are 5, 10, 20, 30 and 40°C/min respectively.

Since the reaction of interest occurs in the temperature range after the completion of the initial decomposition reaction (complete formation of Li_2CO_3 and NiO), the differential weight loss versus temperature of these five samples as shown in Fig. 5-61 begins at 500°C onwards. From Fig. 5-61 the reaction maximum temperature (T_M) can be determined for each sample that was heat treated at each of the different heating rates. The reaction maximum temperature (T_M) for the samples that were heat treated using the heating rates of 5, 10, 20, 30 and 40°C/min are thus determined to be 690°C, 709 °C, 738 °C, 758 °C and 771 °C respectively. It should be noted that the peaks seen after 800°C can be attributed to the decomposition of $LiNiO_2$ as discussed earlier in section 5.10. The activation energy for the formation of $LiNiO_2$ via reaction between Li_2CO_3 and NiO can now be calculated by obtaining the slope of the plot of $\ln[(dT/dt)/T_M^2]$ versus $1/T_M$. The plot $\ln[(dT/dt)/T_M^2]$ versus $1/T_M$ is shown in Fig. 5-62. Linear regression of these points, yields the slope of $-11866 = -Ea/R$. The activation energy for formation of $LiNiO_2$

151

utilizing the reaction of Li_2CO_3 and NiO decomposed from the xerogel prepared using the rotary evaporation process is therefore determined to be 98.65 kJ/mole.
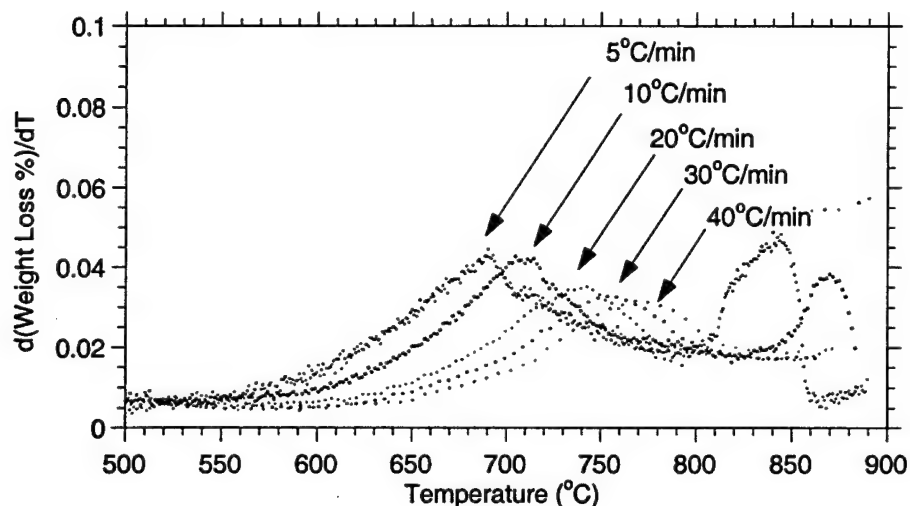

Fig. 5-61. The differential weight loss versus temperature of samples heat treated in air at 5 different heating rates.
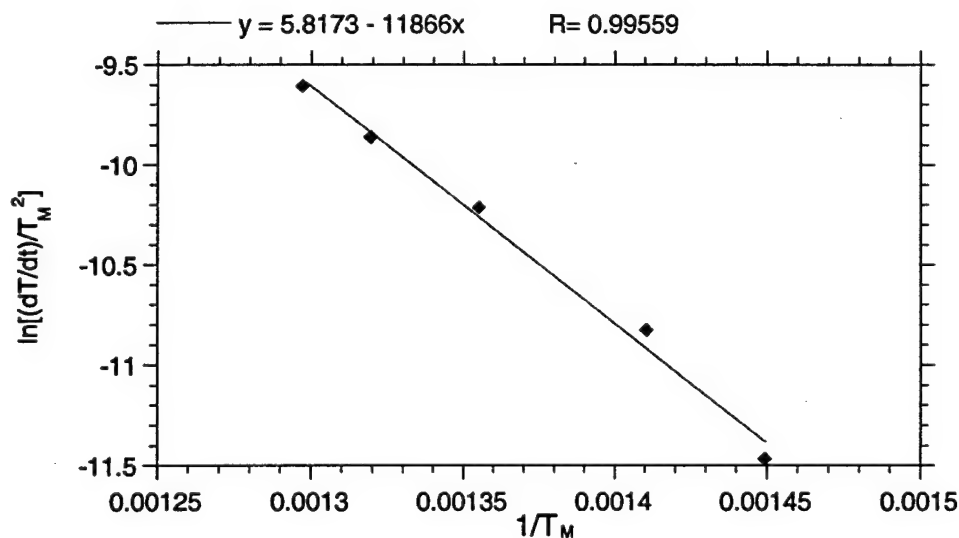

Fig. 5-62. The plot of $\ln[(dT/dt)/T_M{}^2]$ versus $1/T_M$ gives the slope, $-Ea/R$ from which the activation energy (Ea) can be calculated.

5.15 The reasons responsible for faster reaction kinetics of lithium carbonate and nickel oxide decomposed from the xerogel in comparison to the commercial lithium carbonate and synthesized nickel oxide:

1. *Kinetics of formation of LiNiO$_2$ via the reaction between lithium carbonate and nickel oxide obtained by the decomposition of the xerogel:*

The kinetics of formation of LiNiO$_2$ via the reaction of the products obtained from the xerogel can be analyzed from the TGA/DTA analysis. Comparison can also be made with the corresponding reaction between commercially obtained Li$_2$CO$_3$ and NiO syntheszed by decomposing commercially obtained Ni(OH)$_2$ at 800°C in air for 2 h. Fig. 5-63(a) and (b) show the simultaneous TGA/DTA analysis of both the xerogel sample and the sample prepared by mixing commercial lithium carbonate and the synthesized nickel oxide using a mortar and pestle. A heating rate of 10°C/min was used to heat the samples to 800°C, followed by a dwell time of 1 minute and then cooled at a rate of 10°C/min back to room temperature. This was the general heat treatment schedule used for these two experiments. From the DTA analysis of the xerogel shown in Fig. 5-63(a), it can be seen that no distinct endotherm or exotherm is observed representing melting or solidification of lithium carbonate during the heating as well as the cooling process. In contrast, the DTA analysis of the sample consisting of commercial lithium carbonate and synthesized nickel oxide shows both melting and solidification of lithium carbonate. This result suggests that the reaction in the case of the sample containing commercial lithium carbonate and synthesized nickel oxide is not completed during the whole heat treatment process. Moreover, from the weight loss analysis of both samples, the xerogel has already reached the theoretical weight loss of 7.0% before 800°C (see more details in section 5.13) in comparison to only ~41.3% completeness of the reaction for the sample consisting of commercial lithium carbonate and synthesized nickel oxide at 800°C. Thus, the kinetics of formation of LiNiO$_2$ is faster for the PSG derived xerogel than the case of the reaction between commercial lithium carbonate and the synthesized nickel oxide.

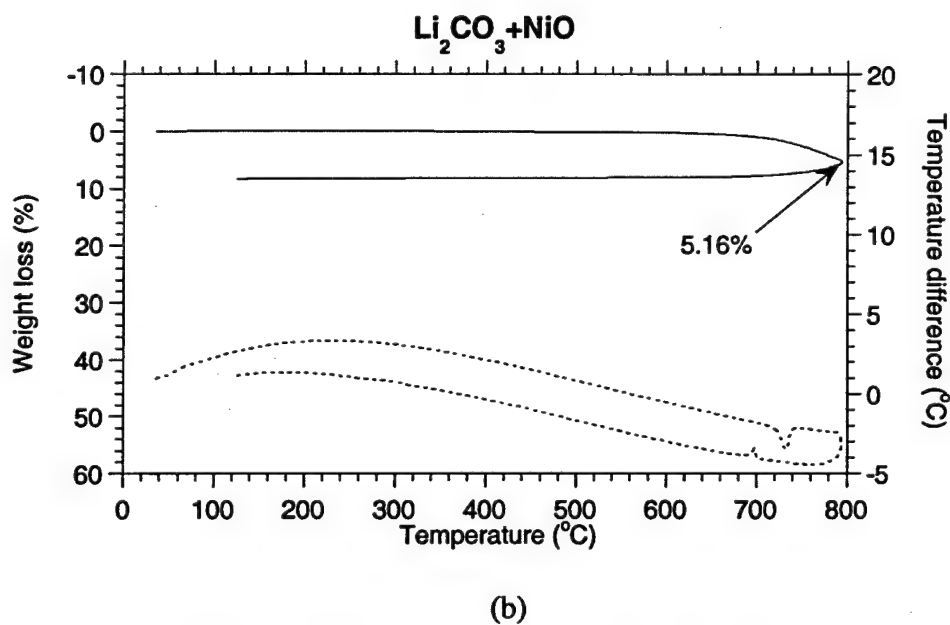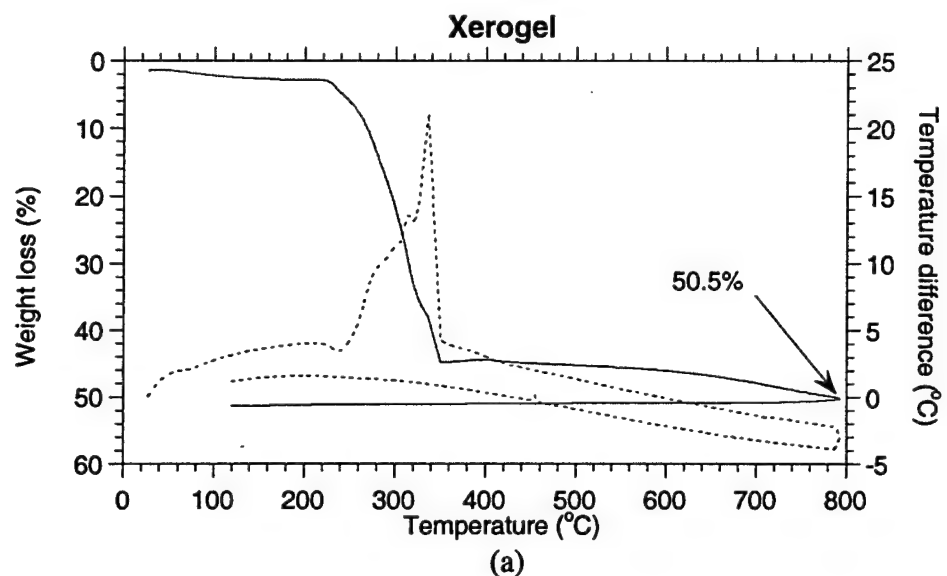Fig. 5-63. The simultaneous TGA/DTA analysis of both the xerogel sample and the sample prepared by mixing commercial lithium carbonate and the synthesized nickel oxide using mortar and pestle. (a) the xerogel and (b) the sample prepared by mixing commercial lithium carbonate and the synthesized nickel oxide using mortar and pestle. (——) represents the TGA curve and (······) represents the DTA curve.

2. *Reasons responsible for faster kinetics of formation of LiNiO₂ obtained via the reaction between lithium carbonate and nickel oxide decomposed from the xerogel:*

The faster kinetics of formation of $LiNiO_2$ in the case of the xerogel compared to the solid state reaction of commercial lithium carbonate and nickel oxide synthesized at 800°C can be attributed to mainly two factors. First, a smaller crystallite size and second, a more intimate mixing of lithium carbonate and nickel oxide achieved in the case of the xerogel. Fig. 5-64(a), (b) and (c) show the morphology of commercial lithium carbonate seen in the SEM at magnifications of 1000X, 10kX and 20kX. Similarly, Fig. 5-64(d), (e) and (f) are the SEM micro graphs showing the morphology of nickel oxide synthesized by decomposing nickel hydroxide at 800°C for two hours. The micro graphs are taken at a magnification of 1000X, 10kX and 20kX respectively. Both commercial lithium carbonate and synthesized nickel oxide consist of distinct crystallites (~2μm for lithium carbonate and ~0.25μm for nickel oxide). An SEM micro graph showing the morphology of the xerogel decomposed at 300°C for 5 hours is also displayed in Fig. 5-65, for comparison. No distinct crystallites are observable in the SEM micro graphs. As discussed earlier in the phase evolution study (section 5.5), the XRD result obtained on the xerogel decomposed at 300°C for 5 hours shows crystalline lithium carbonate and nickel oxide. As a result, the xerogel decomposed at 300°C for 5 hours can be expected to be composed of very fine crystallites of lithium carbonate and nickel oxide.

In order to resolve the smaller crystallite size as well as the intimately mixed state of both nickel oxide and lithium carbonate, TEM was used for resolving the actual crystallite size and the distributions of both lithium carbonate and nickel oxide. The TEM sample was prepared by heat treating the xerogel sample (prepared from the rotary evaporation process) in the TGA unit (TA instrument, model 2960) at 10°C/min to 350°C followed by quenching (~30°C/min) to room temperature. It should be mentioned that the TEM sample was prepared using the TGA unit instead of using the sample prepared from the box furnace (the earlier sample that was heat treated at 300°C for 5 hours). This is because of a better thermal environment (more accurate and homogeneous) that is achievable in the TGA unit.

Fig. 5-66(a) shows the diffraction pattern of the sample. A characteristic ring pattern is observed which gives an indication of the aggregation of small crystallites in

155

the sample. For the purpose of resolving the individual crystallite size and distribution of both lithium carbonate and nickel oxide, the dark field imaging mode was used. The diameter of the rings that are representing nickel oxide and lithium carbonate are calculated and tabulated in Table 5-10. From the information in Table 5-10 it is known that the rings within the first two rings of nickel oxide (indexed as (111) and (200) respectively) should originate from the lithium carbonate. As a result, the following dark field images taken for lithium carbonate are utilizing the diffracted beams coming from the rings within the first two rings of nickel oxide. The dark field images taken for nickel oxide utilize the diffracted beams from the (111) and (200) rings.

Fig. 5-66(b), (c) and (d) are the bright field image, dark field image of lithium carbonate and the dark field image of nickel oxide respectively. All the images are taken at the same magnification of 100kX. From the dark field image of lithium carbonate shown in Fig. 5-66(c), it can be seen that the size of lithium carbonate crystallites are very small (in the range of ~ 20nm or less). This small crystallite nature actually corresponds to the very diffused diffraction ring of lithium carbonate shown in the diffraction pattern (shown in Fig. 5-66(a)). At the same time, the dark field image of nickel oxide is shown in Fig. 5-66(d). The crystallite size of nickel oxide is also very small (30~50nm). From the distribution of both lithium carbonate and nickel oxide shown in the dark field images, it can be concluded that the separation distance between the lithium carbonate and nickel oxide are very small (in the range of nano meters). In other words, the lithium carbonate and nickel oxide originated from the decomposition of the xerogel are intimately mixed.

Since the particle size of both commercial lithium carbonate and the synthesized nickel oxide are large (~20μm in the case of lithium carbonate and ~5 to 20μm in the case of synthesized nickel oxide), the mixing between the lithium carbonate and the nickel oxide would be eventually limited due to the particle sizes of both lithium carbonate and nickel oxide. This actually explains why the lithium carbonates and nickel oxide originated from the decomposition of the xerogel react faster than commercially obtained lithium carbonate and the synthesized nickel oxide.

156
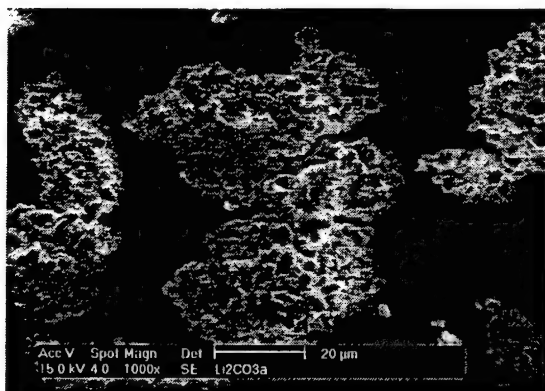
(a)
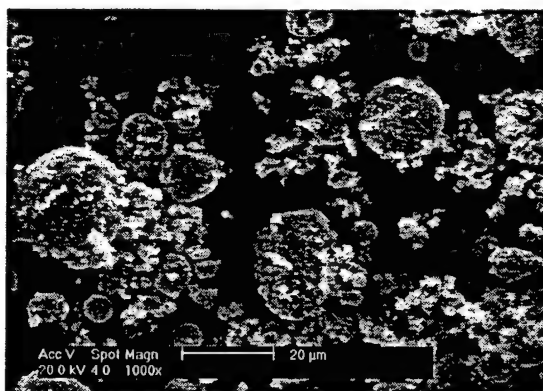
(d)

(b)
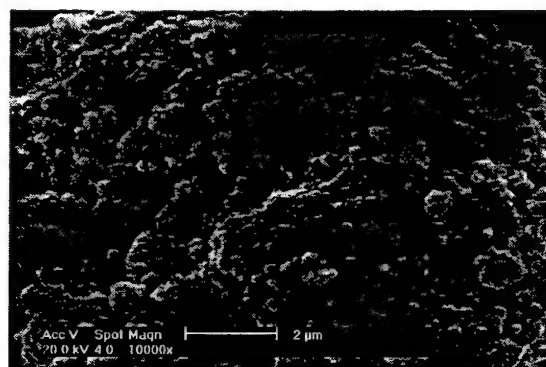
(e)
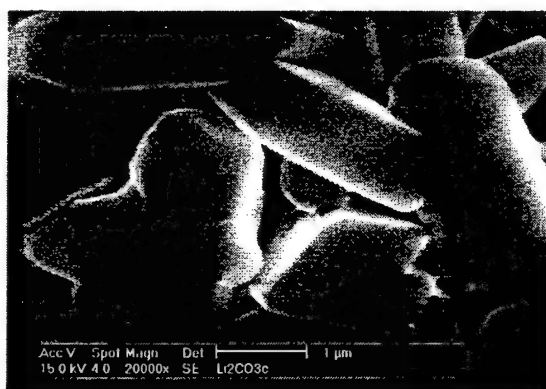
(c)
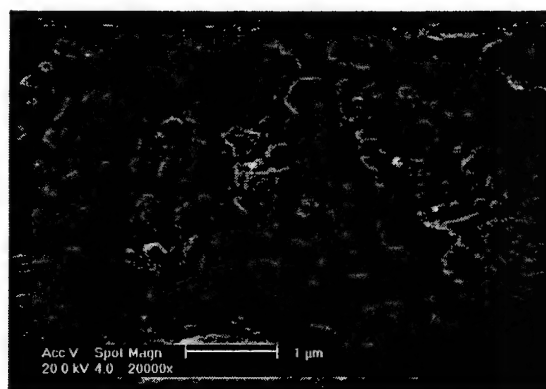
(f)

Fig. 5-64. (a), (b) and (c) are the SEM micro graphs showing the morphology of commercial lithium carbonate taken at magnifications of 1000X, 10kX and 20kX. Similarly, Fig. 5-64(d), (e) and (f) are the SEM micro graphs showing the morphology of nickel oxide synthesized by decomposing nickel hydroxide in air at 800°C for two hours taken at magnifications of 1000X, 10kX and 20kX respectively.

157
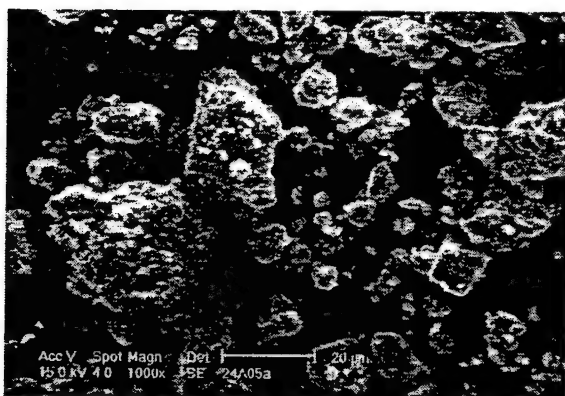
(a)

(b)
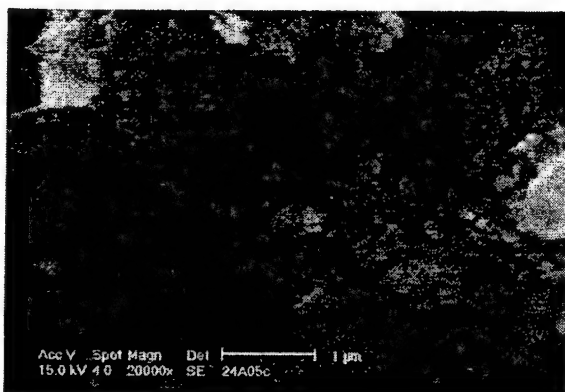
(c)

Fig. 5-65. SEM micro graphs showing the morphology of the xerogel decomposed in air at 300°C for 5 hours. (a) a magnification of 1000X, (b) 10kX and (c) 20kX.

(a)

(b)

(c)

(d)
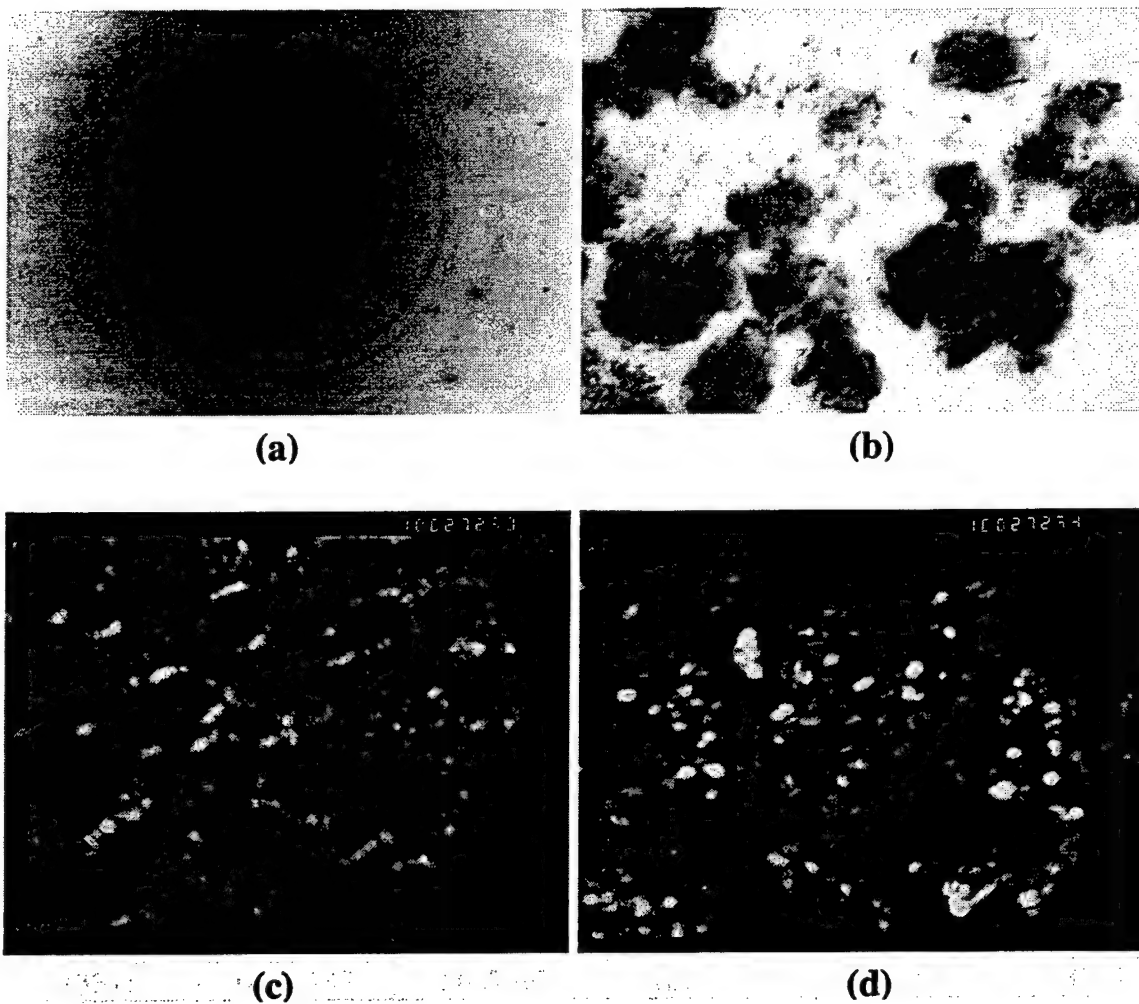
Fig. 5-66. (a) The diffraction pattern of the decomposed xerogel sample decomposed in the TGA instrument. (b) The corresponding bright field image. (c) The dark field image of lithium carbonate taken at the same region as shown in the bright field image. (d) The dark field image corresponding to nickel oxide.

Table 5-10. The diameter of the rings representing nickel oxide and lithium carbonate are calculated and tabulated for the purpose of resolving the individual crystallite size and distribution of both lithium carbonate and nickel oxide using the dark field imaging mode.

Accelerating voltage = 120kV λ = 0.003349 nm						
Camera length = 76.9 cm						
Camera constant Rd = 2.575381 = λL						

| NiO			Li_2CO_3		
Bravais Lattice: Cubic			Bravais Lattice: Monoclinic		
Lattice parameters: a = 4.17690			Lattice parameters: a = 8.37870 b = 4.98642 c = 6.21187 β = 114.75		
$1/d^2 = (h^2+k^2+l^2)/a^2$			$1/d^2 = 1/Sin^2\beta (h^2/a^2+k^2 Sin^2\beta/b^2+l^2/c^2-2hl Cos\beta/ac)$		
Peak index	d spacing	Radius of the ring	Peak index	d spacing	Radius of the ring
(111)	2.411534	1.067943	(-110)	4.170651	0.617501
(200)	2.08845	1.233154	(200)	3.80453	0.676925
(220)	1.476757	1.743943	(111)	3.037009	0.847999
(311)	1.259383	2.044955	(-202)	2.926627	0.879983
(222)	1.205767	2.135886	(002)	2.820634	0.913051
(400)	1.044225	2.466309	(-112)	2.633693	0.977859
(331)	0.958247	2.687597	(020)	2.49321	1.032958
(420)	0.933983	2.757417	(-311)	2.435641	1.057373
(422)	0.852606	3.020599	(021)	2.280423	1.129344
(511)	0.803845	3.203829	(310)	2.260705	1.139194
			(-221)	2.120618	1.214448
			(-220)	2.085326	1.235002
			(-402)	2.016247	1.277314
			(202)	1.914579	1.345142
			(-222)	1.897889	1.356971
			(311)	1.871178	1.376342
			(221)	1.824537	1.411526
			(-313)	1.816949	1.417421
			(130)	1.623849	1.585973
			(-131)	1.598923	1.610698

Table 5-10. The diameter of the rings representing nickel oxide and lithium carbonate are calculated and tabulated for the purpose of resolving the individual crystallite size and distribution of both lithium carbonate and nickel oxide using the dark field imaging mode.

References

1. Nakamoto, Infrared and Raman Spectra of Inorganic and Coordination Compounds, 4th ED. (Wiley, 1986).
2. K. Ito and H. J. Bernstein, Canadian Journal of Chemistry, 34 (1956) 170.
3. M. Cadene, J. Mol. Structure, 2 (1968) 193.
4. P. Baraldi, G. Fabbri, Spectrochimica Acta, 37A (1981) 88.
5. P. Baraldi, Spectrochimica Acta, 38A (1982) 51.
6. G. S. Raghuvanshi, D. P. Khandelwal, H. D. Bist, J. Solid State Chem., 57 (1985) 207.
7. A. M. Heyns, J. Molecular Structure, 11 (1972) 93.
8. M. Cadene, A. M. Vergnoux, Spectrochimica Acta, 28A (1972) 1663.
9. Llewellyn H. Jones, J. Chem. Phys. 22 (1954) 217.
10. D. Aurbach, M. L. Daroux, P. W. Faguy, and E. Yeager, J. Electrochem. Soc., 134 (1987) 1611.
11. R. W. Adams, R.L. Martin, and G. Winter, Australian J. Chem., 20 (1967) 773.
12. R.J. Gummow and M.M. Thackeray, Solid State Ionics, 53-56 (1992) 681.
13. R.J. Gummow and M.M. Thackeray, J. Electrochem. Soc., 140 (1993) 3365.
14. J.R. Dahn, U. von Sacken and C.A. Michal, Solid State Ionics 44 (1990) 87.
15. W. Li, J.N. Reimers and J.R. Dahn, Physical Review B, Vol.46, No. 6. (1992) 3236.
16. Jan N. Reimers, W. Li and J.R. Dahn, Physical Review B, Vol. 47, No. 14. 8486.
17. R.V. Moshtev, P. Zlatilova, V. Manev, Atsushi Sato, Journal of Power Sources 54 (1995) 329.
18. Shuji Yamada, Masashi Fujiwara, Motoya Kanda, Journal of Power Sources, 54 (1995) 209.
19. A. Hirano, R. Kanno, Y. Kawamoto, Y. Takeda, K. Yamaura, M. Takano, K. Ohyama, M. Ohashi, Y. Yamaguchi, Solid State Ionics, 78 (1995) 123.
20. Rougier, A., Delmas, C. & Chadwick, A. V. Chadwick, Solid State Communication, 94 (1995) 123.
21. W. Ebner, D. Fouchard, L. Xie, Solid State Ionics, 69 (1994) 238.
22. F. Izumi, "The Rietveld Method", ed. By R.A. Yound, Oxford University Press, Oxford (1993), Chap. 13; Y.-I. Kim and F. Izumi, J. Ceram. Xoc. Jpn., 102 (1994) 401.
23. J. R. Dahn, R. R. Haering, Solid State Ionics, 2 (1981) 19.
24. M. Broussely, F. Perton, P. Biensan, J.M. Bodet, J. Labat, A. Lecerf, C. Delmas, A. Rougier, and J.P. Peres, J. Power Sources, *54* (1995) 109.
25. T. Ohzuku, A. Ueda, M. Nagayama, J. Electrochem. Soc., 140 (1993) 1862.
26. W. Li, J. N. Reimers, J. R. Dahn, Solid State Ionics, 67 (1993) 123.
27. D. Bloor, R.J. Brook, M.C. Flemings, S. Mahajan (Eds.), The Encyclopedia of Advanced Materials, Elsevier Science, (1994), p. 1917.
28. J.P. Suchet, Crystal Chemistry and Semiconduction, Academic Press, (1971).
29. H. Schmalzried, Chemical Kinetics of Solids, VCH publishers, New York, (1995).
30. W.D. Kingery, H.K. Bowen, D.R. Uhlmann, Introduction to Ceramics, John Wiley and Sons, New York, (1976). Ch. 4.

31. M. S. Whittingham, A.J. Jacobson (Eds.), Intercalation Chemistry, Academic Press, (1982).
32. M.E. Brown, D. Dollimore and A.K. Galwey, in C.H. Bamford and C.F.H. tipper (Eds.),Comprehensive Chemical Kinetics, Elsevier, Amsterdam, Vol. 22, (1985).
33. D. Chen, X. Gao, D. Dollimore, Thermochim. Acta, 215 (1993) 65.
34. D. Chen, X. Gao, D. Dollimore, Thermochim. Acta, 215 (1993) 109.
35. X. Gao, D. Chen, D. Dollimore, Thermochim. Acta, 223 (1993) 75.
36. D. Chen, D. Dollimore, J. Thermal Analysis, 44 (1995) 1001.
37. D. Dollimore, T.A. Evans, Y.F. Lee, F.W. Wilburn, Thermochim. Acta, 188 (1991) 77.
38. D. Dollimore, T.A. Evans, Y.F. Lee, G.P. Pee, F.W. Wilburn, Thermochim. Acta, 196 (1992) 225.
39. D. Dollimore, T.A. Evans, Y.F. Lee, F.W. Wilburn, Thermochim. Acta, 198 (1992) 249.

Chapter 6

Conclusions

Based on the studies conducted thus far, several conclusions can be made. These have been summarized below in two parts. Part I includes the general conclusions made on the basis of the common characteristics observed in the synthesis of $LiMO_2$ (M = Ni, and $Ni_{0.75}Co_{0.25}$). The specific conclusions on the other hand are made based on the solvent systems and the specific process utilized for synthesizing the oxides.

Part I. *Overall conclusions*

1. The particulate sol-gel (PSG) process has been successfully utilized for synthesizing lithiated transition metal oxides $LiMO_2$ (M = Ni, Co and $Ni_{0.75}Co_{0.25}$) for Li-ion battery applications.

2. Nickel oxide (or nickel cobalt oxide in the case of $LiNi_{0.75}Co_{0.25}O_2$ synthesis) and lithium carbonate are the major intermediate compounds formed after decomposition of the xerogels in all the processes. The formation of $LiNiO_2$ and $LiNi_{0.75}Co_{0.25}O_2$ is based on the reaction between the nickel oxide (or nickel cobalt oxide) and lithium carbonate.

3. The formation of the lithiated transition metal oxide is dependent on the instability of the reactive interphase between nickel oxide (or nickel cobalt oxide) and lithium carbonate. Substitution of 25% nickel by cobalt increases the instability of the nickel oxide and lithium carbonate interphase. This observation is supported by the phase evolution study showing the initiation of $LiNiO_2$ and $LiNi_{0.75}Co_{0.25}O_2$ phase at $600^{\circ}C$ and $400^{\circ}C$ respectively.

4. In the case of $LiNiO_2$, the reaction kinetics between nickel oxide and lithium carbonate, and the decomposition of $LiNiO_2$ both determine the defect concentration of the resultant $LiNiO_2$ and therefore the electrochemical properties. In comparison to pure $LiNiO_2$, substitution of 25% nickel by cobalt minimizes the defect concentration of the resultant oxide. This minimization of the defect concentration caused by 25% cobalt substitution could be attributed to faster kinetics of the above reactions which facilitates the formation of stoichiometric compound or stabilization of the structure.

5. The presence of a coating of residual lithium carbonate on the $LiNiO_2$ particles significantly affects the electrochemical property of the synthesized $LiNiO_2$. In contrast, the synthesis of $LiNi_{0.75}Co_{0.25}O_2$ is however free from the problem caused by the presence of lithium carbonate.

6. The morphology of the resultant $LiNiO_2$ and $LiNi_{0.75}Co_{0.25}O_2$ are clearly influenced by the specific processes used for generating the xerogels.

7. Without modifying the heat treatment conditions, the highest capacity obtained for $LiNiO_2$ and $LiNi_{0.75}Co_{0.25}O_2$ synthesized using the PSG process are 135mAh/g for $LiNiO_2$ and 180mAh/g for $LiNi_{0.75}Co_{0.25}O_2$. These materials are obtained using the xerogels generated by the spray drying process using a mixture of water and methanol as the solvent.

8. Modification of the heat treatment conditions helps to prevent the decomposition of $LiNiO_2$. With the modified conditions in place, the capacity of $LiNiO_2$ synthesized by utilizing the rotary evaporation process can be as high as 205mAh/g when tested under a charge/discharge rate of C/2 (Even higher than $LiNiO_2$ synthesized using the spray dried precursor without modification of the heat treatment). Rietveld refinement results show that the defect concentration in $LiNiO_2$ can be minimized to about 2%.

9. The factors that can deleteriously influence the electrochemical property of $LiNiO_2$ can be listed in descending order of importance as: (1) defect concentration, (2) presence and distribution of phase impurity such as lithium carbonate, and (3) the crystallite size.

10. Lithium carbonate and nickel oxide can react according to the following two reactions:

$$Li_2CO_3 \longrightarrow Li_2O + CO_{2(g)} \uparrow \qquad (5.15)$$

$$1/2\ O_2 + Li_2O + 2\ NiO \longrightarrow 2\ LiNiO_2 \qquad (5.16)$$
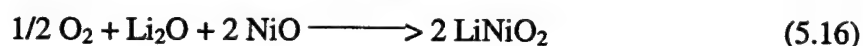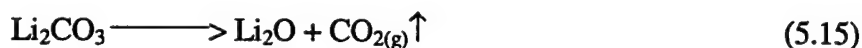
These reactions have been proved to occur at the same time which can be represented as:

$$\overset{E_{a1}}{Li_2CO_3 + 2NiO + 1/2\ O_2 \text{-----------}> 2LiNiO_2 + CO_{2(g)} \uparrow} \qquad (5.14)$$
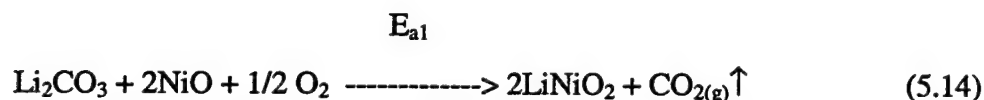
The activation energy for this overall reaction has been determined to be 98.65 kJ/mole using the non-isothermal Kissinger's method.

11. Based on the observations that formation of defects in nickel oxide is not sensitive to the reaction gas environment, it is proposed that $LiNiO_2$ forms via the intercalation of lithium oxide into the nickel oxide host. This intercalation process is postulated because the intercalation process is known to proceed without the existence of lattice defects.

12. The kinetics of the reaction between lithium carbonate and nickel oxide obtained from the xerogel to form $LiNiO_2$ is faster compared to the reaction between commercially obtained lithium carbonate and the nickel oxide synthesized by decomposing nickel hydroxide at 800°C for 2 hours. This can be attributed to the smaller crystallite sizes (~ 20nm in the case of lithium carbonate and ~30~50nm in the case of nickel oxide) as well as the enhanced level of mixing between lithium carbonate and nickel oxide present in the decomposed xerogel.

Part II. *Specific conclusions*

1. Two solvent systems were investigated using nickel acetate and lithium hydroxide as precursors.

2. The xerogel which is obtained using water as a solvent contains a mixture of dehydrated nickel acetate, lithium acetate, nickel hydroxide and nickel hydroxy acetate. On the other hand, in the case of a mixture of aqueous and non-aqueous solvent system, the xerogels are mainly comprised of Ni-O-Ni linkages and lithium acetate. These are formed due to the hydrolysis reaction induced by water and the condensation reaction between the methoxy and hydroxyl groups.

3. The conclusions obtained for the three different variants of the PSG process are described as follows:

   1. *The rotary evaporation process:*

      (i)   The resultant oxide exhibits an inferior electrochemical response. Thus 100mAh/g and 168mAh/g are the highest capacities obtained for the $LiNiO_2$ and $LiNi_{0.75}Co_{0.25}O_2$ generated using the rotary evaporation process. These values are obtained before the modification of heat treatment conditions following an investigation of the reaction mechanism and kinetics.

      (ii) A flocculated, sponge-like morphology is seen for the xerogel generated by the rotary evaporation process.

      (iii) The $LiNiO_2$ powders generated by the rotary evaporation process show a more random morphology devoid of any faceting with a wider crystallite size distribution. Similar morphology is also seen for the $LiNi_{0.75}Co_{0.25}O_2$ powders.

      (iv) The specific surface area of both xerogel (≈ 1 m^2/g) and resultant oxide (≈ 0.5 m^2/g) is generally low.

   2. *The spray drying process:*

(i)   The $LiNiO_2$ and $LiNi_{0.75}Co_{0.25}O_2$ generated using the spray drying process show the best electrochemical activity. 135mAh/g and 182mAh/g are the highest capacities obtained for the $LiNiO_2$ and $LiNi_{0.75}Co_{0.25}O_2$. These values are however obtained without any modification of the heat treatment conditions.

(ii)   Spray dried xerogel shows a distinct morphology comprising of fractured hollow spherical particles.

(iii)   The resultant oxides have a narrower distribution of particle sizes (~ 15-100μm). Faceted crystallites (~1μm), characteristic of the trigonal $R\bar{3}m$ symmetry are observed.

(iv)   Higher specific surface area is observed for both xerogel ($\approx 4m^2$/g) and the resultant oxides (≈ 1 m^2/g) in comparison to the rotary evaporation process.

3.   *The gelation process:*

(i)   The resultant oxides generated using the gelation process generally exhibit electrochemical behavior and morphology similar to oxides generated using the rotary evaporation process.

(ii)   The gelation reaction is dependent on the formation of lithium methoxide that is generated during the dissolution of LiOH in methanol.

(iii)   The kinetics of the gelation reaction is strongly dependent on the concentration of water. This conclusion reflects the possibility of the formation of Ni-O-Ni linkages generated by the formation nickel methoxide as an intermediate product that undergoes hydrolysis and condensation initiated by the addition of water.

Appendix A

Part I. Synthesis and electrochemical characterization
of LiCoO$_2$

Part II. Electrochemical characterization of commercial
LiCoO$_2$ and LiNiO$_2$ obtained from FMC

Part I. _Synthesis and electrochemical characterization of LiCoO₂:_

Since $LiNiO_2$ and $LiNi_{0.75}Co_{0.25}O_2$ were synthesized successfully using nickel (II) (and cobalt(II)) acetate and lithium hydroxide as starting materials, it was decided to investigate the synthesis of $LiCoO_2$ using cobalt (II) acetate and lithium hydroxide precursors. Rotary evaporation however, was the only process employed in this study. The flow chart of the procedure used for rotary evaporation is schematically shown in Figure A-1. The TGA and FTIR analyses for the xerogels generated using the rotary evaporation process are shown in Figure A-2 and A-3. It is clear that the TGA results are very different from the data generated previously for $LiNiO_2$ and $LiNi_{0.75}Co_{0.25}O_2$. The plot shows a two step weight loss in comparison to a single step loss described earlier and normally observed for $LiNiO_2$ and $LiNi_{0.75}Co_{0.25}O_2$ derived using the rotary evaporation process. Figure A-4 shows the X-ray diffraction pattern of the resultant $LiCoO_2$ obtained after heat treating the xerogels derived from rotary evaporation in air at 800°C for 2 hours. The pattern shows almost phase pure $LiCoO_2$ with (Co_3O_4) being the trace secondary impurity.

Figure A-5 shows the cycle number versus capacity and voltage versus composition plots of the synthesized $LiCoO_2$ which was cycled between 3.1 to 4.4V using a current density of 0.25mA/cm². A high capacity, 165mAh/g for the first discharge was observed. Approximately 10% fade in capacity is seen for the first 30 cycles. Since it is reported that cycling of $LiCoO_2$ under high voltage (greater 4.2V) is detrimental to the material, an experiment was conducted to cycle the synthesized $LiCoO_2$ between 3.1 to 4.8V. The cycle number versus capacity and voltage versus composition plots for this test are shown in Figure A-5. No immediate degradation of the material was found although a higher fade in capacity was observed (20% capacity loss for the first 10 cycles). Based on the present results, it is difficult to attribute this loss to either irreversible change in capacity or due to oxidation of the electrolyte. These studies will have to be conducted in the future.
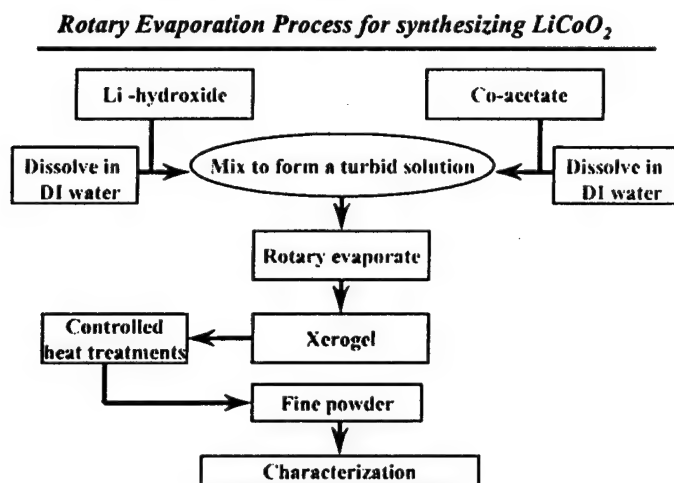
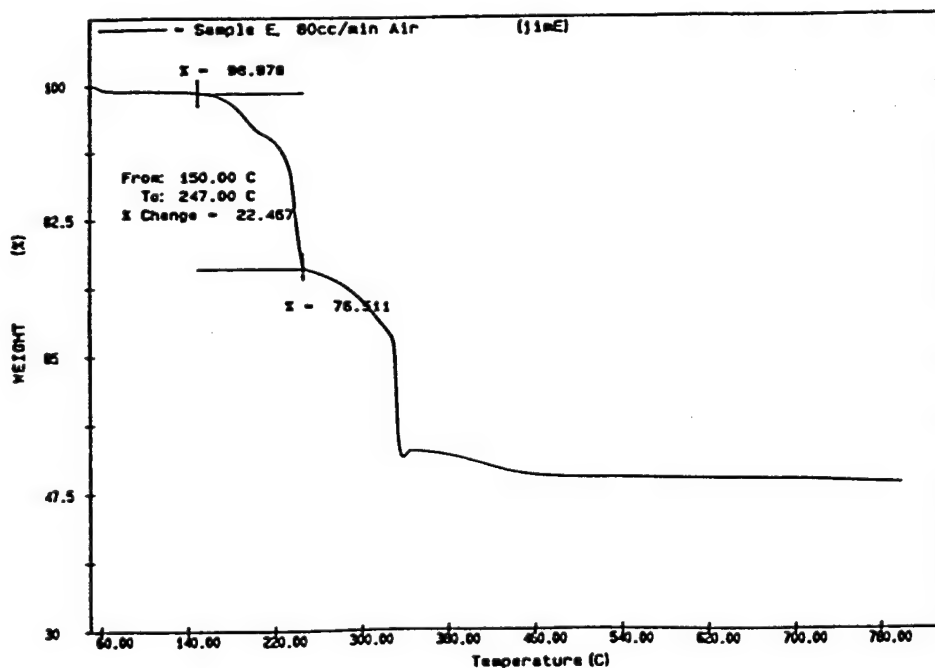Figure A-1 Schematic of the rotary evaporation process used for synthesizing LiCoO₂.

Figure A-2. TGA analysis of LiCoO₂ xerogel which was generated using the rotary evaporation process.

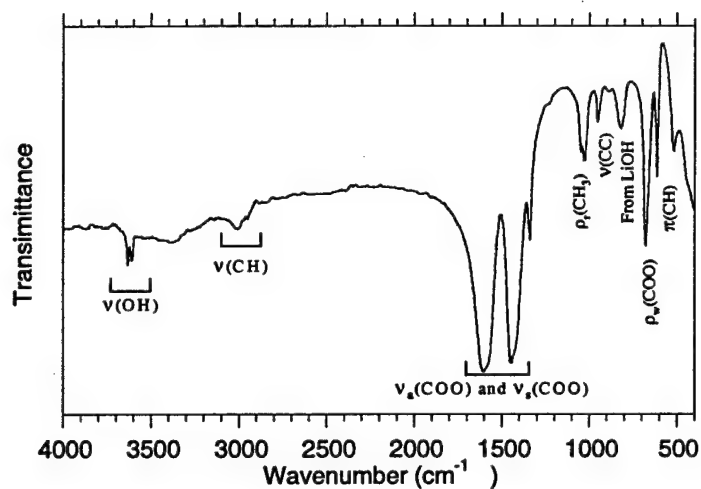Figure A-3. The FTIR data for LiCoO$_2$ amorphous xerogel which was generated using the rotary evaporation process.

Peak	Relative intensity
(003)	100
(101)	33.63
(006)+(102)	15.15
(104)	67.26

Filename: 005apb.02
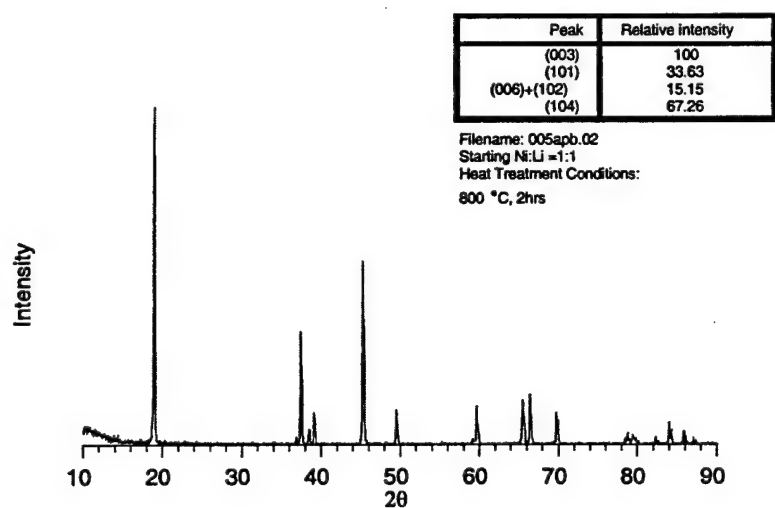Starting Ni:Li =1:1
Heat Treatment Conditions:
800 °C, 2hrs

Figure A-4.The X-ray diffraction pattern of LiCoO$_2$ powders which exhibit the highest capacities synthesized using xerogels generated by the rotary evaporation process.
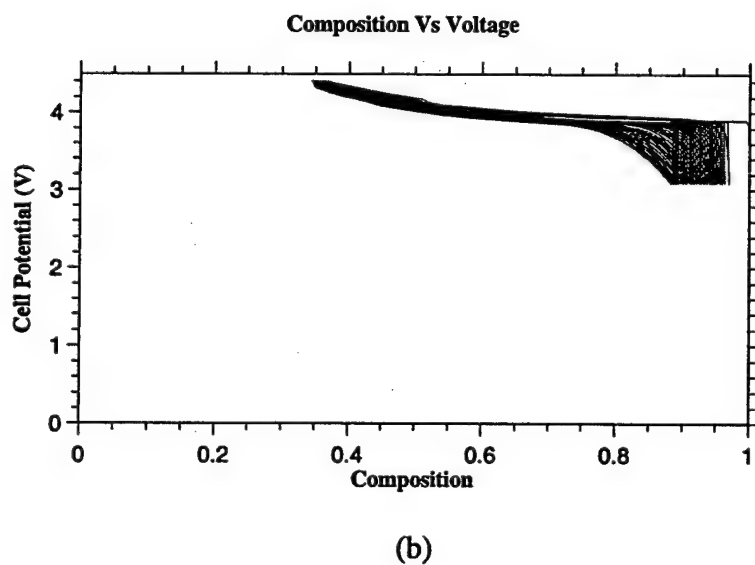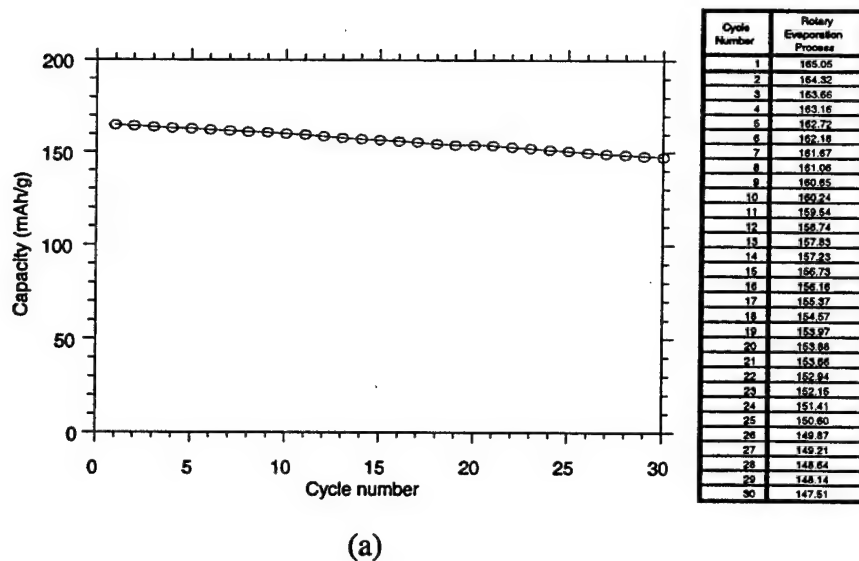
171

Cycle Number	Rotary Evaporation Process
1	165.05
2	164.32
3	163.66
4	163.16
5	162.72
6	162.18
7	161.67
8	161.06
9	160.65
10	160.24
11	159.54
12	158.74
13	157.83
14	157.23
15	156.73
16	156.16
17	155.37
18	154.57
19	153.97
20	153.66
21	153.66
22	152.94
23	152.15
24	151.41
25	150.60
26	149.87
27	149.21
28	148.54
29	148.14
30	147.51

(a)

(b)

Figure A-5. Plots showing (a)variation of capacity versus cycle number and (b)voltage versus composition for LiCoO$_2$ synthesized using the rotary evaporation process. The cathodes were cycled between 3.1 to 4.4V.
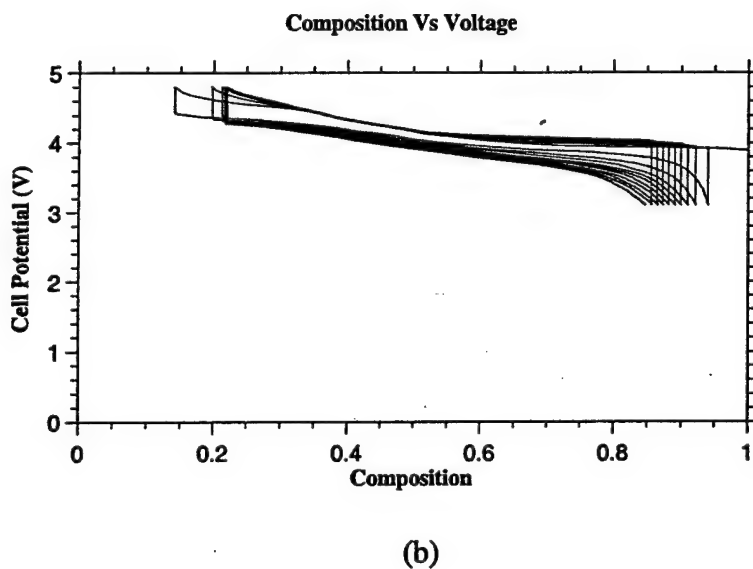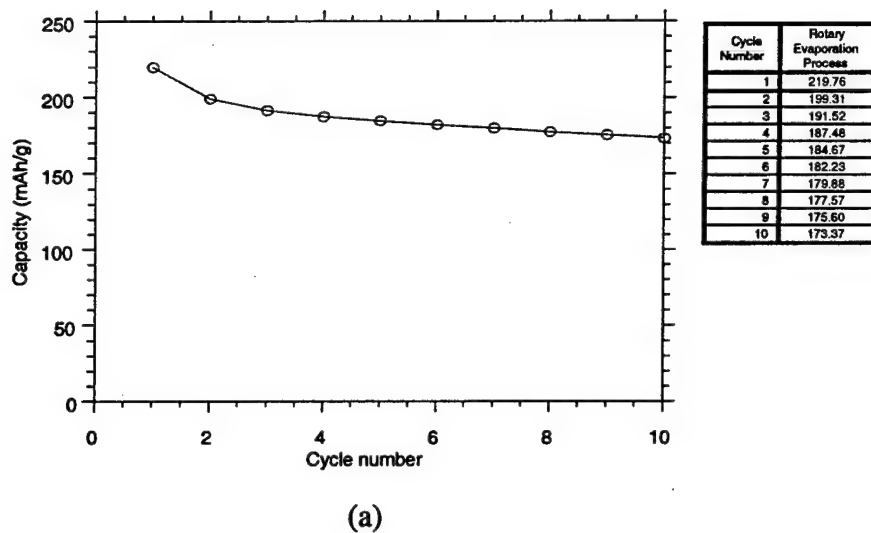
172

Cycle Number	Rotary Evaporation Process
1	219.76
2	199.31
3	191.52
4	187.48
5	184.67
6	182.23
7	179.88
8	177.57
9	175.60
10	173.37

(a)

(b)

Figure A-6. Plots showing (a)variation of capacity versus cycle number and (b)variation of voltage versus composition for the LiCoO$_2$ derived by rotary evaporation. The material was cycled between 3.1 to 4.8V.

Part II. _Electrochemical characterization of FMC LiCoO₂ and LiNiO₂:_

In order to compare the performance of $LiCoO_2$ and $LiNiO_2$ powders synthesized at Carnegie Mellon with commercially available materials, $LiCoO_2$ and $LiNiO_2$ were procured from FMC (Bessemer, NC). The electrochemical performance of $LiCoO_2$ and $LiNiO_2$ were evaluated. The same test conditions (3.1 to 4.4V, $0.25mA/cm^2$, 30 cycles) were used to test the cathodes made from $LiCoO_2$ and $LiNiO_2$ procured from FMC. Figure A-7 shows the capacity versus cycle number of the cathodes fabricated from $LiCoO_2$ and $LiNiO_2$ powders obtained from FMC. A first discharge capacity of 165mAh/g for $LiCoO_2$ and 175mAh/g for $LiNiO_2$ were obtained in all the tests. Although the first discharge capacity of the materials is high, a considerable fade is observed. A capacity loss of 0.34%/cycle for $LiCoO_2$ and 0.94%/cycle for $LiNiO_2$ was observed. Figure A-8 shows a plot of the variation of differential capacity, dQ/dV with voltage, V for the FMC derived $LiCoO_2$ and $LiNiO_2$. The different peaks observed for $LiNiO_2$ are characteristic of phase transformations in $LiNiO_2$ in comparison to $LiCoO_2$. The X-ray diffraction patterns for both $LiCoO_2$ and $LiNiO_2$ procured from FMC are shown in Figure A-9. In comparison to the $LiCoO_2$ and $LiNiO_2$ powders synthesized at Carnegie Mellon, a weaker intensity for the (104) peak is observed in both the materials obtained from FMC. Finally, the morphology of the FMC procured $LiCoO_2$ and $LiNiO_2$ are shown in Figure A-10 and A-11 respectively. A wide distribution of particle sizes was observed for both $LiCoO_2$ and $LiNiO_2$. Sintered agglomerates ($\approx$ 80μm) consisting of primary crystallites ($\approx$ 0.2~0.5μm) is seen in each case which is a characteristic also exhibited by powders synthesized using the spray drying process shown in earlier sections. Overall, the results of the analysis of FMC derived $LiCoO_2$ and $LiNiO_2$ are summarized as follows:

1. In the case of $LiCoO_2$, the discharge capacity of the material fabricated by FMC and the material synthesized at Carnegie Mellon are comparable. Both the materials show a capacity of about 165mAh/g and also show fade in capacity.

2. In the case of $LiNiO_2$, the material fabricated by FMC shows a better capacity compared to the same material synthesized at Carnegie Mellon. Unfortunately, a high

capacity is usually accompanied with high fade. A very high fade in capacity of FMC derived $LiNiO_2$ (0.94%/cycle) was observed during cycling.

3. The shift in the derivative peak positions and intensities in the dQ/dV versus V plot confirms the observed fade in the material during cycling. It should be mentioned that the peak(s) in the dQ/dV versus V plots not only creep down toward the voltage-axis but also shift to higher voltage (or lower) during charging (or discharging).

4. Compared to the FMC derived $LiCoO_2$ and $LiNiO_2$, the X-ray diffraction patterns of $LiCoO_2$ and $LiNiO_2$ synthesized at Carnegie Mellon show stronger intensity of the (104) peak. The reason for this observation could be because the transition metals in the oxide fabricated by FMC oxidize better which minimizes their misposition on Li sites. The exact reasons from the point of view of crystallography will be investigated in the future.

5. FMC materials show a broad particle size distribution which is similar to the materials synthesized at Carnegie Mellon using the rotary evaporation process described in the previous section. The faceted morphology of crystallites are similar to the materials synthesized using the spray drying process.
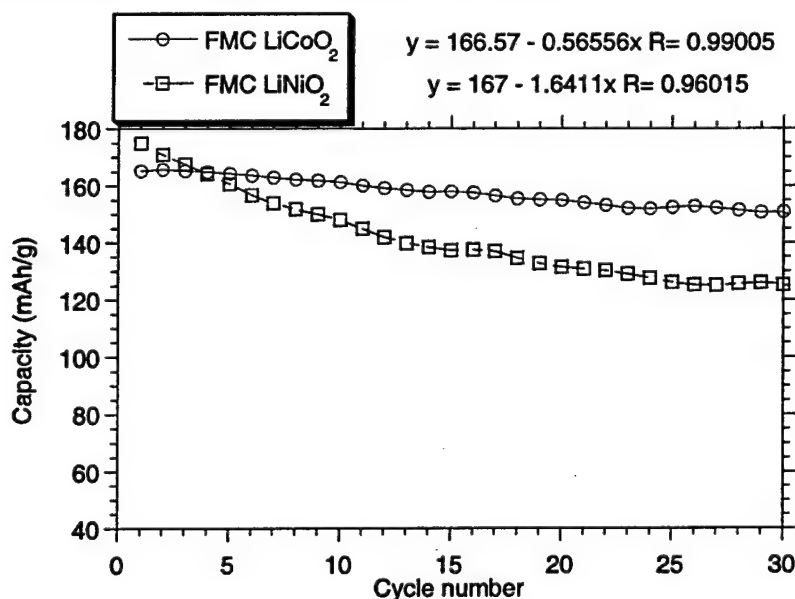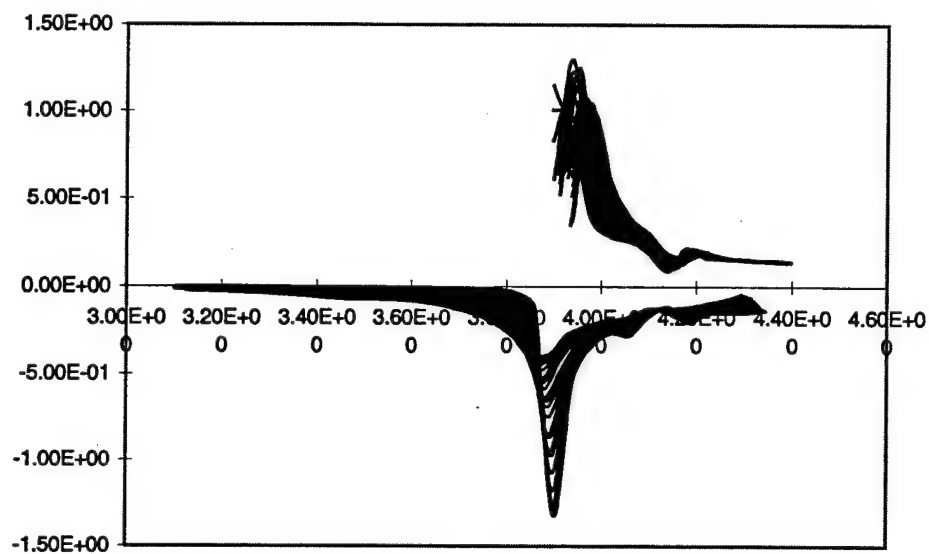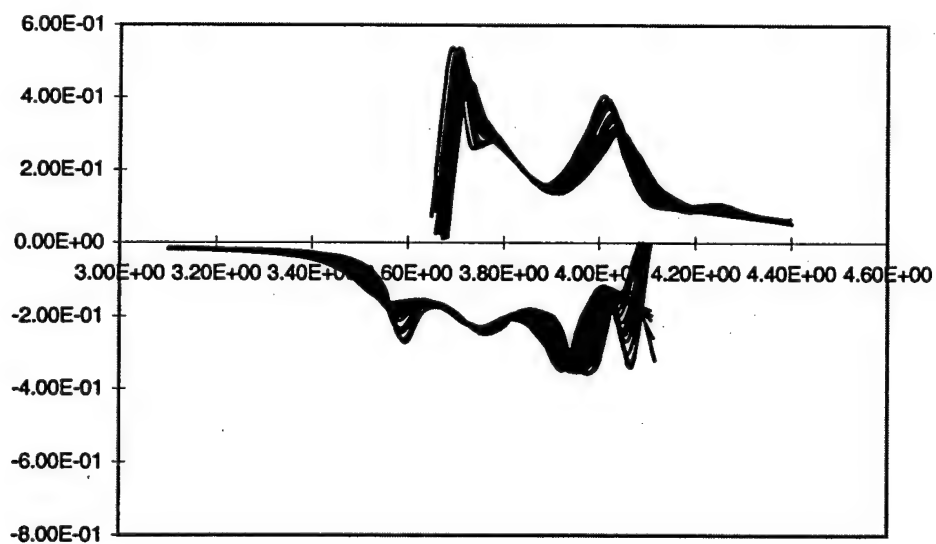

Figure A-7. The capacity versus cycle number of the cathodes of $LiCoO_2$ and $LiNiO_2$ powders procured from FMC. A first discharge capacity of 165mAh/g for $LiCoO_2$ and 175mAh/g for $LiNiO_2$ is observed.
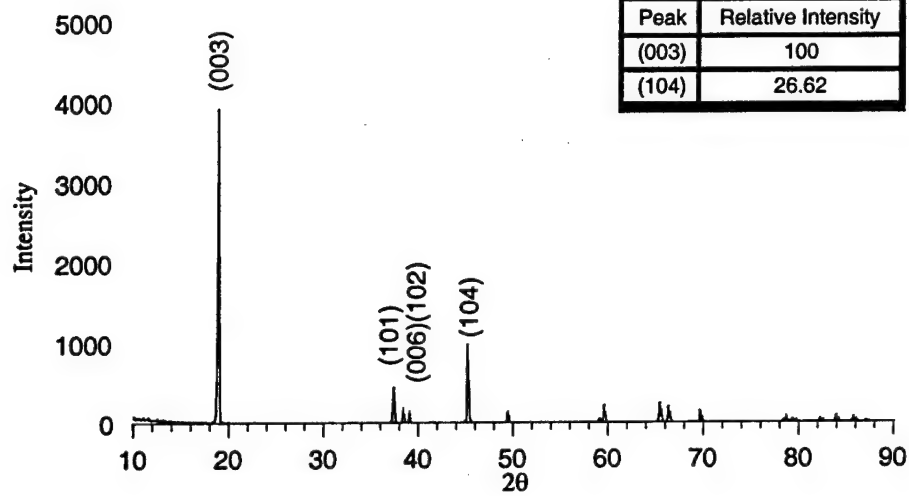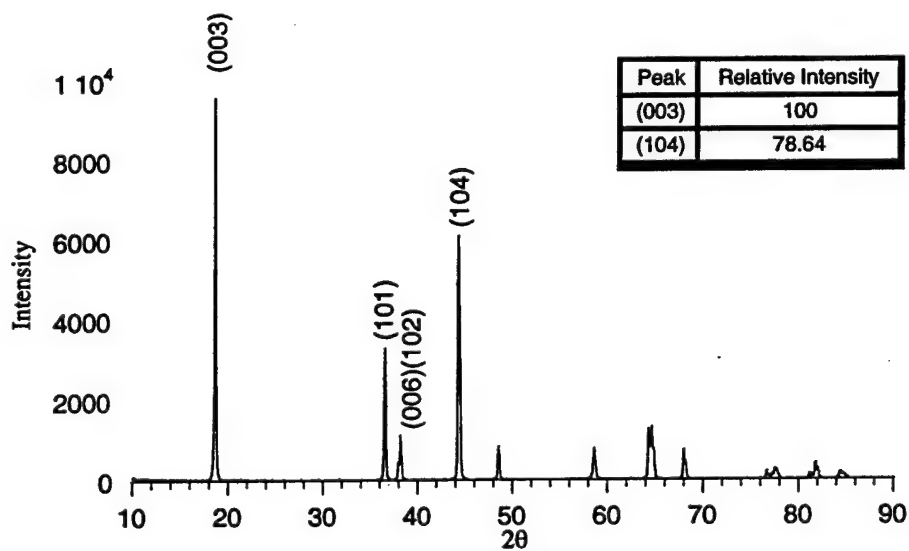
175

(a)

(b)

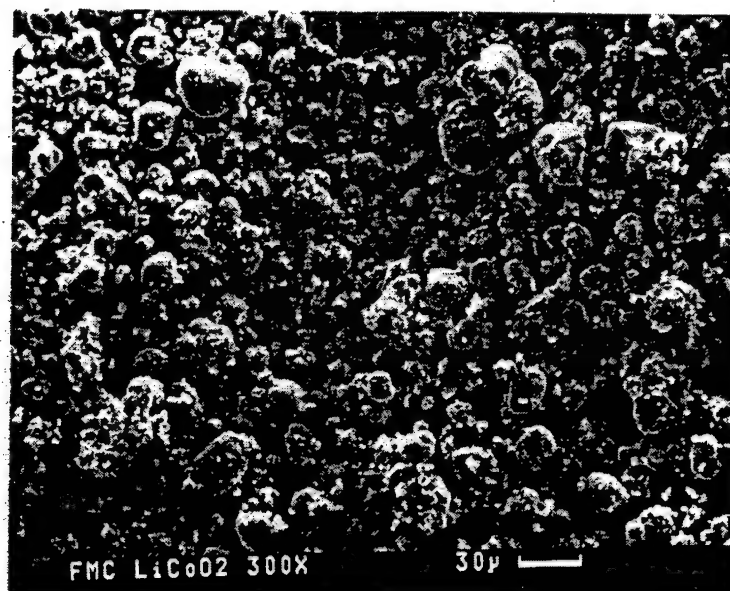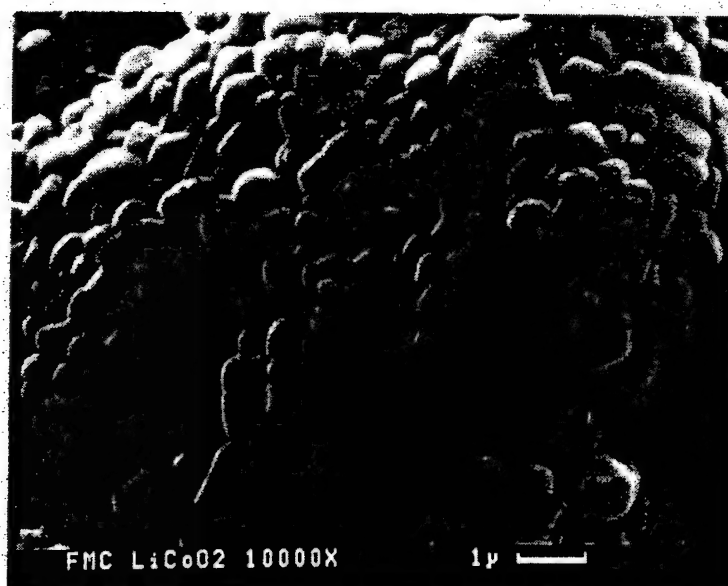Figure A-8. Plot of differential capacity, dQ/dV with voltage, V for (a)LiCoO$_2$ and (b)LiNiO$_2$ procured from FMC.

176

Figure A-9. The X-ray diffraction patterns of (a)LiCoO$_2$ and (b)LiNiO$_2$ procured from FMC. The intensity of the (104) peak is weak in both cases.

(a)

(b)

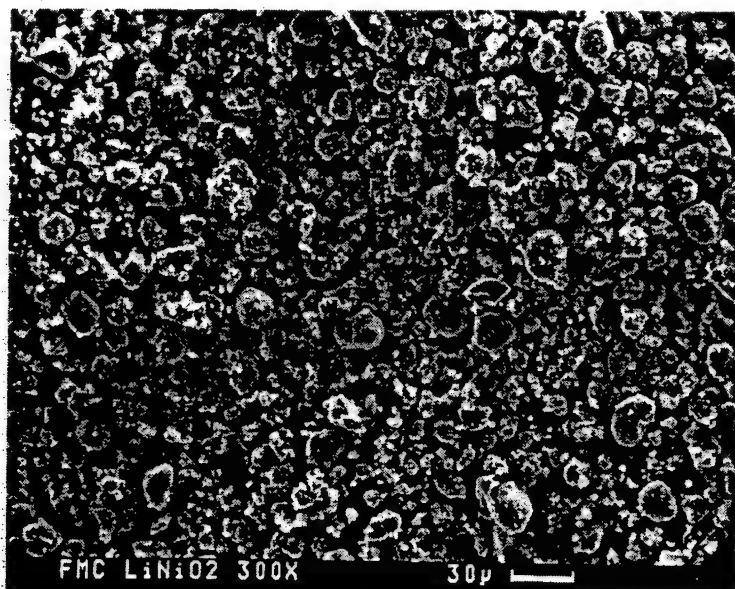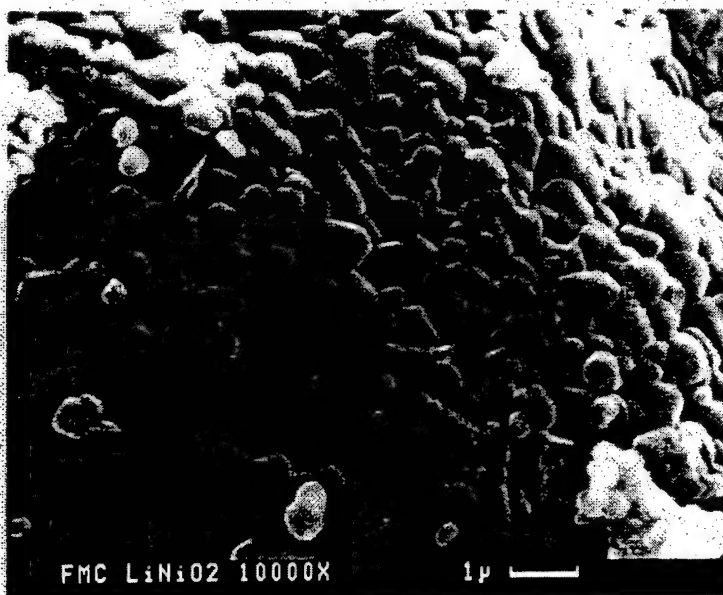Figure A-10. SEM micrographs showing the morphology of FMC procured LiCoO₂ powders. (a) magnification of 300X and (b) 10000X.

(a)

(b)

Figure A-11. SEM micrographs showning the morphology of FMC procured LiNiO$_2$ powders. (a) magnification of 300X and (b) magnification of 10000X.

Appendix B

**Synthesis and structural characterization of lithium carbonate and nickel oxide for kinetic studies**

B.1 The crystal structure and physical property of lithium carbonate

The simultaneous TGA/DTA data of Li_2CO_3 procured from Aldrich (98% purity) is shown in Fig. B-1(a). This data is obtained by using a heating rate of $10^{\circ}C/min$ to $800^{\circ}C$. From the DTA data shown in Fig. B-1(a), it is clear that Li_2CO_3 undergoes melting at $\sim 723^{\circ}C$. The weight loss observed from the TGA curve after melting of Li_2CO_3, is identified to be due to the decomposition of Li_2CO_3 based on the analysis of the gas evolved using the in-situ mass spectrometer attachment as shown in Fig. B-1(b). Since no obvious increase in CO (M.W. = 28) is observed from the mass spectra, the decomposition reaction can be expressed to be the following:

$$Li_2CO_{3\,(l)} \longrightarrow Li_2O_{(s)} + CO_{2\,(g)} \qquad \text{(B-1)}$$
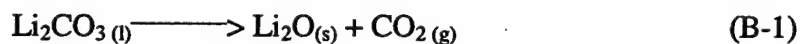
Similar results were obtained by heat treating Li_2CO_3 in argon. The evolution of carbon dioxide when Li_2CO_3 is heat treated in both air and argon is shown in Fig. B-1(c) for comparison. Since the temperature associated with the release of carbon dioxide is not altered with the change in the reactive gas environment, it can be concluded that the decomposition of Li_2CO_3 is not gas assisted. In other words, the decomposition of Li_2CO_3 is mainly a thermally activated process.

The crystallographic data of Li_2CO_3 obtained from National Bureau of Standard (NBS) [1] is shown in Table B-1. By trying the general Wyckoff positions obtained from the International Table of Crystallography [2] and assuming the local structure of Li_2CO_3 as:

$$
\begin{array}{c}
O \\
\| \\
C \\
\diagup \quad \diagdown \\
O^- \qquad O^-
\end{array}
$$
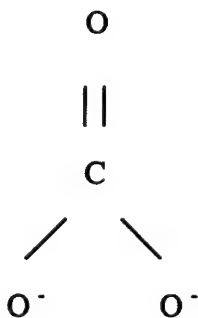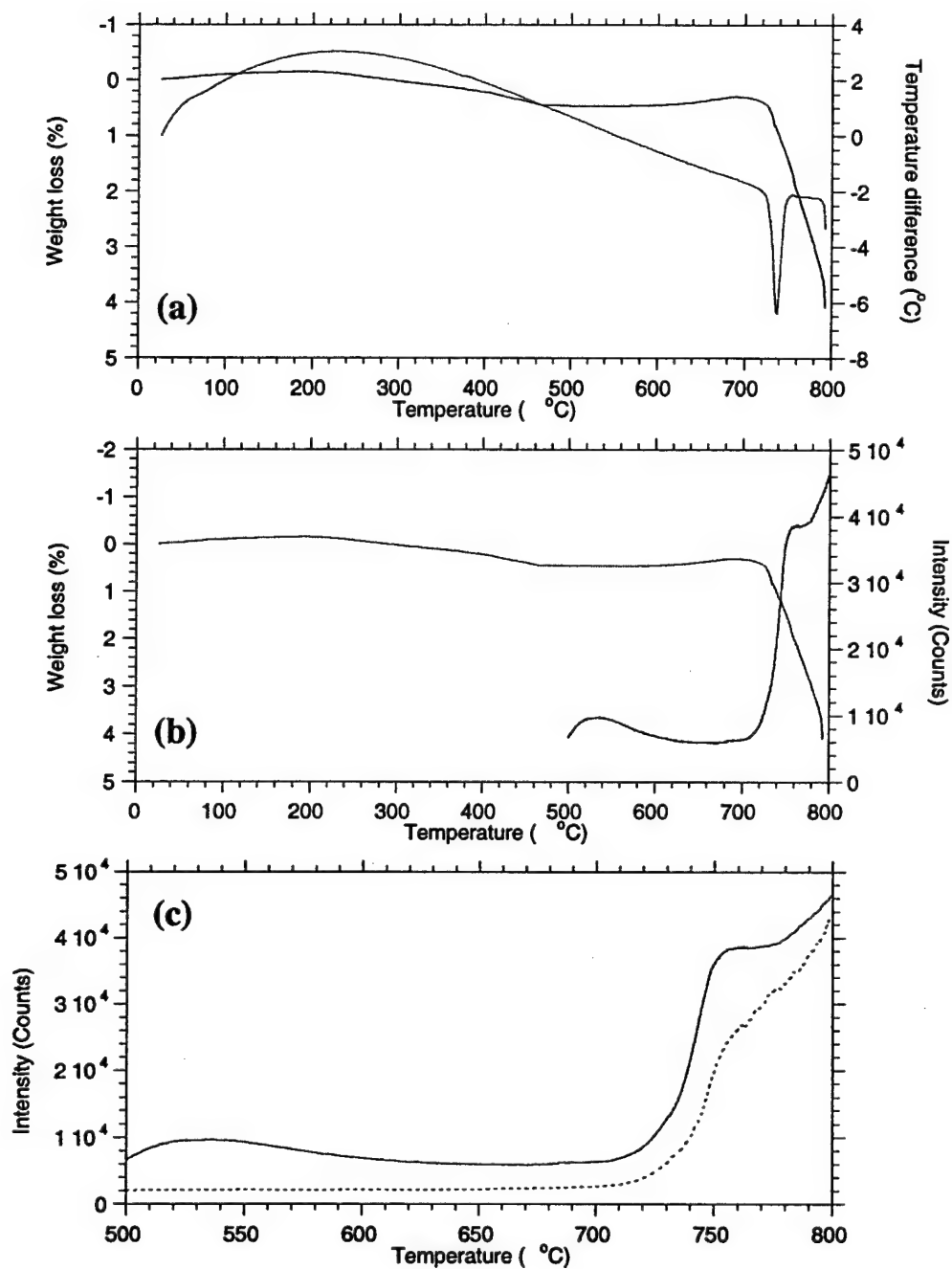
Fig. B-1. (a) The simultaneous TGA/DTA data of Li_2CO_3 procured from Aldrich. The melting of lithium carbonate can be clearly seen from the DTA. (b) The decomposition of Li_2CO_3 with the evolution of carbon dioxide is monitored by the in-situ Mass spectrometer. (c) The mass spectra collected for lithium carbonate heat treated in air (——) and argon (······).

Table B-1

Bravais Lattice	Monoclinic
Space group	C2/c
a	8.359 Å
b	4.9767 Å
c	6.194 Å
β	114.72°
Density	2.096 g/cm^3

Table B-1. The crystallographic data for lithium carbonate (Li_2CO_3) obtained from National Bureau of Standard (NBS)

The crystal structure of Li_2CO_3 is constructed and identified using the Rietveld refinement technique. The refinement results of the X-ray diffraction pattern, the simulated X-ray diffraction pattern as well as the detailed refinement results are shown in Fig. B-2(a), (b) and Table B-2. The simulated XRD was determined using CaRine (Version 2.0) Based on the results of the Rietveld refinement, the carbon atoms and one third of oxygen atoms occupy the 4(e) sites with different y values. The other two third of oxygen atoms and the lithium atoms occupy the 8(f) sites with different x, y and z values respectively. The unit cell of Li_2CO_3 is shown in Fig. B-3. From Fig. B-3 it can be seen that the Li is sitting on the tetrahedral site shared by 4 nearest oxygen anions with a bond length of ~2.8 $\overset{o}{A}$.

The specific surface area of commercial Li_2CO_3 used for the kinetic study is about 1.15 m^2/g.
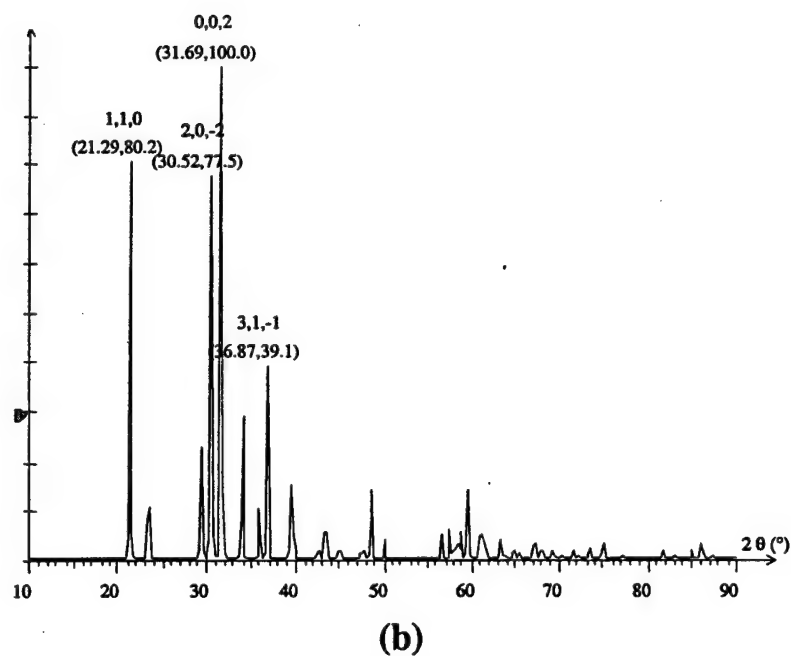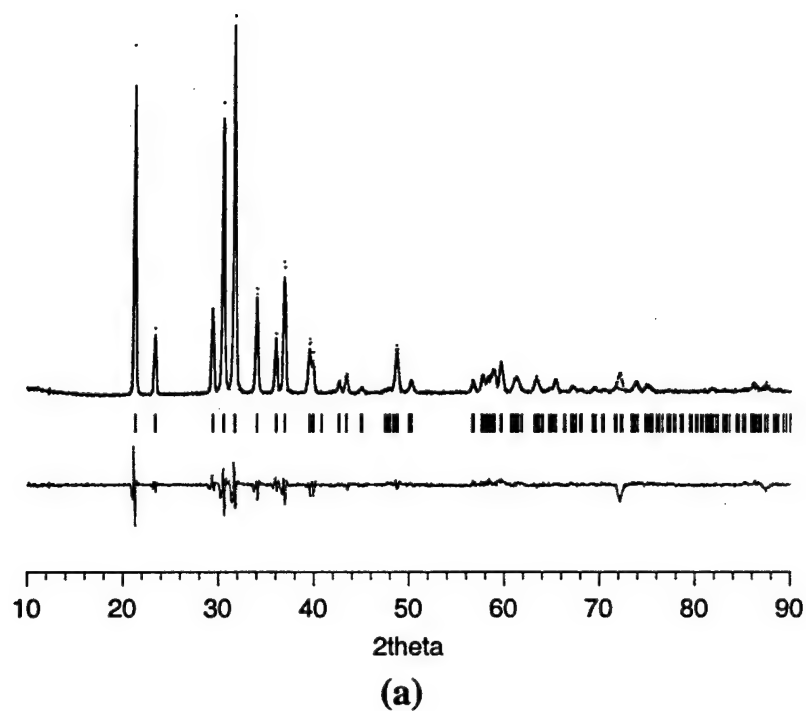
Fig. B-2 (a) The Rietveld refinement results conducted on the experimental X-ray diffraction pattern. The final R_{wp} value obtained is 15.65%. (b) The simulated X-ray diffraction pattern for Li_2CO_3.

Atom positions	
C (4e)	(0, y, ¼) y=0.05754
O (4e)	(0, y, ¼) y=0.32237
O (8f)	(x, y, z) x=0.35297 y=0.43776 z=0.18817
Li (8f)	(x, y, z) x=0.29801 y=0.05521 z=0.15616
Lattice parameters	
a	8.379 Å
b	4.987 Å
c	6.212 Å
β	114.75°

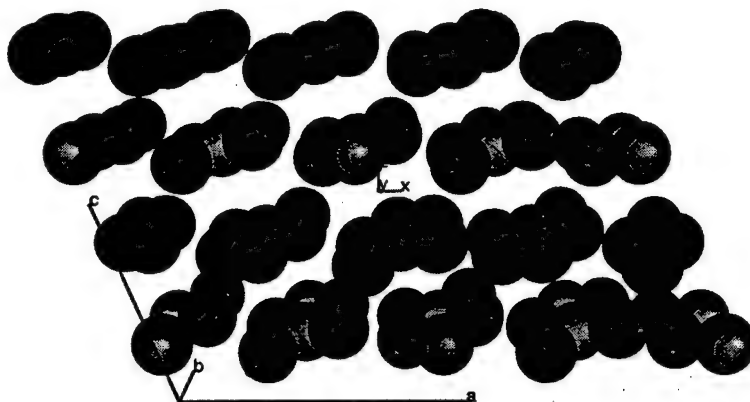Table B-2. Detailed crystallographic parameters of Li_2CO_3 obtained from the Rietveld refinement.

Fig. B-3. The unit cell of Li_2CO_3. Large dark spheres represent O, the light gray intermediate spheres represent C, and the small light gray spheres represent Li ions.

B.2 The crystal structure and defect concentrations in the synthesized nickel oxide

The nickel oxide used for the kinetic study in the present thesis work is synthesized by heat treating commercial nickel hydroxide (Aldrich, 98%) in air at 800°C for 2 hours. The X-ray diffraction pattern of the as-synthesized nickel oxide is shown in Fig. B-4. Similar to lithium carbonate, the crystallographic data of nickel oxide is obtained from the National Bureau of Standard (NBS) [3] which is shown in Table B-3. By calculating the number of atoms in the unit cell using the information of density and lattice parameters obtained from Table B-3, only two special Wyckoff positions (from the International Table of Crystallography) can be chosen, namely (0,0,0) and (½, ½, ½) for both oxygen and nickel respectively. The results of Rietveld refinement are shown in Fig. B-5 and Table B-4 respectively. It should be mentioned that the lattice defects (usually nickel vacancies) are particularly refined in this case, which is important for the study of the reaction mechanism and kinetics of formation of $LiNiO_2$ discussed in section 5.13. Fig. B-6 shows the X-ray simulation pattern for stoichiometric as well as defective nickel oxide. Fig. B-6(a) shows the stoichiometric nickel oxide and Fig. B-6(b) shows the nickel oxide with 10% nickel vacancy. It should be noticed that the (111) peak diminishes with the increase in nickel vacancy. The unit cell of nickel oxide is also shown in Fig. B-7. The synthesized nickel oxide in the present case has a surface area of 1.8 m^2/g.
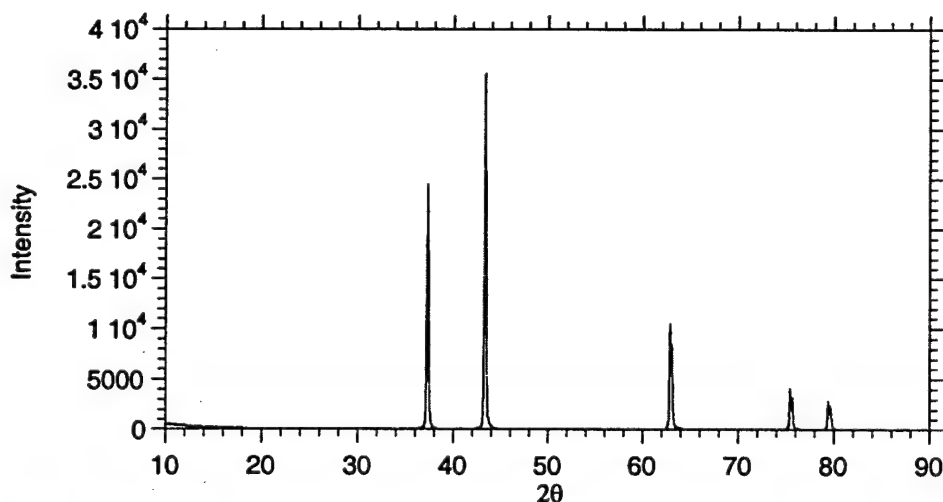

Fig. B-4. The X-ray diffraction pattern of the as-synthesized nickel oxide that was prepared by heat treating nickel hydroxide in air to 800°C for 2 hours.

186

Table B-3

Bravais Lattice	Cubic
Space group	Fm $\bar{3}$ m
a	4.177 Å
Density	6.806 g/cm^3

Table B-3. The crystallographic data of nickel oxide (NiO) obtained from National Bureau of Standard (NBS).

Table B-4

Atom positions	
Ni (4b)	(½,½,½)
O (4a)	(0, 0, 0)
Nickel occupancy	0.9748
Oxygen occupancy	1.0000
Lattice parameters	
a	4.17583 Å

Table B-4. The results obtained from the Rietveld refinement of NiO.
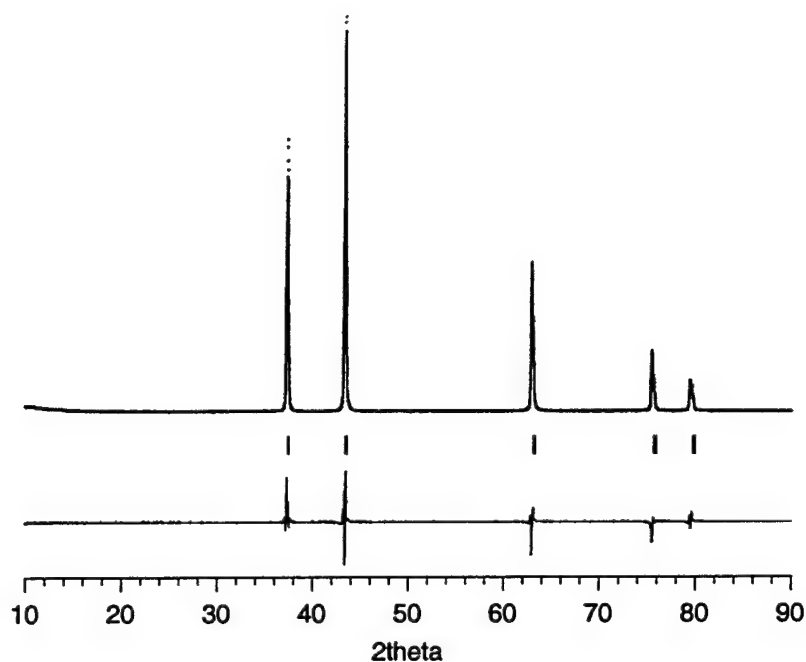
Fig. B-5. The results of Rietveld refinement. The R_{wp} value obtained is 16.85 in this refinement work.
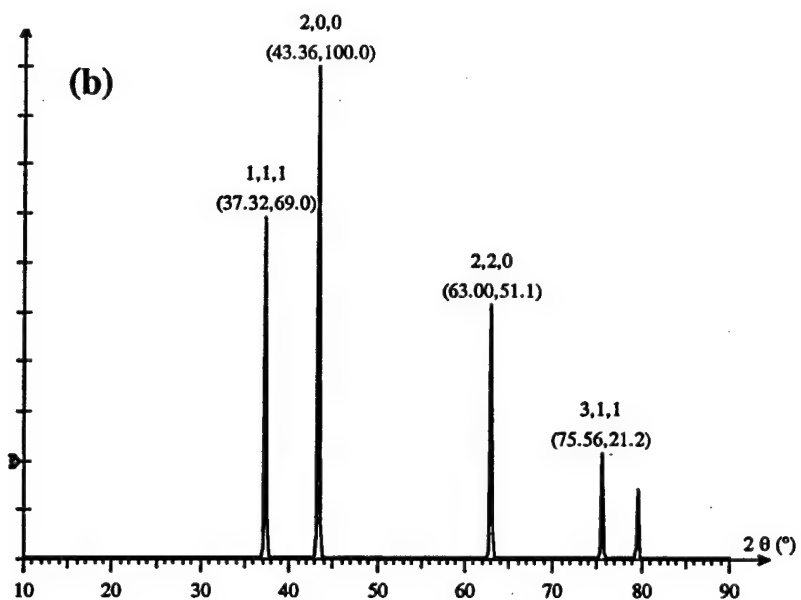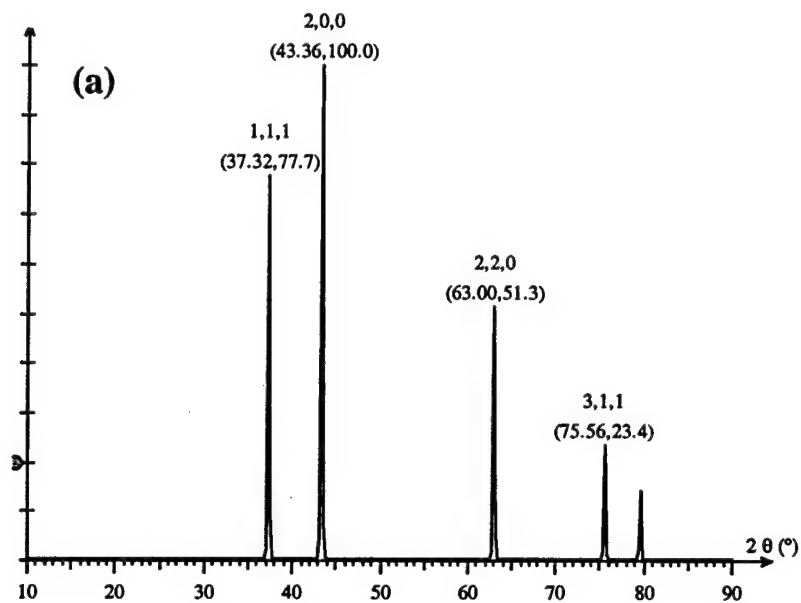
Fig. B-6(a) shows the stoichiometric nickel oxide and Fig. B-6(b) shows the nickel oxide with 10% nickel vacancy. It should be noticed that the (111) peak diminishes with the increase in nickel vacancy.

188
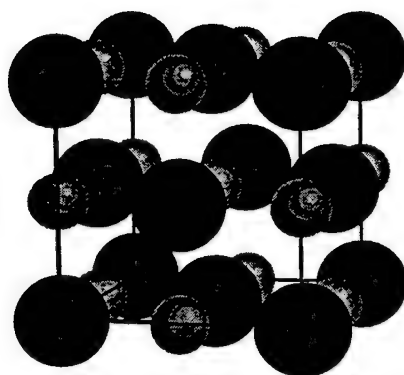
Fig. B-7. The unit cell of nickel oxide. The oxygen atoms are occupying the (0,0,0) positions and the nickel atoms are occupying the (½, ½, ½) positions.

References

1. Swanson, Tatge, Natl. Bur. Stand. (U.S.), Circ, 539,1   47(1953)

Appendix C

**Synthesis and Electrochemical Characterization of
Divalent Cation Substituted Lithium Nickel Oxide**

Abstract

Divalent cation substituted $Li_{1+x}NiMg_xO_{2(1+x)}$ materials, corresponding to $LiNi_{1-y}Mg_yO_2$ ($y=x/(1+x)$), represent a new class of materials with unique electrochemical characteristics. These materials ($x=0$, 0.05, 0.10, 0.15 and 0.20) have been successfully synthesized and electrochemically characterized. Elimination of phase transformations accompanied with smaller changes in unit cell volume during cycling are achieved by inducing divalent cations completely on the transition metal sites alone. Excellent cyclability at high voltages (4.4V) as well as higher thermal stability in comparison to undoped $LiNiO_2$ are the major characteristics of these divalent cation substituted materials. A decrease in the fade in capacity for the initial cycles with the increase in the addition of Mg is attributed to the prevention of decomposition of the oxide caused by its substitution of the transition metals. The reason for the suppression of this decomposition reaction is also investigated by examining the thermal stability of both $LiNiO_2$ and $Li_{1.15}NiMg_{0.15}O_{2.3}$ when charged to the same extent (0.7 of Li) using differential thermal analysis (DTA). This additional result indicates that the suppression of the decomposition reaction is not only due to the prevention of overcharging of the material but also the stabilization of the NiO_2 slabs caused by the substitution of Mg.

Introduction

Layered lithiated transition metal oxides $LiMO_2$ (M= Mn, Ni, Co, Ni_xCo_{1-x}) have been the focus of considerable attention in recent years for lithium-ion battery applications due to their high energy density and capacity [1-11]. Among these compounds, Ni based $LiNiO_2$ is of considerable interest. This is primarily because of the abundance and the environmentally benign nature of Ni as well as the large capacity possessed by the oxide in comparison to $LiCoO_2$. Many attempts have been made to synthesize defect-free stoichiometric $LiNiO_2$ in order to increase the Li diffusivity and therefore the capacity [12-16]. Unfortunately, a large capacity is usually accompanied by large fade. One of the reasons suggested for the capacity fade is the decomposition of the material when charged to high voltages [17-19]. The decomposition reaction of charged cathode materials also causes gas evolution, decreasing not only the lifetime but also the reliability of the batteries. Another important reason for the fade in capacity is significant

volume changes in the material accompanied by phase transformations which lead to microcracking or debonding of the cathode materials and the binder [20].

Several attempts have therefore been made to stabilize the layered structure by substituting the Ni cations with other elements such as Cr, Mn, Fe and Al [21-25]. The effect of stabilizing the Ni based oxide with a combination of Co and Mg, or Ti and Mg have also been reported by us and others recently [26, 27]. However, to the best of our knowledge there has been no systematic work reported relating the incorporation of Mg ions on the transition metal site to the electrochemical properties of these materials. The present work reports the structural and electrochemical changes induced by the introduction of Mg on the transition metal site. Five new compositions based on $LiNiO_2$ as the parent compound have been synthesized and electrochemically characterized. The target materials synthesized in the present work possess a general chemical formula of $Li_{1+x}NiMg_xO_{2(1+x)}$ with x ranging from 0 to 0.2, corresponding to $LiNi_{1-y}Mg_yO_2$ (y=x/(1+x)). The former nomenclature will be followed throughout the manuscript for clarity.

Experimental

All the compositions reported in this work were synthesized using the conventional solid state process. The exact procedure for preparing the precursors is as follows: $LiOH \cdot H_2O$ (Aldrich, 98%), $Ni(OH)_2$ (Aldrich, 98%) and $Mg(OH)_2$ (Aldrich, 98%) corresponding to 0.2 moles of the final product ($Li_{1+x}NiMg_xO_{2(1+x)}$) were first weighed according to the stoichiometry of Li: Ni: Mg = (1+x): 1: x with x = 0, 0.05, 0.10, 0.15 and 0.20. A 2 mol% excess lithium was added to compensate for the volatilization of Li during the synthesis of the materials and thereby minimize the misposition of Ni

192

cations on the Li site creating an anti-site defect. The powders were transferred to a 250ml high density polyethylene (HDPE) container containing zirconia balls (~16 pieces, ~23g/piece). The bottle was then sealed with insulation tape and rotated at a rate of 200 rpm. After 24 hours of milling, the as-prepared precursor powders were subjected to subsequent heat treatments. The heat treatment conditions comprised of two hours of heat treatment at 700°C in air followed by 10 hours of heat treatment in oxygen at 750°C. The heat-treated powders were then ground and sieved under 325 mesh for X-ray diffraction (XRD, Rigaku θ/θ diffractometer) and electrochemical characterization.

Systematic Rietveld refinement using the Rietan94 software were conducted on the X-ray diffraction patterns obtained for the heat-treated powders as well as the electrochemically charged samples.

Cathodes for electrochemical characterization were fabricated by coating aluminum foils with the synthesized powders. A slurry containing 87.1wt% synthesized material, 7.6wt% acetylene black and 5.3wt% copolymer binder (ethylene/propylene copolymer containing 60% ethylene content) was made using TCE (Trichloroethylene) as the solvent. The punched out cathodes were $1cm^2$ in area, ~0.0076cm in thickness and 0.01g in weight. A three electrode Hockey Puck type cell design was used [28, 29] employing lithium foil as an anode and utilizing 1M $LiPF_6$ in EC/DMC (with an EC to DMC wt% ratio of 2 to 1) as the electrolyte. All the electrochemical analysis for the prototype test batteries was conducted using a potentiostat (Arbin electrochemical instrument).

Differential thermal analysis (DTA) on the charged electrodes was also conducted using the simultaneous TG/DTA (TA Instruments, model 2960). Each charged electrode (~10 mg in weight) was analyzed in the DTA using a heating rate of 5°C/min.

Results

The X-ray diffraction patterns of the five synthesized compounds $Li_{1+x}NiMg_xO_{2(1+x)}$ (or $LiNi_{1-y}Mg_yO_2$, y=x/(1+x)) with x= 0, 0.05, 0.10, 0.15 and 0.20 are shown in Fig. 1. Phase pure materials were obtained after heat treatment for each of the doped materials, which is an indirect evidence indicating the occupancy of Mg on the Ni sites. Since the molar ratio of Li / (Ni+Mg) = 1.02/1 in the as-prepared precursor, Mg is presumably residing on the Ni site to maintain the site ratio since Li is not preferably occupying the Ni site due to a larger defect formation energy required for monovalent cations to occupy the trivalent cation sites. The occurrence of Mg cations on the Ni sites is also supported by the results obtained from the Rietveld refinement assuming an $R\bar{3}m$ symmetry. Fig. 2 shows the refinement results for the five samples and Table 1 gives the detailed information obtained for each refinement. The refinement was conducted by allowing Mg ions to sit on both Ni and Li sites. At the same time, two linear constraints were applied, one for the occupancy of Li + Mg(on Li site) = 1 and the other, for the molar ratio of Ni/Mg = 1/x. Thermal parameters were all set to a constant value of 0.4 during the refinement process. From the results of the refinement summarized in Table 1, it can be seen that under the conditions and constraints described earlier, a global minimum can be achieved with a major fraction of Mg ions sitting on the Ni site (99.8% of Mg on the Ni site for x=0.05, 97.6% for x=0.2). The lattice parameters "a" and "c"

194

increase with an increase in the addition of Mg, reflecting an expansion of the cell volume.

The effect of inducing Mg cations on the Ni sites is also reflected in the samples that are charged and discharged at a very small current. Fig. 3 shows a plot of the first cycle voltage versus Li content for five samples that were charged/discharged at a current density of 10 $\mu A/cm^2$ between 3.1 to 4.4 V approximately corresponding to a C-rate of C/100. The voltage detected is related to the open circuit voltage and the intrinsic resistance of the material, represented by the equation:

$$V_{obs} = V_{oc} + V_{IR}$$

V_{obs} is the measured voltage, V_{oc} is the open circuit voltage and V_{IR} is the voltage arising during cycling owing to the resistance of the electrode (positive during charging and negative during discharging). Thus, observed voltage is very close to the open circuit voltage when small charge/discharge currents are utilized. It can be seen in Fig. 3 that the capacity decreases with an increase in the addition of Mg. The decrease in capacity is almost equivalent to the amount of inactive species in the oxide which are Mg^{2+} and identical amount of Ni^{4+} created by the insertion of Mg. The formation of Ni^{4+} can be justified based on charge balance. Thus, the fact that the decrease in capacity is close to twice the molarity of Mg implies the occupancy of Mg on the transition metal sites. It should be mentioned that the lithium content is calculated considering the theoretical capacity of 273mAh/g for $LiNiO_2$ and 278, 282, 286, 290mAh/g for $Li_{(1+x)}NiMg_xO_{2(1+x)}$ corresponding to x=0.05, 0.10, 0.15, 0.20 respectively.

The theoretical capacity is calculated based on the assumption that Mg substitutes for Ni. The increase in the theoretical capacity with increase in the amount of Mg substituted for Ni is due to the lighter weight of Mg in comparison to Ni. In contrast to the observed decrease in capacity due to the introduction of Mg, the cycling voltage is however increased with the addition of Mg. Fig. 4 shows the superimposed plot of voltage versus lithium content for five different compositions. It can be seen in Figure 4 that the cycling voltage is increased with increase in the content of Mg when the samples are charged to an identical depth of charge corresponding to z=0.65 (solid line) in $Li_{1-z}Ni_{1-y}Mg_yO_2$. The average voltage is calculated by using the following formula:

$$\overline{V} = \left(\int_{Q_1}^{Q_2} V dQ \right) \Big/ Q$$

The average voltage for the same depth of charge (z=0.65 in $Li_{1-z}Ni_{1-y}Mg_yO_2$, solid line in Fig. 4) is seen to increase from 3.81V for $LiNiO_2$ to 3.97V for $Li_{(1+x)}NiMg_xO_{2(1+x)}$, x= 0.20. Furthermore, it can be seen that the large number of plateaus in the charge/discharge curve as shown in Fig. 3, which is the characteristic of plain $LiNiO_2$, is significantly diminished with the increase in the addition of Mg. This observation is directly linked to the elimination of phase transformations during the charge/discharge process due to the incorporation of Mg, as revealed by the differential capacity (dQ/dV) versus voltage (V) plot shown in Fig. 5. The occurrence of several peaks during the charge/discharge process for $LiNiO_2$ is due to its characteristic phase transformations [1, 2].

The addition of Mg suggests the suppression of these phase transitions during cycling. The phase pure nature of the synthesized materials revealed by XRD and the

systematic Rietveld refinement conducted on these materials, combined with the loss of capacity shown by the low current charge/discharge profiles (see Fig. 3), clearly suggest the occurrence of Mg cations on the transition metal site and a minimum misposition of Ni on the Li site. It is reported that phase transformations during cycling occurs in undoped $LiNiO_2$ when $LiNiO_2$ is close to stoichiometric [1, 2]. It is also reported that the phase transformations can be delayed during cycling in the non-stoichiometric $LiNiO_2$ possessing a singnificant amount of anti-site disorder of Ni occupying the Li position. The fact that the concentrations of divalent Ni or Mg cations on Li sites are marginal in $Li_{(1+x)}NiMg_xO_{2(1+x)}$, therefore, implies that the suppression of phase transformations during cycling can not be attributed to the presence of divalent cations (divalent Ni or Mg) on the Li sites but rather to the presence of divalent Mg cations on the Ni site. The effect of the suppression of phase transformations on the cycling property of the materials will be discussed in the subsequent sections to follow.

In order to confirm the suppression of phase transformations during cycling with the introduction of Mg cations, as well as to obtain more structural information of the material during the deintercalation process, systematic X-ray diffraction analysis was conducted on $Li_{1+x}NiMg_xO_{2(1+x)}$, x= 0.15 which were charged to different Li contents. The cathodes prepared using $Li_{1+x}NiMg_xO_{2(1+x)}$, x= 0.15 were first charged at a slow rate (~C/20) to different depths based on the weight of the cathode and the theoretical capacity of this material (286 mAh/g). After charging, the cathodes were carefully removed from the test batteries. The residual electrolyte was removed by rinsing the cathodes with acetone followed by drying at 80°C for 30 minutes in the drying oven. The XRD pattern collected on the as-prepared uncharged cathode is shown in Fig. 6(a).

197

Several impurity peaks were observed and identified to be arising from the aluminum foil used as current collector and the acetylene black used as the conducting medium, respectively as shown in Fig. 6(b) and 6(c). In order to eliminate these impurity peaks which can interfere with the refinement results, the XRD peaks obtained from both the cathode film without charging and the as-synthesized material were first normalized to unity. Subtraction of the two data gives a plot that is representative of the data points for the impurity peaks which was utilized for eliminating the peaks of the impurities in the charged cathodes. It should be mentioned that only 7 samples (Li content ranging from 0.1 to 0.7) were obtained owing to the loss in capacity caused by the occupation of Mg cations on the transition metal site which can not be charged further without inducing a rapid increase in the voltage. The XRD results of these seven charged samples are shown in Fig. 7. No variation in the number of peaks during the charging process (up to 0.7 of Li) was observed in XRD patterns. This result implies that the symmetry of the material is maintained during the charging process and the phase transformations are eliminated. Results of the Rietveld refinement conducted on these charged samples are also shown in Fig. 8.

The Rietveld refinement based on an $\overline{R3}m$ symmetry was conducted on these charged samples, applying the following constraints: (i) The occupancy of Ni+Mg = 1. (ii) The molarity of Ni:Mg = 1: 0.15. The refinement results obtained for these charged samples are shown in Table 2. The refinement results clearly shows that the phase transformations have been eliminated during the deintercalation process which is consistent with the result obtained from the dQ/dV versus V curve as shown earlier in Fig. 5. The decrease in the lattice parameter "a" and the increases in the lattice parameter

198

"c" with the increase in the depth of charge is similar to the case observed for $LiNiO_2$ as reported in the literature [30, 31]. However, smaller volume contraction (1.83%) is observed for the present material in comparison to $LiNiO_2$ (2.87% reported by Ohzuku et al. [30] and 2.77% by W. Li et al. [31]) when charged to the same extent (0.3 of Li content).

Results of the cyclability test conducted on the five different compositions are shown in Fig. 9. This figure shows the capacity of the five oxides with different Mg additions versus cycle number for the first 30 cycles. The test batteries were cycled between 3.1 to 4.4 V using a current density of $0.25 mA/cm^2$ corresponding to a C-rate of approximately C/2. It can be seen that the fade rate is highest 0.68%/cycle for the plain $LiNiO_2$ in comparison to 0.19, 0.05, ~0, 0.12%/cycle observed for $Li_{1+x}NiMg_xO_{2(1+x)}$, x= 0.05, 0.10, 0.15 and 0.20 respectively which reveals the fact that the rate of capacity fade is decreased with the increase in the addition of Mg. Fig. 10 shows the differential capacity (dQ/dV) versus cell potential (V) curves corresponding to these five test batteries. The width of the first 30 cycle since dQ/dV versus V curves characterizes the reduction in fade of the materials during cycling with the increase in the addition of Mg. In the case of $LiNiO_2$, the curves shift up to higher voltages during the charging process and shift down to lower voltages during the discharging process with significant reduction in the peak intensity. These results clearly reflect the fade of the material and an increase in the internal resistance of the electrode during cycling. In contrast, with the increase in the addition of Mg, the dQ/dV versus V curves for the first 30 cycles reveal a progressive reduction in these fluctuations. Moreover, the differential capacity curves for

each cycle appear to overlap giving a single curve which clearly characterizes the reduction in fade of the materials during cycling.

In order to exemplify this unusual structural stability, thermal stability tests were conducted employing differential thermal analysis (DTA) on the five materials that were charged up to 4.4 V using a small current ($10\mu A/cm^2$) using the DTA. In order to compare the thermal transformations for the various electrodes, the electrodes were chosen to have similar weight ($0.0100g \pm 0.0002g$) for quantitative analysis. Fig. 11 shows the DTA results obtained on these five charged electrodes. It can be seen that the exothermic peak for undoped pure $LNiO_2$ occurs at around 220^oC which represents the decomposition reaction leading to the evolution of oxygen as reported earlier [26]. However, this exothermic peak intensity is seen to largely decrease with the increase in the addition of Mg. Moreover, the onset temperature of the exothermic reaction is seen to increase with the addition of Mg. The decrease in the exothermic peak intensity and the delay in the exothermic reaction temperature directly shows the increase in thermal stability of the material at high temperatures. Furthermore, the results give an indication of the stronger oxygen affinity of Mg leading to an increase in the thermal stability of the material with an increase in Mg addition, when charged to the same voltage (4.4V). This improved thermal stability suggests that the Mg ions help to lock the oxygen ions particularly during charging due to its strong oxygen affinity. Thus the addition of Mg ions would significantly help to reduce the evolution of oxygen during cycling which is an important issue for safety consideration.

Discussion

Four important characteristics are exhibited by the oxide containing divalent cations such as Mg substituted for the transition element Ni. First, the lattice expansion/contraction during cycling is minimized. Second, the phase transformations during cycling is suppressed. Third, the thermal stability of the charged samples is seen to increase with the increase in the substitution of Mg cations. Finally, the cyclability of the material is improved with the increase in the addition of Mg. It has been reported so far that two factors are mainly responsible for limiting the cyclability of the lithiated transition metal oxides.

a) Decomposition of the materials during charging to high voltages [17-19]:

b) Significant volume change of the material accompanied by phase transformations during cycling which causes micro-cracking of the material therefore increasing the internal resistance of the electrode [20]. As a result, the material exhibits fade in capacity during cycling.

In the present work, the oxide doped with Mg^{2+}, i.e. $Li_{1+x}NiMg_xO_{2(1+x)}$, x= 0.15 exhibits a smaller volume change during charging. Furthermore, the exothermic reaction due to the decomposition of materials is delayed and suppressed to a large extent in comparison to $LiNiO_2$ as shown by the DTA analysis. This implies that the Mg-doped material is strained to a lesser extent in comparison to $LiNiO_2$ during the intercalation/deintercalation process and the tendency of the material to decompose during cycling is also reduced. As a result, the Mg-doped oxide exhibits better cyclability (less fade in capacity during cycling).

The improvement in cyclability by substituting Mg cation into $LiNiO_2$ can be attributed to the minimization of the change in lattice parameter, elimination of phase transformations and the suppression of decomposition during cycling. However, it is not clear which of these factors mainly contribute to the improved cyclability of this material. In order to clarify the contributions of each of these factors to the capacity retention for the initial 30 cycles, a comparison of the cycling behavior between $Li_{1+x}NiMg_xO_{2(1+x)}$, x=0.15 and $LiNiO_2$ charged to the same Li content level (0.3 of Li content) was initiated. The results of $LiNiO_2$ for the first 30 cycles are shown in Fig. 12. Almost no fade in capacity is observed when the material is charged up to 0.3 Li content. This implies that the elimination of phase transformations and the decrease in volume change during cycling of the Mg-doped oxide ($Li_{1+x}NiMg_xO_{2(1+x)}$) are not the main reasons that cause the decrease in fade of these doped materials in the initial cycles. The differential capacity (dQ/dV) versus cell potential (V) plot of the same test battery shown in Fig. 12(b) shows a much narrower line width (no significant shift of the peak) for the first 30 cycles compared to the oxide that was charged 4.4V as shown in Fig. 10. From the thermal analysis results shown in Fig. 11, it can be concluded that the delay of the decomposition reaction is indeed the main factor contributing to the decrease in the initial cycle capacity loss in the Mg substituted oxide. This result reflects the main function of Mg in these oxides to prevent the initial capacity loss for the first 30 cycles, which is shown in $LiNiO_2$ when cycled to 4.4V. Although the elimination of phase transformations and the decrease in volume change during cycling are not largely responsible for the initial capacity loss, it can however be beneficial and therefore necessary to stabilize the cyclability over longer cycles.

Finally, in order to confirm the role of Mg in suppressing the exothermic reaction one more thermal analysis experiment was conducted for comparing two electrodes, $LiNiO_2$ and $Li_{1+x}NiMg_xO_{2(1+x)}$, x=0.15, utilizing an identical weight of the cathodes that was charged to the same Li content (i.e. charged to 0.3 in Li content). The result of the DTA analysis conducted on these charged samples are shown in Fig. 13. It can be seen that $LiNiO_2$ sample still exhibits a much more intense exothermic reaction at a lower temperature compared to $Li_{1+x}NiMg_xO_{2(1+x)}$, x=0.15, although those samples were charged to the same Li content. This results clearly suggest that the delay of the decomposition reaction and the reduction in the exothermic peak intensity observed in the Mg-substituted materials is not due to the larger amount of Li retained after charging, but that the substitution of Mg for Ni indeed enhances the oxygen affinity of the NiO_2 slabs therefore suppressing the exothermic reaction at high temperatures. In other words, substitution of Mg helps to maintain a more rigid oxidation state of the transition metal cations in the Mg-doped materials. As a result, it can be expected that the material exhibits a lesser tendency to undergo decomposition reaction during cycling compared to $LiNiO_2$ during cycling.

Conclusions

Doped oxides, $Li_{1+x}NiMg_xO_{2(1+x)}$ (x= 0, 0.05, 0.10, 0.15 and 0.20), were successfully synthesized and electrochemically characterized. XRD and Rietveld refinements of the structure combined with a low current charge/discharge tests indicate unequivocally that the divalent Mg cations reside on the transition metal site. Increasing the amount of Mg in the oxide leads to a suppression of the phase transformations of the oxides during cycling. The smaller cell volume change of the Mg-doped oxide in

comparison to $LiNiO_2$ is also observed in the Rietveld refinement analysis conducted on $Li_{1+x}NiMg_xO_{2(1+x)}$, $x = 0.15$. However, the elimination of phase transformations and the decrease in volume change during cycling of the Mg-doped oxide ($Li_{1+x}NiMg_xO_{2(1+x)}$) are not the main reasons that cause the decrease in fade of these doped materials. This is the case since $LiNiO_2$ also shows good cyclability when charged to 0.3 in Li content which is the range where $LiNiO_2$ undergoes phase transformations and exhibits a larger volume change. The main role of Mg which causes the capacity fade to decrease when charged to higher voltages can be attributed to the suppression of the decomposition reaction. This suppression of the decomposition reaction of the cathodes when charged to high voltages due to the stabilization of the NiO_2 slab by the stronger oxygen affinity of Mg is confirmed by the DTA analysis.

Acknowledgment

References

[1] M. Broussely, F. Perton, P. Biensan, J.M. Bodet, J. Labat, A. Lecerf, C. Delmas, A. Rougier, and J.P. Peres, *J. Power Sources, 54* (1995) 109-114.

[2] W. Ebner, D. Fouchard, L. Xie, Solid State Ionics, 69 (1994) 238-256.

[3] M. Broussely, F. Perton, J. Labat, J. Power Sources, 43-44 (1993) 209-216.

[4] T. Ohzuku, A. Ueda, M. Nagayama, Y. Iwakoshi, and H. Komori, *Electrochimica Acta, 38* (1993) 1159-1167.

[5] T. Nohma, H. Kurokawa, M. Uehara, M. Takahashi, K. Nishio, T. Saito, J. Power Sources, 54 (1995) 522-524.

[6] R. Yazami, N. Lebrun, M. Bonneau, M. Molteni, J. Power Sources, 54 (1995) 389-392.

[7] A. R Armstrong, P. G. Bruce, Nature, 381, 499 (1996).

[8] B. Banov, J. Bourilkov, and M. Mladenov, *J. Power Sources, 54* (1995) 268-270.

[9] C. Delmas, I. Saadoune, A. Rougier, J. Power Sources, 43-44 (1993) 595-602.

[10] C. Delmas, I. Saadoune, Solid State Ionics, 53-56 (1992) 370-375.

[11] D. Caurant, N. Baffier, B. Garcia, J.P. Pereira-Ramos, *Solid State Ionics, 91* (1996) 45-54.

[12] A. Hirano, R. Kanno, Y. Kawamoto, Y. Takeda, K. Yamaura, M. Takano, K. Ohyama, M. Ohashi, Y. Yamaguchi, Solid State Ionics, 78 (1995)123-131.

[13] J. R. Dahn, U. von Sacken, C.A. Michal, Solid State Ionics, 44 (1990) 87-97.

[14] R. V. Moshtev, P. Zlatilova, V. Manev, A. Sato, J. Power Sources, 54 (1995) 329-333.

[15] C. C. Chang, P. N. Kumta, J. Power Sources, 75 (1998) 44-55.

[16] C. C. Chang, P. N. Kumta, Solid State Ionics, 112 (1998) 329-344.

[17] J. R. Dahn, E. W. Fuller, M. Obrovac, U. von Sacken, Solid State Ionics, 69 (1994) 265-270.

[18] W. Juzkow, S.T. Mayer, The 12th Annual Battery Conference on Applications and Advances, California State University, Long Beach, CA. January 14-17, 1997.

[19] Z. Zhang, D. Fouchard, J.R. Rea, J. Power Sources, 70 (1998) 16-20.

[20] T. Ohzuku, A. Ueda, Solid State Ionics, 69 (1994) 201-211.

[21] C. D. W. Jones, E. Rossen, J. R. Dahn, Solid State Ionics, 68 (1994) 65-69.

[22] E. Rossen, C.D.W. Jones, J.R. Dahn, Solid State Ionics, 57 (1992) 311-318.

[23] J.N. Reimers, E. Rossen, C.D. Jones, J.R. Dahn, Solid State Ionics, 61 (1993) 335-344.

[24] T. Ohzuku, T. Yanagawa, M. Koughchi, A. Ueda, J. Power Sources, 68 (1997) 131-134.

[25] Q. Zhong, U. von Sacken, J. Power Sources, 54 (1995) 221-223.

[26] Y. Gao, M.V. Yakovleva, W.B. Ebner, Electrochemical and Solid-State Letters, 1 (1998) 117-119.

[27] C. C. Chang, J. Y. Kim, P. N. Kumta, J. Power Sources, submitted.

[28] D. Gallet, A. Waghray, P.N. Kumta, G.E. Blomgren and M. Setter, *J. Power Sources*, (1998) in press.

[29] D. Gallet, A. Waghray, P.N. Kumta, G.E. Blomgren and M. Setter, *Proc. Symp. The Role of Ceramics in Electrochemical Devices, 1996,* Vol. 65, p. 177, American Ceramic Society, Cincinnati, OH, USA.

[30] T. Ohzuku, A. Ueda, M. Nagayama, J. Electrochem. Soc., 140 (1993) 1862-1870.
[31] W. Li, J. N. Reimers, J. R. Dahn, Solid State Ionics, 67 (1993) 123-130.

Figure captions

Fig. 1. The X-ray diffraction patterns of the five synthesized doped oxides, $Li_{1+x}NiMg_xO_{2(1+x)}$ (x= 0, 0.05, 0.10, 0.15 and 0.20).

Fig. 2. The curve fitting results obtained from the Rietveld refinement analysis conducted on the five compounds based on the R-3m symmetry.

Fig. 3. Plot of the first cycle voltage versus Li content of the five synthesized samples charged/discharged at a current density of $10\mu A/cm^2$ between 3.1 to 4.4 V corresponding to approximately C/100 in C-rate.

Fig. 4. The superimposed voltage versus lithium content plot of the same samples shown in Fig. 3 during the charging process. The average voltage is calculated to increase from 3.81V for $LiNiO_2$ to 3.85, 3.89, 3.92, 3.97V for $Li_{(1+x)}NiMg_xO_{2(1+x)}$, x= 0.05, 0.10, 0.15, 0.20 respectively, when charged to 0.35 Li.

Fig. 5. The differential capacity (dQ/dV) versus voltage (V) plot of the same samples shown in Fig. 3.

Fig. 6. The XRD analysis conducted on (a) the uncharged as-prepared cathode (b) the aluminum foil used as the current collector, and (c) the acetylene black used as the conducting medium during cathode fabrication. Asterisks represent the impurities coming from either aluminum foil or acetylene black.

Fig. 7. The XRD results of $Li_{(1+x)}NiMg_xO_{2(1+x)}$, x= 0.15 (or $LiNi_{0.87}Mg_{0.13}O_2$) charged to different Li contents.

Fig. 8. The Rietveld refinement conducted on the $Li_{(1+x)}NiMg_xO_{2(1+x)}$, x= 0.15 (or $LiNi_{0.87}Mg_{0.13}O_2$) that was charged to different Li contents based on the R-3m symmetry.

Fig. 9. Plot of the capacity versus cycle number of the first 30 cycles for the five synthesized compounds with different Mg cation additions. The test batteries were cycled between 3.1 to 4.4 V using a current density of $0.25mA/cm^2$ corresponding to a C-rate of approximately C/2.

Fig. 10. Plot showing the differential capacity (dQ/dV) versus cell potential (V) for the same batteries shown in Fig. 8.

Fig. 11. DTA resutls showing the thermal stability of the five materials that were charged to 4.4 V using small current ($10\mu A/cm^2$). Each electrode used for the DTA analysis was chosen to have similar weight ($0.0100g \pm 0.0002g$) for quantitative analysis.

Fig. 12. The cycling behavior of $LiNiO_2$ that is charged to the same Li content level (0.3 of Li content) as $Li_xNiMg_xO_{2(1+x)}$, x=0.15 shown in Fig 9. (a) The capacity versus cycle number for the first 30 cycles. (b) The corresponding dQ/dV versus V plot.

Fig. 13. The DTA analysis for the two electrodes, $LiNiO_2$ and $Li_{1+x}NiMg_xO_{2(1+x)}$, x=0.15 with same weight, that were charged to the same Li content (ie. Charged to 0.3 in Li content).

Table 1 Results obtained from the Rietveld refinement for the five as synthesized materials $Li_{1+x}NiMg_xO_{2(1+x)}$ with x= 0, 0.05, 0.10, 0.15 and 0.20

		a (Å)	c (Å)	Cell Vol.(Å³)	$R_{wp\%}$
$LiNiO_2$		2.87815	14.20032	101.8722	11.8
Ni	1.0000				
Li	0.9785				
Ni on Li site	0.0215				
$Li_{1.05}NiMg_{0.05}O_{2.1}$ $(LiNi_{0.952}Mg_{0.048}O_2)$		2.87865	14.21455	102.0097	12.47
Ni	0.9501				
Li	0.9999				
Mg on Ni site	0.0475				
Mg on Li site	0.0001				
$Li_{1.10}NiMg_{0.10}O_{2.2}$ $(LiNi_{0.909}Mg_{0.091}O_2)$		2.88137	14.22943	102.3096	12.16
Ni	0.9022				
Li	0.9992				
Mg on Ni site	0.0901				
Mg on Li site	0.0008				
$Li_{1.15}NiMg_{0.15}O_{2.3}$ $(LiNi_{0.870}Mg_{0.130}O_2)$		2.88174	14.23695	102.3899	13.63
Ni	0.8569				
Li	0.9978				
Mg on Ni site	0.1282				
Mg on Li site	0.0022				
$Li_{1.20}NiMg_{0.20}O_{2.4}$ $(LiNi_{0.833}Mg_{0.167}O_2)$		2.88419	14.24808	102.6443	13.95
Ni	0.8172				
Li	0.9960				
Mg on Ni site	0.1626				
Mg on Li site	0.0040				

Table 2 Results obtained from the Rietveld refinement for the material $Li_{1+x}NiMg_xO_{2(1+x)}$, x= 0.15 or ($LiNi_{0.87}Mg_{0.13}O_2$) that was charged to different Li content.

	a (Å)	c (Å)	Cell Vol.(Å³)	$R_{wp\%}$
$Li_{0.9}Ni_{0.87}Mg_{0.13}O_2$	2.86934	14.22334	101.4136	15.60
$Li_{0.8}Ni_{0.87}Mg_{0.13}O_2$	2.87099	14.28823	101.9935	11.16
$Li_{0.7}Ni_{0.87}Mg_{0.13}O_2$	2.86162	14.31051	101.4868	14.25
$Li_{0.6}Ni_{0.87}Mg_{0.13}O_2$	2.85201	14.37648	101.2710	15.55
$Li_{0.5}Ni_{0.87}Mg_{0.13}O_2$	2.84625	14.39848	101.0167	15.27
$Li_{0.4}Ni_{0.87}Mg_{0.13}O_2$	2.83878	14.42481	100.6710	16.20
$Li_{0.3}Ni_{0.87}Mg_{0.13}O_2$	2.83666	14.42393	100.5145	14.01

Fig. 1

Fig. 2

Fig. 3

213

Fig. 4

Fig. 5

Fig. 6

216

Fig. 7

217

$Li_{0.3}Ni_{0.87}Mg_{0.13}O_2$

$Li_{0.4}Ni_{0.87}Mg_{0.13}O_2$

$Li_{0.5}Ni_{0.87}Mg_{0.13}O_2$

$Li_{0.6}Ni_{0.87}Mg_{0.13}O_2$

$Li_{0.7}Ni_{0.87}Mg_{0.13}O_2$

$Li_{0.8}Ni_{0.87}Mg_{0.13}O_2$

$Li_{0.9}Ni_{0.87}Mg_{0.13}O_2$

Intensity

2θ

Fig. 8

218

Fig. 9

Fig. 10

Fig. 11

(a)

(b)
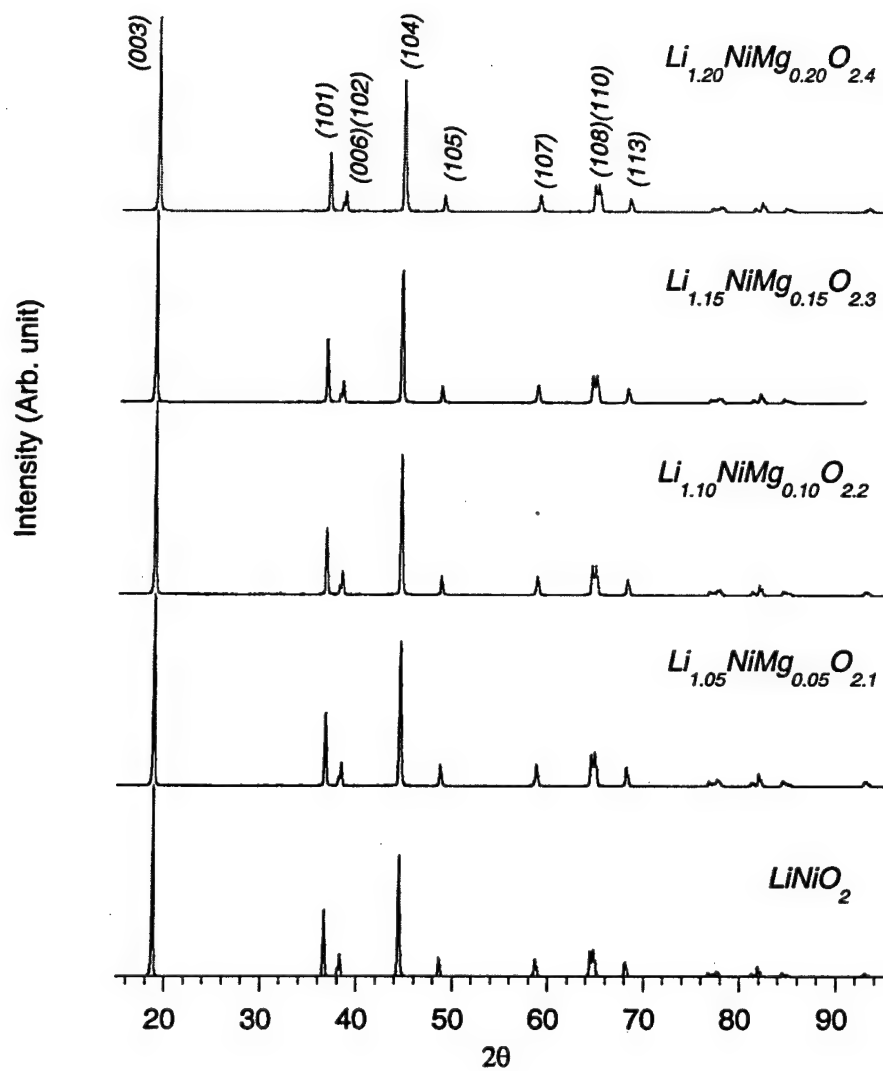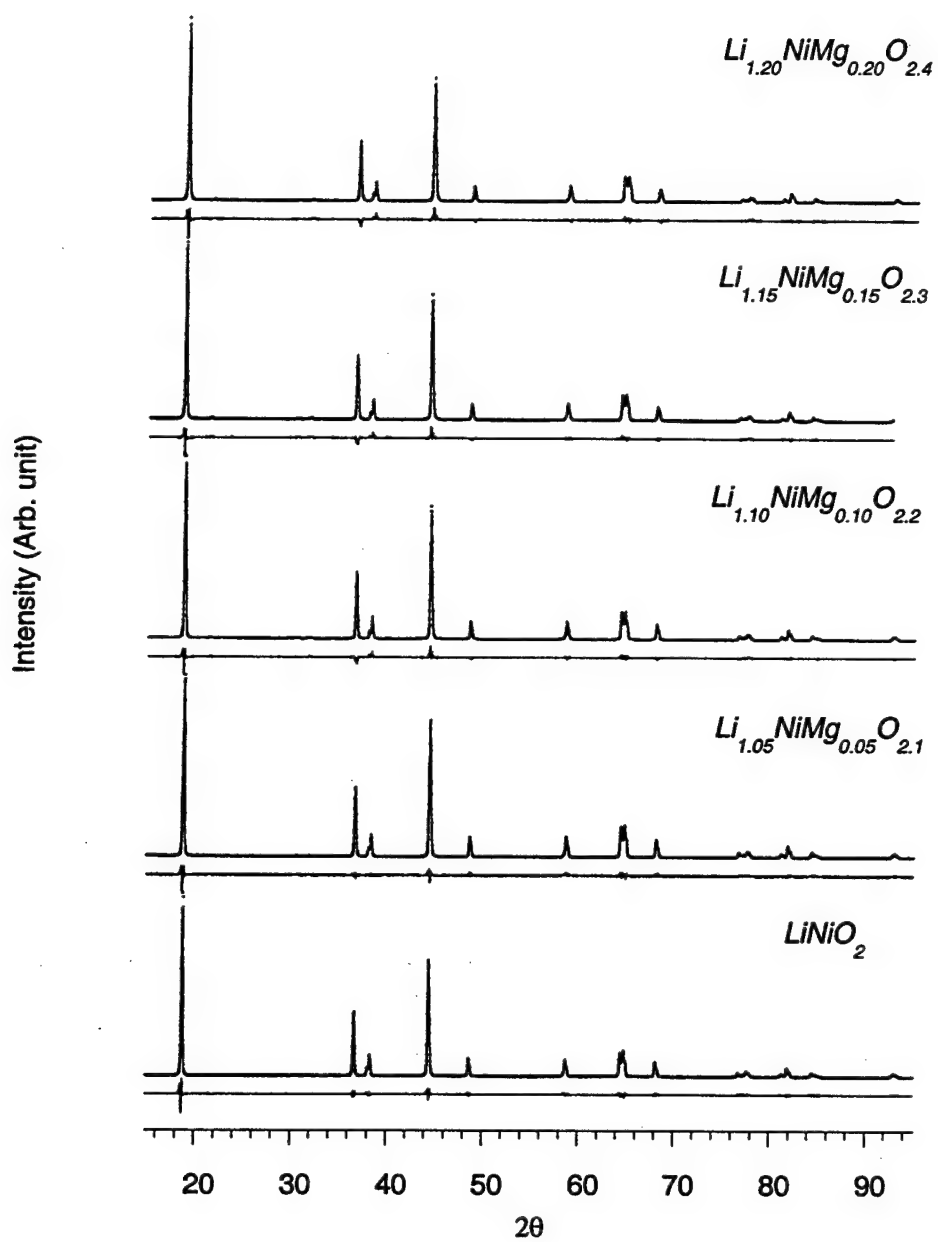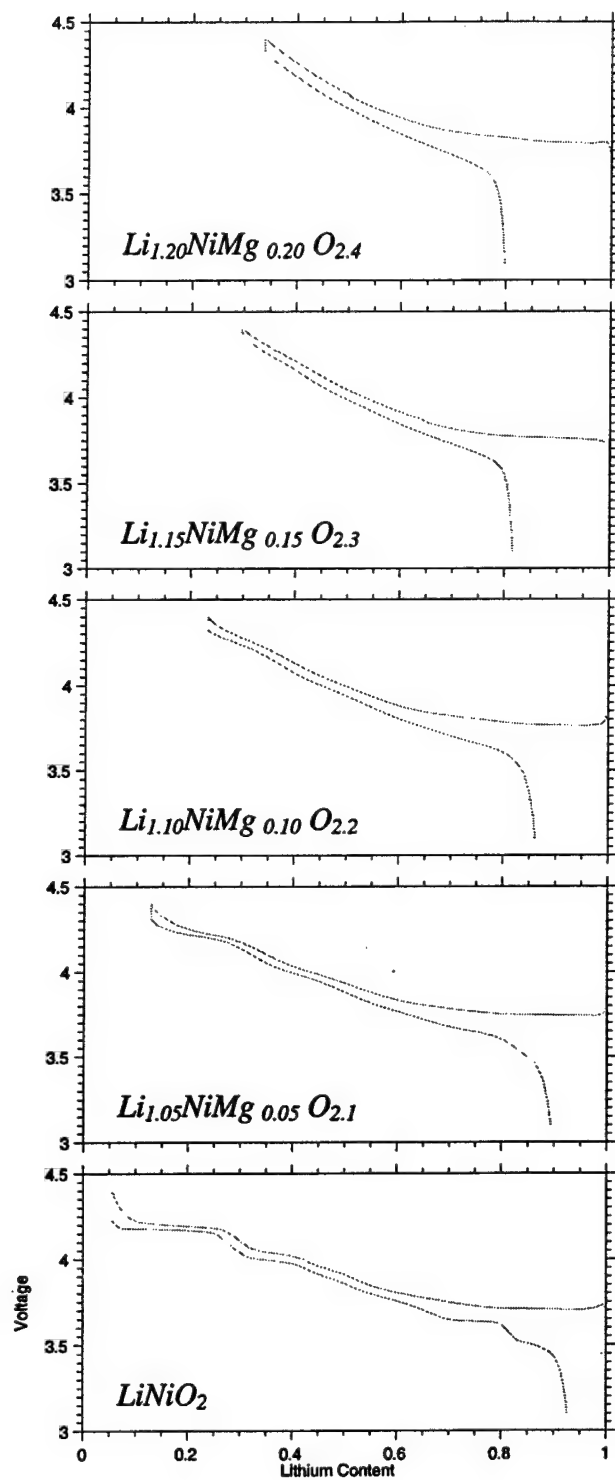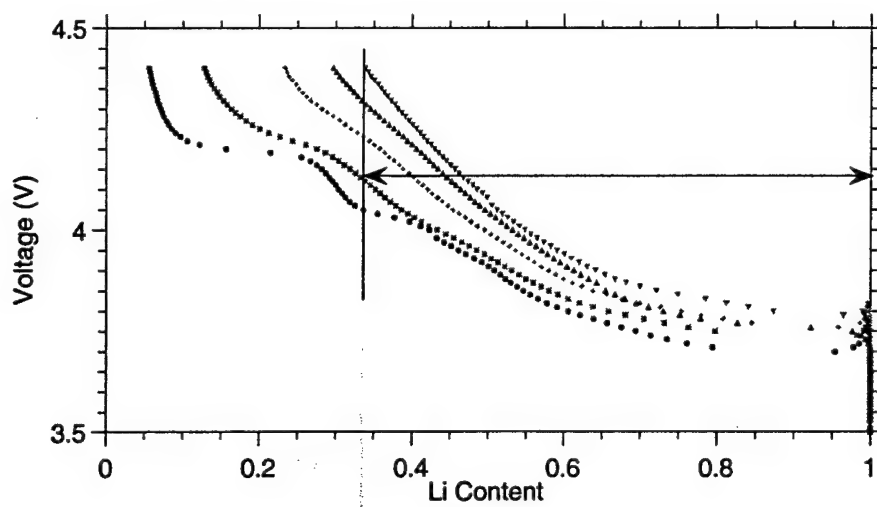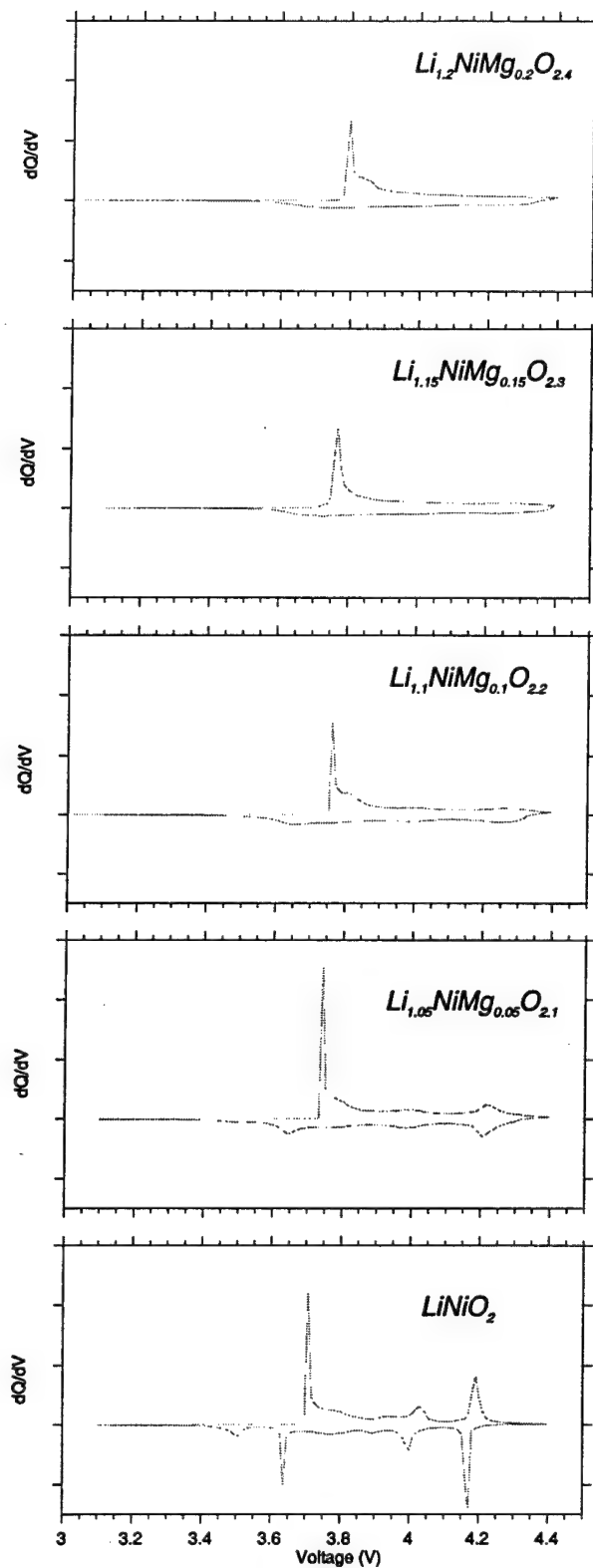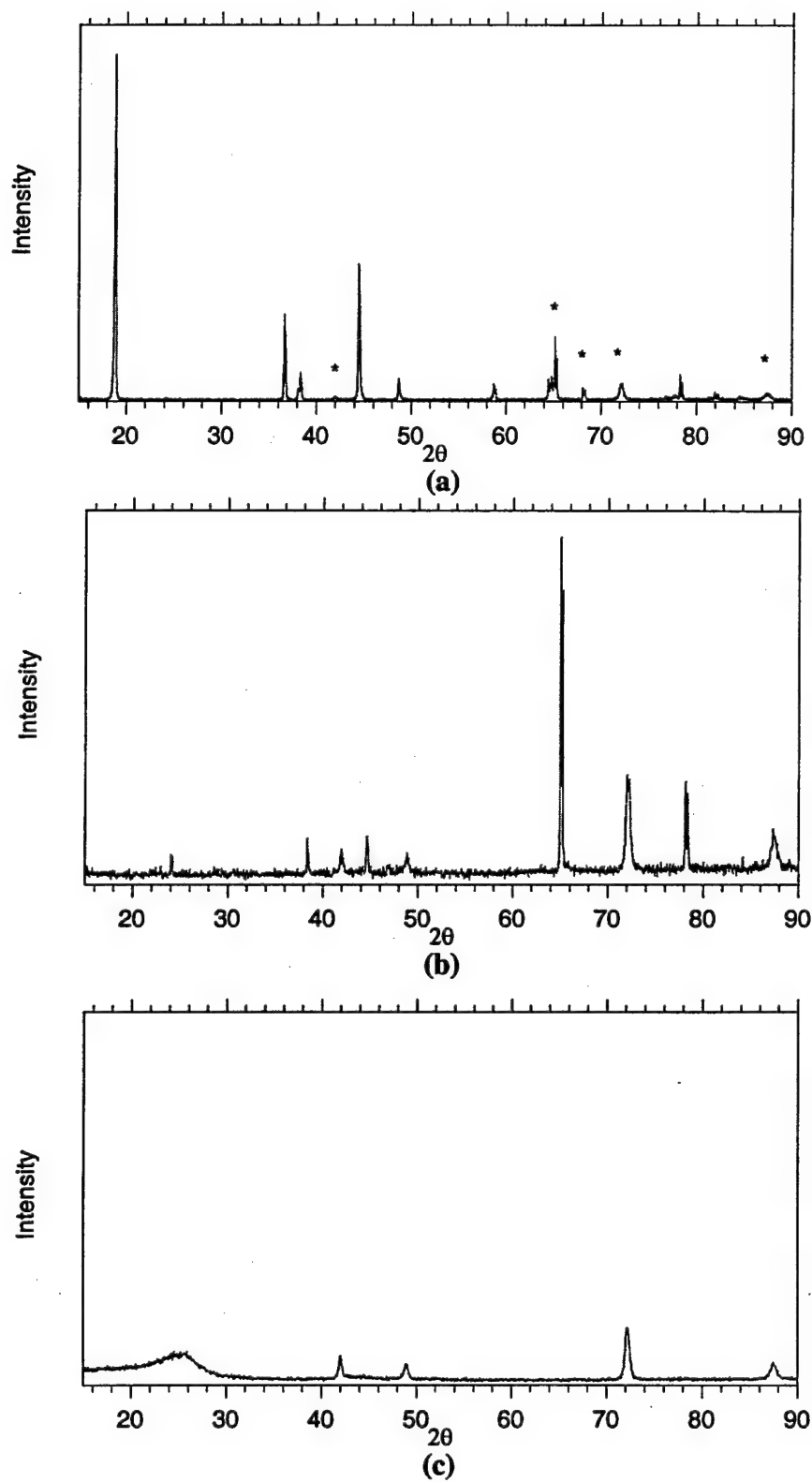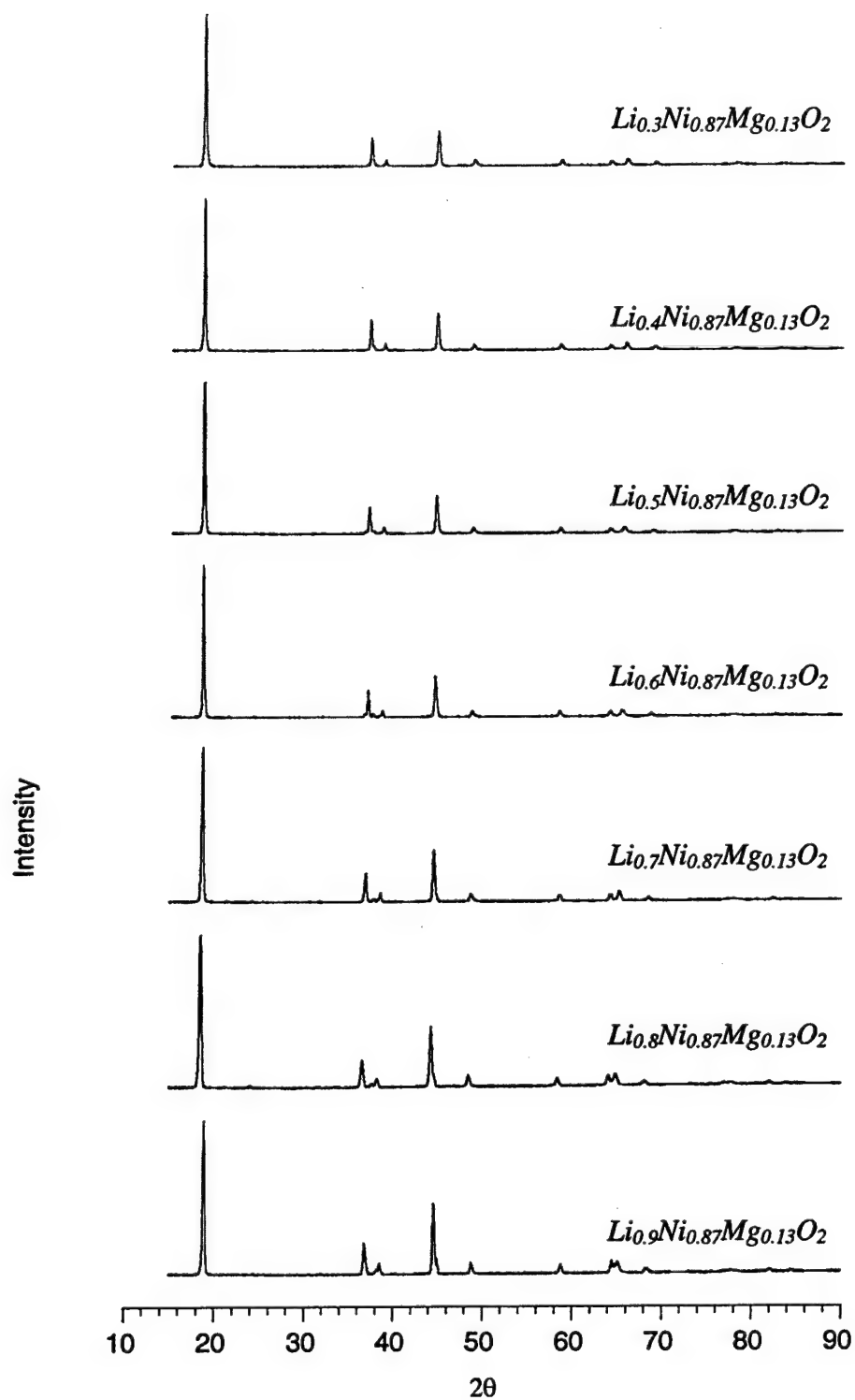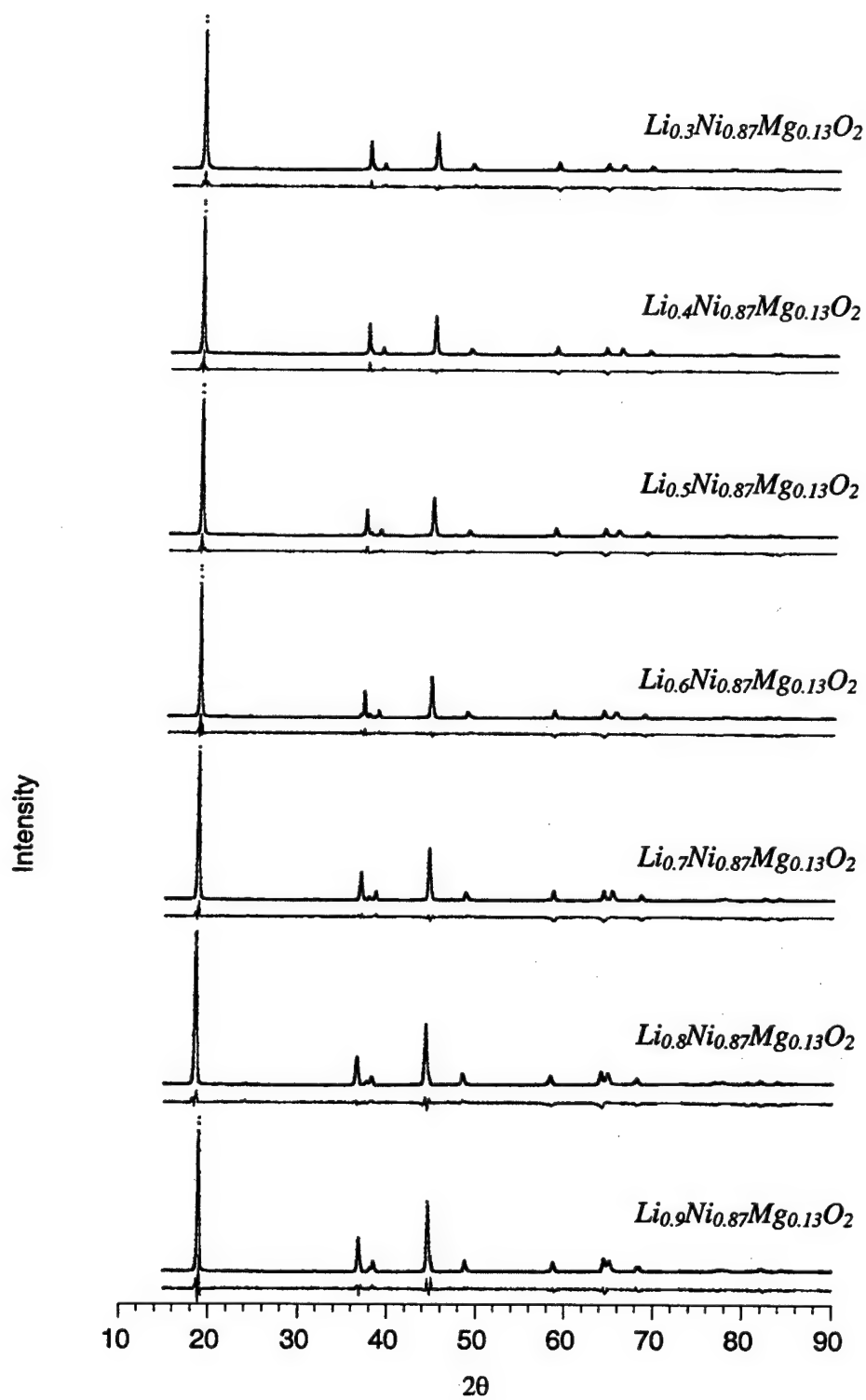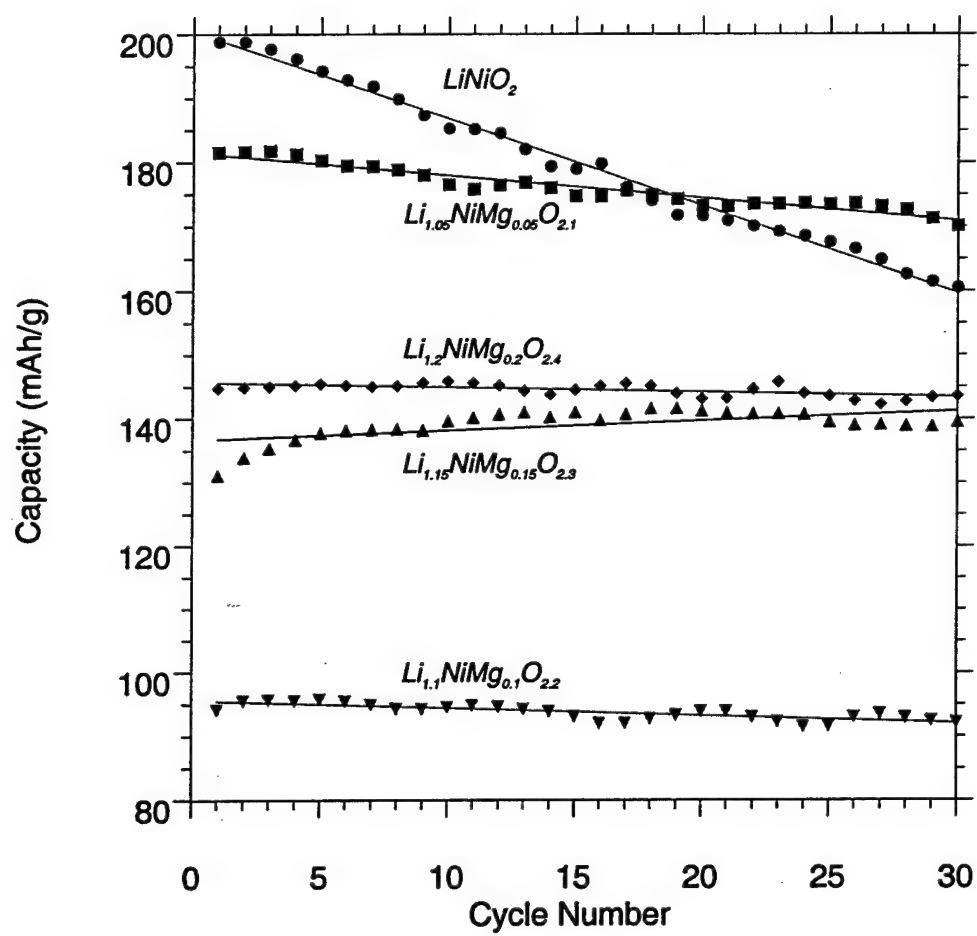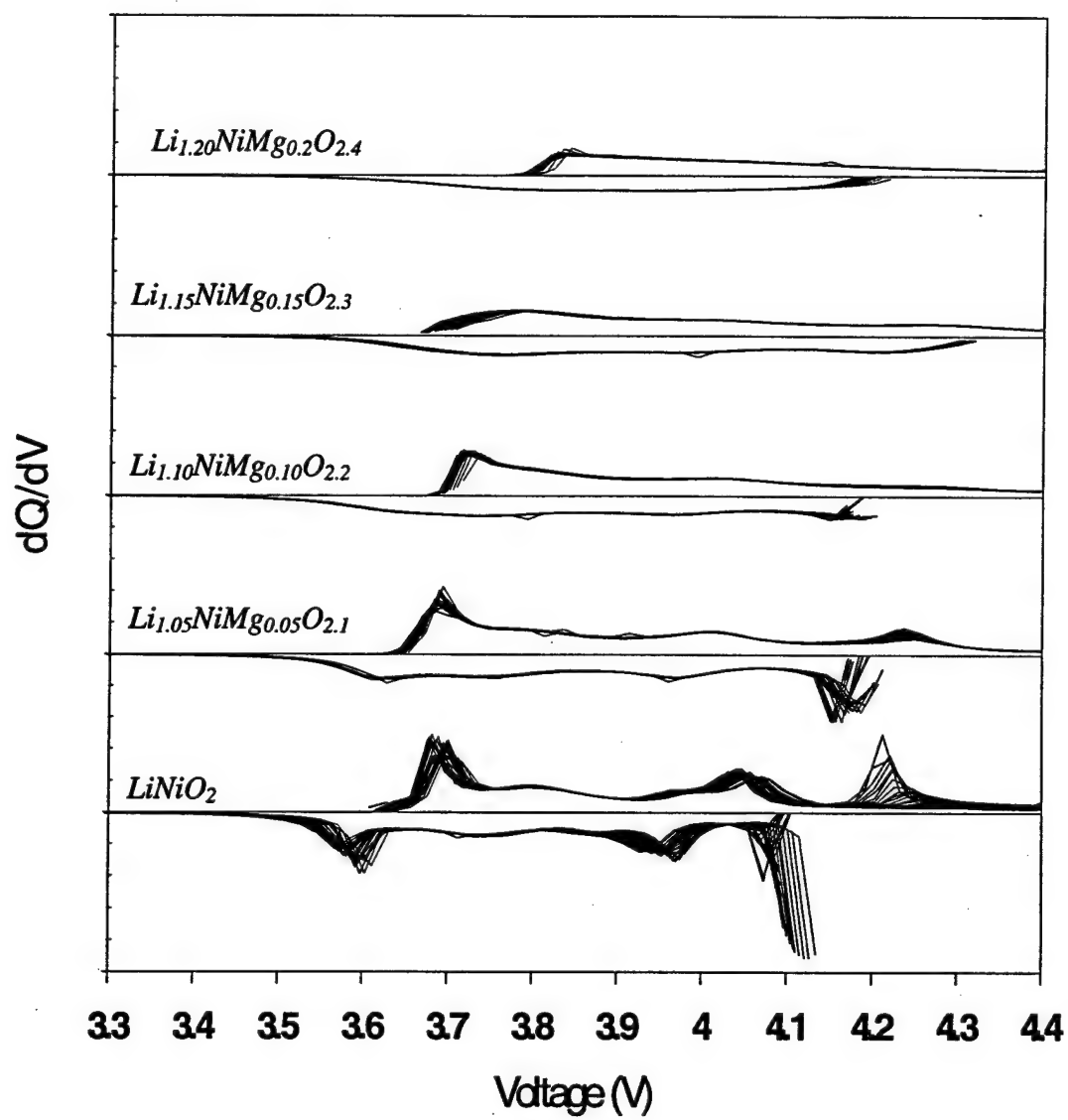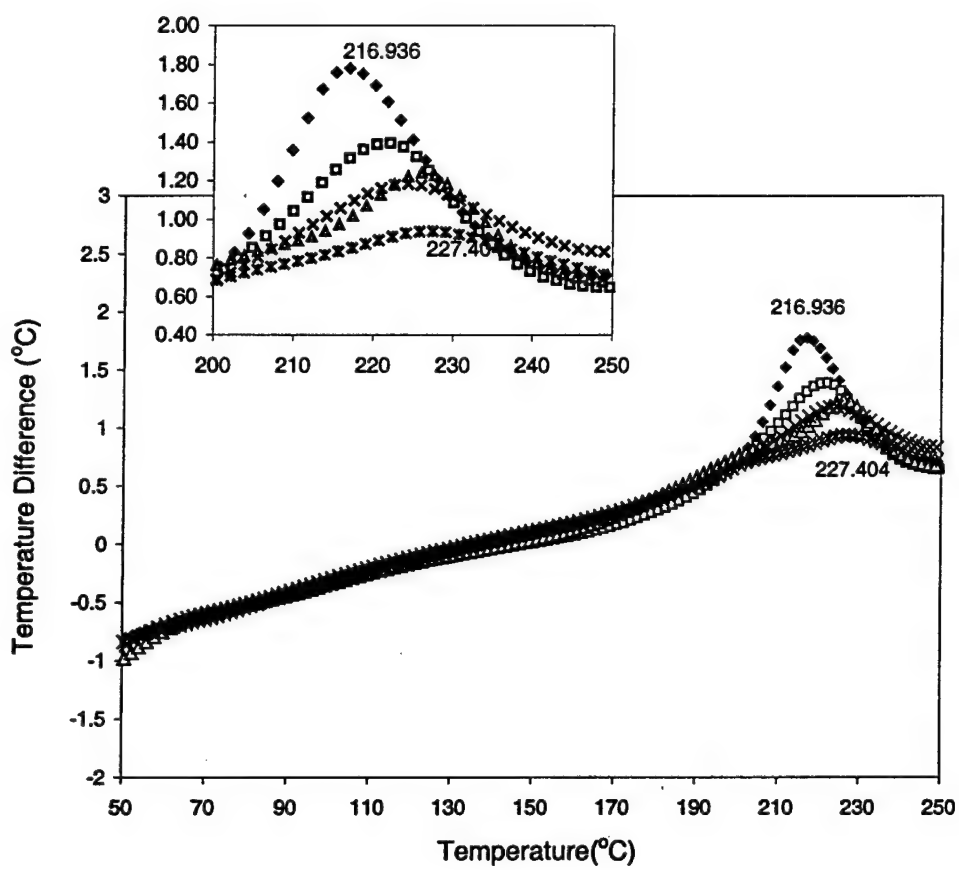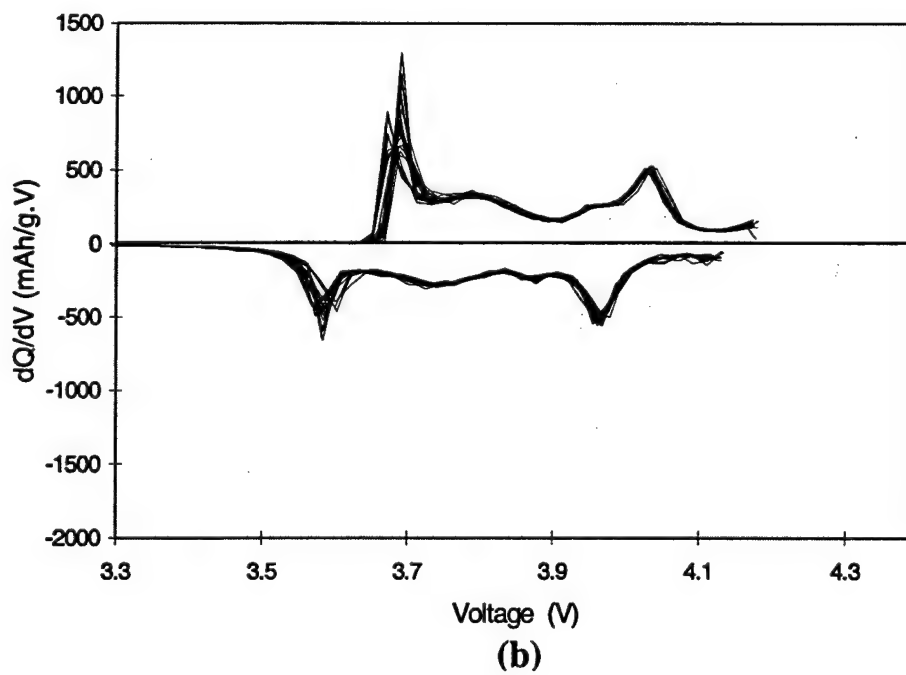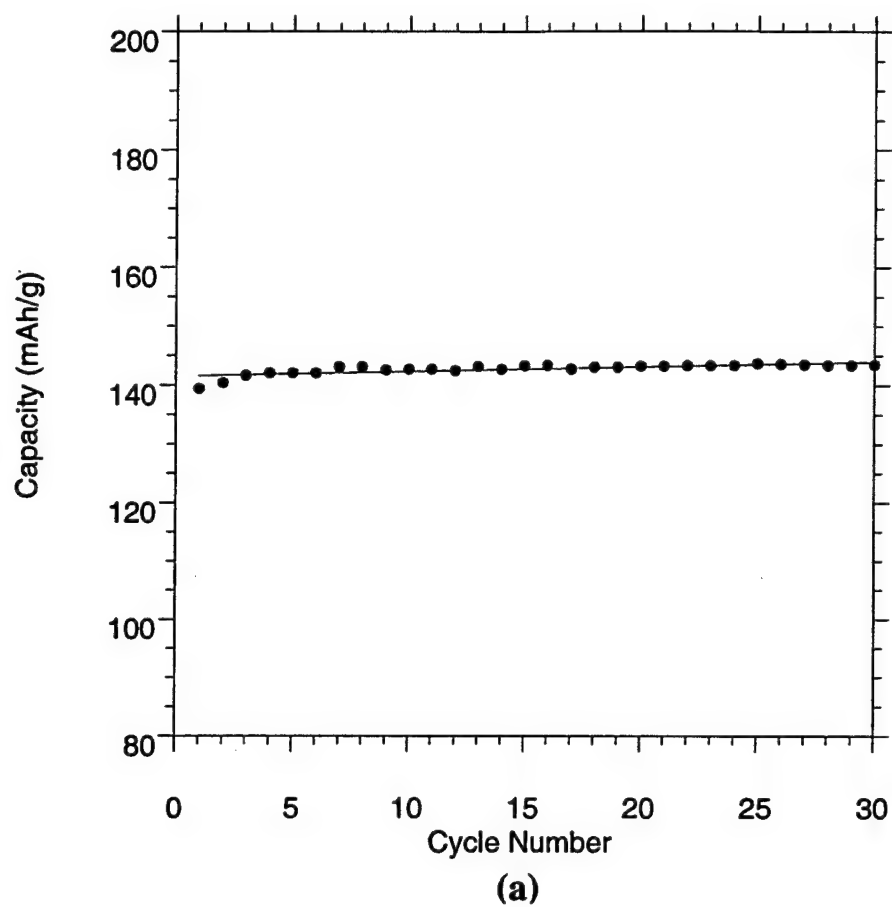
Fig. 12
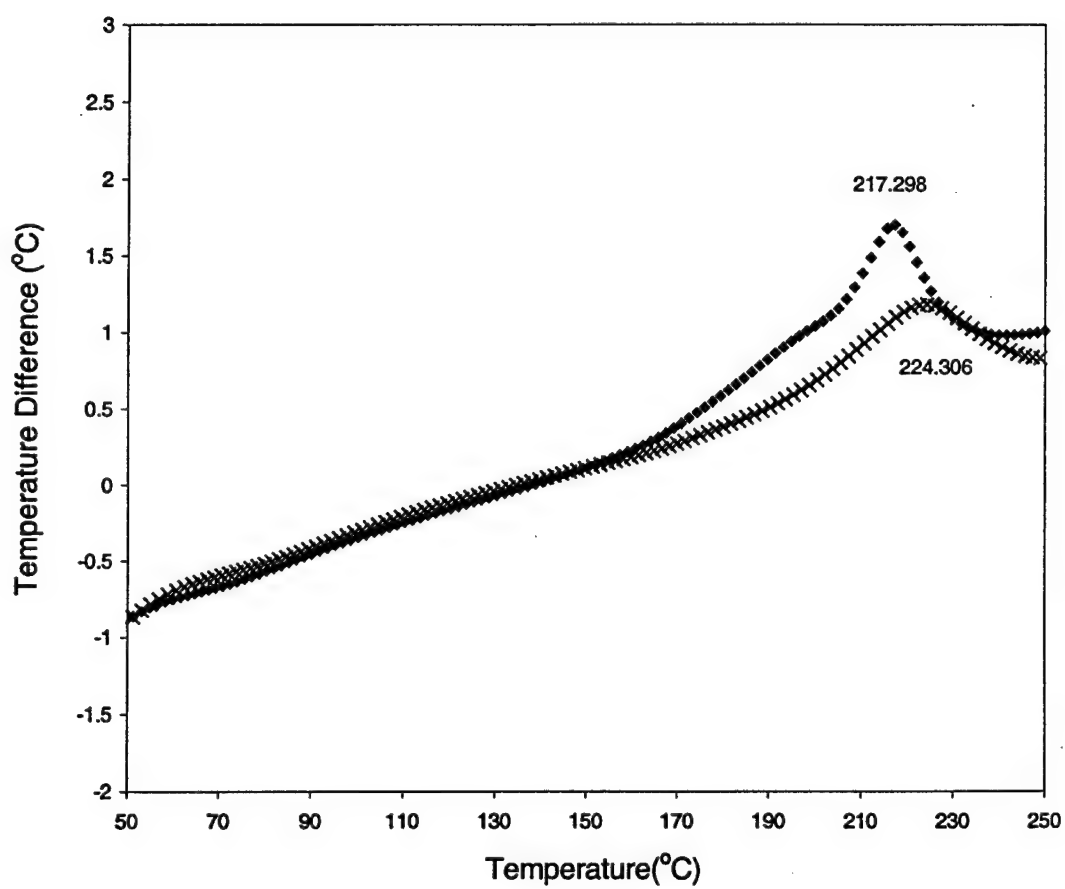
Fig. 13

Appendix D

Divalent Cation substituted $Li_{(1+x)}MN_xO_{2(1+x)}$ (M= $Ni_{0.75}Co_{0.25}$, N= Mg):
Viable Cathode Materials for Rechargeable Lithium-Ion Batteries

Abstract

A new class of divalent cation substituted materials $Li_{1+x}Ni_{0.75}Co_{0.25}Mg_xO_{2(1+x)}$ corresponding to $Li(Ni_{0.75}Co_{0.25})_{1-y}Mg_yO_2$ (y=x/(1+x)), have been successfully synthesized and electrochemically characterized. Good cyclability, high voltage durability (up to 4.4V during charging) and high capacity (>150mAh/g) are the main characteristics of this class of materials. The successful introduction of the divalent cations alone on the transition metal sites help to attain these characteristics while also maintaining a large nominal capacity of the material without the interference of the aliovalent cations on the Li sites. Good cycling behavior at high voltage is probably due to the prevention of overcharging of the material caused by the overoxidation of transition metal as well as the presence of divalent cations on the transition metal site. The presence of the overoxidized transition metal as well as divalent cations not only increases the cycling voltage but also enhances the phase stability of the materials during cycling.

Introduction

Lithiated transition metal oxides $LiMO_2$ (M= Mn, Ni, Co, Ni_xCo_{1-x}) are technically important cathode materials for lithium-ion battery applications because they possess high energy density and capacity [1-11]. These materials are 2-D intercalation compounds which have a layered structure with Li^+ cations inserted in between the MO_2^- (M= transition metal cations) slabs as shown in Figure 1. Among these materials, Ni based layered oxides $LiNi_{1-x}Co_xO_2$ (x = 0~0.25) are especially attractive because they are either less expensive, toxic or relatively easy to synthesize in comparison to $LiCoO_2$ and $LiMnO_2$. In the case of pure $LiNiO_2$, many attempts have been made to synthesize stoichiometric form of the oxide [12-16]. The significance of achieving the stoichiometric form of $LiNiO_2$ is to enlarge the capacity of the material by removing Ni^{2+} from the Li sites that retard the diffusivity of Li. Unfortunately, with the increase in capacity brought about by the synthesis of the stoichiometric form, the cyclability of the material decreases probably owing to the phase transformations during cycling. This leads to significant volume changes in the material causing either microcracking or debonding between the

225

material and the binder [17]. Similarly, although the substitution of Co for Ni alleviates the misposition of Ni^{2+} cations on Li sites [15,16], the material fades in capacity during cycling especially when charged up to higher voltages (eg. 4.4V). In the present study, by the introduction of divalent cations on the transition metal sites alone a new class of materials have been made which are represented by the formula $Li_{1+x}Ni_{0.75}Co_{0.25}Mg_xO_{2(1+x)}$ corresponding to $Li(Ni_{0.75}Co_{0.25})_{1-y}Mg_yO_2$ $(y=x/(1+x))$. The cyclability of these materials is enhanced even when cycled up to 4.4V. Furthermore, in the absence of divalent cations on the Li sites, the materials possess capacities more than 150mAh/g when discharge at a rate of C/2. The former notation is used in this manuscript to represent this family of compounds in order to indicate the complete saturation of lithium sites. The present manuscript discusses the validity of the chemical formula representing the occupation of divalent cations on the transition metal site. This was done by a series of X-ray, chemical, electrochemical and thermal analyses techniques.

Experimental

The particulate sol-gel (PSG) technique which was reported earlier for synthesizing $LiNiO_2$ and $LiNi_{0.75}Co_{0.25}O_2$ [15-16] is employed in the present study for synthesizing $Li_{(1+x)}MN_xO_{2(1+x)}$ (or $LiNi_{0.75/(1+x)}Co_{0.25/(1+x)}N_{x/(1+x)}O_2$, M= $Ni_{0.75}Co_{0.25}$, N = Mg). This particular technique is chosen because of better mixing of cations at a molecular level that is easily achieved in contrast to the conventional solid state processes. The resultant oxides were prepared using lithium hydroxide monohydrate (Aldrich, 99 %) and proper stoichiometric amount of nickel acetate tetrahydrate (Aldrich, 98 %), cobalt acetate tetrahydrate (Aldrich, 98%) and magnesium hydroxide (Aldrich

98%) as starting materials. The specific procedure for synthesizing $Li_{1.1}Ni_{0.75}Co_{0.25}Mg_{0.1}O_{2.2}$ ($LiNi_{0.682}Co_{0.227}Mg_{0.091}O_2$) is as follows: 0.11 mole of lithium hydroxide monohydrate and 0.075 mole of nickel acetate tetrahydrate with 0.025 mole of cobalt acetate tetrahydrate precursors were first dissolved in de-ionized (DI) water separately to obtain clear solutions. 0.01 mole of magnesium hydroxide was dissolved in another 30ml DI water by addition of 3~5ml of nitric acid. Mixing of the individual solutions resulted in dark purple colored suspensions (~210 ml in volume). Ethyl alcohol (90 ml) was then added to the solutions in order to facilitate the removal of liquid products during the subsequent drying process describing later. The dark purple turbid solutions were stirred for 15-20 minutes immediately prior to drying.

A rotary evaporator (Buchi) was used for the subsequent drying process employing an initial pressure of 500 mbar at $120^{\circ}C$ for 3 hours followed by a reduced pressure of 100 mbar at $140^{\circ}C$ for 1 hour to dry the solutions completely. The resultant precipitates were collected and then ground before being subjected to further heat treatments. The heat treatments were conducted in air at the temperature of $800^{\circ}C$ for 5 hours in the case of $Li_{1.03}Ni_{0.75}Co_{0.25}Mg_{0.03}O_{2.06}$ ($LiNi_{0.728}Co_{0.243}Mg_{0.029}O_2$) and $Li_{1.05}Ni_{0.75}Co_{0.25}Mg_{0.05}O_{2.1}$ ($LiNi_{0.714}Co_{0.238}Mg_{0.048}O_2$) and 10 hours for $Li_{1.1}Ni_{0.75}Co_{0.25}Mg_{0.1}O_{2.2}$ ($LiNi_{0.682}Co_{0.227}Mg_{0.091}O_2$). All these compounds represent the case where Li sites are largely saturated. High density alumina boats were utilized as sample carriers during heat treatment. For comparison, $LiNi_{0.75}Co_{0.25}Mg_xO_{2(1+x/2)}$ (or $Li_{1-y/2}Mg_{y/2}(Ni_{0.75}Co_{0.25})_{1-y/2}Mg_{y/2}O_2$, x=0.05, 0.1, 0.2, y=x/(1+x/2)) materials were also synthesized using same procedure described above except that different amounts of Li were used. This formula represents the case where the divalent cation is distributed

equally on both the lithium and transition metal sites. All the heat treatments for these precursors were conducted at 800°C for 5 hours in air.

The synthesized materials were characterized for their phase purity using X-ray diffractometer (XRD, Rigaku θ/θ diffractometer). The XRD patterns were also refined for their structure using the Rietveld refinement technique. Rietveld refinement on the synthesized powders was conducted using the refinement program RIETAN 94. Simultaneous thermogravimetric and differential thermal analysis (TGA/DTA, SDT2960, TA Instruments, New Castle, DE) was used to validate the chemical composition of the final desired oxide. The TGA/DTA analysis was done on ~10 mg of powders employing reconstituted air as the atmosphere. Chemical analysis was conducted by Galbraith Lab Inc. using inductively coupled plasma (ICP). Each sample was dried under vacuum at 150°C for 3 hours before conducting the analysis.

Cathodes for electrochemical characterization were fabricated by coating aluminum foils with the synthesized powders. This was done by making a slurry containing 87.1wt% synthesized material, 7.6wt% acetylene black and 5.3wt% copolymer binder (ethylene/propylene copolymer containing 60% ethylene content) using TCE (Trichloroethylene) as a solvent. The punched out cathodes were 1cm^2 in area, 0.0076cm in thickness and 0.01g in weight. A three electrode Hockey Puck type cell design was used [18, 19] employing lithium foil as an anode and 1M LiPF$_6$ in EC/DMC (with a EC to DMC wt% ratio of 2 to 1) as the electrolyte. All the test batteries (except those tested at high voltage and high current which are specified in the results and discussion section) in this study were cycled in the voltage range of 3.1 to 4.4V employing a current density of 0.25mA/cm^2 which corresponds to a C-rate of ~C/2. All

the electrochemical analysis for the prototype test batteries was conducted using a potentiostat (Arbin electrochemical instrument, College Station,TX).

Results and Discussion

The goal of this work was to introduce all Mg ions on the transition metal sites. However, although this is implied by nominal chemical formula and by the experimental procedure, it is necessary to confirm this in the synthesized materials. This is of particular importance since some of the Mg ion could also occupy the Li sites similar to the Ni ions contributing to the anti-site disorder well known for $LiNiO_2$. The feasibility of introducing divalent cations alone on the transition metal sites is particularly tested on the $LiNi_{1-x}Co_xO_2$ (x=0.25) system. This system is chosen because of its lowest potential probability of exhibiting disorder caused by the misposition of Ni or Co cations on the Li sites. This is largely due to the more oxidizable nature of Ni^{2+} in the presence of Co^{2+} rendering it easier to synthesize this composition in comparison to $LiNiO_2$ [15,16]. In order to introduce Mg cations alone on the transition metal sites, a series of materials have been synthesized by maintaining the ratio of Li : (Ni+Co) : Mg = (1+x) : 1 : x with a general chemical formula of $Li_{1+x}Ni_{0.75}Co_{0.25}Mg_xO_{2(1+x)}$, (x = 0.03, 0.05 and 0.10) which implies the introduction of Mg cations on the transition metal sites alone to maintain a site ratio of Li: M: O = 1: 1: 2 (M= transition metal sites).

This form of the compound thus represents the stoichiometric form of $Li(Ni_{0.75}Co_{0.25})_{1-y}Mg_yO_2$ with all the lithium sites completely saturated. Before initiating a further study on the relationship between structure and property, a set of experiments were conducted to verify the occupancy of divalent cations alone on the transition metal sites. The X-ray analysis show that all the three materials are phase pure. Fig. 2 shows the

229

X-ray diffraction pattern of a representative oxide with maximum Mg (0.10). The phase pure nature of these synthesized materials actually suggests that Mg cations indeed sit on the transition metal sites since the number of Li sites is equal to the sum of Ni, Co and Mg sites, and Li atoms do not preferably sit on transition metal sites because of the large defect formation energy required for monovalent cations to sit on trivalent sites. This aspect is also supported by the results obtained from the Rietveld refinement on the material $Li_{1.1}Ni_{0.75}Co_{0.25}Mg_{0.10}O_{2.2}$ ($LiNi_{0.682}Co_{0.227}Mg_{0.091}O_2$) as shown in Fig. 3. The detailed summary of the Rietveld refinement is shown in Table 1. The result was obtained by assuming the following constraints: (i) The ratio of Co, Ni and Mg is constant. (ii) Occupancy of the transition metal site and Li site is set to unity by allowing for deviation of Mg cations on both sites. The results of the Rietveld refinement can not be used however as a conclusive evidence for determining the site occupancy of Mg. This is because intensity is the only information that can be used for differentiating the sites occupied by Mg cations and the differences in intensity contributed by Mg is smaller in comparison to Ni.

Chemical analysis was conducted for analyzing the stoichiometry of the synthesized materials. The purpose of conducting chemical analysis on these materials is to resolve the site ratio of Li, (Ni+Co+Mg) and O. The results of chemical analysis conducted by Galbraith Lab Inc. is shown in Table 2. These results show that the number of oxygens is actually very close to twice the sum of Ni, Co and Mg (moles of oxygen is twice the sum of moles of Ni, Co, and Mg) which again suggests that the Mg cations are occupying the transition metal sites. It should be noted that there is always some lithium loss as can be seen from the analysis during heat treatment, and the occupation of some

(half of total) Mg on the lithium site can not be discounted. However, the results of the analysis are still a good indicator of the site occupancy of Mg on the transition metal site.

Thermogravimetric analysis was also used to varify the occupation of the divalent cation on the transition metal site. This was done by a conventional solid state reaction of a mixture of hydroxides corresponding to the desired formula. The TGA result also supports the hypothesis of Mg cations occupying the transition metal sites. In the present case, if Mg cations were to occupy the Ni (or Co) sites, the stoichiometry of O would be twice the sum of the stoichiometry of Ni, Co and Mg as explained earlier. Assuming Li: Ni: Co: Mg = 1.1: 0.75: 0.25: 0.1 as an example for illustration, the chemical formula representing all Mg cations occupying Ni (or Co) sites should be $Li_{1.10}Ni_{0.75}Co_{0.25}Mg_{0.1}O_{2.2}$ (or $LiNi_{0.682}Co_{0.227}Mg_{0.091}O_2$) following the $LiMO_2$ convention. The proposed reaction as well as the accompanying theoretical weight loss for the solid state reaction of the hydroxide precursors to yield the oxide with this formula would be represented as follows:

1.1 LiOH·H₂O+ 0.75 Ni(OH)₂+ heat treatment
0.25 Co(OH)₂+ 0.1 Mg(OH)₂ ----------------------------> $Li_{1.1}Ni_{0.75}Co_{0.25}Mg_{0.1}O_{2.2}$
         calculated weight loss = 28.16%
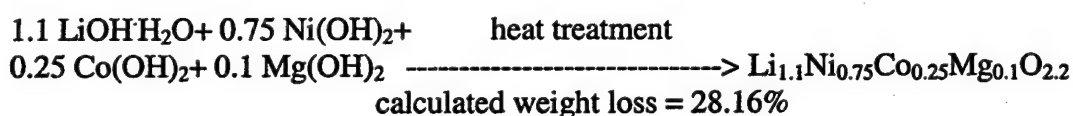
In contrast, if the Mg ions were all occupying Li sites creating equivalent number of vacancies on Li sites, these compounds could assume the chemical formula, $Li_{0.8}Mg_{0.1}Ni_{0.75}Co_{0.25}O_2$. The analogous reaction of the hydroxide precursors to yield the oxide with this formula can also be proposed:

0.8 LiOH·H₂O+ 0.1 Mg(OH)₂ heat treatment
0.75 Ni(OH)₂+ 0.25 Co(OH)₂ ----------------------------> $Li_{0.8}Mg_{0.1}Ni_{0.75}Co_{0.25}O_2$
         calculated weight loss = 27.15%
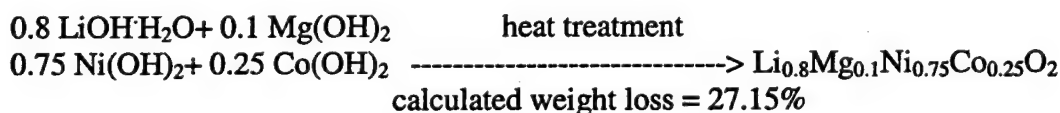
The plot of weight loss using thermal gravimetric analysis (TGA) is shown in Figure 4. The experimental values of the weight change between the starting precursors (LiOH·H$_2$O, Mg(OH)$_2$, Ni(OH)$_2$ and Co(OH)$_2$) and the final products for both formula are listed in Table 3. The results of Table 3 clearly show that the weight loss data support the proposed chemical formula implying that the Mg ions occupy the transition metal site in the case of Li$_{1.1}$Ni$_{0.75}$Co$_{0.25}$Mg$_{0.1}$O$_{2.2}$ materials.

In order to further supplement the chemical analysis results justifying the composition, chemical analysis was also conducted for analyzing the Mg content in the electrolyte before and after 30 charge/discharge cycles. This analysis was conducted to provide additional proof for the occupation of Mg on the transition metal site. It is reported that occupation of Mg on Li sites lead to transport of Mg ions into the electrolyte during cycling [20]. The results of the chemical analysis in Table 4 show a very slight increase in the Mg content of the electrolyte which corresponds to about 1% of total Mg content in the tested cathode. Furthermore, there is no increase in the amount of Mg detected with the increase in the Mg content. The very slight increase of Mg after 30 cycles which is consistent for all the Mg contents of the cathode could be attributed to the contamination from the reusable parts of the battery that were cleaned with detergent. This result therefore implies that Mg occupies the transition metal sites rather than Li site for the materials corresponding to Li$_{1+x}$Ni$_{0.75}$Co$_{0.25}$Mg$_x$O$_{2(1+x)}$ (or LiNi$_{0.75/(1+x)}$Co$_{0.25/(1+x)}$Mg$_{x/(1+x)}$ O$_2$), resulting in no increase in the Mg content in the electrolyte with increase in the Mg content in cathode materials.

Finally, the electrochemical property of the synthesized materials also reflects the differences caused by variations in the site occupancy of Mg. By comparing the materials

synthesized using the formula Li : Ni : Co : Mg = 1 : 0.75 : 0.25 : x (assuming half amount of Mg occupies the Li site and the other half sit on the Li sites) and Li : Ni : Co : Mg = (1+x): 0.75 : 0.25 : x (refer to Figure 5), it is seen that the capacity of the material drops drastically with the increase in Mg addition for the former set of materials. The drastic decrease in capacity caused by the addition of Mg can be attributed to the fact that some Mg cations occupy the Li sites limiting the diffusion of lithium. Therefore, the capacity of the materials can be expected to decrease with increase in the addition of Mg similar to the case of disordered $LiNiO_2$ where Ni atoms occupy Li sites. In contrast, the capacity of the materials do not decrease significantly with an increase in Mg addition even up to at least 10 mol% for the materials of Li : Ni : Co : Mg = (1+x): 0.75 : 0.25 : x. This result implies that Mg cations occupy the transition metal sites in the case of the materials corresponding to Li : Ni : Co : Mg = (1+x): 0.75 : 0.25 : x, thereby showing no interference in the diffusion of lithium during cycling.

Based on the results above, maintenance of the ratio of Li: (Ni+Co+Mg) = 1: 1 suggests that Mg cations occupy the transition metal sites alone. One interesting phenomena which is obtained by introducing Mg cations only on the transition metal sites is that good cyclability of the material can be observed even when the material is cycled up to 4.4V in comparison to phase pure $LiNi_{0.75}Co_{0.25}O_2$. The difference in stability between the phase pure $LiNi_{0.75}Co_{0.25}O_2$ and $Li_{1.1}Ni_{0.75}Co_{0.25}Mg_{0.1}O_{2.2}$ can be seen from the capacity versus cycle number plot as shown in Fig. 6. A capacity fade of 0.01%/cycle is observed for $LiNi_{0.75}Co_{0.25}O_2$ in comparison to virtually no fade per cycle for $Li_{1.10}Ni_{0.75}Co_{0.25}Mg_{0.10}O_{2.2}$. Fig. 7(a) shows the cycling behavior of $Li_{1.10}Ni_{0.75}Co_{0.25}Mg_{0.10}O_{2.2}$ using coke as an anode which is cycled between 3.1 to 4.4V

with a charge/discharge rate of C/2. Since all the Mg cations are sitting on the transition metal sites, the stable cycling behavior can not be attributed to the "pillaring" effect which is caused by the divalent cations on the Li sites in disordered $LiNiO_2$. Additional tests shown in Fig 7(b) for the material $Li_{1.10}Ni_{0.75}Co_{0.25}Mg_{0.1}O_{2.2}$ cycled between 3.1 to 4.6V employing a current density of $0.5mA/cm^2$, together with the battery that was cycled under a high a current density of $2mA/cm^2$ (~ 4C in C-rate) for 150 cycles using Li as an anode as shown in Fig. 7(c), again demonstrates the unique cycling behavior of this material. A capacity of ~130 mAh/g with a capacity fade rate of 0.006%/cycle is observed for this Mg-doped oxide when cycled under high current. These electrochemical results not only demonstrate the remarkable stability at high voltages but also excellent capacity retention (Coulomb efficiency > 0.995) achieved by the introduction of lower valent (divalent) metal cations on the trivalent transition metal site. Thus, both enhanced voltage durability at high voltage and excellent cyclability is exhibited by the introduction of the divalent cations on the transition metal sites.

The stabilization mechanism caused by inducing Mg cations on the transition metal sites is not yet very clear. One of the possible reason for this stabilization is that with the introduction of divalent cations on the trivalent cations sites, an equivalent amount of trivalent cations are forced to be pre-oxidized to 4+ oxidation state based on charge balance. This is evident from the decrease in capacity of the material caused by the presence of inactive Mg^{2+} and Ni^{4+} on the Ni site as shown by the voltage vs. Li content plot for the first cycle shown in Fig. 8. Fig. 8 shows the small current charge and discharge behavior of $LiNi_{0.75}Co_{0.25}O_2$ and $Li_{1.1}Ni_{0.75}Co_{0.25}Mg_{0.1}O_{2.2}$. The presence of inert species (Mg^{2+} and Ni^{4+}) on the transition metal site however helps to prevent

overcharging during the charging process enhancing the cyclability of the material. In addition, the stable cycling behavior at high voltages can be attributed to the upward shift of the voltage during cycling (see the higher voltage for the Mg substituted oxide at a fixed lithium content in comparison to the unsubstituted oxide in Fig. 8) that can be caused by this overoxidation phenomenon. The average cycling voltage for $LiNi_{0.75}Co_{0.25}O_2$ and $Li_{1.10}Ni_{0.75}Co_{0.25}Mg_{0.10}O_{2.20}$ is further calculated using the formula:

$$\bar{V} = (\int_{Q_1}^{Q_2} VdQ) / Q_{sum}$$

where '$\bar{V}$' is the average voltage and 'Q' is the number of Coulombs. The calculations indicate an average voltage during charge ($\bar{V}_{charge}$) and discharge($\bar{V}_{discharge}$) of 3.95 V and 3.87 V, respectively for pure $LiNi_{0.75}Co_{0.25}O_2$ and $\bar{V}_{charge} = 4.01$ V, $\bar{V}_{discharge} = 3.92$ V for $Li_{1.10}Ni_{0.75}Co_{0.25}Mg_{0.10}O_{2.20}$. This tendency of the higher average voltage exhibited by the Mg substituted oxide could also probably be a reason that enhances voltage durability of this oxide when charged to 4.4V. Results of further studies elucidating the exact role of Mg and its contribution to the electrochemical stability of this oxide has been conducted and will be reported elsewhere.

Conclusions

The particulate sol-gel (PSG) process has been used to synthesizing a new family of Mg-doped materials, $Li_{1+x}Ni_{0.75}Co_{0.25}Mg_xO_{2(1+x)}$. The introduction of divalent cations such as Mg on the transition metal sites stabilizes the materials that enhances the cyclability as well as voltage durability of the materials up to at least 4.4V. The long cycle test utilizing coke anode as well as high current test ($2mA/cm^2$ at a C rate of 4C)

demonstrates the remarkable cyclability and stability of the materials. The combined evidences shown by the X-ray analysis, chemical analysis of the synthesized compounds, TGA analysis, chemical analysis on the electrolyte before and after cycling as well as electrochemical characterization on two sets of materials synthesized using different chemical formula of $Li_{1+x}Ni_{0.75}Co_{0.25}Mg_xO_{2(1+x)}$, and $LiNi_{0.75}Co_{0.25}Mg_xO_{2(1+x/2)}$, unequivocally validate the occupation of divalent cations alone on the transition metal sites. The occupancy of divalent cations on the Li site is however not the key to the stabilization of these doped oxides. Instead it decreases the diffusivity of the material which causes the increase in polarization during the charge/discharge process therefore decreasing the nominal capacity during cycling. The capacity drop caused by the occurrence of divalent cations on the Li sites can however be minimized by saturating the Li sites with excess Li while maintaining excellent cyclability of the materials. The stabilization mechanism is not yet well understood. A possible explanation is provided by the creation of inactive Ni^{4+} due to the substitution of Mg which not only helps prevent overcharging but also increase the average voltage of the material. These inactive pairs (Ni^{4+}, Mg^{2+}) contributed to the enhanced voltage durability and cyclability of the material when cycled up to 4.4V.

Acknowledgment

References

[1] M. Broussely, F. Perton, P. Biensan, J.M. Bodet, J. Labat, A. Lecerf, C. Delmas, A. Rougier, and J.P. Peres, *J. Power Sources, 54* (1995) 109-114.

[2] W. Ebner, D. Fouchard, L. Xie, Solid State Ionics, 69 (1994) 238-256.

[3] M. Broussely, F. Perton, J. Labat, J. Power Sources, 43-44 (1993) 209-216.

[4] T. Ohzuku, A. Ueda, M. Nagayama, Y. Iwakoshi, and H. Komori, *Electrochimica Acta, 38* (1993) 1159-1167.

[5] T. Nohma, H. Kurokawa, M. Uehara, M. Takahashi, K. Nishio, T. Saito, J. Power Sources, 54 (1995) 522-524.

[6] R. Yazami, N. Lebrun, M. Bonneau, M. Molteni, J. Power Sources, 54 (1995) 389-392.

[7] A. R Armstrong, P. G. Bruce, Nature, 381, 499 (1996).

[8] B. Banov, J. Bourilkov, and M. Mladenov, *J. Power Sources, 54* (1995) 268-270.

[9] C. Delmas, I. Saadoune, A. Rougier, J. Power Sources, 43-44 (1993) 595-602.

[10] C. Delmas, I. Saadoune, Solid State Ionics, 53-56 (1992) 370-375.

[11] D. Caurant, N. Baffier, B. Garcia, J.P. Pereira-Ramos, *Solid State Ionics, 91* (1996) 45-54.

[12] A. Hirano, R. Kanno, Y. Kawamoto, Y. Takeda, K. Yamaura, M. Takano, K. Ohyama, M. Ohashi, Y. Yamaguchi, Solid State Ionics, 78 (1995)123-131.

[13] J. R. Dahn, U. von Sacken, C.A. Michal, Solid State Ionics, 44 (1990) 87-97.

[14] R. V. Moshtev, P. Zlatilova, V. Manev, A. Sato, J. Power Sources, 54 (1995) 329-333.

[15] C. C. Chang, P. N. Kumta, J. Power Sources, 75 (1998) 44-55.

[16] C. C. Chang, P. N. Kumta, Solid State Ionics, 112 (1998) 329-344.

[17] T. Ohzuku, A. Ueda, Solid State Ionics, 69 (1994) 201-211.

[18] D. Gallet, A. Waghray, P.N. Kumta, G.E. Blomgren and M. Setter, *J. Power Sources*, (1998) in press.

[19] D. Gallet, A. Waghray, P.N. Kumta, G.E. Blomgren and M. Setter, *Proc. Symp. The Role of Ceramics in Electrochemical Devices, 1996,* Vol. 65, p. 177, American Ceramic Society, Cincinnati, OH, USA.

[20] E. Peled, E. Yehuda, C. M. Ariel, A.Gorenshcein, B. Yam, United State patent No. 5,591,543 (1997).

Figure captions

Fig. 1. (a) The unit cell of $LiMO_2$ (M = transition metal) type materials possessing $R\bar{3}m$ symmetry. The Li^+ cations occupy the 3(b) site with Ni^{3+} and O^{2-} occupying the 3(a) site and 6(C) site respectively. (b) The representation of layered structure with Li^+ cations inserted in between the MO_2^- (M= transition metal cations) slabs.

Fig. 2. X-ray analysis on the sample with 10 mole % Mg addition. The "phase pure" nature of the synthesized materials actually suggests that Mg cations should occupy the transition metal sites.

Fig. 3. The Rietveld refinement results on the X-ray diffraction pattern of the material $Li_{1.10}Ni_{0.75}Co_{0.25}Mg_{0.10}O_{2.2}$ (or $LiNi_{0.682}Co_{0.227}Mg_{0.091}O_2$) using $R\bar{3}m$ symmetry.

Fig. 4. Weight loss of starting precursors ($LiOH\cdot H_2O$, $Mg(OH)_2$, $Ni(OH)_2$ and $Co(OH)_2$) during heat treatment revealed by TGA. (———) represents $Li_{1.10}Ni_{0.75}Co_{0.25}Mg_{0.1}O_{2.2}$ and (-----) represents $Li_{0.8}Ni_{0.75}Co_{0.25}Mg_{0.1}O_2$.

Fig. 5. The capacity versus cycle number plots for two sets of materials. (a) The materials synthesized using the formula $LiNi_{0.75}Co_{0.25}Mg_xO_{2(1+x/2)}$. (-o-) represents x = 0.05, (-◊-) represents x = 0.10 and (-Δ-) represents x = 0.20 respectively. (b) The materials synthesized using the formula $Li_{1+x}Ni_{0.75}Co_{0.25}Mg_xO_{2(1+x)}$. (-o-) represents x = 0.03, (-◊-) represents x = 0.05 and (-Δ-) represents x = 0.10.

Fig. 6. The capacity versus cycle number plot showing the difference in stability between phase pure $LiNi_{0.75}Co_{0.25}O_2$ and $Li_{1.1}Ni_{0.75}Co_{0.25}Mg_{0.1}O_{2.2}$.

Fig. 7. (a) The cycling behavior of the same material which is cycled between 3.1 to 4.4V for 100 cycles using coke as an anode. (-o-) represents the specific capacity and (-◊-) represents the Coulomb efficiency of the material during cycling. (b) The high voltage durability test of $Li_{1.10}Ni_{0.75}Co_{0.25}Mg_{0.10}O_{2.20}$ cycled between 3.1 to 4.6V using lithium as an anode with a current density of $0.5mA/cm^2$. (c) same cathode material but cycled under a Current density = 2.0 mA/cm^2 (which corresponds to 4C in C-rate), cycle between 3.1 to 4.4V, lithium anode, 150 cycles.

Fig. 8. Plot of the voltage versus Li content plot showing the 1st charge and discharge cycle for both $LiNi_{0.75}Co_{0.25}O_2$ and $Li_{1.1}Ni_{0.75}Co_{0.25}Mg_{0.1}O_{2.2}$. The cell was cycled using a small current density ($10\mu A/cm^2$). The decrease in capacity of the material should be caused by the presence of inactive Mg^{2+} and Ni^{4+} on the Ni site.

Table 1 Results of the Rietveld refinement obtained for $Li_{1+x}NiMg_xO_{2(1+x)}$, $x = 0.10$ $(LiNi_{0.68}Co_{0.23}Mg_{0.09}O_2)$

Space Group: $R\bar{3}m$ a=2.8655 Å c=14.1859 Å cell volume=100.8754 ($Å^3$)	
Atoms	occupancy
Ni on transition metal sites	0.689
Co on transition metal site	0.230
Mg on transition metal sites	0.081
Mg on Li sites	0.009
Li on Li sites	0.991
O on O sites	1.000

*R_{wp} = 0.158

Table 2

The results of chemical analysis showing the number of oxygens is actually very close to twice the sum of Ni, Co and Mg (moles of oxygen equal to twice the sum of moles of Ni, Co, and Mg)

Composition for Synthesis	Analyzed Composition (wt%)		Suggested Formula
$Li_{1.05}Ni_{0.75}Co_{0.25}Mg_{0.05}$	Lithium	6.89 %	(NiCo): Mg: O = 1.00 : 0.045 : 2.096
	Nickel	43.90 %	
	Cobalt	14.68 %	
	Magnesium	1.09 %	
$Li_{1.10}Ni_{0.75}Co_{0.25}Mg_{0.10}$	Lithium	6.91%	(NiCo): Mg: O = 1.00 : 0.093 : 2.196
	Nickel	42.70 %	
	Cobalt	14.18 %	
	Magnesium	2.19 %	

- Each sample was dried under vacuum at 150°C for 3 hours before analysis.
- The subscripts of the suggested formula were obtained by assuming Ni+Co=1.00.

Table 3

The weight change between the starting precursors precursors ($LiOH \cdot H_2O$, $Mg(OH)_2$, $Ni(OH)_2$ and $Co(OH)_2$) and the final products of both $Li_{1.10}Ni_{0.75}Co_{0.25}Mg_{0.1}O_{2.2}$ and $Li_{0.80}Ni_{0.75}Co_{0.25}Mg_{0.1}O_2$.

Proposed Chemical formula	Weight of starting precursors	Weight of final product	weight change observed (%)	weight change calculated (%)
$Li_{1.10}Ni_{0.75}Co_{0.25}Mg_{0.1}O_{2.2}$	19.6641mg	14.1479mg	28.05	28.16
$Li_{0.80}Ni_{0.75}Co_{0.25}Mg_{0.1}O_2$	18.7807mg	13.6665mg	27.23	27.15

Table 4

The results of the chemical analysis conducted on the electrolyte before and after 30 cycles of the charge/discharge process.

Composition of Cathode	Magnesium Content in electrolyte after 30 cycles (ppm)
$Li_{1.03}Ni_{0.75}Co_{0.25}Mg_{0.03}O_{2.06}$	7.9
$Li_{1.05}Ni_{0.75}Co_{0.25}Mg_{0.05}O_{2.10}$	7.3
$Li_{1.10}Ni_{0.75}Co_{0.25}Mg_{0.10}O_{2.20}$	7.1

* The initial Mg contnet in the electrolyte prior to cycling : 5.7 ppm

Ni

O

Li

(a)

Ni

O

Li

(b)

Fig. 1

243
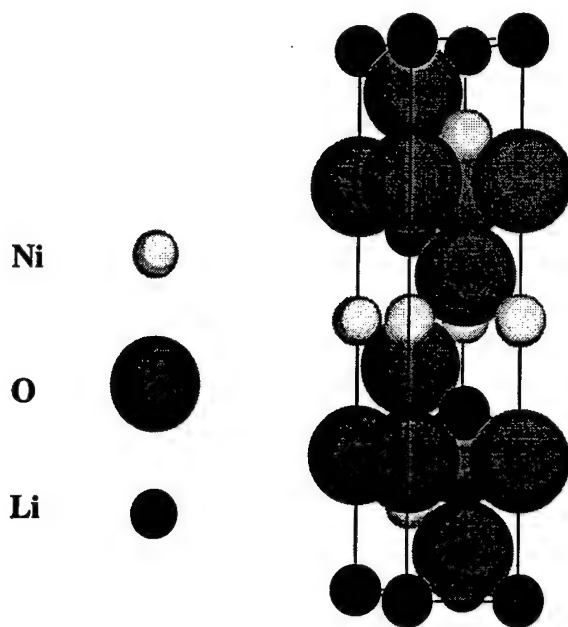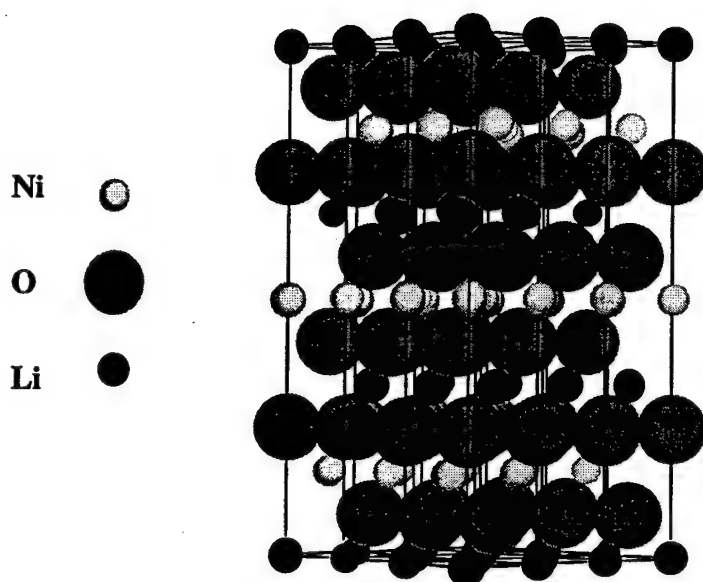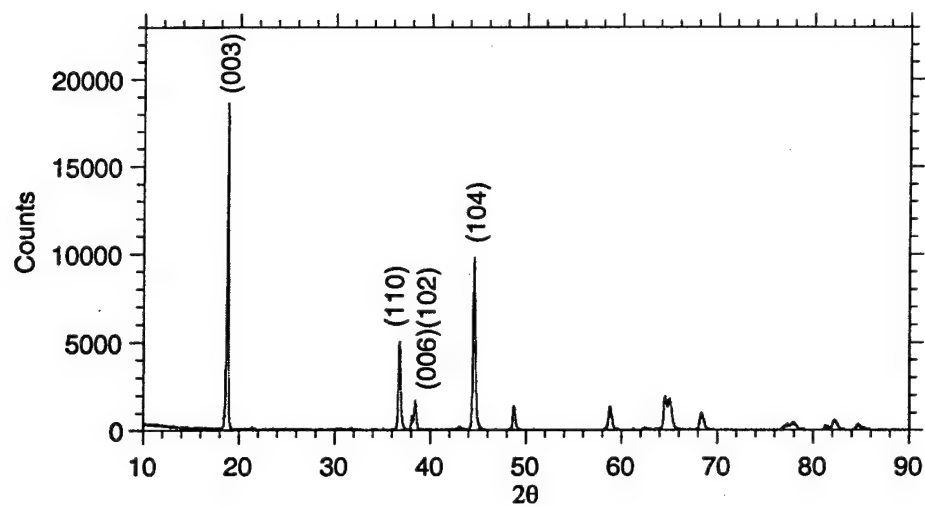
Fig. 2
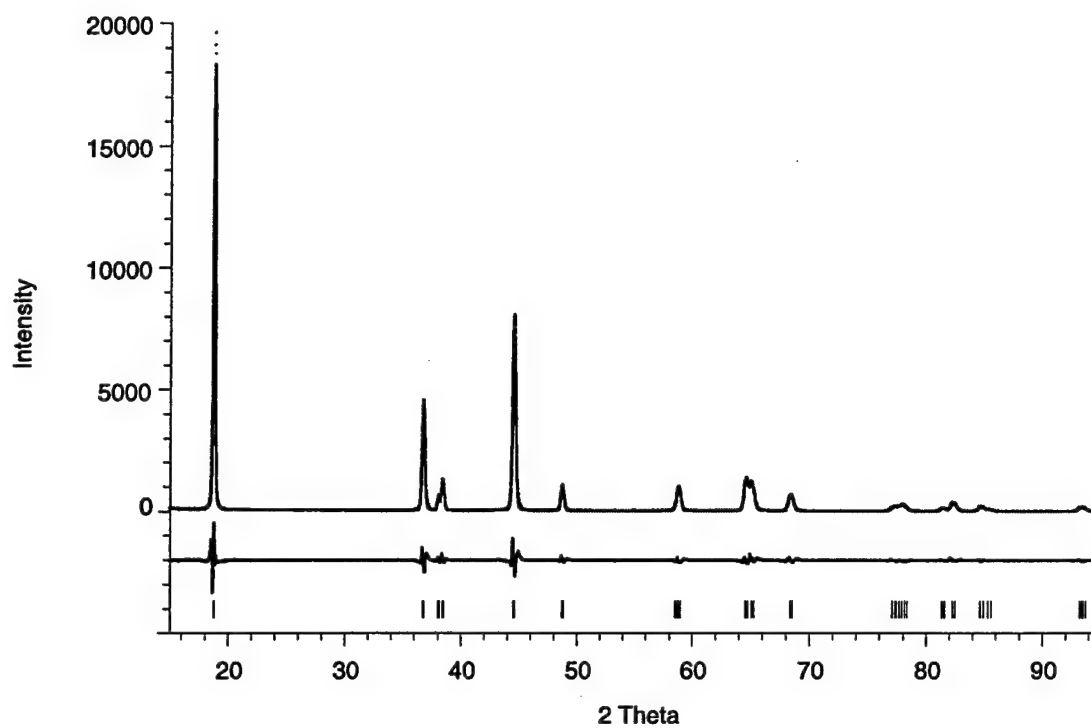
Fig. 3
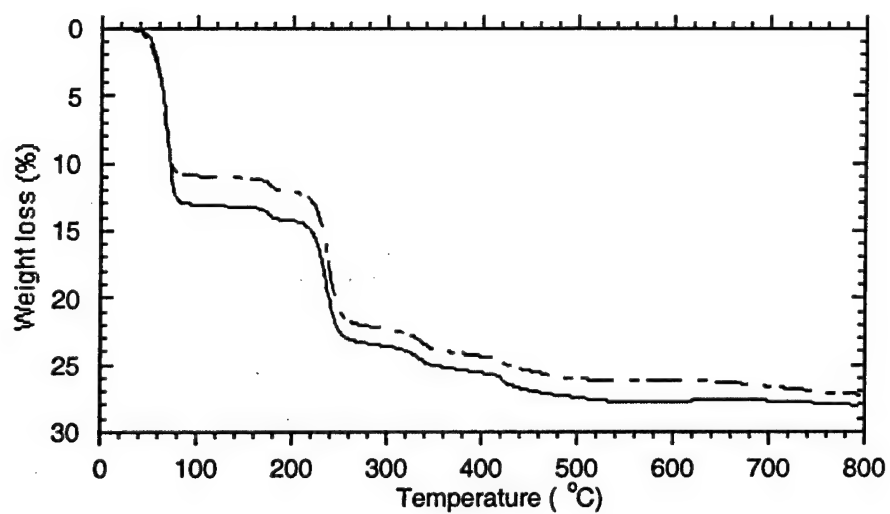
Fig. 4
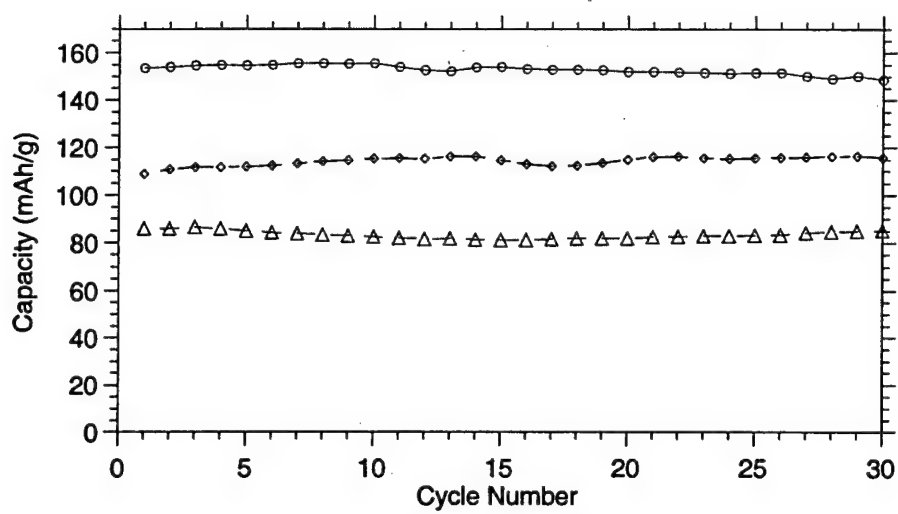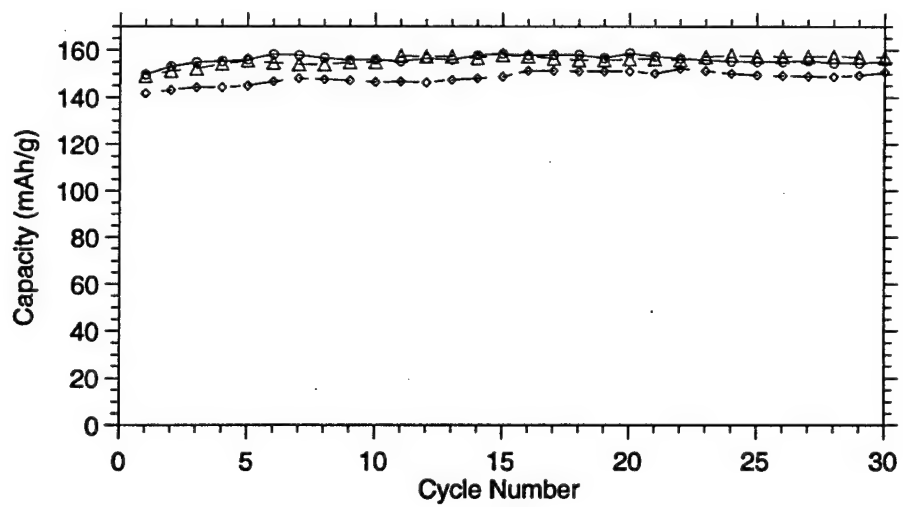
Fig. 5
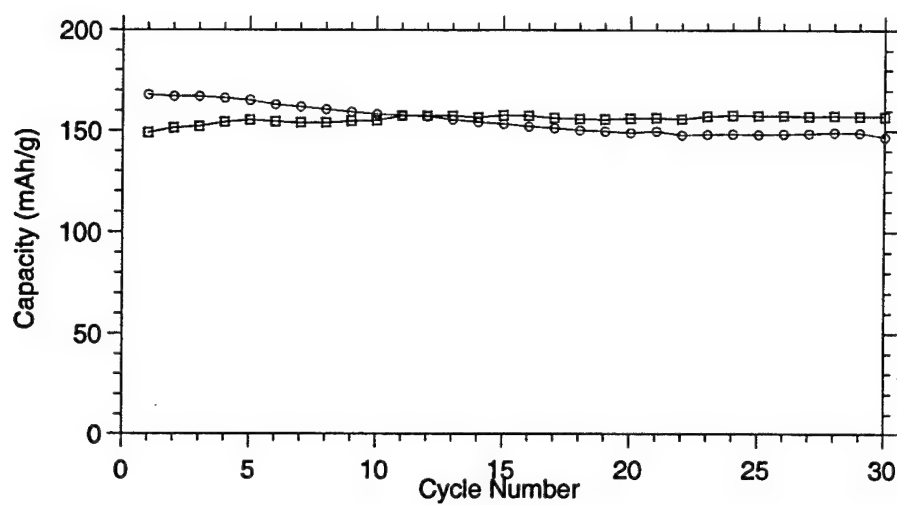
Fig. 6
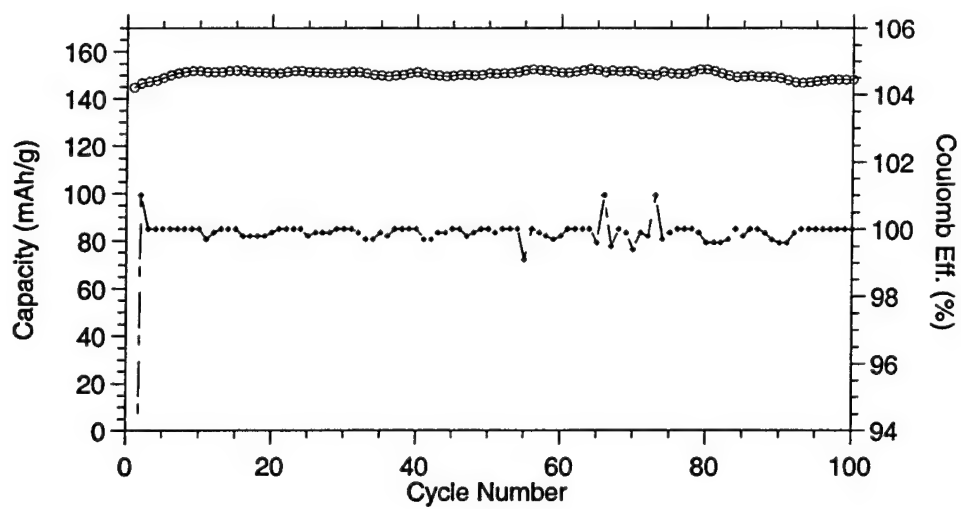
(a)
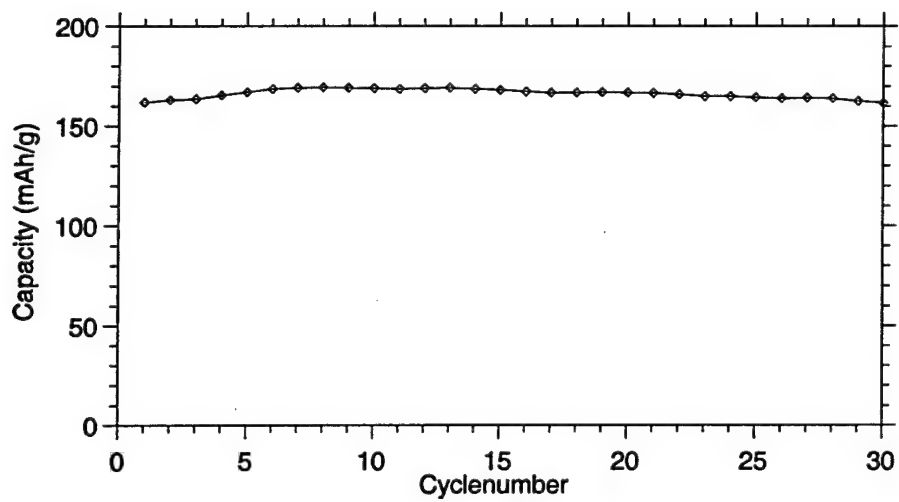
(b)
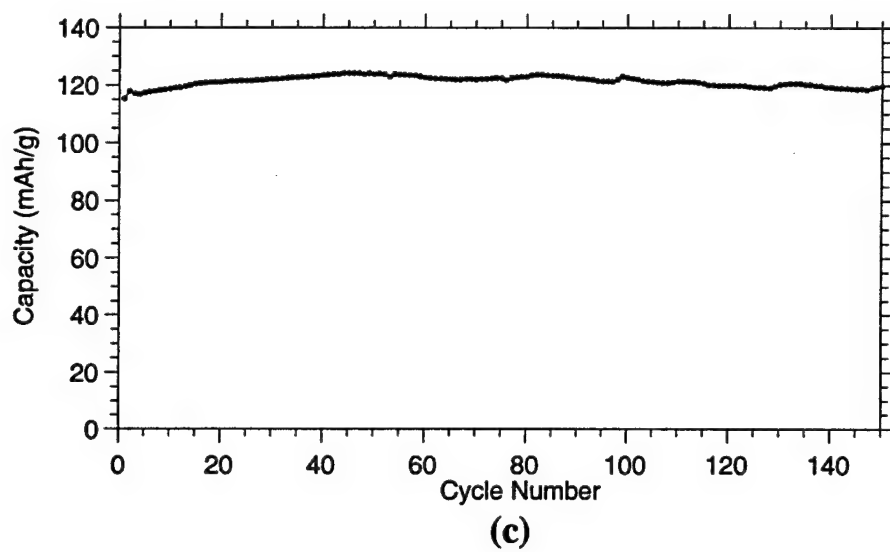
Fig. 7

Fig. 7
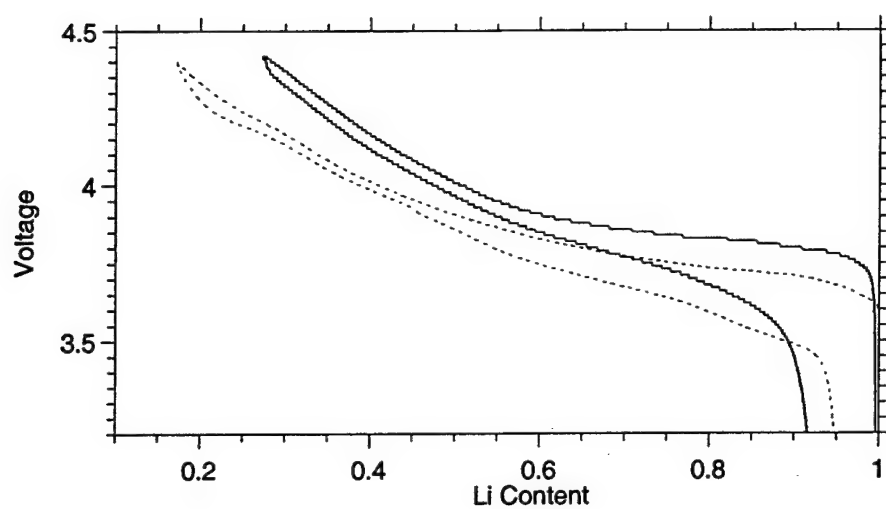
Fig. 8

Appendix E

**Chemical Synthesis and Structural Characterization of
Lithium Orthosilicate (Li$_4$SiO$_4$)**

Abstract

A solution based wet chemistry approach has been developed for synthesizing Li_4SiO_4 powders. Moderate heat treatment temperature (500°C) and short time (2 hours) are the characteristics of this chemical approach. $LiOH \cdot H_2O$ and $LiNO_3$ have been used as precursors for the synthesis of Li_4SiO_4 in the present study. The phase evolution of Li_4SiO_4 formation, surface area measurement and morphology of the as-prepraed and heat treated powders generated from both $LiOH \cdot H_2O$ and $LiNO_3$ are characterized and compared. The feasibility of synthesizing Li_4SiO_4-$LiNi_{0.75}Co_{0.25}O_2$ electrolyte-electrode composite material using this chemical approach is also demonstrated.

Introduction

Lithium orthosilicate (Li_4SiO_4), Lisicon ($Li_{14}Zn(GeO_4)_4$) and their solid solution derivative systems such as Li_4SiO_4-Li_3PO_4, Li_4SiO_4-Li_3AsO_4, Li_4SiO_4-Li_4GeO_4, Li_4SiO_4-Li_3AsO_4-Li_3PO_4, Li_4SiO_4-Zn_2SiO_4, Li_4GeO_4-Li_2ZnGeO_4-Li_3PO_4 are known as a important class of fast Li-ion conducting materials [1-12]. These materials usually accommodate Li vacancies which allows fast Li-ion conduction. In the present study, a low temperature chemical synthesis of Li_4SiO_4 is investigated for the purpose of not only to decrease the concentration of thermally induced point defects caused by high temperature synthesis that can potentially leads to subsequent loss of ionic conductivity, but also to increase the possibility of synthesizing the electrolyte-electrode composite material (eg. $LiMO_2$, M = Co, Ni, Co_xNi_{1-x}) without causing the decomposition of $LiMO_2$ (M = Ni, $Ni_{0.75}Co_{0.25}$) [13,14]. The importance of synthesizing the electrolyte-electrode composite material arises from the fact that the performance (power output) of the solid state batteries is mainly determined by the Li ion conductivity of the electrolyte and the efficiency of Li ion transport from the electrode material to the electrolyte. The efficiency of Li ion transport from the far end of the electrode material to the electrolyte actually determines the critical thickness of the electrode under certain charge/discharge C-rate.

The synthesis of Lithium Orthosilicate is commonly synthesized using tradition solid state methods. These processes typically require high temperature (usually > 1000°C) for long time (1~2 days) [1-5, 7,9,10]. Chemical approaches for synthesizing cathode materials such as $LiMO_2$ (M = Ni, $Ni_{0.75}Co_{0.25}$) at moderate temperature and short times have been shown in our previous works [15,16]. As a result, a solution based wet chemistry approach is utilized for synthesizing Li_4SiO_4 powders. In the present study, the reaction and formation of Li_4SiO_4 powders generated by different precursors ($LiOH \cdot H_2O$ and $LiNO_3$) are investigated. The phase evolution of the Li_4SiO_4 formation is characterized using X-ray diffraction (XRD). The specific surface area as well as the morphology of the resultant powder have also been determined using the Brunauer Emmett and Teller (BET) method and the scanning electron microscope. The feasibility of the low temperature synthesis of $LiNi_{0.75}Co_{0.25}O_2$-Li_4SiO_4 composite material is also demonstrated.

Experimental

The Lithium Orthosilicate powders were prepared by two different precursors, one with $LiOH \cdot H_2O$ and the other with $LiNO_3$. 0.4 mole (16.784g) of $LiOH \cdot H_2O$ (Aldrich, 98%) and 0.4 mole (27.576g) of $LiNO_3$ (Aldrich, 98%) were first dissolved separately using 150 ml deionized (DI) water. After the clear solutions of lithium hydroxide and lithium nitrate are prepared, same amount of 0.1 mole high surface area fume silica (Alfa, %) with a specific surface area of ~350m^2/g was then added to each of those clear solutions. After 20 minutes stirring and mixing, the homogeneously mixed solutions were then subjected to rotary evaporation (Buchi) at a pressure of 600 mbar at 140°C for 1 hour, followed by a pressure of 100 mbar at the same temperature for 2 hours. The as-prepared

powders were then heat treated at 6 different temperatures ranges from 300°C to 800°C with a interval of 100°C for 2 hours. Heat treatments were conducted in a box furnace with air as the atmospheric environment or in a tube furnace using oxygen as the reaction gas. The phase evolution of the heat treated powders was characterized using X-ray diffraction (XRD, Rigaku θ/θ diffractometer). The surface area of the starting precursor, fume silica (SiO_2), the as-prepared powder as well as the heat treated samples were determined using the BET method (Quantachrome Instruments, NY). All samples used for the surface area measurement were dried at 150°C for 3 hours prior to the analysis. Thermal gravimetric analysis (TGA, TA instrument model SDT-2960) was conducted in air atmosphere using a heating rate of 10°C/min. The morphology of the as-prepared and the resultant powders was investigated using the scanning electron microscope (Philips, FEG-XL 30).

Results and Discussion

The phase evolution study suing X-ray diffraction on the samples heat treated in air prepared from $LiOH·H_2O$ is shown in Fig. 1. Lithium orthosilicate starts to form at 500°C with the presence of a very small amount of Li_2SiO_3 and some lithium carbonate. Furthermore, the formation of Li_4SiO_4 is going via the formation of Li_2SiO_3. For the purpose of eliminating the formation of lithium carbonate, another set of samples was heat treated in oxygen for comparison. The result of the X-ray diffraction for the samples heat treated in oxygen is shown in Fig. 2. Again, it is observed that Li_4SiO_4 is formed at 500°C with the presence of both Li_2SiO_3 and Li_2CO_3. In contrast to the samples that were heat treated in air, the oxygen treated samples shows more Li_2SiO_3 and less Li_2CO_3. The increase of Li_2SiO_3 present in the oxygen treated samples can be understood as the result

of the enhanced Li_2CO_3 decomposition under oxygen atmosphere. This point can be supported by the phase evolution of samples heat treated in air, that is observed as more Li_2CO_3 decomposition, more Li_2SiO_3 yields with the increase of temperature.

Similarly, the phase evolution of the samples heat treated in air prepared using $LiNO_3$ as the precursor is shown in Fig. 3. Lithium nitrate is the only observable phase under X-ray diffraction for the samples heat treated at 300°C and 400°C. At 500°C, Li_2SiO_3 starts to form with the presence of a small amount of $Li_2Si_2O_5$. The formation of Li_4SiO_4 is observed to start at 600°C, which is higher than the samples prepared using lithium hydroxide as precursors (500°C) reported earlier. The dependence of Li_4SiO_4 formation temperature on the lithium precursors suggests the formation of Li_4SiO_4 is dependent on the decomposition of either lithium hydroxide or lithium nitrate. This assumption is actually supported by the thermal gravimetric analysis (TGA) data obtained for both $LiOH \cdot H_2O$ and $LiNO_3$ that were heat treated in air as shown in Fig. 4. From the TGA data it can be concluded that the formation of Li_4SiO_4 is going via the reaction between SiO_2 and Li_2O.

The specific surface area measurement for the as-prepared powders derived from both $LiOH \cdot H_2O$ and $LiNO_3$, and the samples that were heat treated at 300°C, 400°C and 500°C using the as-prepared powders are shown Fig. 5. From Fig. 5 it can be seen that the specific surface area of both sets of materials drop with the increase of temperature. The drop of specific surface area with the increase of heat treatment temperature can be explained by the crystallization of the materials during heat treatment. Especially in the case of the as-prepared powder generated from $LiNO_3$, the specific surface area of the as-prepared powders itself is low owing to the crystallization of $LiNO_3$ during the drying

256

process. The crystallization of $LiNO_3$ in the as-synthesized state is shown in Fig. 6 using XRD. Owing to the covering of crystallized $LiNO_3$ on the SiO_2 surface as will be shown later in the morphology characterization section, the XRD result of the as-prepared powders does not show the diffraction peaks originated from SiO_2. The XRD analysis for the fume silica is shown in Fig. 7 for comparison.

The morphology of fume silica is shown in Fig. 8. From Fig. 8(a) it can be seen that SiO_2 powders are in the micro size range which are resulted from the agglomeration of even smaller particles. A fluffy kind of morphology on the SiO_2 powder surface observed at a higher magnification (10,000X) as shown in Fig. 8(b) asserts the validity of SiO_2 particle agglomeration. By comparing the morphology of fume silica with the as-prepared powders generated from both $LiOH \cdot H_2O$ and $LiNO_3$ as shown in Fig. 9 and 10, it is clear that the morphology of the as-prepared powders is not dependent on the morphology of fume silica. The morphology of the as-prepared powders generated from $LiOH \cdot H_2O$ is particular in shape. This can be understood as a consequence resulted from the infiltration of hydroxide solution in between the fume silica particles, that later on causes the agglomeration of fume silica particles during the drying process. In contrast to the morphology of powders generated from $LiOH \cdot H_2O$, the morphology of the as-prepared powders generated from $LiNO_3$ is smooth and continuous. Owing to the observation of $LiNO_3$ peaks from XRD without the presence of diffraction peaks resulted from silica in the as-prepared powders, it is clear that the silica particles are covered by the crystallized $LiNO_3$ which causes the severe reduction in surface area as discussed earlier. Fig. 11 shows the morphology of heat treated powders (600°C) generated from

257

both LiOH·H$_2$O and LiNO$_3$. Both sets of powders show similar morphology as an aggregate of distinguishable crystallites.

Owing to the lower formation temperature of Li$_4$SiO$_4$ sing lithium hydroxide as the precursor, the Li$_4$SiO$_4$-LiNi$_{0.75}$Co$_{0.25}$O$_2$ composite material is synthesized using lithium hydroxide, together with stoichiometric amount of fume silicate, nickel acetate and cobalt acetate. It is observed that the Li$_4$SiO$_4$-LiNi$_{0.75}$Co$_{0.25}$O$_2$ composite material is obtainable after heat treating the as-prepared powders at 700°C for 2 hours. The XRD analysis of the composite material is shown in Fig. 12. From Fig. 12 it can be seen that the disorder of transition metal cations on the Li site is not severe from the peak ratio between the (003) and (104) peaks [15]. This result is quite encouraging not only because of the success in synthesizing the electrode-electrolyte composite material in one step for the first time, the possibility of synthesizing fast ion-conducting electrode with high load of electrode material per unit area is also expected. However, the detailed characterization and the electrochemical behavior of the composite material, which is not the focus of the present paper will be published elsewhere in the future.

Conclusions

Lithium orthosilicate (Li$_4$SiO$_4$) has been successfully synthesized utilizing the chemical process. Low temperature (500°C) and short time (2hours) are the characteristics of the chemical process. The short reaction time is due to the high surface area (368.29 m^2/g) of SiO$_2$ and homogeneous mixing of the precursors during processing. The Li$_4$SiO$_4$ phase starts to form at 500°C using the as-prepared powders generated from LiOH·H$_2$O. In contrast, the powders prepared from LiNO$_3$ starts to form only after 600°C. The difference in formation temperature is resulted from the decomposition temperature

258

difference between LiOH and $LiNO_3$. The BET result shows that the specific surface area of the materials reduces as a function of temperature owing to the crystallization of the materials. Especially in the case of the as-prepared powder generated from $LiNO_3$, the specific surface area of the as-prepared powders is low owing to the crystallization of $LiNO_3$ that covers the silica during the drying process. The success in synthesizing the electrolyte-electrode composite material in one step demonstrates the possibility of developing fast ion conducting/high load electrodes for lithium ion battery applications.

Acknowledgement

References

1. D. Tranqui, R.D. Shannon, H.Y. Chen, Acta Cryst., B35 (1979) 2479-2487.
2. A. Khorassani, A.R. West, Solid State Ionics, 7 (1982) 1-8.
3. Ian M. Hodge, Malcolm D. Ingram, A. R. West, J. Am. Ceram. Soc.,7-8 (1976) 361-366.
4. A. Khorassani, G. Izquierdo, A.R. West, Mat. Res. Bull., 16 (1981) 1561-1567.
5. Y.W. Hu, I.D. Raistrick, R.A. Huggins, Mat. Res. Bull., 11 (1976) 1227-1230.
6. J.G. Kamphorst, E.E. Hellstrom, Solid State Ionics, 1 (1980) 187-197.
7. J. Kuwano, A.R. West, Mat. Res. Bull., 15 (1980) 1661-1667.
8. U.v. Alpen, M.F. Bell, W. Wichelhaus, Electrochim. Acta, 23 (1978) 1395-1397.
9. H. Y-P. Hong, Mat. Res. Bull., 13 (1978) 118-124.
10. P.G. Bruce, A.R. West, Mat. Res. Bull., 15 (1980) 379-385.
11. A.K. Ivanov-Shits, S.E. Sigaryov, Solid State Ionics, 27 (1988) 89-100.
12. A.R. West, J. Appl. Electrochem., 3 (1973) 327-330.
13. Shuji Yamada, Masashi Fujiwara, Motoya Kanda, J. Power Sources 54 (1995) 209.
14. W. Li, J.N. Reimer and J.R. Dahn, Phys. Rev. B 46 (1992) 3236.
15. Chun-Chieh Chang, N. Scarr, P.N. Kumta, Solid State Ionics, 112 (1998) 329-344.
16. Chun-Chieh Chang, P.N. Kumta, J. Power Sources, 75 (1998) 44-55.

Figure Captions

Fig. 1. The phase evolution study of Li_4SiO_4 formation using X-ray diffraction for samples that were heat treated in air from 300°C to 800°C. Li_4SiO_4 is represented by (∗), Li_2SiO_3 and Li_2CO_3 are represented by (∧) and (+) respectively. It should be noticed that Li_2SiO_3 and lithium carbonate are the primary impurity phases.

Fig. 2. The phase evolution study of Li_4SiO_4 formation using X-ray diffraction for samples that were heat treated in oxygen from 300°C to 800°C. Li_4SiO_4 is represented by (∗), Li_2SiO_3 and Li_2CO_3 are represented by (∧) and (+) respectively. It should be noticed that negligible amount of lithium carbonate is observed when samples are heat treated in oxygen.

Fig. 3. The phase evolution study of Li_4SiO_4 formation using X-ray diffraction for samples generated from $LiNO_3$ that were heat treated in air from 300°C to 800°C. Lithium nitrate is the only observable phase before 500°C. (∗) represents $LiNO_3$ and (+) represents $Li_2Si_2O_5$.

Fig. 4. The thermal gravimetric analysis (TGA) data obtained for both $LiOH\cdot H_2O$ and $LiNO_3$ that were heat treated in air. From the TGA data it can be concluded that the formation of Li_4SiO_4 is controlled by the formation of Li_2O from the decomposition of LiOH and $LiNO_3$.

Fig. 5. The specific surface area measurement for the as-prepared powders derived from both $LiOH\cdot H_2O$ and $LiNO_3$, and the samples that were heat treated at 300°C, 400°C and 500°C using the as-prepared powders.

Fig. 6. The crystallization of $LiNO_3$ in the as-synthesized state shown by the XRD analysis.

Fig. 7. The X-ray diffraction pattern of fume silica used as the precursor for synthesis.

Fig. 8. The morphology of fume silica characterized using SEM. (a) At a magnification of 500X and (b) 5000X.

Fig. 9. The morphology of the as-prepared powders generated from $LiOH\cdot H_2O$. (a) At a magnification of 5000X and (b) 10,000X.

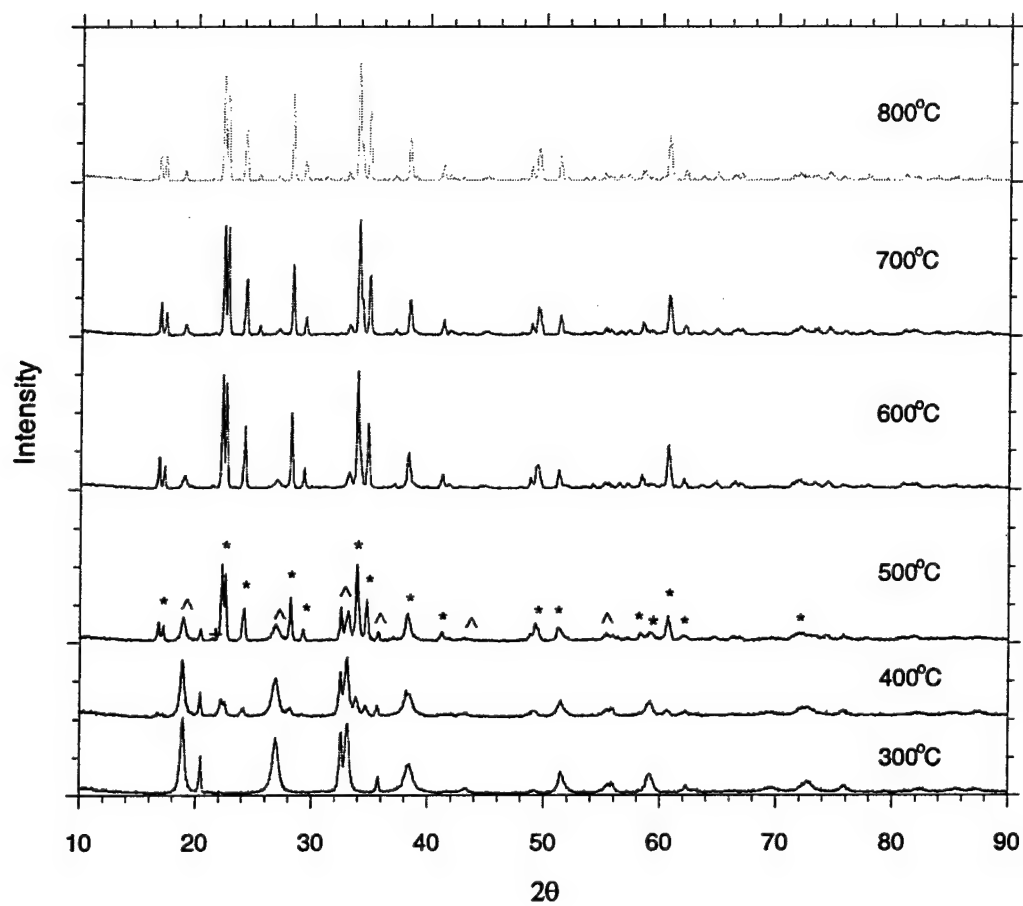Fig. 10. The morphology of the as-prepared powders generated from $LiNO_3$. (a) At a magnification of 5000X and (b) 10,000X.

Fig. 11. The morphology of the of heat treated powders (600°C) generated from both $LiOH\cdot H_2O$ and $LiNO_3$. (a) At a magnification of 5000X and (b) 10,000X.
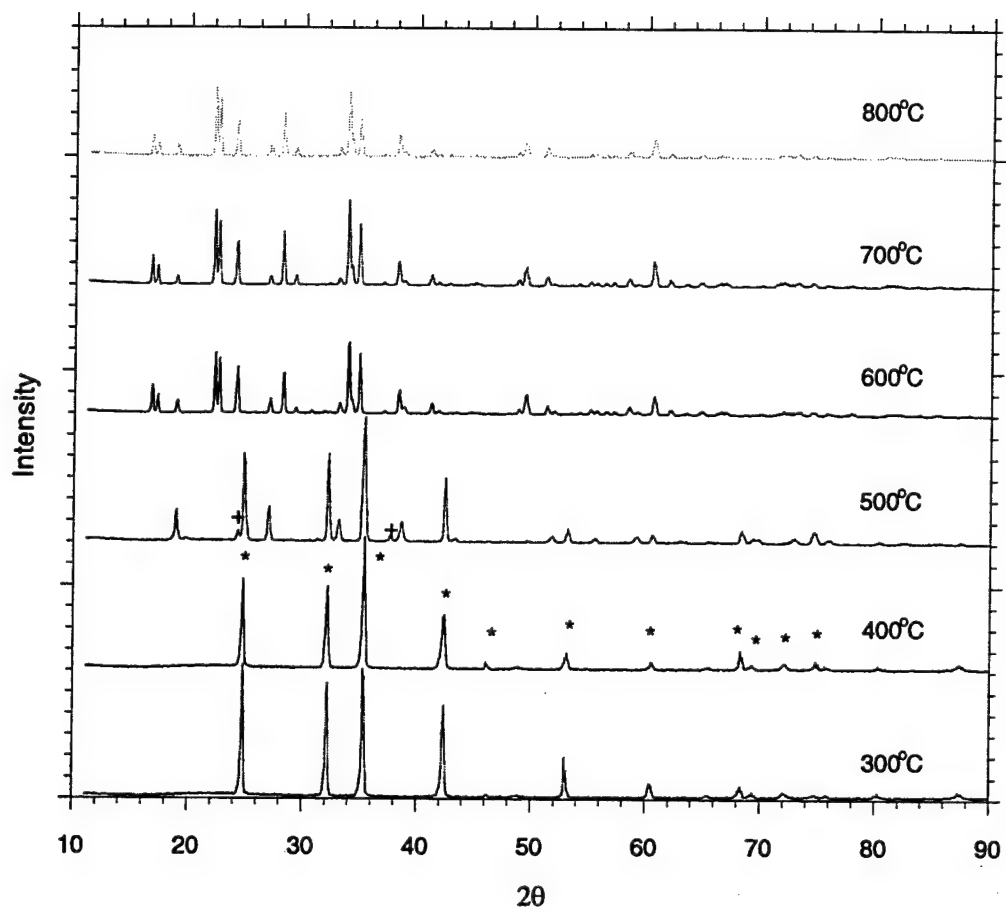
Fig. 12. The XRD analysis conducted for the composite material Li_4SiO_4-$LiNi_{0.75}Co_{0.25}O_2$.
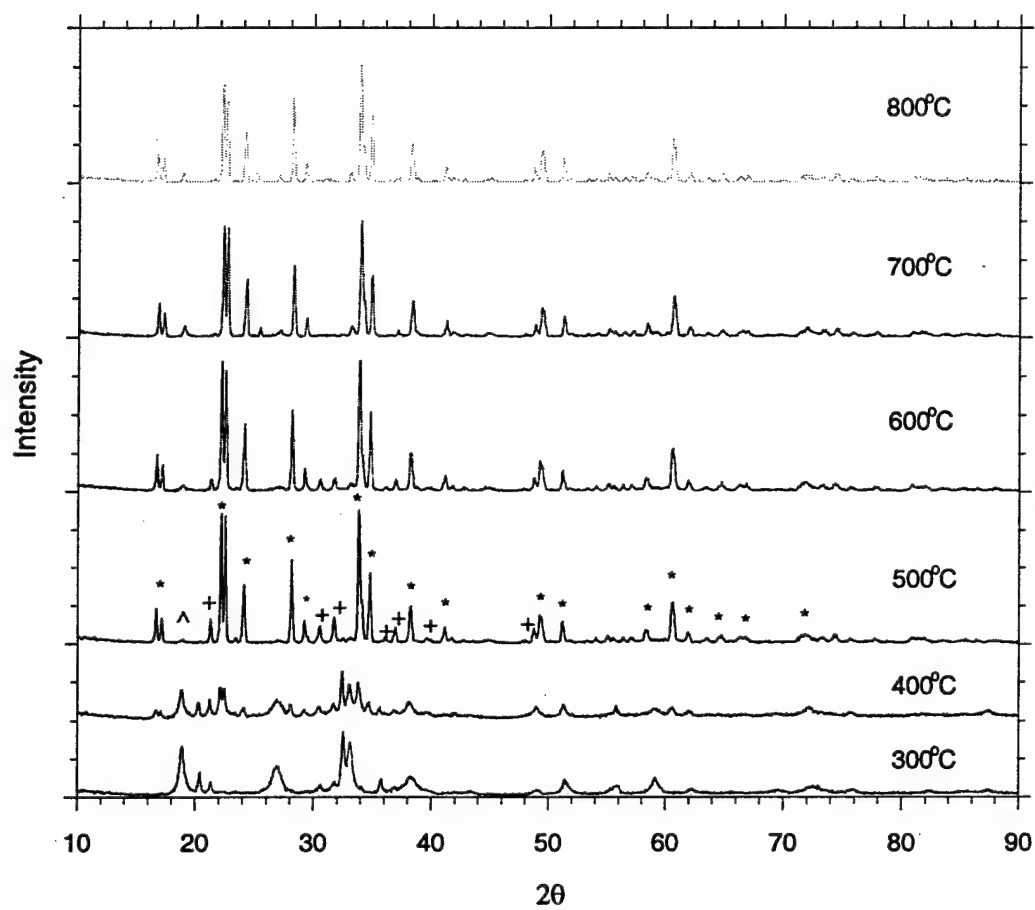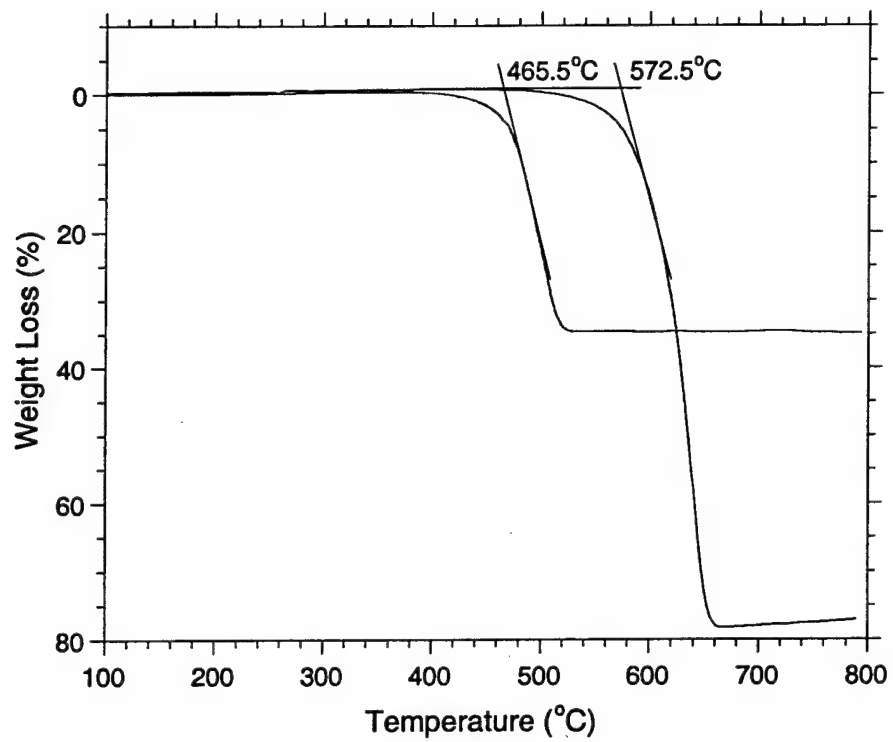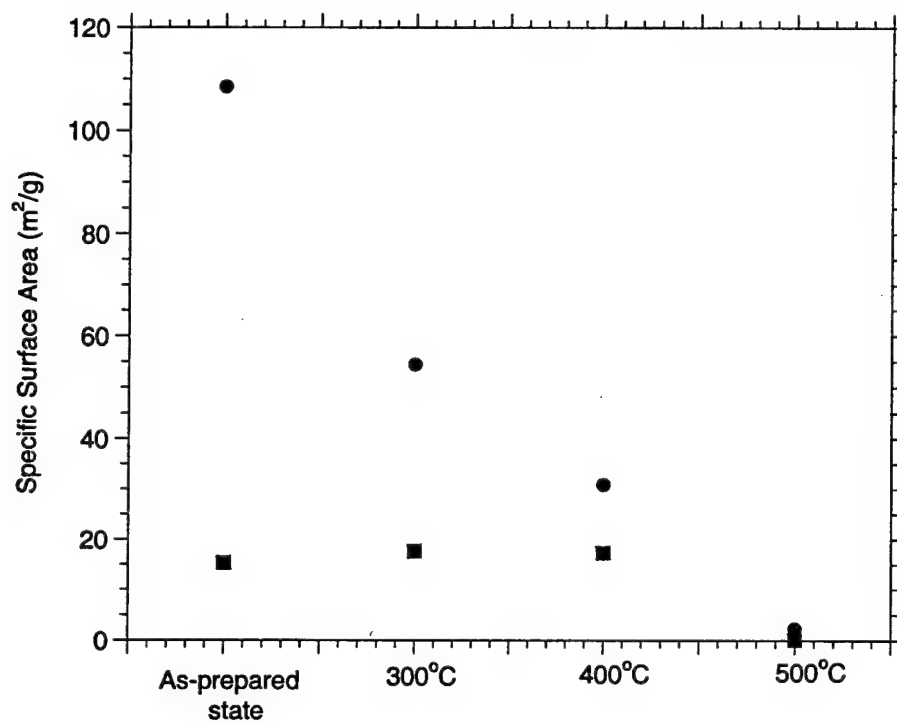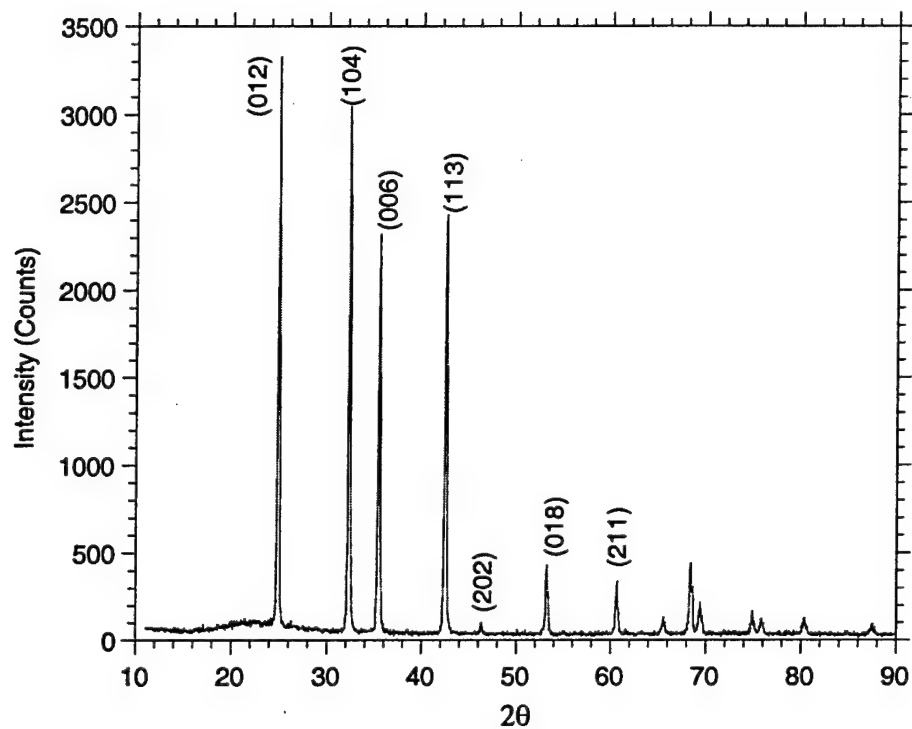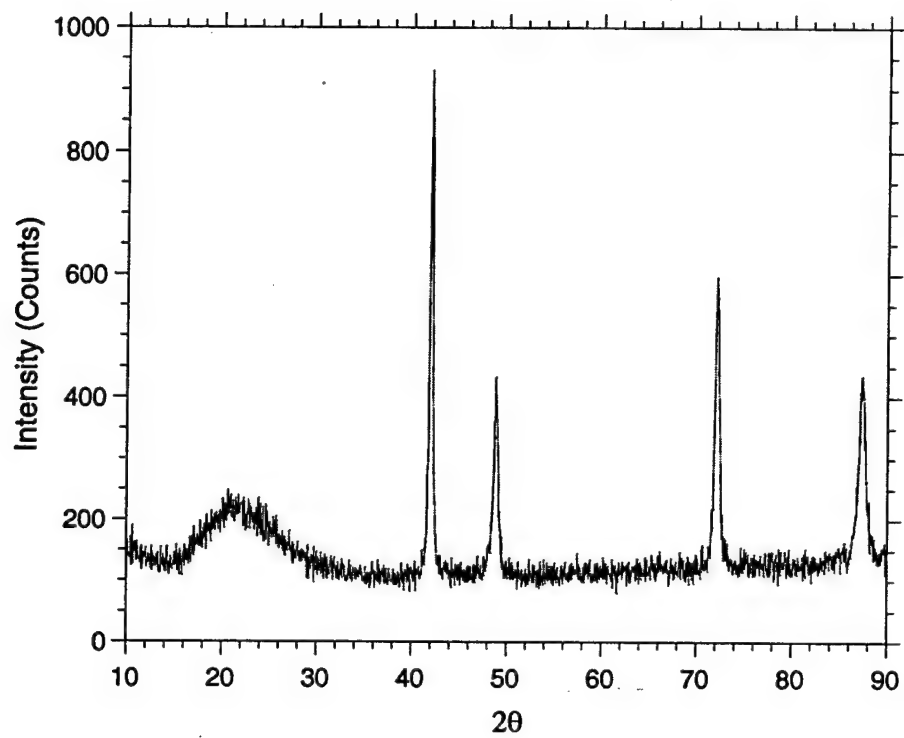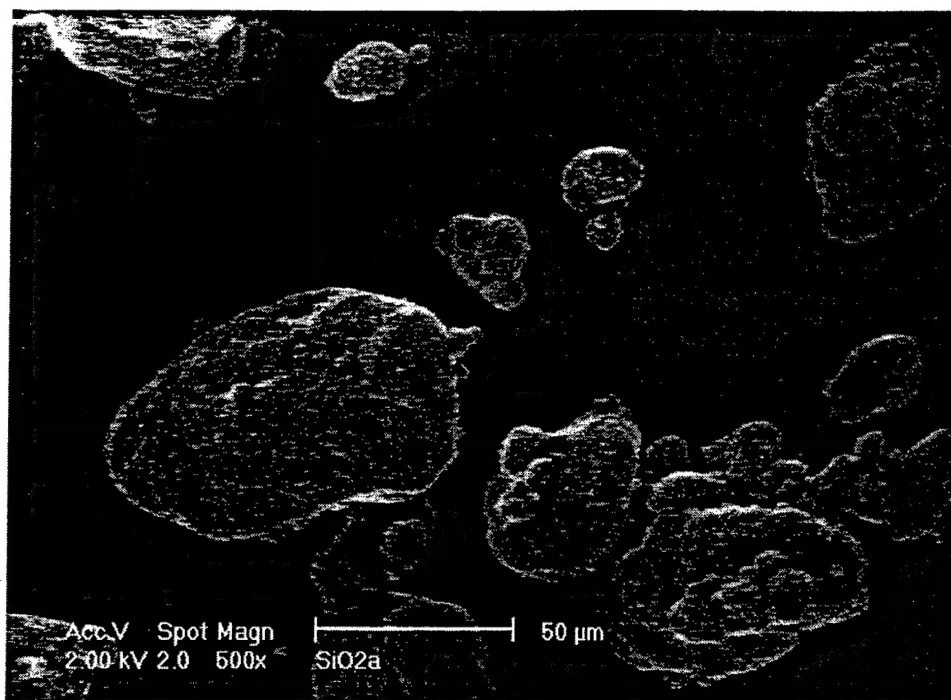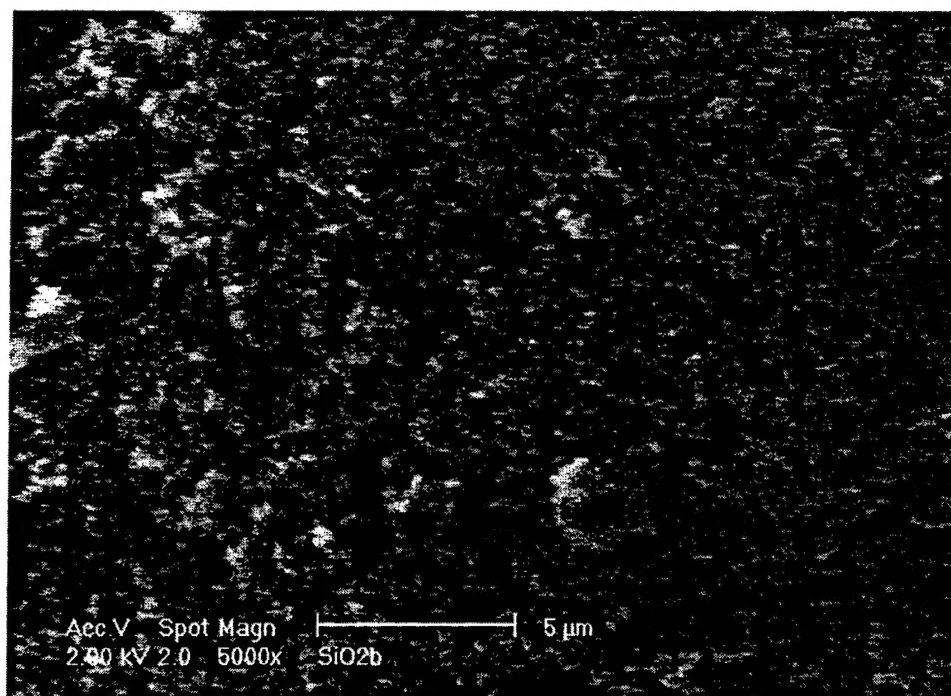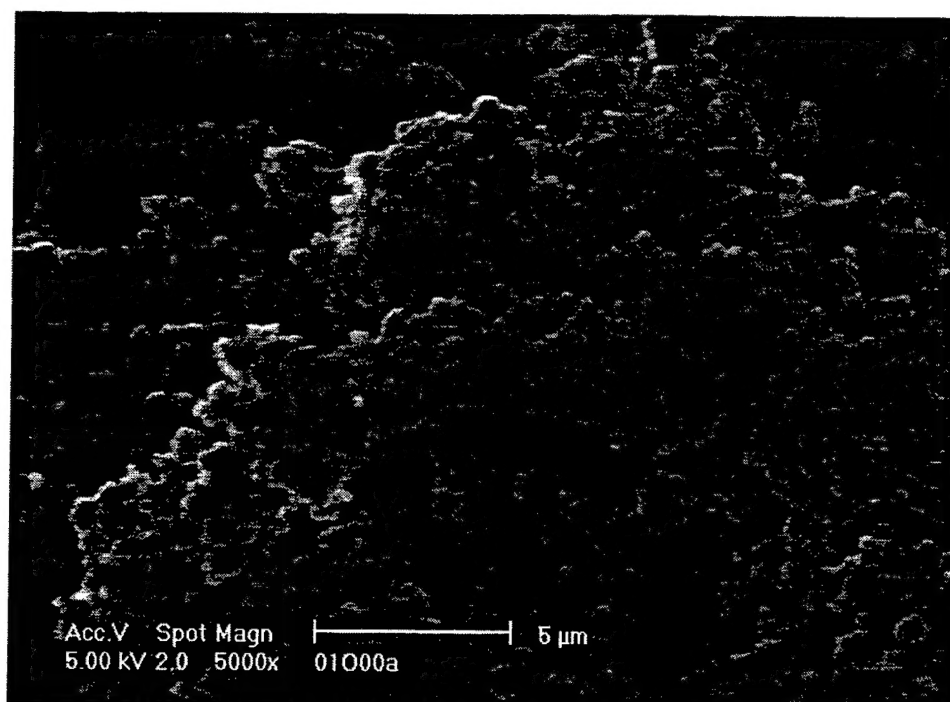
Fig. 1

Fig. 2

Fig. 3
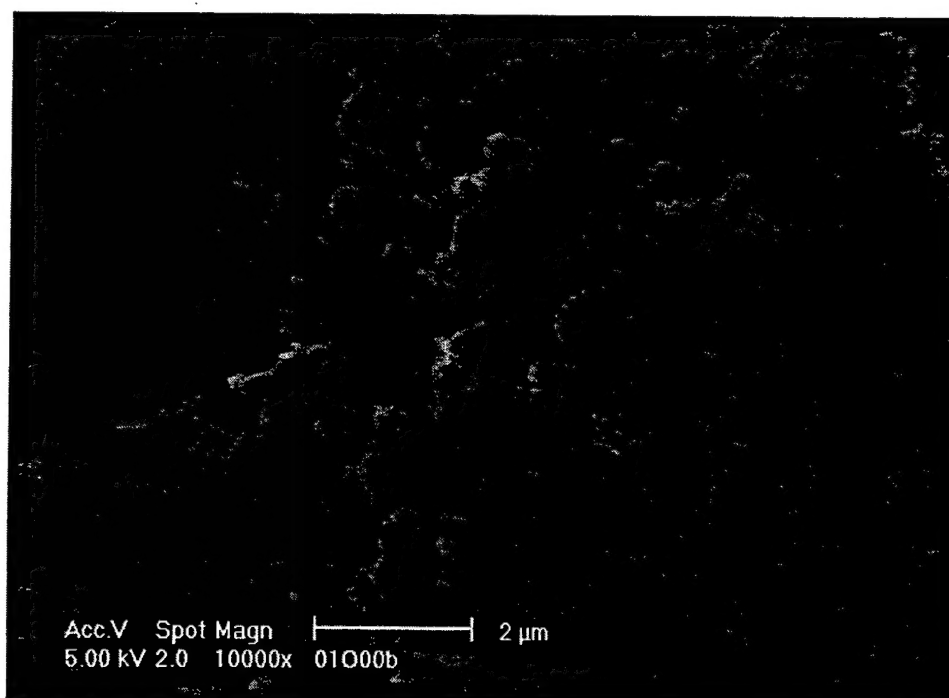
Fig. 4

Fig. 5

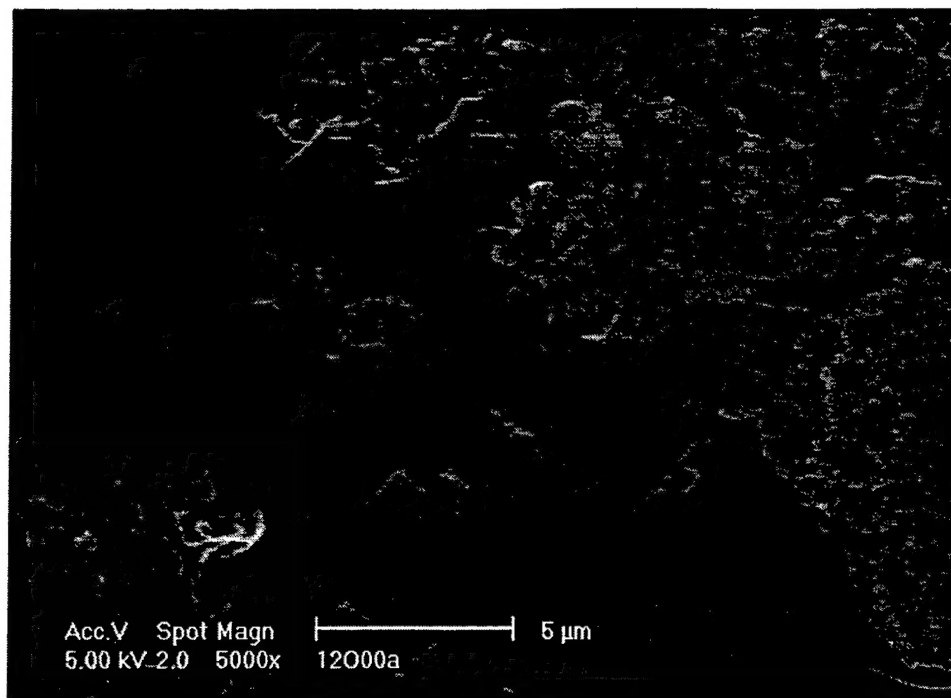**Fig. 6**

Fig. 7

Fig. 8(a)
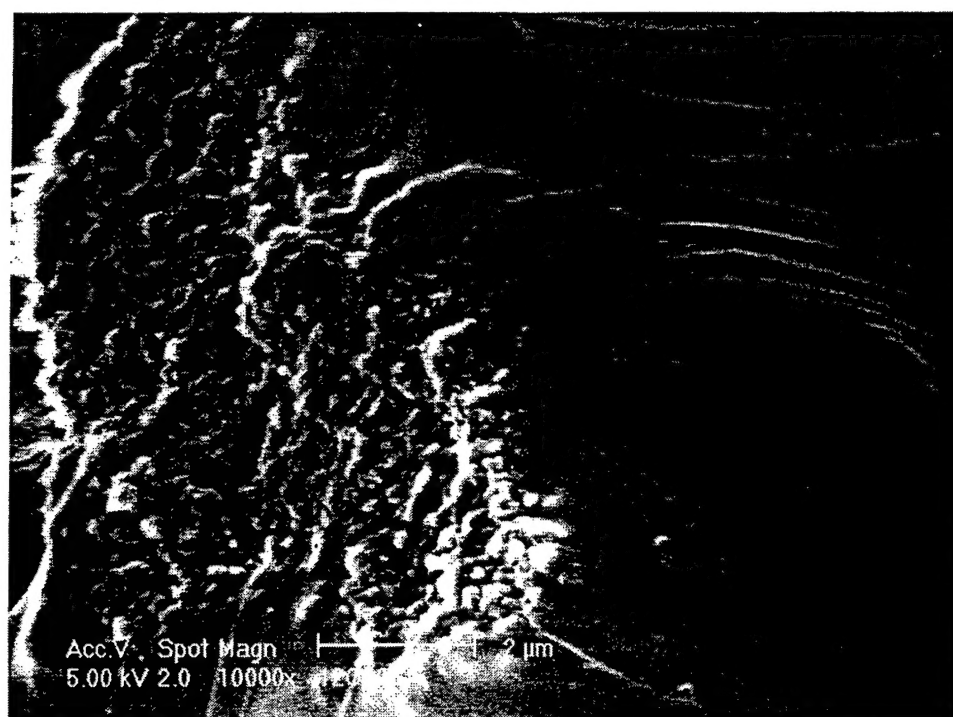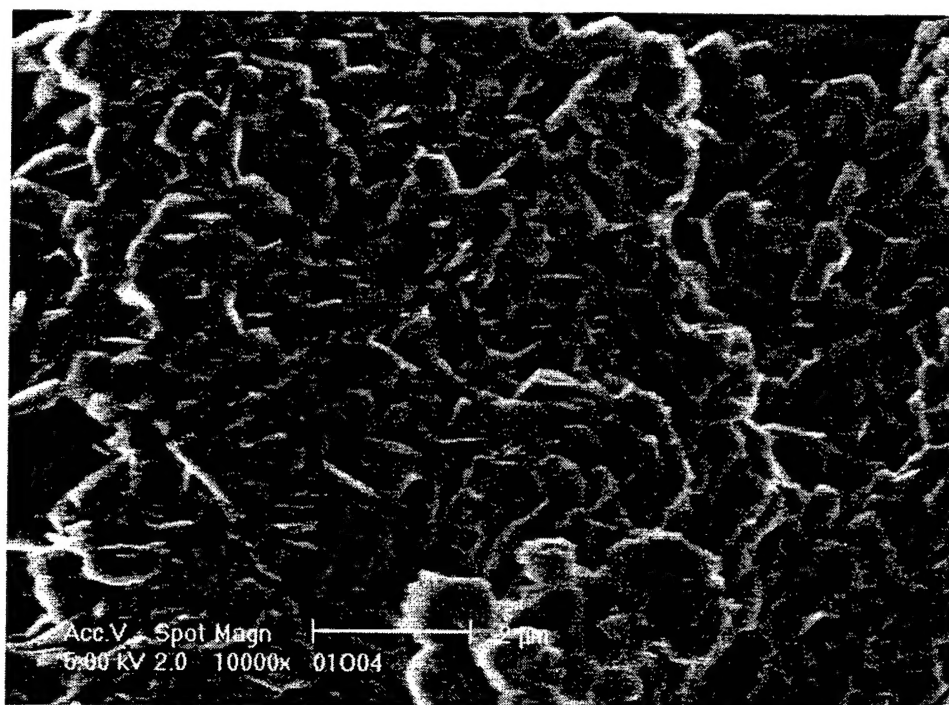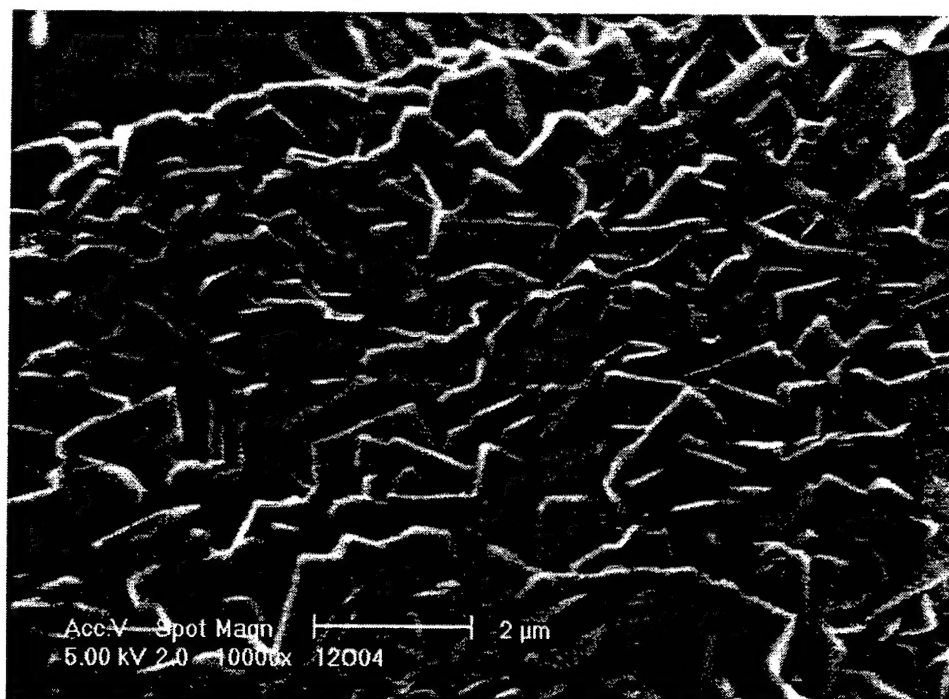

Fig. 8(b)

Fig. 9(a)

Fig. 9(b)

Fig. 10(a)

Fig. 10(b)

Fig. 11(a)

Fig. 11(b)